Identification of Growth Factors and Regulatory Cytokines during Postnatal Cell Cycle Exit in Cardiomyocytes

Inauguraldissertation
zur Erlangung des Grades eines Doktors der Humanbiologie
(Dr. biol. hom.)
des Fachbereichs Medizin
der Justus-Liebig-Universität Gießen

vorgelegt von Adibi, Paniz
geboren in Teheran, Iran

Gießen 2024

Aus dem Fachbereich Medizin der Justus-Liebig-Universität Gießen

Kinderherzzentrum und Zentrum für angeborene Herzfehler,
Zentrum für Kinderheilkunde und Jugendmedizin,
Klinik für Pädiatrische Kardiologie, Intensivmedizin und angeborene Herzfehler

Gutachter:

Prof. Dr. Jux, Christian

Gutachter:

PD Dr. Aslam, Muhammad

Tag der Disputation: 26.02.2025

Table of Contents:

1. Introduction

1.1. Congenital heart diseases:

Structural malformations of the heart lead to 30% of embryonic and fetal lethality prenatally (Hoffman, 1995). Moreover, the leading cause of death worldwide is the result of cardiovascular diseases (CVDs), to which 32% of death cases were attributed in 2019 (World Health Organization, 2021). One type of pediatric CVDs is congenital heart disease (CHD) which is an abnormality in heart structures present at birth. CHD in general can affect normal blood flow within the heart as well as blood circulation. Varieties of CHDs have been reported among which defects in valves such as Ebstein's anomaly (tricuspid valve defect), and aortic and pulmonary stenosis (narrowed valves), or abnormalities in vessels including coarctation of the aorta (narrowing in the aorta), pulmonary stenosis (too narrow or stiff pulmonary valve), interrupted aortic arch, truncus arteriosus, or disturbance in septa such as atrial and ventricular septal defects (a hole in the septa), or under development in heart wall such as hypoplastic left heart syndrome (too small left ventricular chamber), can be mentioned (Hoffmann *et al.*, 2002; National Institute of Health, 2022). Depending on the type of defect, the blood flow can either be decreased or get guided in a wrong direction. The cause of the heart diseases present at birth remains often elusive. Nonetheless, multiple factors have been proven to elevate the risk of CHD. Briefly, certain infections during pregnancy (e.g., rubella), obesity, and poor nutritional status, as well as consumption of certain medications and drugs such as tobacco, alcohol, hydantoin, lithium, and thalidomide by the mother have been mentioned to enhance the incidence of CHDs. Moreover, maternal diseases such as diabetes mellitus, phenylketonuria, and systemic lupus erythematosus can be categorized as environmental risk factors for CHD (Lucile Packard Children's Hospital, 2010). Additionally, a number of genetic conditions namely Down-, Turner-, and Marfan syndrome have been associated with CHD (World Health Organization, 2011). Accordingly, the key factor to build a functional heart is normal and complete embryonic development. Thus, detailed insights into the normal heart function and heart development, as well as the involved factors can be essential in the understanding of the mechanisms contributing to CHDs, as well as prevention and treatment of them.

1.1.1. Function and structure of the mammalian heart

In vertebrates, the heart is the first organ to be fully functional. This organ plays a vital role in nutrients and oxygen distribution (Buckingham *et al.*, 2005). As a muscular organ, it supplements the entire parts of the body with blood, owing to its rhythmic and

continuous contractions. The number of heart contractions (beats) per minute (bpm) in an adult human, at rest ranges from 60 to 100 bpm. With each beat, the heart pumps 60 to 90 milliliters of blood out of itself, which stands for 7600 liters blood transfer per day, or in other words almost over 200 million liters in a lifetime (The Physics Factbook, 2001). In mammals, a mature heart is composed of four valves and four chambers (two cranial atria and two caudal ventricles). Both ventricles are separated from each other via interventricular septum (IVS), which avoids the mixture of blood contents of the ventricles. Likewise, ventricles, the atria exhibit a partition between each other which is called atrial septum. The wall of each heart chamber is constructed from three tissue layers including endocardium (inner layer, endothelial lining of the heart), myocardium (middle layer, cardiac muscle cells) and epicardium (outer layer, source of coronary arteries and cardiac fibroblasts. The arrangement of heart valves and chambers is in such a manner that ensures the unidirectional flow of blood, as well as separation of systemic and pulmonary circulation (Lin, 2012).

The right part of the heart is composed of a cranial right atrium (RA) and a caudal right ventricle (RV) (Figure 1). The cardiac blood circulation includes the pulmonary system, where the RA receives deoxygenated blood from the body periphery via the superior and inferior vena cava vessels. The connection between RA and RV is provided by the tricuspid valve, which allows for a one-way passive flow of deoxygenated blood from the RA into the RV, followed by contraction of the RA and relaxation in RV (Figure 1). From the RV the pulmonary artery arises. As a consequence of RV contraction during systole, the low in oxygen- blood leaves the RV through the pulmonary valve into the pulmonary arteries. Next, the blood is directed to the lungs, where the carbon dioxide is exchanged with oxygen. The left side of the heart is composed of two chambers including the left atrium (LA) and left ventricle (LV). The oxygenated blood from the lungs enters the LA through the pulmonary veins. The flow and subsequent LA contraction transfer the oxygen-rich blood through the mitral valve into the LV (Figure 1). From the LV the aorta arises. As a consequent of LV contraction during systole, the oxygenated blood is transported through the aortic valve into the aorta and distributed into the systemic blood circulation. Thereby the oxygenated blood is delivered to all peripheral organs and tissues of the body. After supplying the body with oxygen and nutrients the blood returns to the RA and thereby another cardiac cycle is initiated (Figure 1).

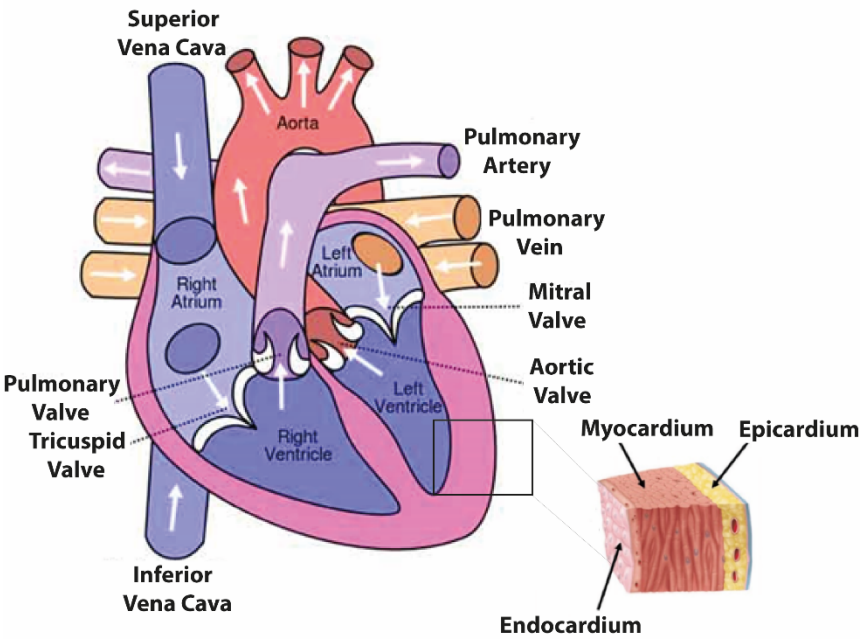

Figure 1. Morphological architecture of the mammalian heart. The mammalian heart is composed of four valves and four chambers. The latter include the right atrium (RA), right ventricle (RV), left atrium (LA), and left ventricle (LV). Each cardiac chamber is composed of three tissue layers: endocardium, myocardium and epicardium. While the RA and RV are separated by tricuspid valve, the LA and LV are separated by mitral valve. The pulmonary valve separates the RV from the pulmonary artery, whereas the aortic valve separates the LV from aorta. The white arrows demonstrate the unidirectional blood flow (scheme modified after Irasto World Health, 2021 and Krishnan *et al*., 2022.

1.1.2. Cardiac cell populations

The heart as a vital organ is composed of various specialized cell populations which interact with each other, to maintain and synchronize heart function. An adult mammalian heart the following main cell types: adipocytes, cardiomyocytes (CMs), endothelial cells (ECs), fibroblasts (FBs), immune cells (e.g., leukocytes), pericytes, mesothelial cells, neuronal cells and smooth muscle cells (SMCs). The determination of these cell types' distribution in the ventricular myocardium is challenging, heavily varies from study to study and is controversial (Litviňuková *et al*., 2020). Accordingly, using fluorescence-activated cell sorting (FACS), Banerjee and colleagues (2007) reported that from the entire cardiac cell population of the adult mouse myocardium, 56% devote to CMs, 7% to ECs, 27% to FBs, and 10% to vascular SMCs. However, in another study performed by Pinto and team (2016), the proportion of murine cardiac nuclei being categorized as CMs were 31% using immunohistochemistry and flow cytometry analyses. Moreover, it was concluded that from the remaining non-myocyte cell population, 64% (of total non-

myocytes) were ECs, 15% FBs, 9% leukocytes, and 12% un-defined cells (Pinto *et al*., 2016). At the outer surface of the heart fat tissue is located. The epicardial fat as a source of free fatty acids, is involved in energy supply and protection against hypothermia of the myocardium (Hatem *et al*., 2016). Additionally, it is also a source of signaling molecules, for example adipokines such as adiponectin. The ECs cover the inner layer of blood and lymphatic vessels. Nonetheless, the EC subtypes among blood and lymphatic vessels are not identical. The ECs not only line the main arterial/venous vessels, but also make up the capillary network. A variety of physiological processes are regulated by EC, including the control of blood flow, vascular permeability, leukocyte trafficking, and angiogenesis. Additionally, the ECs are involved in regulation of nutrition supply of the heart. Upon the interaction with immune cells and fibroblasts, endothelial cell population controls cardiac inflammation and extracellular matrix (ECM) composition (Kamo *et al*., 2015). Fibroblasts (FBs) are composed from several subtypes in the heart, are found throughout the entire cardiac tissue. They surround CMs and bridge 'the voids' between myocardium, in such a way that every CM is closely related to a number of fibroblasts in normal cardiac tissue (Camelliti *et al*., 2005). Cardiac FBs regulate cardiac development, myocardial structure, and electro-mechanical function in both healthy and diseased hearts. Additionally, they produce a variety of extracellular matrix proteins, such as collagens, fibronectin, laminin, and proteoglycans. A large proportion of resident FBs originate from the heart's epicardium during embryonic development (Moore-Morris *et al*., 2016). Studies have revealed that after pressure overload, the ECs give rise to FBs via endothelial-mesenchymal transition (Zeisberg *et al*., 2007). Moreover, the existing FBs are activated to proliferate, produce excessive amounts of ECM and differentiate into myo-fibroblasts following the pressure overload (Camelliti *et al*., 2005; Kanda *et al.*, 2018; Morris *et al*., 2014). The pericytes as part of the cardiac cell populations envelop the ECs of capillaries within the myocardial microcirculation and play an essential role in maintaining blood flow. Additionally, they are able to re-differentiate and thereby give rise to adipocytes, SMCs, and myofibroblasts (Su *et al*., 2021). As another component of cardiac cell populations, neuronal cells should be mentioned. The cardiac autonomic nervous system (CANS) which is composed of the extrinsic and intrinsic innervation of the heart, is involved in regulation of cardiac function. Therefore, its dysfunction causes various heart diseases, for instance cardiac arrhythmias. The cardiac SMC population mainly includes vascular smooth muscle cells (VSMCs), which are located in the medial layer of arteries. VSMCs are crucial for arterial physiology and pathology. These cell

types contract and regulate the blood vessel tone, blood flow and blood pressure. Following vascular injury, VSMCs dedifferentiate from a contractile to a proliferative phenotype. The dedifferentiation stage is characterized by several unique changes, in particular elevated proliferation rates, cellular migration and ECM production (Owens *et al*., 2004; Shi *et al*., 2020). As the most essential cardiac cell population, CMs can be mentioned. Orchestrated sets of contraction-relaxation cycles of CMs drive the pressure needed for heart's function in efficient pumping of blood. Notably, the CM high adenosine triphosphate (ATP) demands for the contractility, is compensated by number mitochondria (Anmann *et al*., 2014; Pasqualini *et al*., 2016). Moreover, to meet the normal heart rhythm, the coordinated contractions of neighboring CMs are needed (Pasqualini *et al*., 2016). Accordingly, the disturbance of this coordinated CM contraction, leads to abnormal heart rhythm.

To build a functional heart, a normal complete embryonic development acts as an essential key player. The developmental mechanisms among various organisms and organ systems are highly conserved. This understanding has provided scientists with multiple model organisms to study heart development. Utilizing an appropriate model organism provides scientists with massive information about the pathogenesis of congenital human diseases and their underlying mechanisms. With this perspective, vertebrates such as mice appear to be appealing models (Rosenthal *et al*., 2007).

1.1.3. Embryonic heart development in mice

1.1.3.1. The development of the primary heart tube

An essential stage during embryonic development is gastrulation that occurs during the second developmental week in humans and seventh embryonic day in mice. It gives rise to three germ layers including endoderm (inner layer, continuous with yolk sac), mesoderm (interstitial layer) and ectoderm (outer layer, continuous with amnion) (Gilbert, 2006). In vertebrates, a variety of organs and cell types are derivatives of mesodermal cells such as cardiovascular system (i.e., heart, blood, and blood vessels), connective tissues, as well as bone, cartilage, and muscle (reviewed by Ferretti and Hadjantonakis, 2019). At embryonic day 6.5 (E6.5) in mice, the mesodermal cells (which later form the myocardial progenitor cells), are positioned in the anterior region of the

primitive streak, and posterior to the node within the embryonic plate (Buckingham *et al*., 2005). Cranial and lateral migration of these mesodermal cells favors the formation of somatic and lateral plate mesoderm on the left and right side of the neuronal tube located under the head folds (Figure 2A) (Moorman A. *et al*., 2003). The lateral plate mesoderm enlarges, which later separates into somatic and splanchnic layers (Onimaru *et al*., 2011). The splanchnic mesoderm is the source for cardiac progenitor cells. At E7.5, a crescent-like cardiogenic plate is formed at the pharyngeal region on both sides of the anterior splanchnic mesoderm (Figure 2B) (Buckingham *et al*., 2005; Gittenberger-de Groot *et al*., 2005; Onimaru *et al*., 2011). The already formed crescent is composed of two groups of progenitors, namely the first heart field (FHF), and the second heart field (SHF). Upon migration of precardiac cells from the FHF into the ventral midline and their fusion, a primary heart tube is formed at E8 (Figure 2C) (DeRuiter *et al*., 1992; Gittenberger-de Groot *et al*., 2005). This linear heart is composed of a myocardial and an endocardial cell layer. The second group of the progenitor cells (SHF) in return, are involved in growth of the primitive heart tube. Accordingly, they migrate anteriorly (atrial pole) and posteriorly (venous pole), and thereby developing to the outflow tract and RV, as well as the parts of atria (Kelly *et al.,* 2001; Zaffran *et al*., 2004). Moreover, signals originating from myocardium cause epithelial to mesenchymal transition of endocardial cells, and thereby formation of mesenchymal endocardial cushion cells (ECCs) which are involved in the separation of atrioventricular canal (Moorman, A. F. M. *et al*., 2003).

The primary linear heart tube composed of the monolayer endocardial cells (basal), cardiac jelly (middle), and monolayer myocardial cells (apical), has an inverted Y-shape. Two inferiorly positioned parts of the Y-shaped heart are known as venous pole that are continuous with the venous branches of the developing embryo, yolk sac, and placenta. Notably, the venous pole will later develop into atrial chambers and inflow tract, whereas its stem will later give rise to the ventricles and outflow tract (De la Cruz *et al*., 1991). The heart tube shows peristaltic contractions, which allows for blood transport in the direction from its posterior (caudal) (venous pole) to (cranial) anterior arterial pole (where the out-flow track is forming).

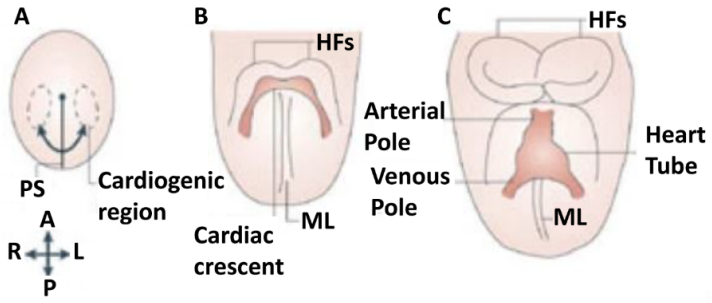

Figure 2. Scheme of the position and morphogenesis of the mouse heart tube. A) The origin of myocardial progenitor cells is the epiblast cells, residing in the lateral sides of the primitive streak (PS). At E6.5 the progenitor cells migrate to the anterior (or cranial) regions of the embryo's PS. B) These mesodermal cells migrate bilateral and localize caudal (or posterior) the head folds (HFs), and form a crescent like structure composed of the anterior first and posterior second heart fields at E7.5 (shown in brown; ML: midline). C) The formation of the linear heart tube at the ML, through fusion of the cardiac crescent (E8). The heart tube is composed of a venous and arterial pole, positioned at its posterior and anterior side, respectively. A: anterior (cranial), *P*: posterior (caudal), L: left and R: right. Modified after Buckingham *et al.*, 2005.

1.1.3.2. Formation of heart chambers

Within the primitive linear heart tube, at the ventral part of the developing ventricular chamber, and dorsal part of the future atrial chamber, the ballooning takes place (Figure 3A). This ballooning results in an S-shaped heart tube, chambers specification and the balboventricular groove or known as interventricular groove (BVG) development (between the developing ventricle) (Anderson *et al*., 2014; Moorman *et al*., 2003). Moreover, the interventricular groove formed within the heart tube, together with the ECCs will later contribute to septal structures (separating all the four chambers) and cardiac valves. In parallel to the ballooning of ventricles, the third cardiac cell layer called epicardium evolves, which later covers the developing heart by the end of looping at E10.5. The so-called pro-epicardial organ is positioned caudal to the heart and forms mesothelial structures, from which cells migrate over the surface of the heart, and thereby form the epicardium. The epicardial mesenchymal cells later contribute to the cardiac fibroblasts, cardiac-cushion mesenchyme (ECCs), and coronary arteries' endothelial and smooth muscle cells (Dettman *et al*., 1998; Mikawa *et* al., 1996).

The mammalian heart is not symmetrical. The symmetrical primary heart tube becomes asymmetrical upon looping, which is conducted by the node. The nodal proteins' spatial expression and activation are involved in the determination of the left and right side of the embryo, which supports proper looping (Gilbert, 2006). As the heart tube grows, it

gradually bends leftwards and loops rightwards. By E8.5, following the rightward looping, the posterior region (venous pole) of the heart tube moves anteriorly (cranial) (Figure 3B) (Buckingham *et al*., 2005). At the end of the looping process, both developing ventricles are positioned at the caudal side of the embryo, whereas the developing atria and the outflow tract are localized at the cranial side. Additionally, ECCs swellings are formed and positioned in the atrioventricular canal (Anderson *et al*., 2014). During E10.5, the first anatomic features of septation are observed, with formation of the primary atrial septum. Subsequently at E11.5, from the atrial groove (Figure 3C, shown in orange), the muscular structure with a mesenchymal cap at its tip expands toward the ECCs in the AV canal. After the cap reaches the atrial side of the ECCs, they fuse and thereby two atria get separated by the atrial septum (Figure 3C to 3G) (Anderson *et al*., 2014).

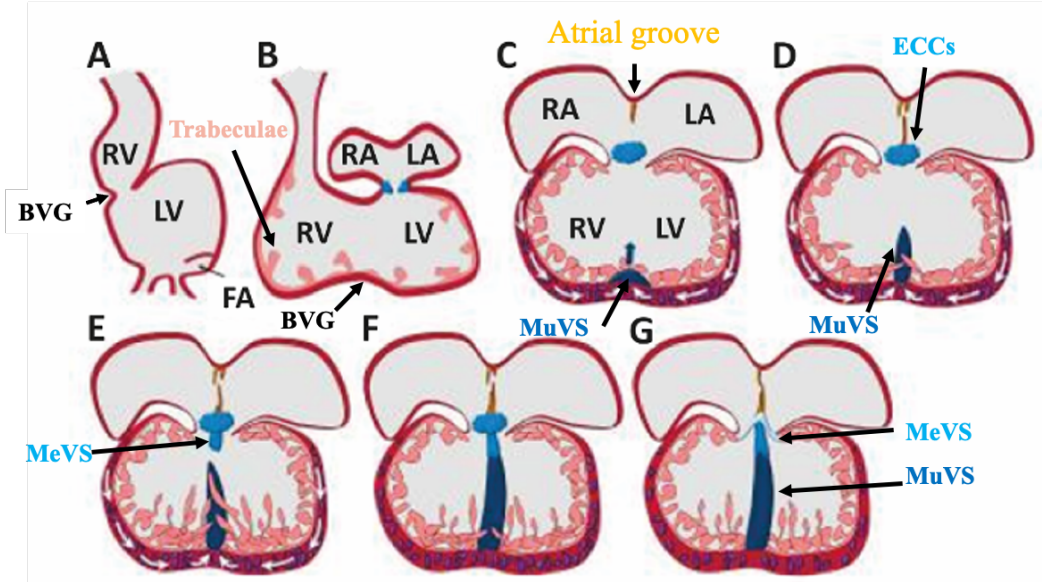

Figure 3. Chamber development and septation in the mouse heart. A) Balboventricular groove (BVG) is formed between the developing left (LV) and right (RV) ventricles as a consequence of the ballooning of the primary heart tube. FA: Future atrium. B) The rightwards looping of the heart tube leads to posterior positioning of the developing ventricles, and anterior positioning of the developing atria. RA: Right atrium, LA: Left atrium. The luminal outgrowths of trabecular structures from the myocardium have been demonstrated in pale red. C) The MuVS (dark blue) is developed by cardiomyocyte (CM) proliferation located at the wall of the developing LV and RV towards the BVG. D) Participation of trabeculae supports muscular ventricular septal (MuVS) development and growth. E) Molecular interactions between MuVS and the cardiac-cushion cells (ECCs) induces formation of membranous ventricular septum (MeVS) in ECCs. F) Fusion of MuVS and MeVS causes the formation of the IVS. G) Atrioventricular valves arise from ECC (light blue) (modified after Wiegering *et al*., 2017).

Septation of ventricular chambers is initiated at E9.5. Both ventricles are separated from each other by an IVS which is composed of two types of tissues, including the muscular and membranous part (Franco *et al*., 2006; Savolainen *et al*., 2009; reviewed by

Wiegering *et al*., 2017). Between E9.5 to E11.5, the proliferation of cardiomyocytes (CMs) localized within the wall of the LV and RV towards the BVG (or interventricular groove), leads to outgrowth of the muscular part of the IVS (MuVS (Franco *et al*., 2006) towards the ECC of the AV canal (Figure 3C-D). At the same time (E9.5), after looping of the linear heart tube, a complex made of ridge-like myocardial muscle cells termed trabeculae carneae appears (Figure 3B, demonstrated in pale red), between the external myocardial layer and internal endocardial epithelium. In the course of trabeculation, the cardiomyocyte (CMs) located at the developing ventricles grow towards the lumen of the ventricles the ridge-like structures (in pale red, Figure 3B).

Trabeculae support the development of the IVS; they fuse with the developing MuVS and boost its outgrowth from the BVG (Figure 3D to 3F) (Ben-Shachar *et al*., 1985; Captur *et al*., 2016; Contreras-Ramos *et al*., 2008). After the MuVS is formed (Figure 3D-G, demonstrated in dark blue), molecular interactions between MuVS and the ECCs (Figure 3F, demonstrated in light blue in form of a cloud) occur, which results in induction of the membranous part of the IVS (MeVS) developing from the ECCs in the AV canal (Eisenberg *et al*., 1995; Franco *et al*., 2006). The MeVS grows towards the MuVS such that after their fusion the IVS is formed (Figure 3E-G) (Anderson *et al*., 2014). By E14.5, the cardiac chambers are septated and the connections to the pulmonary and systemic blood circulation are completed (Buckingham *et al*., 2005).

The early murine embryonic heart does not possess a coronary circulation, which is essential for supplementing the growing myocardium with nutrient and oxygen. Nevertheless, the trabecular structures facilitate the exchange of nutrient and oxygen by increasing the surface area (Sedmera *et al*., 2000). Moreover, at E14.5 the coronary plexus is developed gradually which allows for blood supplementation of the myocardium. Later on, at the basal site the trabeculae merge with the ventricular wall, enhancing the thickness of the compact myocardium. From basal to the apical part, the myocardium gradually compacts inwards the ventricular lumen. Consequently, a ventricular wall which is composed of a compact myocardium covered with smooth endocardium, is formed (Zhang *et al.,* 2013). In the course of ventricular compaction, the spaces between the trabeculae are compressed to capillaries, on one hand. On the other hand, the endothelial cells of the endocardium develop to the intramyocardial coronary vessels (Sedmera *et al*., 2000; Tian *et al*., 2014; Wu *et al*., 2012). Notably, as a consequence of trabeculation two myocardial domains are developed such as a trabecular zone and sub-epicardial compact zone. Studies in mouse and chicken have concluded that the CMs located in these two

domains share the identical origin via lineage tracing. Nonetheless, the compact and trabecular CMs exhibit distinctions in morphogenesis, proliferation capacity, and gene expression. For instance, concerning the proliferation capacity, the CMs of the trabeculae are less proliferative compared to the compact CMs (Chen *et al*., 2004). Collectively, during the later stages of cardiogenesis, the coordinated proliferation of cardiac cell types is essential to ventricular chamber development. With this regard, the enhanced myocardial mass is of critical importance for the adequate mechanical work of the developing heart, which is essential for the blood circulation within the developing embryo (Chien *et al*., 2008).

1.1.3.3. Cell cycle regulation

The proliferation or also known as the cell cycle is a sum of events, based on which the cell components are duplicated and finally divided among two daughter cells. The cell cycle is comprised of interphase and cell division. During interphase, a cell gets gradually prepared for division. Thus, the cell's DNA, organelles, proteins, and size become duplicated, which are later spread equally between two newly formed daughter cells at the end of the cell division. The interphase is further subdivided into three phases: Gap1 (G_1), Synthesis (S), and Gap2 (G_2). In the G1 phase a cell's size, protein content, and organelle number get elevated. After G_1, the cell either decides to continue into S phase, or to terminate the cycle and enter G_0 (resting phase). As the key regulatory molecules which determine the progression of the cell cycle, different Cyclins and Cyclin-dependent kinases (CDKs) are required. The CDKs show catalytic activities only following an interaction to Cyclins, upon which they perform a phosphorylation reaction. This phosphorylation induces activation or inactivation of a target protein, thereby regulating cell cycle progression into the next phase. The cell cycle checkpoint from G_1 to S is orchestrated by CDK4/6. CDK4/6 itself are activated by type-D Cyclins (Cyclin D1, Cyclin D2, and Cyclin D3) and inhibited by Cyclin dependent kinase inhibitors (CDKIs) of the INK4 family ($p16^{INK4A}$, $p15^{INKB}$, $p18^{INK4C}$, and $p19^{INK4D}$). The active cyclin D-CDK4/6 complex phosphorylates the tumor suppressor protein Retinoblastoma (Rb). Normally, unphosphorylated Rb recruits and deactivates E2F transcription factors, and thereby suppresses their transcriptional activity. However, in the presence of cyclin D-CDK4/6, phosphorylated Rb is unable to interact and suppress the E2Fs, which leads to increased expression of G1/S target genes, such as Cyclin E, Cyclin A, and Cyclin B

(Asghar *et al*., 2015; Ding *et al*., 2020). During late G1, the Cyclin E1 and E2 proteins interact with CDK2 and activate it. Under normal conditions and in the absence of Cyclin E1/2, CDKIs such as $p21^{CIP1}$ and $p27^{KIP1}$ inhibit the CDK2. Accordingly, as a consequence of CDK2 inhibition, the E2F transcription factors are suppressed, leading to inhibition of their target genes' expression. However, the active Cyclin E1/2-CDK2 complex by phosphorylation and inactivation of 27^{KIP1} and Rb (leading to release of E2F), promotes the cell-cycle progression from G1 to S, by regulating DNA replication, centrosome duplication, and histone H2B expression. During the DNA replication, the replication factors A and C recruit the DNA polymerase by loading the PCNA protein onto the chromatin, which promotes the DNA synthesis. PCNA in return, is regulated by Rb. Notably, CDK2-induced phosphorylation and inactivation of Rb, has a positive role in DNA replication (Sever-Chroneos *et al*., 2001). Moreover, the Cyclin E1-CDK2-induced phosphorylation of the centrosome proteins including CP110, NPM, and MPS1 leads to centrosome duplication (Chen *et al*., 2002; Fisk and Winey, 2001; Okuda *et a*l., 2000). Finally, the Cyclin E-CDK2-dependant phosphorylation of the nuclear protein coactivator of histone transcription (NPAT), activates the promoter of histone H2B needed for replication (Ma *et* al., 2000). G_1 is followed by S phase during which the nuclear/genomic DNA is duplicated. Close to S phase entry, Cyclin A competes with Cyclin E, and replaces it from the CDK2 complex while Cyclin E1/2 is rapidly ubiquitinated and degraded. By the end of S phase, each chromosome consists of two sister chromatids. The active Cyclin A-CDK2 complex drives S phase termination and S to G_2 transition. After the DNA replication is completed, the cell enters the G_2 phase during which protein synthesis and cell growth essential for mitosis, take place. Here similar to the G_1 phase, a checkpoint (called G_2 /M checkpoint) determines whether the cell can progress to the next phase or not. At this point, any possible damage of the genomic DNA is monitored. Either the damages are repaired, otherwise the cell is sentenced to undergo apoptosis. The Cyclin A-CDK2 complex activates CDK1, which promotes transition to the M phase following an interaction with Cyclin B (Ding *et al*., 2020). The activity of CDK1 favors nuclear envelope disassembly, chromosome condensation, and the mitotic spindle assembly (Ding *et al*., 2020; Gavet *et al*., 2010). Therefore, the chromosome pairs become condensed and attached to the microtubules. Later on, the microtubules pull on of each sister chromatids per chromosome towards the opposite cell poles. This promotes the separation of each sister chromatid, and their localization at opposite cell poles. Furthermore, upon enwrapping of both DNA sets at

each cell side by the nuclear envelope, mitosis is terminated. The outcome of mitosis is karyokinesis that stands for nuclear division and is followed by cytokinesis. During cytokinesis, the already separated nuclei, as well as cytoplasm, organelles and cell membrane are separated and divided in two daughter cells. Hence, as an outcome of cell cycle completion two cells are generated from one cell.

1.1.3.3.1. Cardiomyocyte cell cycle activity and regeneration during the fetal stages

The main driver of cardiac growth during intrauterine development is cardiomyocyte division, which is modulated by several molecular and cellular events (Karra *et al*., 2017). Throughout early cardiogenesis in mammals, cardiac progenitor cells differentiate into cardiomyocytes (Figure 4A). Multiple factors including local activin/nodal, Bone morphogenetic protein (BMP), Fibroblast growth factor (FGF), Wnt and retinoic acid signaling gradients guide and restrict the cardiac progenitor cell pool as well as their addition to the developing linear heart tube. From the looping stage and throughout subsequent phases of cardiac development, immature cardiomyocytes expand in number by cell division resulting in hyperplastic heart growth (Meilhac *et al*., 2003; Karra *et al*., 2017) (Figure 4A). Hyperplasia stands for the enlargement of an organ or tissue owing to cellular proliferation meaning complete progression through the cell cycle (karyokinesis followed by cytokinesis), leading to development of two diploid mononuclear CMs (Chapter 1.1.3.3.). In addition to immature CMs, during the embryonic stages, differentiated CMs showing sarcomeric structures exhibit mitotic figures, revealing the ability of fetal already differentiated CMs to proliferate. Moreover, the proliferation rate at various parts of the developing heart is diverse (i.e., trabecular region vs. compact region of the ventricular myocardium), which is essential for heart morphogenesis before delivery (Yutzey, 2017). The cell cycle activity in CMs has been reported to be at its highest level at E10.5 to E12.5. Indeed, studying the dynamics of CM cell cycle activity during embryonic stages including E12.5, E15.5, and E18.5, Soonpaa and teams (1996) noticed that almost 33% of mouse CMs exhibited an activity in S-phase at E12.5. However, compared to E12.5 at E15.5 and E18.5, this rate was decreased to ~25% and ~10%, respectively (Soonpaa *et al*., 1996). In another study, at E10.5, E12.5, and E14.5 the average of CMs revealing a cell cycle activity was ~22.5% in average. Compared to all three mentioned stages, at E18.5 this rate declined to 10% in mouse ventricular CMs

(Hirai *et al*., 2016). Consequently, it can be pointed out that the cell cycle activity in mouse CMs at early embryonic stages is much higher compared to late fetal stages.

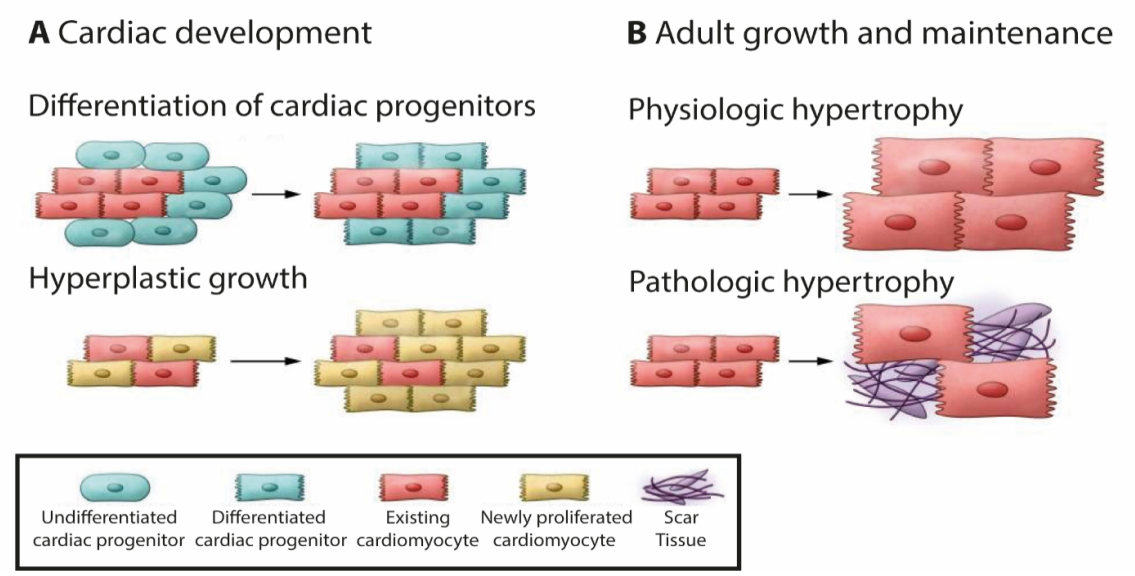

Figure 4. Murine cardiac growth pattern during developmental stage vs. adulthood. A) Embryonic cardiac growth: Undifferentiated cardiac progenitor cells (blue oval cells) are transformed to the differentiated ones (top-left). The already differentiated CMs (in red) perform proliferation, which increases their population (yellow) (bottom-left). B) Growth pattern in adult CMs: Physiological hypertrophic growth observed in adult CMs, which leads to increase in size of pre-existing CM (top-right). CM loss leads to pathological hypertrophy and growth in remaining CMs (bottom-right) (image taken from Karra *et al*., 2017).

1.1.4. Postnatal cardiac growth in mammals

A separation from an intrauterine environment that provides the fetus with the monitored nutrition, oxygen, and temperature by through placental connection to the mother, accounts for an extreme change. Therefore, within the first few hours of the exposure to the extrauterine environment, the neonatal CMs undergo multiple adaptations such as changes in cell cycle activity and growth, morphology, and metabolism (Ahmad *et al*., 2018; Yester and Kühn, 2017).

Mammalian heart size expands by almost 18-fold during adolescence, compared to neonatal heart (Bergmann *et al*., 2015). The increase in postnatal heart size is due to a process called hypertrophy, through which the volume of existing cardiac myocytes enhances (Guo *et al*., 2020). In postnatal mammals, heart growth is synchronized with its functional load demand. Postnatal hypertrophy is accompanied by several hallmarks including enlarged CMs, binucleated CMs, increased myofibrils and mitochondria, and

matured intercalated discs (so CM terminal differentiation). Immediately after birth, the oxygen supply of the mammalian body shifts from the placenta-based to a lung-derived type. This switch demands a complex series of structural and functional modifications, by which the circulating blood is guided from the RV into the lung. Therefore, within the first few hours of the exposure to the extrauterine environment, rapid anatomical and morphological adaptations occur in the mammalian heart (Ahmad *et al*., 2018). Increased hemodynamic load promotes a hypertrophic response to counterbalance the elevated mechanical stress in the ventricular wall (Mc Mullen *et al*., 2007; Zak, 1984). In fact, depending on the duration, type and magnitude of the enhanced cardiac workload, there are two sub classifications of cardiac hypertrophy, namely physiologic and pathologic hypertrophy. Physiological hypertrophy arises as a result of normal cardiac growth and maintained function. During normal postnatal growth, pregnancy and even in the case of physical exercises, physiological growth is promoted, where the pre-existing CMs enlarge (Figure 4B-Top panel). Consequently, the heart to body weight ratio shows an increase of about 10% to 20%, which is not considered a risk factor for heart failure (Maillet *et al*., 2013). It has been demonstrated that during the initial stages of hypertrophy, the $Ca2^{+}$ influx and mobilization are elevated to increase heart function and contractility (Arsenescu *et al*., 1978; Carvalho *et al*., 2006). Additionally, the prolonged pressure overload-induced pathological hypertrophy is involved in increased sarcoplasmic reticulum (SR) Ca^{2+} transport, which is supportive for cardiac function (Limas *et al*., 1980).

Notably, the cell cycle activity and its regulation following a delivery was the main focus of this thesis. Therefore, it is initially essential to address the postnatal cell cycle activity in mouse cardiac cells.

1.1.4.1. CM postnatal growth and cell cycle activity in mouse

The cell cycle withdrawal occurs within the first two weeks after birth in murine CMs (Hirai *et al*., 2016; Porrello *et al*., 2011; Soonpaa *et al.*, 1996). Furthermore, in vertebrates during the postnatal life period, the ability of CMs to re-enter the cell cycle and undergo cell division declines dramatically. Accordingly, at E18.5, the average CM proportion showing a cell cycle activity was reported to be almost 10% in mouse ventricular myocardium. However, after delivery at postnatal day 1 (P1), approximately ~4.5% of the entire CMs exhibited an activity in S-phase of the cell cycle. Compared to P1 the cell

cycle activity in murine CMs was decreased remarkably at P10, reaching to less than 1%. Furthermore, from P14 onwards, the murine CMs revealed almost no cell cycle activity (Soonpaa *et al.*, 1996).

Indeed, understanding the dynamics of CM proliferation and growth pattern after birth may serve as an essential factor concerning regenerative therapies in heart disease. In the course of postnatal heart growth, mammalian CMs undergo several alterations, including binucleation and polyploidization. Notably, mature CMs in mice and humans do not proceed through the final stage of the cell cycle (i.e., cell division). In mice in particular, this incomplete CM division leads to binucleation or polyploidy. Briefly, murine CMs experience karyokinesis (nuclear division) without subsequent cytokinesis (cell division). Consequently, single cells with two nuclei (binuclear) arise from mononucleated CMs, which is observed in 90% of mature cells (Soonpaa *et al*., 1996). In contrast to murine CMs, CMs in humans complete an S-phase of the cell cycle (including DNA replication) but do not undergo karyokinesis. Due to endoreplication in the absence of subsequent karyokinesis, nuclei contain two or more sets of genetic materials within each CM nucleus, which is known as polyploidy (Brodsky *et al*., 1994; Olivetti *et al*., 1996). This polyploidization in human CMs is established in the second decade of life (Bergmann *et al*., 2015). Indeed, polyploidization and binucleation have negative impact on proliferation in CMs. Studies have claimed that some diploid mononuclear adult CMs might have retained proliferative ability following myocardial injury (Patterson *et al.*, 2017). However, polyploidy in CMs has shown to be correlated with increased cell size, which seems to be involved in maturational hypertrophy (González-Rosa *et al*., 2018; Guo *et al*., 2020; Liu *et al*., 2019).

Stereological analyses in mouse hearts have revealed that the total number of CMs in the early neonate on postnatal day 2 (P2) accounts for circa 1.7 x 10^6 cells. Moreover, at P5 this number reaches 2.26 x 10^6 and by P11 reaches a plateau state (2.6 x 10^6), and remains unaltered thereafter (Alkass *et al*., 2015). In parallel, the percentage of multinucleated cardiac myocytes elevates in such a way that from the entire CMs almost 5% at P2, 20% at P5, 50% at P7, 70% at P9, and 90% at P14 undergo binucleation (Alkass *et al*., 2015). Alkass *et al.* also monitored the dynamics of the postnatal DNA synthesis in CMs according to their stereology and flow cytometry analyses. They reported that within the postnatal life stage of mice, the highest CM proliferation devoted to the birth stage. Accordingly, 17.3% synthesized DNA in CMs leading to CM number expansion at P1. This value reduced continuously after birth, such that it reached to less than 3% at P7,

and less than 1% at P14. Collectively, they revealed that CM number expansion accounted for 30% of the CM DNA synthesis, within the second postnatal weeks. Moreover, the authors investigated the state of ploidy in murine CMs by monitoring the nuclear DNA content during the postnatal life span via flow cytometry. Notably, they mentioned that the polyploidization state of CMs, was at its lowest state at birth (0%), whereas it peaked at P14 to almost 4%, meaning that polyploidy accounted for 13% of postnatal DNA synthesis in CMs. Furthermore, they revealed that the multinucleation rate in murine CMs was at its highest value at P7. In this context, the multinucleation was related to 57% of the CM DNA synthesis within the second mouse postnatal weeks. Consequently, the Alkass *et al.* (2015) revealed that concomitant with increased multinucleation and polyploidization in mouse CMs (starting from P1), the CMs proliferation rate declined dramatically, such that from P14 the murine CMs were almost unable to divide. Moreover, polyploidy and binucleation in CMs has shown to be accompanied by maturational hypertrophy (González-Rosa *et al*., 2018; Guo *et al*., 2020; Liu *et al*., 2019).

Collectively, the mammalian CMs reveal the cell cycle withdrawal within the first two weeks after birth. Therefore, discovering the exact timing, as which the cell cycle arrest is initiated in CMs, as well as the molecular mechanism regulating it, can have an important usage in regenerative therapies. The Multiple factors directly or indirectly are involved in cell cycle regulation including the cell cycle regulator, signaling pathways, and metabolism (glycolysis versus fatty acid oxidation), as well as oxidative stress.

1.1.4.1.1. Cardiac growth regulating factors

It has been revealed that during postnatal CM maturation the cell cycle positive regulators like CDKs are repressed, whereas the CDKIs are increased (Mohamed *et al*., 2018; Soonpaa *et al*., 1996). Interestingly, simultaneous overexpression of Cyclins and their corresponding CDKs has been shown to promote postnatal CM proliferation (Mohamed *et al*., 2018). For instance, Pasumarthi *et al*. (2005), using a mouse expressing CM-specific Cyclin D2, noticed that following a myocardial injury, the forced expression of Cyclin D2 in CMs promoted CM DNA synthesis, as well as infarct size reduction in adult mouse hearts. In another study conducted by Soonpaa and colleagues (1997), the overexpression of Cyclin D1 in adult CMs revealed the increased CM nuclei, together with enhanced number of CMs exhibiting an activity in S-phase of the cell cycle, compared to control adult mice. As another positive cell cycle regulator, Cyclin A2 can

be mentioned, promoting the G_1 to S and G_2 to M transitions. CM-specific overexpression of Cyclin A2 enhanced the DNA synthesis and mitotic incidence in adult mouse CM nuclei after an ischemic injury (Cheng *et al*., 2007). In addition to cell cycle positive regulators, the negative proliferation regulators have been studied. In a study conveyed by Di Stefano and colleagues (2011), the multiple knockdowns of three cell cycle inhibitors such as p21(Waf1), p27(Kip1), and p57(Kip2) was conducted in adult and neonatal CMs using siRNAs. Accordingly, they noticed elevated levels of CMs exhibiting an activity in S-phase, as well as increased number of nuclei per murine CMs and enhanced level of mid-body structures. Taken together, these studies conclude the crucial association of cell cycle regulators in the CM proliferation ability.

1.1.4.1.2. Cardiac growth mediating signaling pathways

Multiple signaling pathways have been reported to regulate the growth of heart among which Hippo/YAP, MAPK-kinase, AKT, mTORC, and Neuregulin-1 (NRG1) signaling pathways can be mentioned (Witman *et al*., 2020).

Hippo

As an essential signaling pathway regulating the heart size and growth, Hippo signal transduction cascade can be pointed out (Guo *et al*., 2020; Heallen *et al*, 2011; Heallen *et al*, 2013; Lin *et al*., 2016; Wang *et al*., 2018). In the course of Hippo pathway, the activity of the transcriptional co-activators such as Yes-associated protein 1 (YAP) and Transcriptional coactivator with PDZ-binding motif (TAZ), are negatively regulated. Following an activation of Hippo signaling pathway, mammalian sterile 20-related 1 and 2 kinases (MST1 and MST2) proteins are phosphorylated (MST1 at Thr183, and MST2 at Thr180) (Deng *et al*., 2003; Praskova *et al*., 2004). The activated MST1/MST2 complex form a complex with Salvador 1 (SAV1) (Callus *et al*., 2006), promoting the phosphorylation of Large-tumor suppressors (LATS1/2) (Galan and Avruch, 2016). The LATS1/2 in their activated state, phosphorylate the YAP/TAZ proteins and thereby promoting their degradation (Lei *et al*., 2008; Zhao *et al*., 2007). Nevertheless, under the Hippo inactivation, the YAP/TAZ are not phosphorylated. Instead, YAP/TAZ are localized to nucleus, and the complex interacts with a transcription factor called TEA domain family member (TEAD). Consequently, the genes involved in regulation of apoptosis, cell proliferation, and cell fate, are transcribed (Varelas, 2014). Hippo loss of function promotes the CM hyperproliferation. Accordingly, embryonic CM-specific

knockdown of YAP, has been reported to induce the hypoplasia (reduced proliferation rate) in mouse CMs at E16.5 (induced from E13.5 to E16.5), whereas the CM-specific YAP overexpression has promoted CMs proliferation at E15.5 (induced from E12.5 to E15.5) and P15 (induced from P5 to P15) (von Gise *et al.*, 2012). Collectively, these findings suggest the essential influence of Hippo/YAP signaling in the CM cell cycle activity.

MAPK-Kinase

Another signaling pathway involved in proliferation and growth of cardiac cells Mitogen-activated protein kinases (MAPK-Kinase) can be mentioned, which belong to a class of serin/threonine protein kinases (Raingeaud *et al*., 1995). The main branches of the MAPK-kinases pathway include Erk1/2, c-JNK, p38/MAPK, and Erk5 (Purcell et al., 2007; Qi and Elion, 2005). Stimuli such as growth factors interact with the receptor tyrosine kinase. As a consequence of receptor/stimuli interaction, depending on the branch, the Erk1/2, JNK, p38, or Erk5 get phosphorylated. Finally, following a nuclear signal transduction, the expression pattern of the downstream target genes is modified. In this thesis, we mainly, focused on the activity of Erk1/2 and p38 branches. As the main receptors upstream to Erk1/2 activation in CMs Integrins, G-protein-coupled receptors (GPCRs), and tyrosine-kinase receptors, can be pointed out. The integrin receptors are mainly involved in mechanotransduction. In this context, an increase in pressure in the heart, leads to CM enlargement, which is induced by integrin receptor. Indeed, in adult CMs the integrin-induced activation of Erk1/2 and p70S6 kinase (p70S6K1), has led to hypertrophy (Balasubramanian and Kuppuswamy, 2003). Moreover, multiple studies have highlighted the importance of integrin-mediated Erk activity in respond to cardiac mechanical stress (De Acetis *et al*., 2005; Dorn *et al.*, 2021; Häuselmann *et al*., 2011). Similar to integrins, GPCRs-derived activation of Erk has also been reported to regulate the CM hypertrophy. Following an extracellular signal such as epidermal growth factor (EGF), platelet-derived growth factor (PDGF), and insulin, the receptor tyrosine kinase translates the signal into a modification in Erk signaling, leading to cellular proliferation regulation (Cohen, 1965; Ek *et al*., 1982; Kasuga *et al*., 1982). As a member of receptor tyrosine kinase, IGF-1R can be mentioned, which exhibits an affinity to Insulin-like growth factor 1 (IGF-1). Following an IGF-1R/IGF-1 interaction, the Erk was reported to be activated, leading to CM hypertrophy (Carrasco *et al.*, 2014). Moreover, CM-specific overexpression of IGF-1 in mice has been reported to promote cardiomegaly as a

consequence of increased CM proliferation in transgenic mice compared to control group (Reiss *et al*., 1996). Another branch of MAPK-kinase signaling pathway is p38. Following an activity of p38, the signaling molecules involved in regulation of differentiation and hypertrophy in CMs are activated (Liang and Molkentin, 2003). Multiple studies have reported the negative influence of p38 in cell cycle activity, and its positive role in hypertrophy in CMs (Engel *et al*., 2005; Liang and Molkentin, 2003; Nemoto *et al*., 1998; Wang *et al*., 1998). With this respect, a treatment of rat adult CMs with p38 inhibitor SB203580 together with FGF1, enhanced the level of Cyclin A2, phosphorylated histone H3 (pHH3), and Aurora B in CMs, as well CM proliferation. However, the treatment of CMs with only p38 inhibitor did only elevate the BrdU incorporation and pHH3 rate. Moreover, the p38 was reported to disturb the FGF1-promoted S-phase to mitosis transition through an inhibition of PI3K and AKT. Collectively, these data suggest the negative involvement of p38 in CM proliferation by suppression of FGF1 activity (Engel *et al*., 2005).

AKT

Apart from the Erk signaling activity, the IGF-1 is also reported to be involved in activity of the core signaling element AKT, leading to elevated heart size as a consequence of CM proliferation (Reiss *et al*., 1996). As a target of the AKT, glycogen synthase kinase 3β (GSK-3β) can be mentioned. GSK-3β is a negative regulator of CM proliferation by destabilization and degradation of β-Catenin. However, following an IGF-induced AKT activation, the GSK-3β is phosphorylated and thereby inactivated. As a consequence of GSK-3β deactivation, the β-Catenin is not degraded and is localized to nucleus. Consequently, the genes essential for cell cycle progression, are expressed, which collectively leads to CM proliferation in mice during development (Xin *et al*., 2011). Indeed, studies have concluded the increased CM proliferation incidence following a GSK-3β suppression (Kim *et al*., 2016; Xu *et al*., 2016; Zhou *et al*., 2016). A model exhibiting a cooperation between Hippo, canonical Wnt, and IGF pathway, has been suggested which reveals the united involvement of these pathways in CM proliferation induction (Heallen *et al*., 2020). In this model, the inactivity of Hippo pathway, promotes the YAP nuclear localization, as well as its interaction with TEAD. The YAP/TEAD later form a complex with β-catenin/T-cell factor/lymphoid enhancer factor (Tcf/Lef) on promoter regions of DNA in nucleus, leading to expression of genes regulating the cardiac growth. The combined YAP/β-catenin signaling leads to expression of IGF signaling

genes (Xin *et al*., 2011). The expressed IGF pathway genes induce the activation of PI3K and AKT phosphorylation. Furthermore, as a consequence of the AKT activation, the GSK-3β is degraded, which leads to stabilization and nuclear localization of β-catenin. Finally, the nuclear YAP/β-catenin promotes the CM proliferation.

mTOR

In CMs the transition from glycolysis to fatty acid oxidation is concurrent with the loss of regeneration ability in the mammalian hearts. The mechanistic target of rapamycin (mTOR) as another signaling pathway regulating the organ size, is activated in response to growth factors and nutrients. Depending on the protein complexes that it forms, the serine/threonine protein kinase mTOR is known as mTOR complex 1 (mTORC1) and mTORC2. The Following an activation of mTORC1, the protein synthesis and cellular metabolism are regulated. In this context, the levels of enzymes involved in glycolysis and oxidative phosphorylation, as well as fatty acid synthesis, are regulated (Paltzer *et al*., 2023). To regulate the protein synthesis and metabolism, the activated mTORC1 phosphorylates the eukaryotic translation initiation factor 4E (4EBP1) and ribosomal protein S6 kinase (S6K1) (Ma and Blenis, 2009). The phosphorylation of 4EBP1 leads to prevention of 4EBP1's inhibitory role on its downstream target cap-binding protein eukaryotic translation initiation factor 4E (EIF4E). Consequently, the active EIF4E forms a complex essential for cap-dependent translation initiation (Richter and Sonenberg, 2005). The 4EBP1-induced activation of S6K1 promotes the synthesize of messenger ribonucleic acid (mRNA) as well as enhanced translational initiation and elongation via phosphorylation of ribosomal protein S6 and eukaryotic translation initiation factor 4E (EIF4B) (Ma and Blenis, 2009). Notably, AKT is a potential mTORC1 upstream effector. Using transgenic mice with the ability to express the constitutively active AKT, it was reported that the overexpression of AKT as well as activation of mTORC1 signaling pathway induced the enhanced the heart size in 3- to 4-month-old mice, compared to controls (Shioi *et al*., 2002). The prenatal inhibition of mTORC1 via rapamycin treatment was associated with declined phosphorylation of S6 and 4EBP1. Moreover, ss a consequence of mTORC1 suppression, the heart size to body size of the neonatal mice was reported to be decreased (Hennig *et al.*, 2017) compared to the control group. Collectively, these findings suggest the essential role of mTORC1 in regulation of heart size. In the study conveyed by Paltzer and colleagues (2023) studying the role of mTORC1 in postnatal heart development, they noticed that the acute suppression of

mTORC1 decreased the CM proliferation. Additionally, the ability of neonatal mouse heart to regenerate following an injury was inhibited by mTORC1 suppression. Notably, they reported that the transient mTORC1 inhibition shifted the cardiac proteome from glycolysis to fatty acid oxidation during the injury in neonatal mouse hearts. Taken together, they concluded that mTORC1 suppression concurrent by cardiac injury induced the metabolic switch. Moreover, as a consequence of metabolic switch, the CM maturation and cell cycle arrest were induced in mouse hearts. Consequently, these data reveal the potential role of mTORC1 in CM proliferation and heart regeneration.

NRG1

The NRG1 interacts with receptor tyrosine kinases including ErbB1, ErbB2, ErbB3, and ErbB4. Following the NRG1 and ErbB4 interaction, the ErbB4 interacts to ErbB2, inducing the cell PI3K-mediated cytokinesis (Bersell *et al*., 2009). Under the *in vitro* situations, NRG1 was reported to induce the cell cycle reentry and division, in primary rat adult CMs (Bersell *et al*., 2009). Following a cryoinjury in neonatal mouse hearts, the administration of NRG1 recombinant protein, reduced the scars and induced the CM regeneration (Polizzotti *et al*., 2015). Administration of NRG1 in primary mouse CMs isolated from P1 hearts, promoted the CMs cell cycle progression. Moreover CM-specific knockdown of ErbB2 has been reported to reduce the left ventricular wall thickness and mouse CM total number per heart compared to control mice. However, postnatal over-expression of ErbB2 in CMs, in particular, accelerated the heart weight to body weight, and CM proliferation rate. Accordingly, the phenotypes such as CM hypertrophy, dedifferentiation, and proliferation, were reported to be mediated by Erk, AKT, and GSK-3β signal transduction cascades (D'Uva *et al*., 2015). Collectively, these data suggest the association of NRG1 signaling in the regulation of CM cell cycle activity.

Collectively, these findings reveal the essential involvement of the cell cycle regulators as well as the activity of Hippo/YAP, MAPK-kinase, AKT, mTORC1, and NRG1 in cardiac growth and proliferation. Therefore, the investigation of their possible role in regulation of postnatal cell cycle arrest in CMs is beneficial for cardiac regeneration.

1.1.4.1.3. Postnatal metabolic switch from glycolysis to fatty acid oxidation

The metabolic transition from the cytosolic glycolysis to mitochondrial fatty acid oxidation has been reported to regulate the proliferation, differentiation, and postnatal maturation in CMs (Lopaschuk and Jaswal, 2010). Before birth, the majority of energy

source of heart is produced by glycolysis and lactate oxidation, whereas a very small ATP portion (less than 15%) is generated via fatty acid oxidation (Lopaschuk *et al*., 1991; Lopaschuk *et al*., 1992). Accordingly, it is speculated that the availability of energy substrate (glucose or fatty acids) determines the type of metabolism (glycolysis or fatty acid oxidation). Notably, in contrast to the available glucose circulating level which is similar in fetus, newborn, and adult, the circulating fatty acid level in fetus is reported to be very low compared to newborn and adults (Girard *et al*., 1992). Therefore, this low fatty acid level in fetus, leads to the low contribution of fatty acids in the ATP generation in fetal hearts (Girard *et al*., 1992). In addition to the substrate availability, the fetal glycolytic phenotype is suggested to be mainly regulated by the hypoxia-inducible factor 1α (HIF-1α). HIF-1α acts as a key regulator of genes which express the proteins essential for an anaerobic glycolysis. In the fetal low oxygen surroundings, the transcription factor HIF-1α interacts with the hypoxia response elements (HRE) DNA regions of its target genes (Wood *et al*., 1998). Accordingly, hypoxia-induced interaction of HIF-1α with HRE within the nucleus, promotes the expression of the genes encoding the proteins involved in glycolysis such as enolase (Eno), glucose transporter (GLUT), hexokinase (HK), lactate dehydrogenase (LDH), and pyruvate dehydrogenase kinase (PDK) (Lyer *et al.*, 1998; Postic *et al.*, 1994; Wood *et al*., 1998). While the GLUTs are glucose transporters, the other HIF-1α-regulated genes encoding the proteins such as ALDOA, Eno-I, HK, PFKL, and PKM, are essential for converting glucose to pyruvate during glycolysis (reviewed by Semenza, 2012). Notably, in the fetal heart in addition to GLUT1 the HK-I is concluded to support the glucose transport (Postic *et al.*, 1994). In the course of glycolysis, the imported glucose is initially phosphorylated to glucose-6-phosphate by HK. Following the activity of phosphofructokinase (PFK)-1 and (PFK-2), the glucose-6-phosphate is converted to fructose 1,6-bisphosphate. Furthermore, the ALDO converts fructose 1,6-bisphosphate to dihydroxyacetone-phosphate which is used to generate the 2-p-glycerate following multiple enzymatic activities. Next, the Eno uses 2-p-glycerate as a substrate to generate p-enol-pyruvate. Later on, following a phosphorylation of p-enol-pyruvate by pyruvate kinase, the pyruvate is formed (reviewed by Semenza, 2012; Tran and Wang, 2019). As a consequence of cytosolic glycolysis (conversion of glucose to pyruvate) 2 mol ATP/mol glucose is generated (Lopaschuk *et al*., 2010). The postnatal hearts demand high levels of ATP to fuel the CM contractile function. At postnatal day 7 (P7), the glycolysis pattern of metabolism shares less than 10% of total cardiac myocardial ATP production (Lopaschuk *et al*., 1991; Postic *et al.*, 1994). In return the

lactate oxidation and the fatty acid oxidation, are the dominant types of metabolism in P7 hearts. During the postnatal heart development specifically within the first week after birth in humans and mammals, the mitochondrial mass as well as the expression of the genes involved in mitochondrial biogenesis, expands (Hallman, 1971; Piquereau *et al*., 2010; Pohjoismäki *et al*., 2012, 2013). According to a study conducted by Puente and team (2014), the number of mitochondrial cristae exhibited a significant enhancement at P7 in comparison to P1 hearts. Specifically, from almost 18 cristae per μm observed at P1, the number cristae increased to almost 27 at P7. Moreover, the mitochondrial cristae remained unmodified in later postnatal mouse life compared to P7. They suggested a correlation between increased mitochondrial complexity and the cell cycle withdrawal in CMs. In addition, they concluded that at P7 the protein level of 68.7% of the enzymes involved in glycolysis was downregulated compared to P1 hearts, whereas over 80% of the enzymes involved in mitochondrial Krebs cycle and fatty acid β oxidation, were upregulated at P7 compared to P1 (Puente *et al*., 2014). Collectively, these data reveal that within the first week after birth the murine metabolism switches from the anaerobic glycolysis to mitochondrial fatty acid oxidation. Furthermore, in proliferative compared to differentiated cells, the type of the energy metabolism differs. With this regard, the proliferative cells such as hematopoietic cells as well as CM progenitor cell, exhibit the enhanced glycolysis rate together with elevated lactate production (Bauer *et al*., 2004; Chung *et al*., 2007). Notably, a switch to oxidative metabolism is reported to be essential to induce the transition of embryonic stem cells to CMs. Moreover, concomitant with the enhanced mitochondrial oxidative capacity, the proliferative CM are switched to non-proliferative terminally differentiate state (Chung *et al*., 2007). In differentiated cells revealing the well-organized mitochondrial cristae, the factors including oxygen consumption, and ATP production, together with enzymes of the electron transport chain and citric acid cycle are reported to be elevated. In contrast, the glycolytic enzymes are concluded to be reduced (Cho *et al*., 2006; Chung *et al*., 2007). CM-specific HIF-1α knockout, has been reported to reduce the LV chamber diameter, also to decrease the expression of genes involved in angiogenesis and glycolysis (GLUT1, PDK, and HK-II), whereas it enhanced mitochondrial-related gene expression, and respiratory function, as well as mitochondrial DNA content and surface in mouse heart (Huang *et al*., 2004). Finally, this knockout led to reduced contractility and vascularity, revealing the essential role of glycolysis in normal heart function.

Consequently, according to the previous studies together with the findings of Puente and team (2014), it can be concluded that there is a correlation between the postnatal cell cycle exit in CMs and the metabolic transition from glycolysis (reduced glycolysis-involved enzymes) to fatty acid oxidation (increased fatty acid oxidation enzyme and enhanced ATP generation).

1.1.4.1.4. Postnatal mitochondrial oxidative stress

Pyruvate which is generated as a consequence of glycolysis and lactate oxidation, is transported to the mitochondrion and is decarboxylated to acetyl-CoA. The intracellular fatty acids form fatty acyl-CoA, which enters the mitochondrion (reviewed by Lopaschuk *et al*., 2010). In addition to pyruvate, following a mitochondrial fatty acid β oxidation of fatty acyl-CoA, Acetyl CoA is generated. The generated acyl-CoA (either from glucose or fatty acids as substrates), are used for ATP generation in mitochondria. Notably, the fatty acid oxidation generates 105 mol ATP/mol palmitate (Lopaschuk *et al*., 2010). Collectively, it can be speculated that while the glycolysis facilitates the cell division, the oxidative phosphorylation supports the cellular contraction and growth by generating high yield of ATP. It is essential to mention that despite the high yield of mitochondrial ATP generation compared to cytosolic glycolysis (2 mol ATP/mol glucose generation upon glycolysis), the transition to the mitochondrial oxidative phosphorylation leads to the production of free radicals. In this context, as a consequence of leaky mitochondrial electron transport chain, the reactive oxygen species (ROS) are generated (Cadenas and Davies, 2000; Turrens, 2003). ROS consist of free radicals, as well as their non-radical intermediates including alkoxyl ($RO^{\bullet}$), hydroxyl ion ($OH^{\bullet}$), hydrogen peroxide (H_2O_2), ozone (O_3), singlet oxygen ($^1O_2$), and superoxide anion ($O2^{\bullet-}$) (Burton and Jauniaux, 2011). In body in order to maintain a balance between the ROS generation and its depletion, a complex antioxidant system is evolved. Accordingly, the ROS-derived oxidative stress is defended by antioxidant enzymes among which superoxide dismutase (SOD), catalase, peroxiredoxin (PRDX), and thioredoxin (TRX) can be mentioned (reviewed by Lei *et al*., 2016). As the first defender against ROS, SOD can be pointed out, which converts two superoxide anions into oxygen and hydrogen peroxide (Buettner, 2011). Due to SOD localization, the SODs are categorized into three types such as copper/zinc-containing SOD (SOD1) being located in cytosol, manganese SOD (SOD2) found in mitochondria, and extracellular SOD (SOD3) that is secreted into the

extracellular fluid. SOD1 and SOD2 are essential antioxidants reducing the intracellular levels of superoxide. In transgenic mice with a CM-specific SOD2 deficiency, led to lethal cardiomyopathy. Moreover, the SOD2 knockout, caused disturbed mitochondrial architecture and thereby impaired mitochondrial respiration, and the enhanced ROS level (Sharma *et al*., 2020). As another essential antioxidant enzyme defeating against the oxidative stress, catalase can be mentioned, which is predominantly located in peroxisome (Sepasi Tehrani and Moosavi-Movahedi, 2018). It has been reported that the cardiac mitochondrion-derived hydrogen peroxide is relatively high, which is being detoxified by the key enzyme catalase (Radi *et al.*, 1991). The hydrogen peroxide is catalyzed to water and oxygen by the activity of catalase (Radi *et al.*, 1991; Reviewed by Sepasi Tehrani and Moosavi-Movahedi, 2018). PRDX is another antioxidant enzyme being highly abundant in heart. Similar to catalase, PRDX uses hydrogen peroxide as a substrate to generate water (Kisucka *et al*., 2008). At its active site, the PRDX contains cysteine. As a consequence of peroxide reduction, the cysteine (Cys51) is oxidized to Cys51-SOH. The unstable Cys51-SOH is homodimerized by forming a disulfide with another Cyc51-SOH. Following activity of thioredoxin-thioredoxin reductase, the already formed disulfide is later reduced to PRDX active thiol. This disulfide reduction is relatively slow. Moreover, under high oxidative stress, is hyperoxidized to Cys-SO2 and Cys-SO_3. Indeed, the PRDX has been reported to be hyperoxidized at the peroxidatic cysteine to a mixture of SO_2 and SO_3 acids after treatment of the 4–6-week-old rat hearts with hydrogen peroxide concentration larger than 100 µM (Schröder *et al*., 2008). The TRX, has been concluded to protect the cells from oxidative stress. Accordingly, TRX repairs DNA and proteins by decreasing the ribonucleotide reductase and regulating the redox-sensitive transcription factors (Lu and Holmgren, 2014).

Although the cells have developed an antioxidant enzyme-defense system, the massive overproduction of ROS disturbs the balance between ROS generation and its elimination (Wang and Kang, 2020). Indeed, the ROS overproduction causes damages to lipids, proteins, or nucleic acids (Judge and Leeuwenburgh, 2007), leading to modifications in protein functions and signaling pathways. Notably, ROS damage to the nucleic acids have negative impact on cell cycle activity in CMs, thinking about postnatal CM cell cycle arrest. The ROS has been reported to promote the modification in nucleoside bases, leading to the formation of 8-hydroxyguanine, thymine glycol, 5-hydroxymethyluracil, 6-hydroxy-5, 6-dihydrocytosine, and 5-hydroxyuracil (Marnett, 2000). As the most well

studied ROS-induced nucleoside base modifications, the 8-hydroxyguanine can be named. In the course of ROS activity, at position C-8 the guanine is oxidized to 8-hydroxyguanine, leading to G to T substitution. This leads to a mismatched pairing between 8-hydroxyguanine and adenine (Kasai and Nishimura, 1983). ROS-induced oxidization of DNA is reported to promote the apoptosis, or cell-cycle arrest (Hoeijmakers, 2009; Marnett *et al*., 2003; Puente *et al*., 2014). In the study performed by Puente and team (2014), a transition from hypoxic intrauterine surrounding to oxygen-rich extrauterine environment was concluded to induce the DNA damage promoted by mitochondrial-derived ROS, and thereby the cell cycle arrest in mouse postnatal CMs. In adult mouse CMs, there is a negative correlation between cell cycle activity and the oxidative stress (Kimura *et al*., 2015). Attempts including ROS depletion by antioxidant *N*-acetylcysteine administration, or chronic hypoxia exposure to the mice, have been reported to enhance the proliferation rate in CMs during the normal postnatal development (Puente *et al*., 2014). In 2017, Nakada and colleagues investigated the impact of aerobic respiration suppression on cell cycle activity in adult mouse CM. In their experiments, gradual reduction of inspired oxygen (1% reduction per day), from 20% to 7% was reported to induce cell cycle activity in adult mouse CMs paralleled by the oxidative metabolism inhibition together with reductions in the cardiac mitochondrial cristae density, ROS production, and oxidative DNA damage. Moreover, they reported that the gradual inspired oxygen reduction induced initially from one week after a myocardial infarction in adult mouse, promoted the myocardial regeneration and reduced fibrotic scar reduction. These data reveal the essential impact of metabolism type and oxygen availability on CM proliferation ability.

Collectively, multiple factors are suggested to be involved in the regulation of postnatal cell cycle arrest in mammalian CMs, including cell cycle regulator availability, the cardiac growth-regulating pathway activity, metabolism pattern, and oxidative stress damages, as well as CM growth pattern and maturation. It is noteworthy to mention that the loss of proliferation ability in CMs is linked to the regenerative ability of the postnatal mammalian heart.

1.1.4.2. Heart regeneration in vertebrates compared to zebrafish

The ability to regenerate a variety of organs in adulthood has been connected to newts, zebrafish, and frogs (to some extend). The newt heart is constructed from an atrium, a

ventricle, and an aortic trunk. In order to investigate the regeneration ability of newt heart (*Notophthalmus viridescens*) Piatkowski and colleagues (2013) injured 50% of the newt ventricle (right half) mechanically by repeated squeezing with fine forceps. Accordingly, they concluded a clearance of the damaged part as a consequence of necrosis in CMs within the first week after injury. Moreover, 200 days after injury, the myocardium was fully reconstituted. In this context, at the injury side, the thin trabeculae were filled up with new immature CMs. Notably, they reported that to reconstruct the trabeculated network, the ECM was as an essential guidance player (Piatkowski *et al.*, 2013).

Adult zebrafish heart regeneration ability

In order to address the question, whether the adult zebrafish heart would possess a regenerate ability after an injury, in 2002 Poss *et al*. designed an experiment referred to apical resection. Thereby, 20% of the apex of the zebrafish heart was amputated and its regeneration ability was monitored. Indeed, BrdU-incorporation studies, histological analyses, and phosphorylated Histone H3 (pHH3) immunostainings (detecting mitotic cells), revealed that the zebrafish hearts exhibited complete and scarless regeneration following 20% of apical resection likely by CM proliferation (Poss *et al*., 2002). However, the origin of the newly generated cardiac myocytes was unclear. It was yet to discover if these cells would arise from pre-existing CMs or from cardiac progenitor cells differentiating into CMs. Several lineage-tracing experiments were performed, concluding that cardiac regeneration in zebrafish occurs as a consequence of proliferation of already pre-existing cardiac myocytes. It is essential to mention that compared to mammals, the CMs of adult zebrafish are relatively immature (i.e., mononucleated, diploid, and glycolytic, with low metabolic and contractile demand), which largely explains why adult zebrafish can regenerate their hearts but mammals cannot. Indeed, the ability of the CMs to proliferate is essential for cardiac regeneration following an injury.

Regeneration ability of the fetal mouse hearts

In the course of regeneration, a coordinated sum up of cellular dedifferentiation, proliferation, and differentiation, as well as morphogenic rearrangement, is needed to restore the tissue architecture. Fetal cardiac injury induced by temporal ischemia, maternal malnutrition, or toxin exposure has been proved to be resolved in mice (Drenckhahn *et al*., 2008). Using a mouse model containing 50% healthy and 50% diseased CMs, Drenckhahn and colleagues (2008) noticed a fully functional heart at birth.

In this context, the proliferation rate in healthy CMs was enhanced to compensate for the cell cycle activity decline which was observed in diseased CMs. In another study performed by Sturzu and team (2015), a chimeric mouse embryo in which a different degrees of CM death was observed in the embryonic heart was analyzed to assess the embryonic heart regeneration capability. Accordingly, they noticed that in embryonic murine hearts following 50 to 60% of CM loss, the lost CMs were replaced by enhanced proliferation rate in residual CMs. Collectively, these findings highlight the regeneration ability of the fetal mouse hearts.

Postnatal mouse heart capability of regeneration

Commonly, the postnatal mammalian heart has been considered as a terminally differentiated organ with a limited regeneration capability. As a result of a transient hypoxia due to myocardial infarction, the affected CMs undergo necrosis (Thygesen *et al*., 2012). Following an inflammatory respond, the necrotic cells are cleared by recruited macrophages and neutrophils, leading to thinning of the ventricular wall. Since the adult heart's ability to replace a large number of CMs is limited, therefore, the entire lost CMs are not compensated for new CMs. Instead, this CM loss is replaced by non-contractile fibrotic scars, limiting the heart pumping function and leading to heart failure. In contrast to adult hearts, studies performed on neonatal hearts, have reported that during the early postnatal window, the neonatal murine hearts exhibit a regeneration ability following injuries induced by either left anterior descending coronary artery (LAD) ligation, or ventricular apex resection, or cryoinjury (Darehzereshki *et al.*, 2015; Haubner *et al.*, 2012; Lavine *et al*., 2014; Porrello *et al.*, 2011; Porrello *et al*., 2013). For instance, an induced apical resection in P1 mice, led to infiltration of inflammatory cells at the site of the injury and a formation of new ECM. Using lineage tracing, it was reported that the new CMs were derived from the pre-existing CMs present globally in the heart (Porrello *et al*., 2011). However, concomitant with the increased CM maturation, enhanced hypertrophic growth, and lost cell cycle ability at P7 the ability of hearts to regenerate following the apical resection and myocardial infarction was lost (Günthel *et al*., 2018; Porrello *et al*., 2011; Porrello *et al*., 2013). Indeed, in mice, a transient regeneration capacity of the heart was reported at postnatal day 1 but not 7 (Porrello *et al*., 2013).
Similar to zebrafish, in mice, after 15% of apical resection at P1, cardiac regeneration has been reported within 21 days (Porrello *et al*., 2011). However, the methods used in this study are restricted and limited while distinguishing between proliferation and

binucleation in CMs. Yet it is noteworthy to mention that 21 days post resection the ventricular weight and the surface area, were restored (Porrello *et al*., 2011). In an experiment performed by Haubner and team (2012), the regeneration capability of the neonatal mouse hearts following a severe heart attack model was studied. Accordingly, the induced-left LAD ligation in neonatal mouse hearts, triggered an enormous cell death, detected by cleaved caspase 3 detection. However, 7 days after LAD ligation, a complete cardiac regeneration in neonatal mice was reported. Moreover, using a lineage tracing, they reported that the CM loss following LAD ligation, was compensated by proliferation of proliferation of pre-existing CMs (Haubner *et al*., 2012). Additionally, in 2014, cardiac regeneration after an apical resection in neonatal mice was investigated by Andersen *et al*. Here, 5% to 10% of the neonatal mouse apex was amputated and the amputated parts were weighted. Interestingly, their observations were not in agreement with previous studies claiming cardiac regeneration following 15% of the apical resection. Moreover, the size and weight of the heart, as well as the proliferation rate of CMs post injury remained unchanged, although the mouse strain and the injury-induction methods were identical between this study and the study performed by Porrello and coworkers. In addition, the study concluded myocardial fibrosis and cardiomyocyte hypertrophy after apical resection (Andersen, R. H. *et al*., 2014). The disagreement in the regeneration ability studies in neonatal hearts may be as a consequence of diverse analytic and experimental methods performed by various groups.

Pig regeneration

Cariad regeneration ability in neonatal pigs and neonatal humans

In larger mammals like pigs, an acute myocardial infarction induced by LAD ligation at P1 and P2, was reported to be recovered at 30 days after infarction. Accordingly, the CM proliferation was enhanced in infarct hearts compared to control groups (Ye *et al*., 2018; Zhu *et al*., 2018). Notably, the LAD ligation-associated injury at early postnatal ages (P1 or P2), was improved by CM proliferation. Furthermore, the cardiac function and wall thickness were recovered, and no or minimal scars were detected (12 or 30 days after infarction) (Ye *et al*., 2018; Zhu *et al*., 2018). It is essential to mention that from P3 or later, the acute myocardial infarction, was not improved in pig hearts. Compared to P1, in P3-induced LAD ligation hearts, the cell cycle activity was remarkably reduced, revealing a short window of regenerative ability in pigs after delivery (Zhu *et al*., 2018).

In pigs, the acute myocardial infarction induced at P7 and P14, has been noted to lead to generation of fibrosis, drop in left ventricular anterior wall thickness, and reduction in cell cycle activity compared to control and at P1-induced LAD ligation animals (Ye *et al*., 2018; Zhu *et al*., 2018). Accordingly, these data suggest the reduced regeneration ability of the porcine within the very early postnatal stages (Haubner *et al*., 2012; Ye *et al*., 2018; Zhu *et al*., 2018).

A recovery from myocardial infarction in newborn humans has also been investigated. A child who was born at the gestation week 39, demonstrated no signs of complications during the mother's pregnancy. However, at birth, there were signs of reduced oxygen saturation and severe cyanosis (body tissues' color change to bluish-purple hue). Since the ventilation therapy was failed, the child was undergone examination of the heart. Moreover, the electrocardiography and echocardiography results concluded a severe myocardial ischemia and impaired left ventricular functions with abnormal regional wall contractions, respectively. Indeed, having performed Doppler echocardiography, electrocardiogram, and cardiac angiography, they observed a complete thrombotic occlusion of the LAD. The thrombotic cardiac artery occlusion in the child was reported to exhibit a huge cardiac damage determined by CM cell death analyses. Amazingly, the fully cardiac recovery was observed within weeks after the recovery from the ischemic insult, revealing the ability of human newborn hearts to regenerate (Haubner *et al*., 2016). Collectively, these investigations suggest that the cardiac regeneration ability is observed in newborn porcine and humans and reduced within the early postnatal life period.

Adult mammalian hearts' regeneration ability

In adult mammalian organisms (including humans), following cardiac injury, the mechanism of replacement of lost CMs fails such that they are replaced with scar tissues, which limits the heart pumping function. Depending on the extend of the injury, this loss in regeneration could lead to heart failure and eventually death of an individual (Porrello *et al*., 2014). In summary, mammalian hearts exhibit a short regeneration capability after birth following an injury, which is lost within the next two weeks after delivery. Concomitant with the lost regeneration ability in the heart, the CMs undergo cell cycle arrest. Accordingly, from postnatal day 14 on, rodent CMs lose their proliferative ability and grow by hypertrophy (Velayutham *et al*., 2019). At this stage, 90% of murine CMs have been reported to undergo multinucleation (Alkass *et al*., 2015, Chapter 1.1.4.1.). This huge increase in multinucleation interferes with the regeneration ability of the heart

from this age on. The stable number of total CMs and the low rates of CM turnover, as well as limited regeneration ability during the postnatal life span in humans, could highlight the possible role of birth in the induction of cell cycle withdrawal in CMs. If birth would serve as the main reason for the postnatal cell cycle arrest in cardiac myocytes, this can affect humans born preterm. Thus, the preterm individuals would show reduced numbers of CMs in the heart at birth and throughout life. In this context, the birth-related cell cycle withdrawal would lead to a limited heart function in preterm-delivered humans compared to term-born ones.

1.1.4.3. Cardiomyocyte proliferation and turnover in postnatal human hearts

It is challenging to investigate whether humans are limited to the total CM number present at birth or whether generation of new CMs also might proceed later in life. In order to determine the number of CMs in humans, Bergmann *et al*. (2009), performed stereology in the postmortem hearts of 29 humans in the age range from one month to 73 years old, with no detectable signs of heart pathology. These analyses demonstrated that the total number of CM nuclei per heart remained constant, approximately 3 x 10^9 ($3.2 \times 10^9 \pm 0.75 \times 10^9$), during the entire lifespan of humans and showed an age- and gender-independent pattern (Bergmann *et al*., 2015). To address the question whether new CMs are generated in the postnatal human heart, the cells' birth date needs be estimated. During the cold war, due to nuclear bomb tests, the environmental carbon-14 (^{14}C) isotope was integrated into the DNA of humans, which was used to estimate the age of human CMs based on carbon dating (Bergmann *et al*., 2009; Spalding *et al*., 2005). Underlying this method, the enhanced atmospheric ^{14}C level, formed $^{14}CO_2$ following its reaction with oxygen. During photosynthesis this atmospheric $^{14}CO_2$ gets absorbed by plants. Human diets are thereby enriched for ^{14}C, such that the ^{14}C concentration in the human body correlates with the concentration in the atmosphere at a given time. When a cell goes through a final division and exits the cell cycle, its nuclear DNA gets stable. Thus, the DNA ^{14}C content allows to estimate the date when a cell is generated. The ^{14}C dating analysis was performed by Bergmann *et al*. (2009 and 2015) using the hearts of the same study group used for stereology described above (one month to 73 years old). Accordingly, they noticed that the within the postnatal life period, the cardiac DNA synthesis occurs at its highest level within the first 20 years after birth, reaching from

100% (standing for diploid situation) at birth to 150% per nucleus at the age of 20 (Bergmann *et al*., 2015). They also showed that the CM turnover was at its highest value within the first 20 years of life. From 5% at birth, this rate declines to 0.8% in 20-year-old and to ~0.3% in 73-year-old individuals.

In another study conducted by Mayhew and colleagues (1997), the human hearts were obtained from gestational week 16 (16 wk) to postnatal-week 40. Using physical dissectors, the number of CM nuclei per ventricular volume was estimated. Moreover, considering factors such as the ventricular volume and tissue density, as well as CM volumes per nucleus (using a combination of volume of all CM and the CM nucleus number), the number of CM nuclei was determined. Accordingly, they reported a linear increase in number of ventricular CM nuclei from 16 wk (1.5×10^8) to 42 wk (10.1×10^9). However, from gestational week 42 to postnatal-week 40 the number of ventricular CM nuclei did not change in human hearts. Consequently, both studies conducted by Mayhew *et al*. and Bergmann *et al*., revealed no evidence for addition of new CMs to human hearts after birth in the course of physiological growth.

In 2013 Mollova *et al*., analyzed the CM proliferation from birth to adolescence in humans from birth to 59-year-old. They concluded that the highest rate of CM exhibited an activity in mitosis and cytokinesis in infants, which was reduced to low levels in 20-year-old individuals. Paralleled by decreased cell cycle activity within the first 20 years after birth, the number of CMs in the LV enhanced by 3.4-fold (from $\sim 1.5 \times 10^9$ at birth to $\sim 6 \times 10^9$ in 20-year-old). Notably, the huge increase in CM number reported by Mollava and team, was based on immunostaining methods using the mitosis and cytokinesis marker, as well as the CM nuclei number. Collectively, these data do not necessarily reflect the real increase in CM number. Accordingly, the detection of centralspindlin or AuroraB do not guarantee the complete cytokinesis. Therefore, the increased mitosis rate or CM nuclei might be as a consequence of multinucleation in CMs of humans within the first two decades of life.

Collectively, the previous studies highlight that the number of CM nuclei from birth to the adulthood remain unchanged in humans. This understanding highlights the role of birth on cell cycle activity in CMs. With this regard, as a consequence of a termination of embryonic heart development earlier than term, numbers of total CMs would decline in preterm-born humans, leading to limited heart function in preterm individuals. Addressing the question whether the CM numbers in premature born humans would be less than those term-born individuals, is not possible due to ethical reasons.

1.1.5. Humans born preterm and potential consequences for postnatal heart function

Currently, 12% and 5-9% of live births in the United States of America and Europa, respectively, are reported as premature (Ueda *et al*., 2014). Likewise, in 2020 out of each 10 newborns, one was delivered preterm (World Health Organization, 2023). In this context, 10% of the future adult population will be involved in any health influence of the incomplete developmental pattern; which highlights the importance of a deep understanding about premature born-inducing factors, as well as its impact on the human health. According to the World Health Organization (WHO), humans born alive before 37 completed weeks of gestation are defined as preterm. According to the gestational age at delivery, there are three sub-categories of preterm birth, including extremely preterm (less than 28 weeks), very preterm (28 to 32 weeks) and moderate to late preterm (32 to 37 weeks). It has been concluded that there is a positive correlation between the low age of gestation and elevated mortality rates in newborns, children, and early adults (World Health Organization, 2023). Various factors including genetic background, infections, multiple pregnancies, and chronic conditions such as maternal diabetes and high blood pressure, act as key players in preterm birth. The geographical location has a positive impact on the survival of the preterm individuals. More than 90% of extremely preterm infants born in economically poor countries pass away within the first few days of life. Only less than 10% of extremely preterm infants born in the economically rich countries do not survive. Issues such as lack of effective care including no possibilities for supplementation with mother's milk, as well as infection, and breathing difficulties, account for poor survival in preterm born humans (World Health Organization, 2022). It is essential to highlight that within the past ten years, preterm birth has been linked to cardiovascular diseases, including changed left ventricular mass, geometry, and function, as well as impaired exercise capacity, elevated risk of stroke and heart failure later in life (Carr *et al*., 2017; Huckestep *et al*., 2018; Lewandowski *et al.*, 2013; Ueda *et al*., 2014).

1.1.5.1. Previous studies concerning the heart function and risk factors

Concomitant with the delivery, the cardiomyocyte growth pattern is switched from fetal hyperplasic to hypertrophic growth pattern (Chapter 1.1.4.). During the final trimester,

the CMs are relatively immature. In the course of preterm birth, the immature CMs are exposed to an early switch from low-resistance fetal to high-resistance postnatal blood circulation (Gessner *et al*., 1965; Parer, 2008; Rudolph *et al*., 1961; Rudolph *et al*., 1970), prior to completed embryonic development. This early switch has been associated with remarkably enhanced hypertrophic growth pattern together with deposition of interstitial collagen in myocardium. Consequently, these cardiac structural modifications would be involved in left ventricular remodeling in mammals (Bensley *et al*., 2010; Kluckow, 2005; Rudolph, 2000). In 2013, Lewandowski *et al*. conducted a study to unveil the possible correlation between preterm birth and any specific alteration in the structure and function of LV in adult humans. Therefore, they performed cardiovascular magnetic resonance imaging on 234 individuals between 20 to 39 years of age. Among the entire study group, 102 were born preterm (30.3 ± 2.5 weeks of gestation) with a birth weight of 1.3 ± 0.3 kg, while the remaining 132 individuals were born at term without any complications. The study revealed that the preterm-delivered young adults (PTYA) demonstrated decreased ventricles length, reduced left ventricular cavity diameter, and increased left ventricular wall, as well as an apical orientation shift away from the RV, compared to term-born young adults (TYA). Concerning the systolic function of the heart, both longitudinal peak systolic strain and peak systolic strain rate were reported to be significantly lower in PTYA than in TYA. Furthermore, the diastolic heart behavior in PTYA was described to be modified compared to TYA. Specifically, the longitudinal peak diastolic strain rates were slower in PTYA than in TYA. Taken together, compared to term delivery, the preterm born conditions seem to coincide with accelerated left ventricular mass, together with reduced systolic and diastolic function parameters (Lewandowski *et al*., 2013). Nevertheless, to fully unveil their left ventricular functional capacity, it is essential to investigate the preterm-born cardiac response in respect to physiological stress. Indeed, in 2018 Huckstep *et al*. studied the link between preterm birth and left ventricular contractility in response to continuously enhanced intensity of physical activity. In this survey, 101 normotensive young adults from 18 to 40 year of age were studied, among which 47 were born preterm (32.8 ± 3.2 weeks) and 54 were delivered at term. Both groups were requested to perform exercises on a seated stationary cycle ergometer at 40%, 60%, and 80% of peak exercise capacity. Notably, in the course of physical activity, the echocardiography was recorded. Under the resting conditions, they noticed that the resting heart rate was higher in PTYA than in TYA, whereas the resting ejection fraction (EF) in both groups were almost identical. However, the peak systolic

longitudinal strain was reported to be lower in preterm ones at rest. Moreover, the E-to-A ratio, E-to-A velocity-time integral, and a velocity-time integral were significantly lower in PTYA compared to TYA. Collectively, they concluded a modified resting LV function with intact EF in PTYA in comparison to TYA. Considering the heart function following physical activity, they revealed that at 40% of peak exercise intensity the EF and the peak systolic longitudinal strain were not statistically noticeable among PTYA and TYA groups. Nonetheless, upon increasing the exercise intensity to 60%, compared to TYA, the PTYA exhibited a noticeable drop in EF and peak systolic longitudinal strain. Specifically, at 60% of peak exercise intensity the EF of PTYA was reported 71.9 ± 8.7%, whereas the EF was 78.6 ± 5.4% in YTA. Moreover, while in PTYA the peak systolic longitudinal strain was noted to be −19.3 ± 2.5%, in TYA this value was −21.6 ± 3.3%. It is noteworthy to mention that as a consequence of increased exercise intensity to 80%, the EF in PTYA was remarkably lower (69.8 ± 6.4%) in comparison to TYA (77.1 ± 6.3%). These results demonstrated an impaired exercise capacity in preterm born adults (Huckstep *et al*.,2018).

In early adulthood, a higher rate of cardiovascular mortality has been linked to premature birth (Ueda *et al*., 2014). Notably, it is yet to be investigated which conditions do underlie this mortality. To investigate a possible association between the elevated cerebrovascular and ischemic heart diseases to premature birth in young adulthood, Ueda *et al*. screened 1,306,943 individuals born between 1983 and 1995 with no congenital malformations accounting for cerebrovascular and ischemic heart disease, in Sweden (Ueda *et al*., 2014). Among the investigation cohort, 5.6% of the participants were born earlier than 37 weeks of gestation (preterm individuals), and inhabiting in Sweden follow-up from 15 years of age at the age to December 31st, 2010. The investigation revealed a positive correlation between preterm birth and a nearly two-fold increase in the risk of cerebrovascular disease in adulthood, but no correlation between premature birth and later ischemic heart disease. They reported the average hazard ratios 1.45 (95% CI) in the young adults born preterm, compared to term-born individuals. In addition to the study performed by Ueda *et al* (2014), in another study conducted by Crump *et al*., (2019), the correlation between preterm birth and the enhanced risk of ischemic heart disease in adulthood, 2,141,709 humans (48.6% female and 51.4% male) born in Sweden between 1973 to 1994, was studied. Depending on the gestational age at birth, the participants were categorized into five groups including early preterm (<34 weeks), late preterm (34-36 weeks), early term

(37-38 weeks), full term (39-41 weeks), and post-term (≥42 weeks). Their data suggested that a negative correlation between gestational age at birth and the incidence of ischemic heart disease in adulthood. In this context, the risk of new-onset ischemic heart disease at ages 30 to 43 years was 53% in preterm (both early and late preterm groups) and 19% in early term group. Consequently, Crump and colleagues reported an increased ischemic heart disease risk in adulthood as a result of premature birth. Notably, since the preterm birth has been associated with enhanced incidence of hypertension and diabetes risk in adulthoods, they claimed that the methodological issues might be a reason for the previous study performed by Ueda *et al* (2014) where no correlation between premature delivery and increased risk of ischemic heart diseases in adulthood was concluded (Crump *et al*., 2019).

In 2017, an investigation was carried out to address the question, whether there is an association between preterm birth and enhanced risk of incident heart failure (HF) in childhood and young adulthood (Carr *et al*., 2017). The study cohort was composed of 2,665,542 subjects, among which 5.14% were born moderately (32 to 36 weeks), 0.56% very (28 to 31 weeks), and 0.18% extremely preterm (22 to 27 weeks), between 1987 and 2012 followed-up until December 31st, 2013. In 501 cases HF was reported whilst follow-up (initiating from one year after birth). Following a normalization of birth weight for gestational age, they reported that the HF risk in early adulthood increased with reduced gestational age at birth. Accordingly, the incidence rate ratio of HF in moderate, very, and extremely preterm individuals, as well as term born young adults was reported as, 1.36, 3.58, 17.00, and 1.00, respectively. Thus, the survey outcome unveiled a negative correlation between the gestational age at birth and the risk of heart failure in early adulthood.

Collectively, all of the previously mentioned studies point out the impact of declined gestational age at delivery on the cardiac function and structure of LV. Since the heart function relies on the CM growth, therefore, it is essential to investigate the impact of premature birth on CMs. Indeed, in 2018 the Bensley and colleagues studied the influence of premature delivery on the structure of myocardium and the development of CMs, using heart tissues obtained from autopsies of 16 infants. The infants were delivered between 23 and 36 weeks of gestation and aged for 1 to 42 days. In the control group, the heart samples from appropriately grown stillborn infants who died *in utero*, were used. All the samples belonged to the achieve of the Women's and Children's Hospital, Adelaide, Australia, between 1996 and 2009. The exclusion criteria were reported to be maternal

smoking, maternal infectious diseases, acute/chronic chorioamnionitis, auto immune disease, congenital defect, chromosome abnormality, intrauterine growth restriction, oligohydramnios, polyhydramnios, two vessels in the umbilical cord, or viral infections. Having investigated the cell cycle activity (conducted by using Ki67-immunostaining) following birth, they reported that the rate of cardiac nuclei exhibiting a Ki67 staining was remarkably lower in preterm compared to the control group with the identical gestational age. Notably, with two exceptions the majority of the preterm infants was concluded to demonstrate a cardiac proliferation rate of <0.5%. It is essential to mention that the cross-sectional area, as well as the nucleation and ploidy state between two study groups were similar. Collectively, these data reveal the impact of preterm birth on the cell cycle activity in human cardiac cells. Indeed, the reduced CM proliferation rate concluded in preterm delivered individuals, would lead to a decrease in number of total CMs, which would explain the limited heart function reported in the previous follow-up studies. Therefore, a deep understanding about the influence of birth on CM cell cycle activity and the molecular mechanism regulating the postnatal cell cycle activity in CMs, will indeed have essential implications in those humans delivered preterm. Studying the molecular mechanisms underlying the CM cell cycle activity in premature humans is limited due to ethical reasons. Moreover, the premature delivery is a consequence of multiple genetical, maternal, and environmental issues, which might limit or bias the identification of the factors regulating the birth-relevant cell cycle activity in CMs. Therefore, animal models of the premature birth are essential for the study the molecular mechanism regulating the postnatal cell cycle withdrawal in CMs.

1.1.5.2. Animal models of preterm birth and consequences for the heart

In order to investigate the impact of premature birth on the heart, animal models are studied. Sheep as a large mammalian organism, is a highly investigated model organism for studying the mammalian hearts.

Sheep

In 2010, Bensley *et al*. aimed at determining the preterm birth-induced modifications in the postnatal structure of the myocardium using sheep as models. Term birth in lambs was designated to those born spontaneously at 147 days post conception, whereas those delivered after 133 days were determined as preterm animals. To induce the preterm delivery, an anti-progesterone medication (Epostane) was administered. Therefore, 48 h

before (at 131 days post conception) the desired delivery date, the ewes were injected intravenously with 50 mg Epostane. 4 weeks after birth, the heart rate in preterm lams (136.9 ± 9.0 b.p.m.) was remarkably lower than in term individuals (167.3 ± 9.3 b.p.m.). However, 4 weeks later, the heart rate among preterm and term lambs was not significantly different (pre-term 98.0 ± 6.9 b.p.m.; term, 89.6 ± 7.1 b.p.m.). 9 weeks after birth, they reported a severe collagen deposition in entire preterm study group. Notably, compared to term lambs, in preterm groups the collagen contents of the LV, IVS, and RV were reported to be larger. Specifically, in preterm lambs the collagen content of RV was 6.6-fold more, and of LV and IVS were 4.8-fold greater than in term ones. They also investigated the CM numbers using an optical dissector-fractionator approach followed by counting the CM nuclei. Accordingly, no significant variation was reported between term and preterm-delivered lambs concerning the total CM number of RV, and LV + IVS. In this context, the total CMs number at RV was 4.76 ± 0.54 x 10^8 in term, and 6.90 ± 1.30 x 10^8 in preterm. Moreover, the total CM counts of LV + IVS were 2.45 ± 0.43 x 10^9 in term and 2.41 ± 0.23 x 10^9 in preterm lambs. Comparing the volume of mono- and binucleated CM, they concluded that the preterm CMs irrespective to the nucleation state, were larger in size than term lambs. In RV, as well as LV + IVS, the huge number of CMs were binucleated in term lams, whereas in preterm ones the ventricular CMs were mainly mononucleated with some trinucleated CMs. Furthermore, the number of binucleated CMs in preterm was lower than the term lambs. Having investigated the ploidy state of the lamb CMs, they concluded that the huge proportion of the mononucleated CMs in preterm hearts were tetraploid. Briefly, in RV 86.4 ± 0.9%, and in LV + IVS 94.1 ± 2.2% of the mononucleated CMs were tetraploid. However, in the term hearts the ploidy state of the mononucleated CMs were remarkably lower in comparison to preterm ones. Accordingly, 47.7 ± 0.9% of mononucleated CMs in RV, and 61.9 ± 5.4% in LV + IVS were tetraploid. Collectively, they reported that the premature delivery in sheep moderately promoted the myocardium remodeling. With this regard, the preterm delivery led to CM hypertrophy, enhanced collagen deposition, and altered CM maturation (Bensley *et al*., 2010).

In order to study the influence of preterm delivery on the function and the cellular structure of the RV, the Mrocki *et al*. (2018), studied two lamb populations consisting of those delivered preterm (132 ± 1 days; n = 7) or at term (147 ± 1 days; n = 7). To induce the delivery in preterm individuals, 48 h before delivery, epostane (20 mg in 2 mL 100% ethanol) was administrated on ewes. The term delivery was induced by epostane

administration at 24 h before delivery. 14.5 months after delivery, they reported no noticeable differences in systolic arterial pressure between the preterm- and term-delivered sheep. Moreover, the heart rate (b.m.p.) was similar in both study group, meaning 88.2 ± 29.2 in term, and 90.2 ± 15.0 in preterm sheep. Notably, they reported a significantly lower peak systolic blood flow in the pulmonary artery of the preterm in comparison to term sheep. The body weight, as well as heart weight to body weight ratio did not differ between preterm and term groups at 14.5 months after birth. Compared to the term study groups, the preterm-delivered sheep revealed a reduced right ventricular wall thickness, measured at 14.5-month-old. Having assessed the CM number in the RV, they concluded a noticeable drop in the number of CMs in preterm animals at 14.5-month-old compared to term individuals. In this context, the right ventricular total CM number was $2.06 \pm 0.42 \times 10^9$ in preterm and $2.48 \pm 0.29 \times 10^9$ in term-born sheep. To a huge degree the adult right ventricular CMs were binucleated (≥86%). It is essential to mention that compared to term-delivered adult sheep, the preterm group possessed lower number of binucleated and greater proportion of mononucleated CMs. While the right ventricular CM cross sectional area in both groups was similar, the CMs of the those preterm-delivered sheep were remarkably smaller than term-delivered sheep (at 14.5-month-old). Consequently, they concluded significant reductions in the RV wall thickness, RV cardiac myocyte number, and peak systolic blood flow in the pulmonary artery as a consequence of preterm delivery in sheep (Mrocki *et al*., 2018).

In another study conducted by Lê and colleagues (2020), the ventricular structure of the lambs at the former-preterm delivered days (128-day) was investigated. Whereas the term individuals (19) delivered spontaneously (approximately at the gestation day 150), the preterm fetus (16) were born by cesarean section (at gestation day 128). The organ collection was carried out at two months after birth in term-born lambs, and two months after the term-equivalent age in preterm-delivered animals. They concluded a reduced birth weight in preterm-born lambs in a sex-independent manner, in comparison to term-born individuals. Moreover, after 5 months the final body weight was reported to be remarkably larger in term- compared to preterm-delivered lambs. Notably, compared to male individuals, the female lambs were lighter. The heart weight to body weight ratio followed a sex- and gestational age at birth-independent pattern. Briefly, after five months, in term-born lambs the heart weight to body weight ratio was 4.42 ± 0.32 in females and 4.53 ± 0.21 in males. In addition, in preterm-delivered lambs this rate was 4.26 ± 0.12 in females and 4.80 ± 0.34 in males. Indeed, assessing the cell cycle activity

in CMs using Ki67 staining, they reported that the proportion of the nuclei exhibiting a Ki67 staining, was noticeably low (<0.001%) in the LV+S and RV of the both term and preterm individuals at 2 and 5 month after delivery. They concluded no significant changes in the total CM number between term- and preterm-delivered lambs at 2 and 5 months after birth. Moreover, the gestational age at birth did not influence the size of the CM cross-sectional area at 2 and 5 months after birth (Lê *et al*., 2020). Furthermore, they reported that the percentage of myocardium interstitial collagen percentage in LV+S was increased at 2 and 5 months after birth (Lê *et al*., 2020). However, in the LV+S of the preterm-delivered individuals the collagen percentage was remarkably larger than in term-delivered lambs. Collectively, despite previous studies, their data suggested that the severe-preterm delivery did not influence the CM proliferation, number, and growth. However, levels of interstitial collagen in the LV+S was increased in lambs delivered at the gestational day 128 compared to the term-delivered individuals. The increase in interstitial collagen might lead to impaired contractility and conductivity of the ventricles. To investigate the influence of an intrauterine infection on the postnatal cardiac growth in preterm lambs, Vrselja *et al*. (2022), injected the pregnant sheep with either lipopolysaccharide (intra-amniotic injection) or saline at the gestational day 129 (preterm born), and seven days later the hearts were studied. As the control group, the fetal hearts were studied at gestational age 136. As expected, both preterm lambs (saline or lipopolysaccharide injected) revealed lower body wight as well as heart weight at birth, compared to the age-matched control group (136). Notably, the heart weight to body weight ratio among all three study groups was similar. They revealed that the wall thickness of the LV was identical between the study groups, whereas the wall of IVS was thinner preterm compared to control group. Moreover, the wall of RV was reported to be thinner in saline-received lambs compared to the lipopolysaccharide infected preterm lams and fetal controls. In the LV+S, they noted increased levels of interstitial collagen both preterm delivered lambs compared to the fetal control group. Furthermore, the collagen levels in infected preterm lambs were larger compared to saline received preterm individuals. Having investigated the CM proliferation, they revealed that in both preterm groups the percentage of CM nuclei demonstrating a Ki67 staining was remarkably higher in LV+S (2-3%) than in RV (<1%). However, the proportion of CM nuclei exhibiting a Ki67 staining was similar in RV and LV+S of the fetal control group (almost 6%). Concerning the total CM number, they reported remarkably lower CM number in LV+S of both preterm groups compared to fetal groups. Nevertheless, in the RV region the total

CM number was similar among all the study groups. Comparing the cross-sectional area, they noted increased CM cross-sectional area in both preterm groups in the LV+S compared to the fetal group. However, unlike the LV+S CM, in the RV region the CM cross-sectional area was smaller in preterm groups than in fetal controls. Having assessed the nucleation state of CMs, they unveiled that in all three ventricular regions the proportion of mononucleated CMs was lower in preterm lambs than in the fetal controls. Compared to controls, in preterm individuals the percentage of binucleated CMs was significantly increased. Consequently, these data revealed that preterm birth was associated with adverse influence on the structure of heart and CM growth. Moreover, an additional induced infection to the preterm delivery, leads to myocardial immune response and immature heart remodeling. Collectively, these data might highlight the association of preterm birth with enhanced probability of cardiac dysfunction.

In almost all of the previously described studies, the preterm delivery was associated by multiple disorders in sheep CM growth and maturation. However, the total CM numbers were usually not altered among term- and preterm-born sheep (Bensley *et al*., 2010; Lê *et al*., 2020). Yet, this uncertainty arises, whether the sheep would be an appropriate model to address the birth-related cell cycle arrest and the mechanism regulating it. With this regard, in 2015 Jonker *et al*. assessed the impact of delivery on the CM growth and maturation in sheep. Comparing the fetal and neonatal hearts obtained from male (n=54) and female sheep (n=48), they reported that the heart weight to body weight ratio between both sexes was similar. Moreover, the weight of LV and RV followed the identical pattern until birth, however, from delivery to the P60 the weight of the LV increased sharper than the weight of RV. Considering the cell size, they noted that the length and width of the CMs in RV and LV region accelerated from gestational age 95 to the postnatal day 60. The binucleated and multinucleated CMs located in the RV and LV regions were noted to be longer and wider than the mononucleated CMs. In the RV, the CM width exhibited a constant growth rate from fetal (day 95) to neonatal periods. Moreover, it was mentioned that the volumes of all myocytes accelerated sharply from birth on. The CM volume normalized to the nucleus numbers, revealed that the size of the binucleated CMs were twice the size observed in mononucleated CMs across all investigated ages. At gestational age 95 in LV and RV almost 100% of CMs were concluded to be mononucleated. Moreover, from E95 the number of nucleated CMs (binucleated) continuously increased, such that at gestational day 125 almost 20% of CMs were binucleated in LV and RV regions. Furthermore, at delivery the proportion of binucleated CMs was reported to be

almost 70% in LV and RV parts, whereas almost 25% of entire CMs were mononucleated at birth. The proportion of mononucleated CMs dropped further, in such a way that 8 weeks after delivery only 5% of CMs in LV, and 2.9% in RV were mononucleated. Indeed, mainly the mononucleated CMs exhibited a cell cycle activity (Ki67 staining). Coincide with the enhanced nucleation rate, the cell cycle activity was reported to be decreased. Briefly, at E95 almost 8% of entire CMs in LV and 6% of CMs in RV, exhibited a cell cycle activity. Moreover, at E135 almost 2.5% of CMs in LV and RV were active in the cell cycle. The average percentage of CMs showing a Ki67 staining was reported to be 1% within a week after birth in LV and RV regions. Having studied the total CM number from cell volumes and the nucleation states in LV and RV, they mentioned that the highest CMs number was observed at E135 (almost 1.5×10^9 in LV and 1×10^9 in RV) within the investigated developmental stages (from E95 to P60). Furthermore, from delivery on (to the P60), the total CM numbers in the LV and RV remained almost intact (almost 1×10^9 in LV and 0.5×10^9 in RV). It is essential to note that in contrast to left ventricular CM numbers, in the RV the CM numbers increased (to 0.8×10^9) at P60. Taken all together, they revealed that in sheep the CM growth pattern changed much earlier than birth. For instance, they observed about 33% of CM loss from E135 to birth. In this context, it seems that sheep would not be an appropriate model to study the influence of delivery on CM growth and cell cycle activity.

Pig

In 2012, Eiby and colleagues investigated the correlation between preterm birth and the heart ability to respond to an acute shift from preload and afterload in pigs at the time of delivery. The study group was composed of two sets of piglets including preterm (gestational day 92) and term (day 115) piglets, both of which were delivered by means of cesarean section. They concluded that the heart and body weight of the term piglets were twice the values observed in preterm ones. To assess myocardial and coronary vascular function, the study was performed *ex vivo* on isolated working heart models. Accordingly, assessing the cardiac output at an adjusted 6 mmHg preload and 35 mmHg afterload, they reported that the cardiac output in preterm piglets were remarkably lower than in term ones. Briefly, the cardiac output (ml/min) in preterm piglets was 103 ± 36 in female and 121 ± 15 in male, whereas in term group the cardiac output was 376 ± 33 in female and 281 ± 16 in male individuals. The outcome revealed a significant reduction in LV cardiac output (almost 50% lower) and aortic blood flow per kilogram body weight

in preterm compared to term individuals. The outcome was similar to a previous study on humans (Groves *et al*., 2011). Moreover, their results concluded that the increased preload pressure (from 2 to 14 mmHg), increased the left ventricular output with the same degree in preterm and term hearts. Nonetheless, the values in preterm hearts were half of the one observed in term hearts. In this context, at 2 mmHg the left ventricular output was 100 ml/min/kg body weight in preterm and 200 ml/min/kg body weight in term, whereas at 14 mmHg this was 125 ml/min/kg body weight in preterm and 250 ml/min/kg body weight in term ones. Moreover, they assessed the effect of afterload on left ventricular output, revealing that at 20 mmHg afterload pressure, the left ventricular output was almost 150 ml/min/kg body weight in preterm, however, in terms this was 225 ml/min/kg body weight. Following an acceleration in afterload pressure to 45 mmHg, the left ventricular output remained unchanged in both preterm and term samples. However, at 55 mmHg this value had a dramatic reduction in preterm compared to term ones. Briefly, the left ventricular output at 55 mmHg was almost 75 ml/min/kg body weight in preterm and 180 ml/min/kg body weight in term. They claimed that preterm birth might impair the functional capacity of the heart in response to an acute change in postnatal afterload (Eiby *et al*., 2012).

Mouse

Due to various reasons including having short gestation time, being easily genetically manipulated, and being inexpensive, mouse is an appealing model to study the birth timing. Mice as the common animal model in biomedical research, have 4 to 10 pups which are rather immature at birth. Potential mouse models for studying preterm conditions have been generated by a variety of treatments including maternal infection (intrauterine infection with *E. coli,* or lipopolysaccharide), inflammation (i.e., interleukin-1), anti-progesterone treatment (to induce delivery) and cesarean section (McCarthy *et al*., 2018). To induce premature birth, cesarean section may have the lowest side effects on proliferation analyses in the heart. Hereby, the murine fetuses are surgically removed at the desired gestational age without any medical treatments of the mothers. However, the survival of the pups outside of the uterus is only possible if cesarean section is performed at a maximum of one day before the physiological birth date (Loctin *et al*., 1983). In this context, in the mouse specious with the gestational age of 20, the pup survival was reported to be 0% when the cesarean section had been conducted at E18.5. Moreover, the mortality rate in the pups being delivered at E19.5 was 13.2%, and at E20.5

was 1.4%. During the first 6 days after cesarian section, the mortality rate in the preterm pups (delivered at E19.5) was 21.3%, whereas the mortality rate in term-born mice was 8.7%. Furthermore, the mortality rate in both preterm (delivered at E19.5) and term (born at E20.5) mice which survived up to P7, was reported to be 0%. Assessing the body weight at 1 hour after birth in term and 30 min after reanimation in preterm (E19.5), revealed that the body weight in term-born pups was remarkably greater than the preterm-delivered mice. Specifically, while the average body weight in the term group was almost 1.6 g, the body weight in survived preterm group was almost 1.3 g and in dead preterm mice was 1.05 g (Loctin *et al*., 1983).

Taken together, the premature birth has been concomitant with multiple structural and functional cardiac abnormalities in both humans and animal models. In this context, the termination of embryonic development due to an early exposure to an extrauterine environment, is associated with developmental defects of the heart and pediatric heart disease. Thus, these questions arise, whether birth itself would act as a key terminator of cell cycle activity in cardiomyocytes, or whether the birth-induced cell cycle withdrawal in CMs would lead to a reduced total CM number in hearts of premature-born humans throughout life limiting their heart function. Accordingly, the answer to these uncertainties as well as undercovering the mechanism upstream the possible birth-related cell cycle arrets in CMs can be beneficial in preterm-delivered humans concerning the postnatal cell cycle-reentry in CMs.

1.1.6. Hypotheses and aims of the study

In the course of embryonic developmental, the cardiac growth is primarily regulated by cardiomyocyte (CM) proliferation. Indeed, previous studies performed in mice and humans showing a reduced rate of proliferation in cardiomyocytes after birth and unchanged numbers of CMs during postnatal life, respectively, highlight the involvement of birth in proliferation termination of CMs. If the cell cycle withdrawal in CMs would be tightly associated to birth, this would mean that the human-delivered preterm might have lower total CM numbers than term ones. Since the cardiac function relies on the CM contractility, therefore, as a consequence of possible lower CM total numbers (in preterm humans), the heart function would be influenced in preterm-delivered individuals. Indeed, disturbed fetal growth and development as observed in preterm born humans and animals

have been reported to be connected to multiple structural and functional disorders of the hearts in adulthoods (Chapter 1.1.5.). Previous findings about premature birth together with data concerning the unchanged total CM numbers in humans from birth to the late adulthood, revealed a limited heart function later in life. Moreover, this limited heart function might be as a consequence of declined CM total number following an early separation from the intrauterine environment earlier than term. Thus, a detailed understanding about the influence of an exposure to the environment outside the uterus on cardiac development might have implications for the life quality of humans-born preterm. In this context, initially the aim of this study was to elucidate the exact time point after birth at which cell cycle arrest in CMs would be induced, as well as undercovering the molecular mechanism upstream of it. Notably, in order to monitor a possible association between the sex and the regulation of perinatal cardiac growth pattern, the male and female mice were investigated separately. Firstly, we assessed the dynamics of the cell cycle activity in CMs using perinatal C57BL6/J mice. It is essential to mention that in our study design, the gestational ages of the fetal and neonatal mice were precisely monitored, allowing us to avoid any wrong data interpretations. The hearts were isolated from seven perinatal stages including two final fetal stages (E17.5 and E18.5), birth (NB18.5 or NB19.5), 24 h after delivery (NB18.5+1 or NB19.5+1), and 48 h after birth (NB19.5+2). It is noteworthy to point out that comparing the cell cycle activity at E17.5 and E18.5 allowed us to investigate whether the cell cycle arrest in CMs would follow a pre-programmed mechanism or not. Additionally, to assess the influence of birth on CM cell cycle exit, we compared heart samples obtained from mice at E18.5 and NB18.5. Both E18.5 and NB18.5 mice shared an identical gestational age (18.5), whereas only NB18.5 mice were shortly exposed to an extrauterine surrounding. Therefore, comparing these two mice allowed us to study the influence of birth on cell cycle activity. Moreover, to address this uncertainty, whether the gestational age at delivery would influence the CM cell cycle activity, we investigated the NB18.5 and NB19.5 mouse hearts. Specifically, NB18.5 and NB19.5 stages determine the samples isolated from mice immediately after birth. Nonetheless, the gestational age of mice at birth differed among NB18.5 and NB19.5 mice. To monitor the dynamics of perinatal cell cycle activity in murine cardiac myocytes, immunofluorescence analyses were performed using antibodies against CMs and proliferation markers.

Later on, our next objective was to unveil the key factors influencing the postnatal cell cycle activity in mouse CMs. According to the knowledge which was already described

in Chapters 1.1.4.1.3 and 1.1.4.1.4., within the first two weeks after birth, the cell cycle arrest in mouse CMs was reported to be associated to the metabolic switch to fatty acid oxidation, ROS generation and ROS-induced DNA damage. Nonetheless, it is still elusive, whether immediately after birth the cell cycle arrest would be associated to a rapid metabolic switch to fatty acid oxidation or not. Accordingly, we next investigated the availability of glycolysis-involved enzymes, as well as oxidative stress and ROS-induced DNA damage in perinatal mouse hearts.

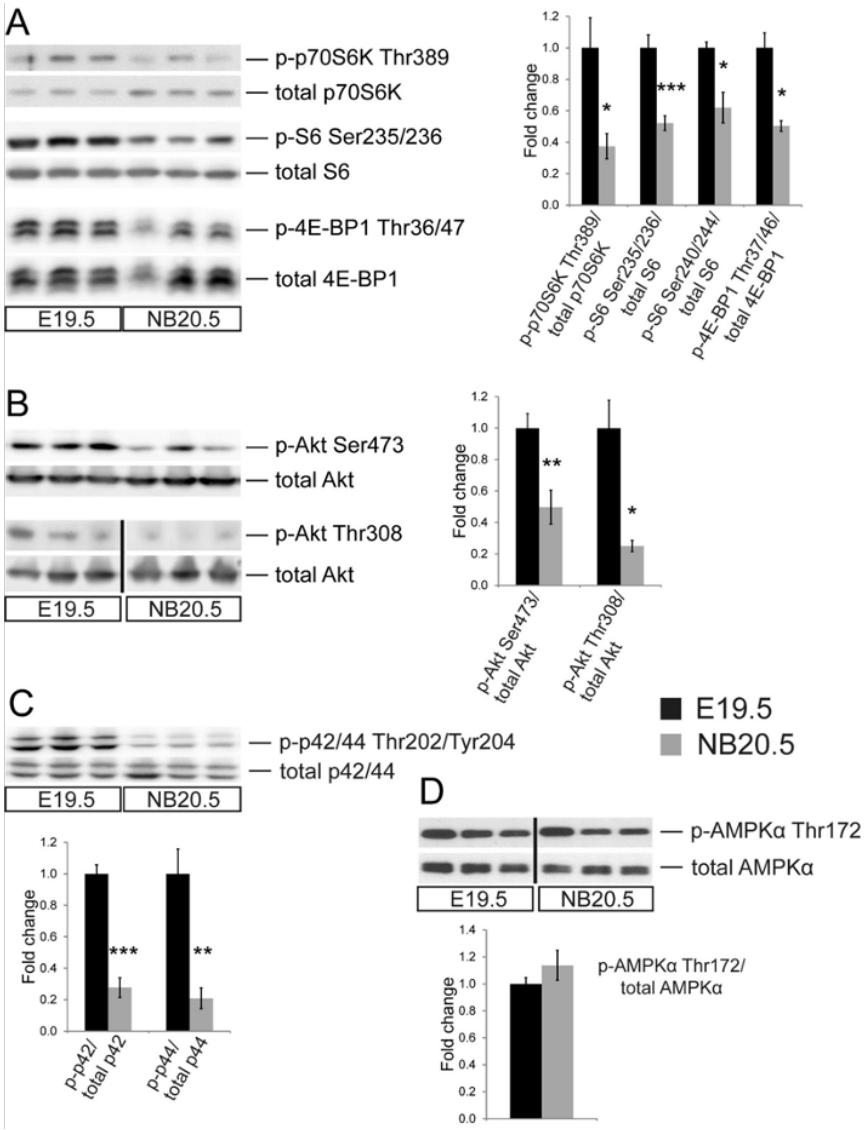

Figure 5. Drops in activities of various signaling pathways regulating cardiac growth in ventricular myocardium obtained from mice. The activity of mTORC1, AKT, p42/44, AMPKα was monitored by measuring the phosphorylation intensity of their members using WB experiments using whole hearts at E19.5 and NB20.5. **A)** The activity of mTORC1 downstream targets was reduced in mouse hearts immediately after birth compared to fetal stage E19.5. **B)** and **C)** The phosphorylation state of Akt at two phosphorylation positions as well as p42/44, was declined shortly after birth in mouse hearts compared to E19.5. **D)** In comparison to the E19.5, the phosphorylation of AMPKα was not modified in NB20.5 mouse hearts. The sample size was six. The results were illustrated as the fold change mean values ± SEM. Statistical significance among groups was assessed by unpaired 2-tailed student *t*-test using SPSS. *: $P<0.05$, **: $P<0.01$, ***: $P<0.001$ (unpublished data).

Beside the metabolic pattern together with oxidative stress, the activity of cardiac growth-mediating signaling pathways are involved in regulation of cardiomyocyte proliferation. Indeed, in order to determine the molecular mechanism regulating the cell cycle arrest in heart after birth, the activity of various signaling pathways involved in cardiac growth and CM proliferation, were already assessed in our team. Accordingly, the phosphorylation state of the mTORC1 pathway members such as p70S6K (threonine at position 389), S6 (serine at position 235 and 236), as well as 4EBP1 (threonine at position 37 and 46) were studied in whole hearts isolated from mice at E19.5 and NB20.5 (Figure 5) via western blot experiments.

Interestingly, our data concluded that shortly after delivery at NB20.5 compared to E19.5, the activity of the mTORC1 pathway declined remarkably (Figure 5A). Moreover, assessing the activity of AKT and MAPK-kinase p42/44 in mouse hearts at E19.5 and NB20.5, our team concluded significant reductions in phosphorylation levels of Akt together with p42/44 at NB20.5 in comparison to E19.5 hearts (Figure 5B and C). Collectively, these data suggest that shortly after a separation from an intrauterine surrounding, the activity of pathways like mTORC1, AKT, and MAPK-kinase p42/44 dropped significantly compared to the fetal hearts. Yet it is essential to assess whether immediately after a separation from an intrauterine environment, the activity of the mentioned pathways would be modified compared to shortly before birth.

In this context we compared the activity of AKT, Hippo/YAP, mTORC1, and p42/44 in hearts obtained from E18.5 and NB18.5, allowing for studying the influence of birth in these pathways' activity.

Once again, another factor involved in postnatal cell cycle endowment in CMs is a metabolic switch to fatty acid oxidation. Indeed, studying the phosphorylation state of the APMK as an essential regulator of metabolic switch from glycolysis to fatty acid oxidation (Makinde *et al*., 1997), we revealed no significant alteration in the phosphorylation level of AMPKα at NB20.5 versus E19.5 hearts (Figure 5D). With this respect, our preliminary findings revealed a birth-associated reduction in activities of various signaling pathways. It is essential to highlight that the signaling pathways are partially regulated by the activity of cytokines and growth factors. Consequently, we hypothesized that immediately after a separation from an intrauterine environment, the altered accessibility of neonatal hearts to growth factors and cytokines would influence the cell cycle activity in mouse CMs.

Therefore, our objective was to identify the growth factors and cytokines with a possible involvement in cell cycle regulation. In this context, the factors exhibiting an alteration in their levels were investigated in mouse hearts following delivery using multiple *in silico* and proteomic experiments. Due to previous investigations, it has been concluded that CMs in humans and mammalian organisms undergo cell cycle arrest after birth. Therefore, our final ambition was to induce CM cell cycle re-entry under *in vitro* conditions using the identified growth factors and cytokines. The outcome of this doctoral thesis could be beneficial for humans delivered preterm.

2. Materials and Methods

2.1. Materials

2.1.1. Laboratory devices

Table 1. Laboratory equipment

Equipment	Manufacturer	City, Country	Item Number
Axio Observer Fluorescence Microscope: Camera Axiocam 503 mono Camera Axiocam 305 color HXP 120 V Lamp N-Achroplan 10x/0,25 Ph1 M27 LD A-Plan 20x/0.35 Ph 1 Plan-Apochromat 20x/0.8 M27 N-Achroplan 40x/0,65 M27	Carl Zeiss Microscopy	Jena, Germany	-
CellDrop BF Cell Counter	DeNovix Inc.	Wilmington, USA	-
Consort Electrophoresis Power Supply	MERCK	Darmstadt, Germany	#E835
Centrifuge Rotina 38	Hettich	Tuttlingen, Germany	#1703
Centrifuge Universal 320R	Hettich	Tuttlingen, Germany	#1406
Cryostat Microm Cryo Star HM 560	Microm International GmbH	Walldorf, Germany	#M-HM-560
Disc rotator LLG-uni*LOOPMIX* 2	LLG Labware	Meckenheim, Germany	#6.263 665
Electrophoresis chamber (Agarose gel electrophoresis)	Keutz Labortechnik	Reiskirchen, Germany	-
Fusion CCD-Imaging System SOLO 6S EDGE	VILBER Lourmat Deutschland GmbH	Eberhardzell, Germany	#SOLO S
GeneAmp PCR System 2700 (Cycler)	Applied Biosystems	Waltham, USA	#S12522
gentleMACS™ Octo Dissociator with Heaters	Miltenyi Biotec	Bergisch Gladbach, Germany	#130-096-427
HeraFreeze HFU700TV (Freezer -80°C)	Thermo Fisher Scientific	Asheville, USA	#3959
Hera Safe: EN 12469: 2000, class II, Safety Cabinet (cell culture hood)	Thermo Fisher Scientific	Langenselbold, Germany	#40867914
IKA® shaker, Rocker 2D digital	IKA®-Werke	Staufen, Germany	#4003000
Incubator BD 115 (Cell culture)	Binder GmbH	Tuttlingen, Germany	#9010-0325

Magnetic stirrer MR Hei-Standard	Heidolph Instrument	Schwabach, Germany	#27230
Micro Centrifuge 22 R	Hettich	Tuttlingen, Germany	#24572
Micro Centrifuge 5418	Eppendorf AG	Hamburg, Germany	#VB-1866
Micro Centrifuge 5424	Eppendorf AG	Hamburg, Germany	#Z722960
Microm SEC35 Low Profile Blades (Microtome Paraffin)	Elektro Med™	Wola Zabierzowska, Poland	#EP-152215
Microm STS & Cool-Cut (Microtome Paraffin)	Thermo Fisher Scientific	Schwerte, Germany	#HM355
Microwave 700	Severin	Sundern, Germany	-
Mini Plate Spinner MPS 1000 (96-well plates)	Labnet International	Edison, USA	#16058
Mini-PROTEAN® tetra cell system (Western blot)	Bio-Rad Laboratories	Hercules, USA	#1658006FC
Mini Nutating, 3-D Mixer	VWR International	Darmstadt, Germany	#444-0148
MS3-Basic Vortexer	IKA®-Werke GmbH	Staufen, Germany	#0003617000
MS2 Mini Shaker	IKA®-Werke GmbH	Staufen, Germany	#510
Nano Photometer®	IMPLEN GmbH	Westlake Village, USA	#NP80-Touch
Olympus SZX7 Light microscope (Stereo-/Dissection Microscope)	Olympus	Tokyo, Japan	-
OTS 40 Slides-stretching table	MEDITE Medical	Burgdorf, Germany	#OTS 40.1540
Paraffin incubator INCU-Line® IL10	VWR International	Darmstadt, Germany	#390-0384
pH meter SevenDirect SD20	Mettler Toledo	Columbus, USA	#30671550
Pioneer Precision Scales	Ohaus	Parsippany, USA	
PowerPac™ Basic (Western blot)	Bio-Rad Laboratories	Hercules, USA	#1645050
Precellys Evolution Homogenizer	Bertin Technologies SAS	Paris, France	#P000062-PEVO0-A
Rotilabo staining chamber	Carl Roth	Karlsruhe, Germany	#HA48.1
Rotilabo Slide Holder	Carl Roth	Karlsruhe, Germany	#HA49.1
Rocker 2D digital	IKA®-Werke GmbH	Staufen, Germany	#0004003000
Steamer Type 3216 (Antigen retrival)	De'Longhi-Braun-Household GmbH	Neu-Isenburg, Germany	#FS3000
StepOnePlus™ Real-Time PCR System	Applied Biosystems	Waltham, USA	#4388817 A.1
4375786 Veriti™ 96-Well PCR Thermocycler	Thermo Fisher Scientific	Vilnius, Lithuania	#VAR-9627
ThermoMixer C (DNA isolation)	Eppendorf	Hamburg, Germany	#5382000015
ThermoMixer F1.5	Eppendorf	Hamburg, Germany	#460-0224
Thriller Thermomixer	PEQLAB Biotechnologie,	Erlangen, Germany	-

Tissue-TeK® TEC™ 6 (Cryostat sectioning)	Sakura Finetek Germany	Umkirch, Germany	#5110
Trans-Blot® Turbo™ Transfer System (Western blot)	Bio-Rad Laboratories	Munich, Germany	#1704150EDU
Tribute Collection Food steamer FS 3000 (Antigen retrieval)	Braun GmbH	Kronberg, Germany	#0X23611001
Weighing device SAC 62 (Scales)	Scaltec	Göttingen, Germany	-
ELISA Reader FLUOstar (Plate Reader)	BMG labtech	Ortenberg, Germany	-

2.1.2. Common labware and consumable materials

Table 2. Common laboratory consumables

Materials	Company	City, Country	Item Number
Amersham Protran 0.45 NC Nitrocellulose Blotting Membrane	Merck KGaA	Darmstadt, Germany	#GE10600002
Bemis™ Curwood Parafilm™	Bemis	Neenah, USA	#11772644
Cell culture multiwell plate, 6-Well	Greiner Bio-One	Kremsmünster, Austria	#657160
Cell culture multiwell plate, 12-Well	Greiner Bio-One	Kremsmünster, Austria	#665180
Cell culture petri-dish	Greiner Bio-One	Kremsmünster, Austria	#664160
Cell Scarper S (Western blot)	TPP Techno Plastic Products AG	Trasadingen, Switzerland	#99002
Cover slips 24x50 mm	R. Langenbrinck	Emmendingen, Germany	-
Paraffin Embedding Cassettes, Macro	Carl Roth	Karlsruhe, Germany	#EE16.1
Feather Disposable Scalpel	Feather Safety Razor	Osaka, Japan	#02.001.30.010
gentleMACS™ C Tubes (Primary CM isolation)	Miltenyi Biotec	Bergisch Gladbach, Germany	#130-096-334
Kimtech Precision Wipes	Kimberly-Clark®	Dallas, USA	#1559044
MACS SmartStrainer (70 µm) (Primary CM isolation)	Miltenyi Biotec	Bergisch Gladbach, Germany	#130-098-462
MicroAmp™ Optical Adhesive Films (RT-qPCR)	Applied Biosystems	Waltham, USA	#4311971
Micro-Amp® 96-Well Platten (RT-qPCR)	Applied Biosystems	Waltham, USA	#N8010560
Microvette® 200 Z (Serum isolation)	Sarstedt	Nuembrecht, Germany	#20.1290
Needle: BD Microlance ^{TM} 3, 27G $^{3}/_{4}$ ^{II} - Nr.20 (Blood sampling)	Becton, Dickinson and Company Limited	Louth, Ireland	#302200

PAP pen for immunostaining	Sigma-Aldrich	St. Louis, USA	#Z377821-1EA
Pipette tips (10, 20, 100, 200, and 1000 µl)	Sarstedt	Nümbrecht, Germany	-
Pipette tips 5000 µl	Gilson	Middleton, USA	#F161370
Pipette tips 10 µl (Filter)	nerbe plus GmbH	Winsen/Luhe, Germany	#07-602-8300
Pipette tips 200 µl (Filter)	nerbe plus GmbH	Winsen/Luhe, Germany	#06-662-5300
Pipette tips 1000 µl (Filter)	nerbe plus GmbH	Winsen/Luhe, Germany	#06-693-5300
SuperFrost *Ultra* plus® microscopic slides 25x75x1.0 mm	R. Langenbrinck	Emmendingen, Germany	#03-0062
Syringe: Injekt®-FluerSolo, 0.01 ml - 1 ml (Blood sampling)	ALMO-Erzeugnisse Erwin Busch	Bad Arolsen, Germany	#9166017V
Tissue-TeK® Cryomold®	Sakura Finetek Germany	Torrance, USA	#4557
Whatman™ filter paper (Western blot)	GE Healthcare Life science	Bukinghamshire, UK	#3030-335
0.5-ml, 1.5-ml, and 2-ml reaction tubes	Eppendorf	Hamburg, Germany	-
2 ml tubes for Precellys® homogenizer	VWR Interntional	Darmstadt, Germany	#P000945-LYSK0-A
8-well PCR strips	Kisker Biotech GmbH	Steinfurt, Germany	#G006-TUCA
8-well cell culture chamber slides	Sarstedt	Nümbrecht, Germany	#94.6140.802
15-ml falcon tube	Greiner Bio-One	Kremsmünster, Austria	#188261
1.4 mm Ceramic beads (Cell lysate preparation)	Cole-Parmer GmbH	Wertheim, Germany	#GZ-04728-56
2.8 mm Ceramic beads (Cell lysate preparation)	Cole-Parmer GmbH	Wertheim, Germany	#GZ-04728-66
50-ml falcon tube	Greiner Bio-One	Kremsmünster, Austria	#227261

Table 3. Instruments used for tissue dissection

Instrument	**Company**	**City, Country**	**Item Number**
Dumont #5 Forceps	Fine Science Tools	Foster City, USA	#11252-20
Dumont Tweezers Style 5/45	Emgrid Australia Pty Ltd	Adelaide, Australia	#0208-5/45-PO
Fine Scissors - Sharp	Fine Science Tools	Foster City, USA	#14061-11
Student Adson Forceps	Fine Science Tools	Foster City, USA	#91106-12
Surgical Scissors - Sharp	Fine Science Tools	Foster City, USA	#14002-12
Surgical Scissors - Sharp-Blunt	Fine Science Tools	Foster City, USA	#14001-18

2.1.3. Chemicals and inhibitors

Table 4. Chemicals, inhibitors, and size standards

Materials	Company	City, Country	Item Number
30% Acrylamide (Western blot)	Carl Roth	Karlsruhe, Germany	#3029.1
β-mercaptoethanol (β-ME)	Carl Roth	Karlsruhe, Germany	#4227.3
cOmplete mini (EDTA free) Protease Inhibitor Cocktail Tablets	Roche Diagnostics GmbH	Rotkreuz, Switzerland	#04 693 124 001
DAPI	Carl Roth	Karlsruhe, Germany	#6335.1
DC ™ Protein Assay	Bio-Rad Laboratories	Munich, Germany	#500-0112
DMSO (Dimethyl Sulfoxide)	AppliChem GmbH	Darmstadt, Germany	#A3672,0100
Dulbecco's PBS Cell culture grade	Life Technologies Limited	Paisley, UK	#14190-094
dNTPs: ROTI-MIX PCR3	Carl Roth	Karlsruhe, Germany	#L785.3
Ethanol Absolut (DNA isolation)	Otto Fishar GmbH	Saarbrücken, Germany	#27694
SuperSignal™ West Femto Maximum Sensitivity Substrat (Western blot)	Thermo Fisher Scientific	Rockford, USA	#34095
Fibronectin (Cell culture)	Sigma Aldrich	St. Louis, USA	#F1141-5MG
GeneRuler 100bp DNA Ladder	Thermo Fisher Scientific	Vilnius, Lithuania	#SM0243
HPLC H_2O: LiChrosolv®	Merck KGaA	Darmstadt, Germany	#1.15333.1000
37% Hydrochloric Acid (HCl)	Carl Roth	Karlsruhe, Germany	#9277.1
Methanol	Sigma Aldrich	St. Louis, USA	#32213-2.5L-M
Normal Goat Serum	Jackson ImmunoResearch Europe	Ely, UK	#005-000-121
PageRuler™ Prestained Protein Ladder (Western blot)	Thermo Fisher Scientific	Vilnius, Lithuania	#26616
Paraffin: Tissue-Tek® Paraffin Wax TEK IV, 4 x 2.5 kg 54 - 57 °C)	Sakura Finetek	Alphen aan den Rijn, Niederlande	#4523-0113
PhosStop Phosphatase Inhibitor Cocktail Tablets	Roche Diagnostics GmbH	Rotkreuz, Switzerland	#04 906 837 001
ProLong® Gold mounting medium	Cell Signalling Technology	-	#9071
2-propanol	Carl Roth	Karlsruhe, Germany	#9866.1
200 U/µl M-MuLV reverse transcriptase (NEB) (RT-qPCR)	New England BioLabs	Ipswich, USA	#M0253L

Random hexamer primer (RT-qPCR)	Eurofins Genomics	Ebersberg, Germany	#24-3139-1/1
10x reverse transcriptase reaction buffer (RT-qPCR)	New England BioLabs	Ipswich, USA	#B0253S
40 U/µl RibiLock® ribonuclease inhibitor (RT-qPCR)	Thermo Fisher Scientific	Vilnius, Lithuania	#EO038
RLT buffer (RT-qPCR)	Qiagen	Hilden, Germany	#1030963
SsoAdvanced™ Universal SYBR®Green Supermix (RT-qPCR)	BioRad Laboratories	Hercules, USA	#1725272
Saccharose (Cyrostat preparation)	Carl Roth	Karlsruhe, Germany	#9286.1
Tissue-Tek® O.C.T.™ Compound (Cryostat preparation)	Sakura Finetek	Alphen aan den Rijn, Niederlande	#SA62550-01
Toluene	Carl Roth	Karlsruhe, Germany	#9558.1
Trypan Blue (Cell culture)	Sigma Aldrich	St. Louis, USA	#T8154-100ML
Xylene	Carl Roth	Karlsruhe, Germany	#28975.325

2.1.4. Buffer and solutions

Table 5. Buffer and chemicals recipes

Buffer Name:	Recipes:	Manufacturer:	Item Number:
Organ Isolation:			
1x PBS-Tab	1x PBS Tablet	Life Technologies Limited	#18912-014
	In 500 ml Aqua B. Braun	B. Braun Melsungen AG	#82479E-E
4% PFA	4% (w/v) Paraformaldehyde	Carl Roth	#0335.3
	In 1x PBS-Tab	-	-
Genotyping:			
Lysis buffer (DNA isolation)	100 mM TRIS-Hydrochloride	Carl Roth	#9090.3
	0.2% (v/v) SDS	Sigma-Aldrich	# 74255-250G
	5 mM EDTA (pH 8.0)	Carl Roth	#CN06.2
	200 mM NaCl	Carl Roth	# 3957.1
	In ddH_2O	-	-
Proteinase K (DNA isolation)	0,02 % (w/v) Proteinase K	Carl Roth	#7528.1
	In 1× TBS (described later in-details)	-	-
Agarose	2% (w/v) in 1x TBE	peQlab	#35-1020
GelRed™ solution	0.03% (v/v) GelRed™	Biotium	#41003

	In ddH_2O	-	-
1x TBE	89 mM Tris-Base	Carl Roth	#4855.2
	89 mM Boric Acid	Carl Roth	#6943.1
	2 mM EDTA pH 8.0	Carl Roth	#CN06.2
	In ddH_2O	-	-
Immunohistochemistry Staining (IHC) on Paraffin Sections:			
Antibody solution (IHC)	1% (w/v) Albumin Fraction V (BSA)	Carl Roth	#T844.2
	0.1% (v/v) Triton X® 100	Carl Roth	#3051.3
	0.05% (v/v) Tween® 20	Carl Roth	#9127.2
	0.05% (w/v) Sodium Azide	Carl Roth	#4221.1
	In 1x TBS	-	-
1x TBS	50 mM Tris-Base	Carl Roth	#4855.2
	150 mM NaCl	Carl Roth	#3957.1
	HCl to adjust pH to 7.6	Carl Roth	#9277.1
	In ddH_2O	-	-
1x TBST (IHC and Western blot)	0.05% (v/v) Tween® 20	Carl Roth	#9127.2
	In 1x TBS	-	-
1x Tris-EDTA pH 9.0 (Antigen retrieval buffer)	10 mM Tris-Base	Carl Roth	#4855.2
	1 mM EDTA	Carl Roth	#CN06.2
	0.05% (v/v) Tween® 20	Carl Roth	#9127.2
	HCl to adjust pH to 7.6	Carl Roth	#9277.1
	In ddH_2O	-	-
Western Blot (WB):			
RIPA buffer (Tissue samples)	0.1% (w/v) SDS	Sigma Aldrich	#74255-250G
	1% (v/v) IGEPAL® CA-630	Sigma Aldrich	#13021-50ML
	0.5% (w/v) Sodium Deoxycholate	Sigma Aldrich	#D6750-25G
	1 mM EDTA pH 8.0	Carl Roth	#CN06.2
	In 1x TBS	-	-
1x CLB (*in vitro*)	1:10 CLB (10x concentrated)	Cell Signaling Technology	#9803
	In ddH_2O	-	-
10% APS	10% (w/v) in ddH_2O	AppliChem	#A1142,0250
5x Laemmli buffer	50 mM Tris/HCl (pH 6.8)	Carl Roth	#9090.3
	87% (=43.5% v/v) Glycerin	Carl Roth	#3908.2
	3% (w/v) SDS in ddH_2O	Sigma Aldrich	#74255-250G

	3% (v/v) β-Mercaptoethanol	Carl Roth	#4227.3
	0.003% (w/v) Bromophenol blue	Carl Roth	#A512.2
	In 1x TBS	-	-
1x SDS running buffer	25 mM Tris-Base	Carl Roth	#4855.2
	192 mM Glycin	Carl Roth	#3908.2
	0.1% (w/v) SDS	Sigma Aldrich	#74255-250G
	In ddH_2O	-	-
5% BSA	5% (w/v) Albumin Fraction V (BSA) in 1x TBST	Carl Roth	#T844.2
5% milk	5% dry milk (w/v) in 1x TBST	Carl Roth	#T145.2
Transfer buffer	48 mM Tris-base	Carl Roth	#4855.2
	39 mM Glycin	Carl Roth	#3908.2
	20% (v/v) Methanol	Sigma Aldrich	#32213-2.5L-M
	In ddH_2O	-	-
Solution A	0.1 M Tris-base pH 8.5	Carl Roth	#4855.2
	2.5 mM Luminol	Sigma Aldrich	#123072-5G
	0.396 mM P-Coumaric Acid	Sigma Aldrich	#C9008-25G
	In ddH2O	-	-
Solution B	0.1 M Tris-base pH 8.5	Carl Roth	#4855.2
	3% (v/v) Hydrogen Peroxide (H_2O_2)	Carl Roth	#9681.4
	In ddH2O	-	-
Stripping buffer	62.5 mM Tris-base pH 6.8	Carl Roth	#4855.2
	2% (w/v) SDS	Sigma Aldrich	#74255-250G
	0.7% (v/v) β-Mercaptoethanol	Carl Roth	#4227.3
	In ddH2O	-	-
ELISA Experiments:			
2x Lysis buffer	1:1 Lysis buffer (2x concentrated)	RayBiotech	#EL-Lysis
	In ddH2O	-	-
***In vitro* Experiments:**			
Neonatal CMs culture	1% (v/v) Penicillin-Streptomycin	Biochrom	#A2213
	0.1 mM Ascorbic acid	Sigma Aldrich	#4544-100G
	0.5% Insulin-Transferrin-Selenium	Fisher Scientific	#12097549
	5% (v/v) Horse serum	Fisher Scientific	#11540636
	In DMEM/F12	PAN-Biotech	#P04-04510
Neonatal CMs treatment medium	1% (v/v) Penicillin-Streptomycin	Biochrom	#A2213

	0.1 mM Ascorbic acid	Sigma Aldrich	#4544-100G
	0.5% (v/v) FCS (Lot#BCCC6626)	Sigma Aldrich	#F7524
	In DMEM/F12	PAN-Biotech	#P04-04510
Immunofluorescence Staining (IF) for *in vitro* Experiments:			
Antibody solution-IF	Antibody solution IHC	Carl Roth	#T844.2
	In PBS (pH 7.4) (instead of 1x TBS)	-	-
Blocking solution	5% (v/v) NGS	Jackson ImmunoResearch	#005-000-121
	In Antibody solution-IF		
PBS (pH 7.4)	0.137 M NaCl	Carl Roth	#3957.1
	2.7 mM KCl	Carl Roth	#6781.3
	10 mM Na_2HPO_4	Carl Roth	#4984.1
	1.8 mM KH_2PO_4	Carl Roth	#3904.1
	In ddH_2O	-	-

2.1.5. Antibodies

Table 6. Primary antibodies (AB)

Primary AB	Source	Dilution	Solution	Company	Order number
Immunofluorescence (IF) and Immunohistochemistry-IF (IHC) Experiments					
Anti-Actinin	Mouse	1:800	Antibody Solution in PBS	Sigma Aldrich	#A7811
Anti-BrdU	Rat	1:1000	Antibody Solution in PBS	Abcam	#ab6326
Anti-Caveolin 3	Mouse	1:100	Antibody Solution in TBS	Santa Cruz Biotechnology	#SC-5310
Anti-Cyclin D3	Mouse	1:1000	Antibody Solution in TBS	Cell Signalling Technology	#2936
Anti-pHH3 (Ser10)	Rabbit	1:200	Antibody Solution in TBS	Cell Signalling Technology	#9701
Anti-8-Hydroxyguanosine	Mouse	1:300	Antibody Solution in TBS	Abcam	#ab62623
Anti-Ki67	Rat	1:500	Antibody Solution in TBS/PBS	Invitrogen	#14-5698-82
Anti-MEF2A/C	Rabbit	1:500	Antibody Solution in TBS	Abcam	#ab197070
WGA-488 conjugate	-	1:500	Antibody Solution in TBS	Thermo Fisher Scientific	#W11261
Western Blot (WB) Experiments					

Anti-p-Akt (Ser473)	Rabbit	1:1000	5% BSA	Cell Signalling Technology	#4060
Anti-Akt (pan) total	Rabbit	1:1000	5% BSA	Cell Signalling Technology	#4691
Anti-Cyclin D1	Rabbit	1:1000	5% BSA	Cell Signalling Technology	#2978
Anti-Cyclin D2	Rabbit	1:1000	5% BSA	Cell Signalling Technology	#3741
Anti-Cyclin D3	Mouse	1:2000	5% BSA	Cell Signalling Technology	#2936
Anti-p-4E-BP1 (Ser65)	Rabbit	1:1000	5% BSA	Cell Signalling Technology	#9451
Anti-4E-BP1 total	Rabbit	1:1000	5% BSA	Cell Signalling Technology	#9644
Anti-GAPDH	Mouse	1:50000	5% milk	Thermo Fisher Scientific	#MA-16757
Glycolysis Antibody Sampler Kit	Rabbit	1:1000	5% BSA	Cell Signalling Technology	#8337
Glycolysis II Antibody Sampler Kit	Rabbit	1:1000	5% BSA	Cell Signalling Technology	#12866
Anti-p-GSK-3ß (Ser9)	Rabbit	1:1000	5% milk	Cell Signalling Technology	#9336
Anti-GSK-3ß total	Mouse	1:1000	5% BSA	Cell Signalling Technology	#9832
Anti-LDHA	Rabbit	1:1000	5% BSA	Cell Signalling Technology	#2012
Anti-p-MST1/2 (Thr183/180)	Rabbit	1:1000	5% BSA	Cell Signalling Technology	#3681
Anti-MST1 total	Rabbit	1:2000	5% milk	Epitomics	#1941-1
Anti-MST2 total	Rabbit	1:1000	5% BSA	Cell Signalling Technology	#3952
Anti-p21	Rabbit	1:1000	5% milk	Santa Cruz Biotechnology	#SC-471
Anti-p27	Rabbit	1:1000	5% BSA	Cell Signalling Technology	#3686
Anti-p-p38 (Thr180/182)	Rabbit	1:1000	5% BSA	Cell Signalling Technology	#4511

Anti-p38 total	Rabbit	1:1000	5% BSA	Cell Signalling Technology	#8690
Anti-p-p44/42 (Thr202/204)	Rabbit	1:2000	5% BSA	Cell Signalling Technology	#4370
Anti-p44/42 total	Rabbit	1:1000	5% BSA	Cell Signalling Technology	#4695
Anti-p-p70S6K (Thr389)	Rabbit	1:1000	5% BSA	Cell Signalling Technology	#9205
Anti-p70S6K total	Rabbit	1:1000	5% BSA	Cell Signalling Technology	#2708
Anti-p-S6 (Ser235/236)	Rabbit	1:2000	5% BSA	Cell Signalling Technology	#4858
Anti-S6 total	Rabbit	1:1000	5% BSA	Cell Signalling Technology	#2217
Anti-Vinculin	Mouse	1:5000	5% milk	Sigma Aldrich	#V9131
Anti-p-YAP (Ser127)	Rabbit	1:1000	5% BSA	Cell Signalling Technology	#13008
Anti-YAP total	Rabbit	1:1000	5% BSA	Cell Signalling Technology	#4912

Table 7. Secondary AB

Secondary AB	Source	Dilution	Company	Order number
IHC and IF Experiments				
Anti-Mouse Alexa-488	Goat	1:500	Invitrogen	#A-11001
Anti-Mouse Alexa-555	Goat	1:500	Invitrogen	#A-21424
Anti-Mouse Alexa-647	Goat	1:500	Invitrogen	#A-21235
Anti-Rabbit Alexa-plus-555	Goat	1:1000	Invitrogen	#A-32732
Anti-Rabbit Alexa-plus-647	Goat	1:1000	Invitrogen	#A-32733
Anti-Rat Alexa-555	Goat	1:500	Invitrogen	#A-21434
Anti-Rat Alexa-647	Goat	1:500	Invitrogen	#A-21247
Western Blot (WB) Experiments				
Anti-mouse IgG HRP-linked	Horse	1:2000	Cell Signalling Technology	#7076
Anti-rabbit IgG HRP-linked	Goat	1:2000	Cell Signalling Technology	#7074

2.1.6. RT-qPCR

Table 8. Primers used for RT-qPCR. The primers were diluted in HPLC H_2O as suggested by manufacturers.

Gene, Product	Primer ID/name (F/R)	Sequence (5' → 3')	Company	Product size	Stock, P_C [µM]	T_A [°C]
Cell Cycle Regulators						
***Ccnd1*, Cyclin D1**	F-08969-22 (F)	TGACCCCGCACGATTTCATT	BioTez	143-bp	1	62
	R-08970-23 (R)	CATGGAGGGCGGATTGGAAA				
***Ccnd2*, Cyclin D2**	Cyclin D2-E4/5_fwd (F)	GATGAAGTGAACACACTCACG	BioTez	178-bp	10	62
	Cyclin D2-E4/5_bwd (R)	CCGGATCTTCCACAGACTTG				
***Ccnd3*, Cyclin D3**	05206-22 (F)	GGCCTCCAAGCTGCGCGAAACC	BioTez	128-bp	1	62
	05207-22 (R)	GGTCCCACTTGAGCTTCCCCAG				
***Ccna2*, Cyclin A2**	28013945 (F)	CAGCTGTCTCTTTACCCGGAGC	Eurofins	255-bp	1	62
	28013946 (R)	CCACAAGGATGGCCCTCATGC				
***Ccnb1*, Cyclin B1**	08975-20 (F)	GCTGACCCAAACCTCTGTAG	BioTez	132-bp	5	62
	08976-21 (R)	GAGGATAGCTCTCATGTTTCC				
***Cdkn1a*, p21**	08971-23 (F)	TCGCTGTCTTGCACTCTGG	BioTez	136-bp	5	60
	08972-23 (R)	TCTTGCAGAAGACCAATCTG				
***Cdkn1b*, p27**	12714-19 (F)	GACTCGTCAGACAATCCGG	BioTez	155-bp	1	60
	12715-19 (R)	GTCTGCTCCACAGTGCCAG				
Cytokines and Growth Factors						
***Angptl3*, Angptl3**	Angptl3-F (F)	GAGCACCAAGAACTACTCCCC	Eurofins	113-bp	2	62
	Angptl3-R (R)	GCCACTTGTATGTTCGCCTC				
***Col18a1*, Endostatin**	30-3213-3/12 (F)	AGGTGAGGATCTGGGCCAC	Eurofins	185-bp	5	62
	30-3213-4/12 (R)	CAAAGCAGCCACCTCATTGC				
***Igf1*, Igf1**	Igf1-F (F)	TTCAGTTCGTGTGTGGACCGAG	Eurofins	94-bp	5	60
	Igf1-R (R)	TCCACAATGCCTGTCTGAGGTG				
***Igfbp-6*, IGFBP6**	Igfbp6-F (F)	CCAACCCCGAGAGAACGAAG	Eurofins	116-bp	10	62
	Igfbp6-R (R)	CTCCTTGGGGTTTGCTCTCC				

***Pdgfa*, PDGFA**	Pdgfa-F (F)	TACTGAATTTCGCC GCCACAG	Eurofins	186-bp	5	62
	Pdgfa-R (R)	AGCCGCTCGATCA ACTCC				
***Spp1*, Osteopontin**	SPP1-F-28.02.2022 (F)	GCTTGGCTTATGGA CTGAGGTC	Eurofins	114-bp	5	64
	SPP1-R-28.02.2022 (R)	CCTTAGACTCACCG CTCTTCATG				
***Polr2a*, Polr2a**	m-Polr2a-cDNA-F (F)	GAGAAGCTGGTCC TTCGAATC	Eurofins	121-bp	5	56-62
	m-Polr2a-cDNA-R (R)	GCATGTTGGACTCA ATGCATC				
Glycolysis-Involved Enzymes						
***Aldolase-a*, ALDOA**	AldoA-F (F)	TTAGTCCTTTCGCC TACCCA	Eurofins	300-bp	12.5	60
	AldoA-R (R)	AATGCGGTGAGCG ATGTCA				
***Enolase I*, Eno-I**	mEnol-F (F)	CCTTAAGGCTCTCC TCGGTG	Eurofins	263-bp	10	60
	mEnol-R (R)	TGAGACACCCTTCC CCATGA				
***Hexokinase II*, Hk-II**	mHKII-F (F)	ACAAGATGATCGC CTCGCAT	Eurofins	226-bp	1.25	61
	mHKII-R (R)	CCATCCGGAGTTG ACCTCAC				
***Lactatedehydrogenase A*, LDHA**	mLdhA-F (F)	CAGTTGTTGGGGTT GGTGCT	Eurofins	196-bp	12.5	63
	mLdhA-R (R)	GAGTTCGCAGTTAC ACAGTAGT				
***Pyruvatekinase-M*, PKM1/2**	mPKM-F (F)	GTGATGTGGCCAA TGCAGTC	Eurofins	153-bp	1.25	60
	mPKM-R (R)	CTTCAAACAGCAG ACGGTGG				

2.1.7. ELISA

Table 9. ELISA kits

Materials	Company	City, country	Order number/ID
Mouse Adiponectin Immunoassay	R&D Systems	Minneapolis, USA	#MRP300
Mouse Angiopoietin-like 3 Immunoassay	R&D Systems	Minneapolis, USA	#MANL30
Mouse Endostatin ELISA Kit	Abcam	Cambridge, UK	#ab263894
Mouse IGF-1 Immunoassay	R&D Systems	Minneapolis, USA	#MG100
Mouse IGFBP-1 ELISA Kit	Abcam	Cambridge, UK	#ab213865
Mouse IGFBP-6 ELISA kit	RayBiotech	Norcross, USA	#ELM-IGFBP6
Mouse Osteopontin (OPN) ELISA Kit	R&D Systems	Minneapolis, USA	#MOST00

Mouse PDGF-AA ELISA Kit	RayBiotech	Norcross, USA	#ELM-PDGFAA

2.1.8. Other kits

Table 10. Kits

Materials	Company	City, Country	Item Number
Mouse Growth Factor Array C3	RayBiotech	Norcross, USA	#AAM-GF-3-8
Neonatal Heart Dissociation Kit, mouse and rat	Miltenyi Biotec	Bergisch Gladbach, Germany	#130-098-373
Proteome Profiler Mouse XL Cytokine Array	R&D Systems	Minneapolis, USA	#ARY028
RNase-Free DNase Set (RT-qPCR)	Qiagen	Hilden, Germany	#79254
RNeasy® Plus Mini Kit (RT-qPCR)	Qiagen	Hilden, Germany	#74134
Taq DNA polymerase kit (PCR)	Qiagen	Hilden, Germany	#201205

2.1.9. Software and online tools

Table 11. Software and program information

Software	Company	City, Country
Adobe Illustrator CS6 16.0	Adobe Systems	San José, USA
Adobe Photoshop CC 2018 19.1	Adobe Systems	San José, USA
Bio-ID advanced	Vilber Lourmat	Collégien, Frankreich
Capture Edge	Vilber Lourmat	Collégien, Frankreich
Excel v16.72	Microsoft	Redmond, USA
FLUOstar OPTIMA v1.30-0 (ELISA)	BMG Labtechnologies	Ortenberg, Germany
IBM SPSS Statistics v29.0.0.0	IBM	Armonk, USA
Image J (Open source)	National Institutes of Health	Maryland, USA
Primer-BLAST	U.S. National Library of Medicine	Bethesda, USA
Prism v9.5.1	Graphpad Software	San Diego, USA
StepOne v2.3	Life Technologies	Carlsbad, USA
ZEN 2.3 pro (Image Acquisition)	Carl Zeiss Microscopy	Jena, Germany
ZEN 2.3 Image Analysis (ZEN 3.8 desk with Image analysis toolkit)	Carl Zeiss Microscopy	Jena, Germany

2.2. Methods

2.2.1. Animal housing

The entire animal procedures were carried out in compliance with the guidelines of the "Federation of European Laboratory Animal Science Associations" (FELASA) and have previously been approved by institutional (JLU approval numbers: 709_M (this refers to killing/euthanasia of postnatal mice for scientific purposes, so all heart preparations after birth) and governmental authorities (*Regierungspräsidium Gießen*, approval number GI 20/12 Nr. G 49/2017 and G 47/2020 (this refers to preparation of embryos and fetuses in the final quarter of gestation, so all heart preparations before birth). In order to minimize suffering of the mice, the ARRIVE guidelines were followed (Kilkenny *et al*., 2010).
The mouse strains in this study were housed and bred at the Justus-Liebig University in Giessen, Germany. Animal welfare, health and housing conditions were monitored by the trained staff of the facilities. Thereby, the mice were kept under standard conditions with 10/14 h dark-light cycle, as well as food and water *ad libitum*.

2.2.1.1. Mouse strains and breeding strategy

2.2.1.1.1. C57BL/6J mouse strain

In this thesis, multiple factors including cell cycle activity and the mechanisms underlying its regulation at defined perinatal stages will be analyzed. Therefore, the central key player in our study, is a sensitive control over the determination of exact gestational ages of mice. In this context, C57BL/6J inbred mouse strain are used, exhibiting averaged 19.5 gestational days (C57BL/6J mice were purchased from Charles River, i.e., #159683//C57BL/6J_1). In the course of our experience concerning C57BL/6J mice, in order to estimate the exact animal gestational age, the optimal breeding strategy is to allow the mating process occur upon overnight (O/N) housing of a C57BL/6J breeding pair. Therefore, a male and a female mouse will be put in a breeding cage in the afternoon. The next day in the morning, the breeding pair will be separated to avoid further mating and a wrong estimation of gestational ages. 14 days later, the state of mouse pregnancy will be monitored and the non-pregnant mice will be used for further mating process. In pregnant mice, based on the mating date, the exact gestational age of the fetal or newborn

(NB) individuals can be determined. As another breeding strategy monitoring the "vaginal plug" can be mentioned. In this method, the housing of breeding pair is conducted for several days. Each day in the morning, the animal mating is monitored by checking the vaginal plug presence in female mice. However, this method is not sensitive enough while determining the exact gestational age of fetal and NB mice.

18 days after mating, at 8:00 and at 16:00 the cages will be monitored for possible NB individuals. Depending on the stage of interest, the animals will be dissected and desired organs will be isolated and prepared for various experiments. A key central stage in this study is gestational day 18.5. Notably, the birth does not necessary take place at day 18.5. On one hand, at this stage some of the female mice have already delivered mice (known as NB18.5). On the other hand, some pregnant mice have not delivered yet. Accordingly, the fetus will be isolated via cesarean section of the pregnant mice and the desired organs will be isolated for further experiments (known as embryonic 18.5 (E18.5) samples). In this context, comparing the samples obtained from the NB18.5 (already exposed to an extrauterine environment) and the E18.5 mice, the role of birth on multiple factors can be investigated. Furthermore, assuming that any modifications observed in the postnatal life period, would be initially programed within the final embryonic stages or not, the embryonic stages will also be compared to each other. Therefore, in addition to E18.5 samples, E17.5 samples will be prepared. In some cases, the delivery occurs at gestational age 19.5 (NB19.5). Comparing the NB18.5 and NB19.5 allows for studying the gestational age. To study further influence of extrauterine environment, the NB animals were housed with the mothers for 24 h known as NB18.5+1 and NB19.5+1, or 48 h named as NB18.5+2 and NB19.5+2. Taken together, the sampling was performed at the following days: E17.5, E18.5, NB18.5, NB18.5+1, NB19.5, NB19.5+1, and NB19.5+2.

2.2.1.2. Isolation of mouse fetal hearts, liver and blood at defined gestational stages and blood samples from mother

As soon as the fetal stage of interest (i.e., E17.5 or E18.5) was reached, pregnant mice were euthanized by cervical dislocation. The blood collection was conducted from the pregnant mother by a syringe and a needle from the inferior vena cava (Chapter 2.1.2., Table 2, 0.4 x 19 mm). Thus, after cervical dislocation and opening the abdominal cavity, the inner organs were pushed to a side and 200 µl blood was collected from the inferior vena cava and immediately transferred into a 1.5 ml reaction tube. Next, the fetuses were

immediately dissected from the uterus and separated from the placenta and surrounding membranes. To minimize harm or suffering, the fetuses were euthanized by decapitation. Using Microvette® 200 Z capillary collection tubes, about 20 to 50 µl of blood (mixed venous and arterial blood from the decapitation site) from each embryo was collected for serum isolation. Subsequently, the fetuses were immediately placed in fresh ice-cold 1x Phosphate buffered saline (1x PBS-Tab). In order to stop cellular activities, all procedures were performed on ice. To determine the gender of the individual fetuses, tails were collected and stored at -20°C until DNA preparation. The hearts were prepared by opening the thoracic cavities and dissecting the entire organ from the great vessels near the outflow tract. Depending on the procedure of interest, the hearts were either fixed in 4% PFA for immunohistochemistry studies or snap-frozen in liquid nitrogen for RNA and protein analyses.

After the hearts were collected, the abdominal cavity of fetal pups was opened and the whole liver was isolated. The isolated livers were shortly washed in ice-cold 1x PBS-Tab and transferred into 1.5 ml-reaction tubes. The tubes were directly snap-frozen in liquid N_2 and stored at -80°C for future experiments.

2.2.1.3. Heart isolation from newborn mice at defined gestational stages

After applying the breeding strategy described above (Chapter 2.2.1.1.1.) pups were naturally born either at gestational day 18.5 or 19.5 based on a biological variability in the delivery date (Murray *et al*., 2010), and categorized as NB18.5 or NB19.5 (NB=Newborn), respectively. To analyze a prolonged impact of exposure to the extrauterine environment on cardiac growth and cell cycle regulation, some litters were kept for further 24 and 48 hours in the cage with the mother. Based on the gestational age at birth, these mice were either identified as NB18.5+1 or NB19.5+1 (born at gestational age 18.5 or 19.5, and housed for 24 h with mother), and NB18.5+2 or NB19.5+2 (48 h after birth). As soon as the age of interest was reached, the newborn mice were sacrificed by decapitation. The blood samples were collected using Microvette® 200 Z as described before (2.2.1.2.). Tails were collected for gender determination, as well. Moreover, the hearts were excised from the thoracic cavity and washed in fresh ice-cold 1x PBS-Tab. The non-cardiac tissues were removed and the hearts were either snap-frozen in liquid nitrogen or fixed in 4% paraformaldehyde (PFA).

After collecting hearts, the whole liver was isolated. The isolated livers were shortly washed in ice-cold 1x PBS-Tab and transferred into 1.5 ml-reaction tubes. The tubes were directly snap-frozen in liquid N_2 and stored at -80°C for future experiments.

2.2.1.4. Blood collection and serum preparation from perinatal and adult mice

Blood collection from fetal and newborn mice was performed using Microvette® 200 Z, while blood collection from pregnant and non-pregnant female mice was done by a syringe and a needle from the inferior vena cava. Notably, similar to pregnant mice, the blood sampling from adult female non-pregnant mice was conducted on the animals that had been already sacrificed for other organ isolations, as described previously, using a syringe and a needle from the inferior vena cava (Chapter 2.1.2., Table 2, 0.4 x 19 mm). The Microvette® 200 Z is composed of a thin capillary and a connected collection tube. After the decapitation of perinatal pups, the blood emerging from the thoracic wound (originating from carotid and other arteries and veins) is sucked up into the Microvette® 200 Z capillary. Using gravity force, the collected blood is next guided into the connected collector of the Microvette® 200 Z, and used for serum preparation.

All collected blood samples were incubated for 1 h, at room temperature (RT) in order to allow complete coagulation. To get rid of cellular components, blood clots and coagulation factors, serum isolation was carried out via centrifugation of coagulated blood at 18407 rcf, for 10 min, at RT (Micro Centrifuge 5424, Eppendorf AG). After the centrifugation step, the serum supernatant was gently collected for further studies and stored at -80°C.

2.2.2. Sex determination of perinatal mice

2.2.2.1. Genomic DNA purification from murine tissue

The gender determination of perinatal mice was carried out by polymerase chain reaction (PCR) analyses on genomic DNA isolation from the collected tail tissue (Chapters 2.2.1.2. and 2.2.1.3.). The tails were digested in 400 µl lysis buffer supplemented with 1% (v/v) proteinase K (from the stock solution) over night at 55°C, by constant shaking at 700 rpm using a thermomixer. The next day, the cell debris was spun down for 15 min, at 21910

rcf, at RT. Carefully, 100 µl of the supernatant containing genomic DNA was transferred into a fresh sterile 1.5 ml reaction tube. Afterwards, DNA precipitation was carried out via administration of 100 µl 2-propanol into each tube which were immediately vortexed and incubated for 30 min at -20°C. The precipitated DNA was isolated from the remaining cellular contents by centrifugation at 21910 rcf for 10 min at RT. The supernatant was discarded and the DNA pellet was washed with 200 µl 70% ethanol (EtOH) followed by a final centrifugation at 21910 rcf for 10 min at RT. The supernatant was discarded and the DNA pellets were dried in a thermomixer at 700 rpm, for 30 min, at 37°C. The precipitated DNA was diluted in 100 µl ddH_2O by shaking for 1 h, at 700 rpm, at 50°C. The isolated DNA was stored at -20°C.

2.2.2.2. Nucleic acid concentration determination via NanoDrop

In order to determine the concentration and purity of the isolated DNA or RNA, a Nano Photometer® (NP80-Touch, IMPLEN GmbH) was used. Using NanoDrop spectrophotometer the samples are exposed to ultraviolet (UV) light at a wavelength of 260 nm. The absorbed light correlates with the nucleic acid concentration. Next, an optical density (OD) is calculated. Moreover, using the OD and the Beer Lambert Law, the sample concentration is determined. The NanoDrop can measure the absorbance in small volume of samples (0.5 to 2.0 µl). The DNA was diluted in ddH_2O, therefore 1.5 µl ddH_2O was used as blank. Next, the OD and concentration of DNA of each sample were determined at a wavelength of 260 nm in 1.5 µl of sample. The measurements can be affected by different salts, solvents and proteins in the sample. To monitor the degree of contamination with other molecules, two ratios are considered such as OD at wavelength of 260 nm (OD_{260}, for nucleic acids) divided by OD_{280} (for proteins) and OD_{260}/OD_{230} (OD_{230} for salt detection) ratio. The DNA samples with OD_{260}/OD_{280} equal to 2.0±0.1 and OD_{260}/OD_{230} greater than 1.0 had the optimum DNA purity and therefore were used for PCR.

2.2.2.3. Determination of sex by polymerase chain reaction (PCR)

To monitor the possible effect of animal gender on the activity of various cellular processes, the mice's gender was determined by PCR. PCR was performed for amplification of the *sex determining region of chromosome Y* gene (*Sry*), which is only detectable in male mice. Additionally, to assure PCR efficiency the X-chromosomal

holocytochrome c synthase (*Hccs*) gene was amplified as internal PCR control. Since the PCR products of both primer pairs differ (250 bp for SRY and 390 bp for HCCS) and can be distinguish after electrophoresis, they can be run in the same PCR reaction.

The reaction mixture for PCR, in addition to DNA template and primer pairs complimentary to upstream and downstream parts of the sequences of interest, consists of nucleotides (dNTPs) and thermostable DNA-polymerase. PCR relies on thermo-cycling, which allows for exposure of PCR reaction mixture to repeated cycles of heating and cooling events. Each cycle of PCR consists of three steps including denaturation, primer annealing and elongation. During the denaturation step, the double-stranded DNA is melted into single strands via application of high temperature (usually 95°C). Denaturation is followed by annealing to allow for binding of primers to the single-stranded template DNA. The DNA-polymerase then interacts with the 3'-OH (hydroxyl) end of primers and links complimentary nucleotides (dNTPs) to the template DNA and thereby elongates the nucleic acid. The Taq DNA polymerase used in this experiment originates from thermophilic bacterium *Thermus aquaticus,* which is stable at high temperatures during the denaturation step (95°C) (*Taq* DNA polymerase kit, Qiagen).

The PCR reaction mixture was prepared as listed below (Table 12) and added into 0.2 ml PCR tubes placed on ice. The PCR tubes were placed in a thermocycler (GeneAmp PCR System 2700, Applied Biosystems) and the PCR was run according to the cycling program outlined below (Table 13). After the PCR was completed, the products were either stored at -20°C or directly used for application on a 2% agarose gel.

Table 12. PCR reaction mixture for gender determination and genotyping.

components	Concentration	Volume [µl]
ddH2O	-	18.4
10× PCR buffer	1x	2.5
10 µM *Hccs* forward primer	0.2 µM	0.5
10 µM *Hccs* reverse primer	0.2 µM	0.5
10 µM *Sry* forward primer	0.2 µM	0.5
10 µM *Sry* reverse primer	0.2 µM	0.5
2.5 mM dNTPs	0.1 mM	1
5 U/µl Taq polymerase	0.02 U/µl	0.1
50 to 70 ng/µl genomic DNA	-	1
Total Volume	-	25

Table 13. PCR running program.

Step	Temperature [°C]	Duration	Cycles [x]
Initialization	95	3 min	1
Denaturation	95	30 s	40
Primer annealing	60	45 s	
Elongation	72	1 min	
Final elongation	72	8 min	1
Storage	4	unlimited	-

Table 14. List of primers used for gender determination and genotyping. T_A stands for annealing temperature.

Gene	Primer ID/name	Sequence (5' → 3')	Product size	T_A [°C]
Hccs	mHccs23-fwd	TCATTCAGGCCAGGACTTCT	380-bp	60
	mHccs24-rev	GTTACGGAAAGGGTGAGTGA		
Sry	mSRY-fwd	AGAGATCAGCAAGCAGCTGG	249-bp	60
	mSRY-bwd	TCTTGCCTGTATGTGATGGC		

2.2.2.4. Agarose gel electrophoresis

To separate the PCR products agarose gel electrophoresis is performed. The agarose gel serves as a three-dimensional matrix with pores in which biomolecules can be separated depending on their size. The PCR products are loaded onto the agarose gel (here 2%) which is placed in an electric field. Due to the phosphate backbone, the nucleic acids carry a negative charge; thus, within the electric field, they move towards the positively charged anode. The gel matrix is responsible for the DNA separation by size during electrophoresis. The smaller the molecules are, the faster they move, which allows for their separation by size. The agarose gel percentage correlates with the degree of separation. In this study, 2% gels are used which give satisfying resolution for small fragments (0.1 to 1 kb). Thus, the gel was prepared by dissolving 2% agarose in 1x TBE buffer (w/v) via heating in a microwave. The solution was chilled in a gel cast containing chamber and a comb for 30 min at RT. Later on, the 2% gel was positioned in an electrophoresis chamber, filled with 1x TBE buffer and the comb was removed. 6 µl GeneRuler™ 100 bp DNA ladder (as size standard) and 8 µl of PCR products were loaded onto each lane of the gel. The 10x PCR buffer provided in the Qiagen kit allows for direct loading of the PCR product onto the gel. Additionally, it contains two marker dyes

including an orange and a red dye, which facilitate the estimation of the DNA migration within the gel.

After the gel was loaded with PCR products, the electrophoresis was carried out at 100 V for 2.5 h in 1x TBE buffer. After the running was terminated, in order to make the DNA fragments visible, the gel was incubated in GelRed™ solution for 30 min at RT. GelRed™ is a DNA intercalating reagent, which is inserted between the planar base pairs in nucleic acids. Upon exposure to UV light at 320 nm, GelRed™ is detectable in its DNA-conjugated state, which makes the separated DNA fragments within the agarose gel visible. After incubation of the gel in GelRed™, it was washed in ddH_2O to get rid of surplus GelRed™. Finally, the PCR products were imaged in a gel documentation system (Fusion CCD-Imaging System SOLO S). Depending on the size of the bands, the gender of the pups was determined.

2.2.3. Immunofluorescence staining on paraffin sections

2.2.3.1. Preparation of paraffin sections

For histological analysis isolated fetal and newborn hearts (Chapter 2.2.1.2. and 2.2.1.3.) were embedded in paraffin. Prior to paraffin embedding, the hearts must be fixed to avoid autolysis of the tissues. As one of the most common fixatives paraformaldehyde crosslinks proteins and DNA molecules. Therefore, after heart isolation, fixation was conducted by 48 h incubation in 4% PFA at 4°C, under gentle agitation. The fixation was followed by dehydration, which facilitates the embedding of tissues in water-insoluble paraffin. Accordingly, the hearts were gradually dehydrated by immersion in increasing concentrations of ethanol namely 70% for O/N, 80% for 2 h, 90% for 2 h, 96% for 2h, and 100% for O/N, under constant agitation. Prior to incubation in paraffin, the remaining ethanol needs to be replaced with the substance that is miscible with the liquid paraffin embedding medium. Therefore, after the dehydration step, two incubations were performed using the clearing agent toluene, for 45 min each at RT. Subsequently, to let the paraffin infiltrate the samples, hearts were incubated in three consecutive baths of melted paraffin (DMSO free TEK IV Processing and Embedding Wax, Sakura Finetek) for 2 h, O/N and 2 h, at 60°C using an incubator (INCU-Line® IL10). The organ embedding was performed using a Tissue-Tec Embedding Console system (Tissue-TeK®

TEC™). Metal moulds were filled with a small volume of paraffin and hearts were positioned as desired. In order to maintain the desired sample position, the moulds were shortly placed on a 4°C-plate of the Tissue-Tec station. As soon as the paraffin at the bottom of the mould hardened, the moulds were filled up completely with paraffin. The paraffin was completely hardened by further incubation on the 4°C-plate (part of the Tissue-Tec Embedding Console system), for 1 h. The paraffin blocks were taken out of the metal moulds and stored at RT. Per each slide, four to five 5 µm-thin sections were prepared from each block by using a microtome (Microm Cool-Cut) equipped with a cooled block holder and water slide to transfer sections on water bath. Hence, a SEC35 Low Profile Blade (Microm) was installed in the microtome and carefully 5 µm-thin heart slices were prepared form each paraffin block. The sections were next transferred (via water slide) and stretched on the surface of a 48°C water bath for 20 min. Afterwards, four to five slices were transferred on a positively charged microscope slide (SuperFrost *Ultra* plus®). Upon O/N incubation at RT, the prepared slides were dried and the day after were ready for histological analyses.

2.2.3.2. General immunofluorescence (immunohistochemistry) protocol and imaging

In order to visualize a specific epitope *in situ*, immunofluorescence (IF) staining is performed, which provides information about the spatial localization and expression of the epitope. A species-specific primary antibody specifically binds its epitope and subsequently is detected using a fluorophore-coupled secondary antibody specific for the species of the primary antibody. Prior to staining, the prepared heart sections need to be firmly attached to the glass slides by incubation of slides on a stretching plate (OTS 40.1540) for 20 min, at 60°C. For the IF staining, the sections need to be free of paraffin and get rehydrated. Therefore, deparaffinization was carried out by three consecutive incubations in three xylene baths for 5 min each at RT. Subsequently, the samples were rehydrated by incubation in a decreasing series of ethanol/ddH_2O including 100%, 100%, 96%, 80%, and 70%, each time for 3 min, as well as two final incubations in ddH_2O for 3 min each at RT.

The fixation step in 4% PFA (after heart isolation) masks epitopes, which prevents the epitope-antibody interaction. In order to set the epitopes free, heat-mediated antigen retrieval was performed on rehydrated sections, using 1x Tris-EDTA (pH 9.0) buffer.

Therefore, the slides were transferred to a chamber supplemented with pre-heated 1x Tris-EDTA (pH 9.0) buffer and incubated in a steam cooker (Tribute Collection Food steamer FS 3000) for 22 min. Subsequently, the slides were cooled for 30 min at RT and washed three times for 5 min in 1x TBST washing solution with a slight agitation at RT on a shaker (IKA® shaker Rocker 2D digital). Sections were encircled with a hydrophobic pen (PAP pen), prior to proceeding with the blocking step. 150 µl of blocking solution (5% normal goat serum (v/v) diluted in antibody solution) was applied onto each slide and the incubation was performed for 1.5 h in a humidified chamber at RT. After the blocking step, the solution was discarded and sections were incubated in antibody solution containing primary antibodies (ABs) for O/N at 4°C. The day after, the unbound primary antibodies were washed off by rinsing the slides in 1x TBST for three times for 5 min. The sections were next incubated in fluorophore-conjugated secondary antibodies specific to the primary ABs' host species, together with a nuclear staining dye DAPI, for 2 h, at RT, in a humidified chamber. Since the fluorophore is sensitive to light, it can get bleached. Thus, the upcoming steps were performed in the dark. After the incubation in secondary antibodies, the slides were washed in 1x TBST (4x for 5 min) and mounted with cover slips and ProLong® Gold mounting medium. The day after the slides were used for microscopic imaging using an Axio Observer 7 Fluorescence Microscope (Carl Zeiss Microscopy). Accordingly, two sections were selected per slide, from which five images from each ventricular part (LV, IVS, and RV) were taken using a N-Achroplan 40x/0.65 M27 microscope objective. Notably, the samples were blinded prior to microscopic imaging, such that the investigators were unaware of animal stages or genders.

2.2.3.3. Studying cell cycle activity via Ki67 immunostaining

To assess the cell cycle activity in the perinatal mouse heart, IF staining for the cell cycle marker Ki67 was conducted. Ki67 is a protein expressed in all active phases of cell cycle (Kim *et al*., 2017) and its nuclear detection labels cycling cells. In this study, the aim was to determine cell cycle activity in perinatal mouse ventricular cardiac nuclei, via IF staining using anti Ki67 antibody and nuclear staining (DAPI) on heart paraffin sections (Chapter 2.2.3.2.). After blinded microscopic imaging of the samples, the total number of nuclei was determined by counting DAPI signals using the cell-counter-plugin of the

Image J software. Additionally, the nuclei showing Ki67 staining were counted. Consequently, the data were represented as percentage of cardiac nuclei positive for Ki67.

2.2.3.4. Quantification of mitosis rates in cardiomyocytes

In addition to Ki67, IF staining for phosphorylated Histone H3 (pHH3) was used to assess cell cycle activity specifically in cardiomyocytes (CMs). During late G_2 and mitosis phases Histone H3 is phosphorylated at serine 10, which is essential for cell cycle progression from metaphase to anaphase (Kim *et al*., 2017). Cardiac tissue is composed of diverse cell types, such that for the identification of cardiac myocytes IF detection of several antigens has been established, including transcriptional factors, sarcomere proteins and membrane proteins. As a membrane protein restricted to myocytes, Caveolin 3 is observed in straited muscle cell types including skeletal muscle cells and CMs (Fiala *et al.*, 2018). Immunostaining against Caveolin 3 in combination with co-staining against the general membrane marker wheat germ agglutinin (WGA) allows to discriminate CM and non-myocytes. WGA selectively interacts with *N*-acetylneuraminic acid residues found in all mammalian cell membrane, which allows for membrane staining of all cardiac cell populations. Therefore, after co-staining of Caveolin-3 and WGA cells which are only stained with WGA, are determined as non-myocytes, while cells showing double staining are identified as CMs.

After IF staining of mouse heart paraffin slices using pHH3 antibody in combination with Caveolin 3, WGA, nuclei staining, the slides were used for microscopic imaging in a blinded fashion (as described in Chapter 2.2.3.2.). Using Image J and Zen 2.3 software, CMs (Caveolin 3 and WGA positive cells) and non-myocytes (WGA positive cells) were counted manually. Additionally, the number of pHH3 signals in each cell type (CMs or non-myocytes) was determined. Finally, mitosis in CMs and non-myocytes was calculated as a percentage of the respective pHH3 positive cell population. All measurements were conducted in a blinded fashion, such that the investigators were not aware of the stage and gender of each sample.

2.2.3.5. Investigation of bone morphogenic protein 7 (BMP7) signaling activity birth using p-p38 staining

It has been reported that the BMP7 signaling is involved in CM proliferation in mice during the early postnatal phase (Yang *et al.*, 2023). Following an activation of BMP7

signaling pathways, p38 and SMAD1 get phosphorylated, on one hand. On the other hand, the YAP becomes dephosphorylated. As a consequence of nuclear localization of YAP, as well as phosphorylated p38 and SMAD1, the cell cycle activity in CMs is induced. However, a suppression of BMP7 signaling promoted maturation and proliferation arrest in cardiac myocytes (Yang *et al.*, 2023). Accordingly, in order to monitor BMP7 signaling activity following birth (NB18.5 vs. E18.5), we investigated the intensity of p-p38 in CM nuclei using immunofluorescence antibody staining on paraffin sections prepared from mouse hearts at E18.5 and NB18.5. In this context, in addition to p-p38 immunostaining, the CM nuclei were differentiated from other cardiac cell types, using Caveolin 3 and WGA co-staining, as described above (Chapters 2.2.3.2. and 2.2.3.4.). Using Colour-threshold and ROI-manager plugins, the intensity of p-p38 signals in CM nuclei (Caveolin 3 and WGA positive nuclei) was measured. After data decoding, the intensity value of each study group was normalized to the mean value of E18.5 samples, setting the E18.5 mean-value as 1. Consequently, the BMP7 signaling activity following birth, was represented as the fold change of p-p38 intensity in CM nuclei (Caveolin 3 and WGA double-stained nuclei).

2.2.3.6. Determination of oxidative DNA damage via 8'-Oxo-Guanosine staining

Reactive oxygen species (ROS) causes oxidative DNA damage which can be detected as 8-hydroxy-2'-deoxyguanosine (8'-Oxo-G). Therefore, to assess the degree of oxidative DNA damage in perinatal murine cardiac myocytes, immunofluorescence antibody staining for 8'-Oxo-G and MEF2 (a transcription factor found in CMs) was carried out using heart paraffin sections. From each heart, the MEF2A/C and 8-Hydroxyguanosine images were analyzed in Image J. Via Colour-threshold and ROI-manager plugins, the mean intensity of 8-Hydroxyguanosine signals in CM nuclei (MEF2A/C positive nuclei) was measured. Following data decoding, the intensity value of each study group was related to E18.5 hearts (which were set as 1). Finally, the DNA damage in mouse CMs at perinatal stages from E18.5 to NB18.5+1, at LV, IVS, and RV was reported as the fold change of 8'-Oxo-G intensity in MEF2A/C positive cells.

2.2.4. Western blot analysis

Using western blot (WB) analyses specific proteins within a tissue or cell extract are detected. In this method, proteins are first denatured and then loaded with a negative charge. Next, proteins are loaded onto a sodium dodecyl-sulphate- (SDS-) poly acrylamide gel, which is placed in an electric field. Within the electric field, negatively charged proteins move towards the anode with different speeds due to their size. The smaller the proteins, the faster they move within the gel matrix. After electrophoresis, proteins are transferred onto a nitro cellulose membrane via blotting. Using antibody detection, desired proteins are visualized on the membrane by chemiluminescence

2.2.4.1. Protein preparation from tissues for western blot

In order to have an access to the intracellular and membrane proteins within a tissue sample, cells need to be lysed. The protein lysate from neonatal hearts was prepared following homogenization in RIPA buffer which contains a mixture of detergents to mobilize proteins from all cellular compartments. Tissues and cells contain large amounts of proteases, which are released during lysis, and thereby can degrade proteins. Therefore, to avoid proteolytic activities, the RIPA buffer was supplemented with protease inhibitors (Roche Diagnostics GmbH). In addition, to preserve the phosphorylation state of proteins, a phosphatase inhibitor (Roche Diagnostics GmbH) was added to the RIPA buffer. To improve protein extraction mechanical lysis was performed using tissue homogenization. Therefore, 2-ml homogenization tubes were supplemented with five 2.8 mm and twelve 1.4 mm ceramic beads (Cole-Parmer GmbH). Afterwards, 300 µl of RIPA buffer was added into each homogenization tube. The snap-frozen perinatal hearts were shortly rinsed in 1x PBS and transferred to the tubes. Two homogenization steps were performed at 5500 rpm, for 20 s, with 30 s breaks in between in a Precellys Evolution homogenizer. After homogenization, to reduce foam, the tubes were shortly centrifuged at 18407 rcf, for 1 min, at 4°C using a Micro Centrifuge 5424 (Eppendorf AG). During the entire cell lysate preparation, in order to avoid protein degradation, all experimental steps were performed on ice. Moreover, to increase protein yield, the tubes were incubated on a rocker at 24 rpm, for 1 h, at 4°C. Tissue debris was then spun down by short centrifugation at 21910 rcf, 1 min, 4°C. The entire lysate was transferred into a fresh 1.5 ml-reaction tube. Following centrifugation at 21910 rcf, 10 min at 4°C, the proteins were separated from cell debris. The protein lysates were collected, and stored at -80°C.

2.2.4.1.1. Protein isolation from cultured cells

In order to isolated proteins from cultured cells used for WB analyses, cells were cultured in 6-well plates. Per well, 50 µl of cell lysis buffer (CLB) was prepared and supplemented with the protease and phosphatase inhibitors. Subsequently, culture medium was discarded and the cells were briefly washed with cold Dulbecco's PBS cell culture grade buffer (Life Technologies Limited). 50 µl of the CLB (containing inhibitors) was added to each well, spread over the entire surface and incubated for 5 min, on ice. To detach the cells from plates and for mechanical disruption, cell scrapers were used (TPP Techno Plastic Products AG). The cell lysates were collected into pre-chilled 1.5 ml reaction tubes and centrifuged for 10 min, at 21910 rcf, at 4°C. The protein enriched supernatants were collected and stored at -80°C.

2.2.4.2. Determination of total protein concentration using Lowry assay

In order to load identical amount of proteins among different samples for WB analyses, protein concentration in lysates is measured. Therefore, a detergent compatible (*DC*) protein assay is performed (Bio-Rad Laboratories), a colorimetric assay to quantify total protein concentrations following detergent solubilization. Using a standard curve with this assay, it is possible to calculate the concentration of proteins in the range between 0.2 to 1.5 mg/ml. Therefore, the prepared cell and tissue protein lysates were 5x diluted in ddH_2O to the final volume of 25 µl. In parallel, duplicates of a standard dilution series were prepared using a BSA stock solution (2 mg/ml) (according to manufacturer's instruction). Additionally, a pseudo-blank of RIPA buffer and/or 1x CLB was prepared (5x dilution in ddH_2O, to the final volume of 25 µl). Moreover, per sample 125 µl working reagent composed of 122.5 µl protein assay reagent A and 2.5 µl protein assay reagent S (all provided in the kit), was prepared. Next, the working reagent was added to each standard, sample, and blank, and the samples were mixed immediately by vortexing. 1 ml protein assay reagent B was added to each sample. The samples were vortexed again and incubated for 15 min, at RT. Subsequently, the samples were transferred into disposable cuvettes and the absorption was measured photometrically at a wavelength of 750 nm in a spectrophotometer (NP-80, IMPLEN GmbH). The pseudo-blank absorption was subtracted from the sample's absorption values. Moreover, using Microsoft Excel

software, the BSA concentrations were plotted against the mean values of each corresponding absorption duplicates. Finally, the samples' total protein concentrations were calculated by applying the linear equation of the standard curve and the dilution factor of each sample.

2.2.4.3. Sodium dodecyl sulphate-polyacrylamide gel electrophoresis (SDS-PAGE)

The proteins are separated using sodium dodecyl sulphate-polyacrylamide gel electrophoresis (SDS-PAGE). Prior to SDS-PAGE, proteins need to be denatured in Laemmli buffer, containing SDS, β-mercaptoethanol (β-ME), glycerol, Tris, and bromophenol blue. The combined use of SDS and β-ME allows for optimal linearization of proteins (SDS denatures proteins while β-ME is a reducing agent). Additionally, the negatively charged SDS binds proteins, and thereby facilitates their movements towards a positively charged electrode within an electric field. The glycerol due to its high density facilitates loading of protein lysates in the wells of an SDS-gel. As a colour agent bromophenol blue supports protein tracking within the gel, as well as progression of electrophoresis. Appropriate volumes of protein lysate corresponding to 15 to 30 µg proteins was mixed with 5x Laemmli buffer, and protein denaturation was carried out by incubation for 10 min, at 95°C. PAA-SDS gels are composed of two gel compartments including a low-percentage (4%) stacking gel overlaying a high-percentage (12%) separating gel. PAA-SDS gels used in this study were 1.5 mm thick consisting of a 4% stacking gel and a 12% separating gel. Gels were prepared using glass plates and a gel cast device as part of the Mini-PROTEAN® Tetra System (Bio-Rad Laboratories) using the materials listed in Table 15. Briefly, the solution mixture for 12% Separating gel were mixed together (as listed in Table 15) and the mixture were transferred between the glass plates. In order to remove bubbles, reach the flat gel surface, and keep the gel humid, 2 ml of isopropanol was gently added onto the separating gel. As soon as the separating gel was polymerized, the isopropanol was discarded and the stacking gel mixture was added on top of the separating gel. Afterwards, the combs were installed and polymerization of the stacking gel was conducted following an incubation for 45 min, at RT. Later on, the polymerized gels were positioned in the Mini-PROTEAN® Tetra cell electrophoresis chamber (Bio-Rad Laboratories) filled with 1x SDS running buffer. The combs were carefully removed and desired volumes of each denatured protein samples were loaded

onto the wells of the PAA-SDS gel. In order to estimate molecular weights of proteins during WB analyses, a size standard (5 µl of PageRuler™ pre-stained protein ladder (Invitrogen)) was loaded onto the gels. The run was initiated for 30 min, at 50 V, at RT. As soon as the proteins migrated into the separating gel, the run was proceeded at a higher voltage (100 V for ~2 h). Once the blue running front reached the end of the gels, the run was terminated.

Table 15. PAA-SDS gel composition for the SDS-PAGE experiment

	ddH_2O	**Acrylamide 30%**	**1 M Tris/HCl pH 8.8**	**1 M Tris/HCl pH 6.8**	**10% SDS**	**10% APS**	**TEMED**
4% Stacking gel	7.26 ml	1.33 ml	-	1.25 ml	100 µl	50 µl	10 µl
12% Separating gel	3.55 ml	6.8 ml	6.38 ml	-	170 µl	85 µl	17 µl

2.2.4.4. Semi-dry blotting and antibody detection

Following SDS-PAGE, separated proteins are transferred out of the gel onto a solid matrix such as a nitrocellulose membrane. Accordingly, after an SDS-PAGE run, stacking gels were discarded and the separating gel compartment was carefully removed from glass plates. The gel and blotting materials including a nitrocellulose membrane and six Whatman® papers were incubated in a Transfer buffer for 10 min, at 24 rpm, at RT. Next, the blotting sandwich was prepared composed of three sheets of Whatman® papers, a sheet of nitrocellulose membrane (Merck), the gel, and another three sheets of Whatman® papers. The sandwich was placed inside a semi-dry blotter Trans-Blot® Turbo cell (Bio-Rad Laboratories) and the blotting was conducted for 30 min, at 25 V and 1 A. Afterwards, to avoid unspecific binding of primary antibodies, a blocking step was performed. Thus, the membrane was carefully separated from the sandwich and blocked in 5% dry milk in 1x TBST for 1 h, 24 rpm, at RT. After blocking, the membrane was incubated with primary antibody (in either 5% BSA or 5% milk diluted in 1x TBST), for O/N, 24 rpm, at 4°C. The day after, following three times 5 min washing in 1x TBST, the membrane was incubated with horseradish peroxidase (HRP-) linked secondary AB for 1.5 h, 24 rpm, at RT. Subsequently, three washing steps were performed as described above. Next, an enhanced chemiluminescence (ECL) reaction was performed by incubating the

membrane in a solution composed of ECL reagent A and B (volumes mixed 1:1, Table 5), for 1 min. Light emission was detected with the Fusion Solo 6S Imaging system (VILBER Lourmat Deutschland). To quantify the density of the protein bands, densitometric analyses were performed using Capture Edge software (VILBER Lourmat Deutschland). For final quantification, values (i.e., densitometric volumes of the band) of phosphorylated proteins were normalized to the respective total protein levels. In addition, protein levels were normalized a housekeeping protein (loading control) such as α-Tubulin, Vinculin, or GAPDH. Finally, results of postnatal stages were related to the fetal stage 18.5 (E18.5), which was set to equal 1.

2.2.4.4.1. Stripping membranes for re-probing

In order to minimize multiple western blot experiments and optimize usage of sparse samples, stripping and re-probing of a blotted membrane is performed. Due to stripping primary and secondary ABs are removed from the nitrocellulose membrane and the membrane can be reused for another AB staining. Therefore, the membrane was washed three times in 1x TBST to remove excess chemiluminescent substrate. Next, stripping was carried out by incubation of the membrane in stripping buffer for 35 min, at 55°C. After stripping, the membrane was washed six times in 1x TBST, each time for 5 min, 24 rpm, at RT, blocked in 5% dry milk in 1x TBST for 30 min, 24 rpm, at RT and was subsequently used for another round of antibody detection

2.2.5. Cytokine and growth factor screening

2.2.5.1. *In silico* analyses

Prior to proteomic studies using murine hearts, *in silico* analyses were conducted. Using the mouse genome database (reachable under: https://www.informatics.jax.org/go/term/GO:0008083) we searched for the genes with the gene ontology ID number of 0008083, demonstrating a cell growth and proliferation function. Next, the RNA expression patterns of 161 growth factors and cytokines derived from mouse and human genome bioinformatic databases were monitored in hearts. A database tool provided by Cardoso-Moreira *et al*., in 2019 reports developmental gene

expression pattern in several organs in various mammalian species including humans and mice. The study conducted by Cardoso-Moreira and colleagues is publicly available and accessible under the following web-address: https://apps.kaessmannlab.org/evodevoapp/ . To start the analysis, the gene name, species (for examples mouse and human), and preferred organ (heart) were selected in the online application and the search was initiated. The expression level for each gene was represented as Read Per Kilobase of transcript per Million mapped reads (RPKM). By using RPKM, the abundancy of transcripts from sample sets sharing one common variable is normalized to a standard which allows for quantitative comparison within the study groups. Thus, for each mouse gene encoding a growth factor and cytokine, a graph was generated showing its RNA expression pattern in the heart (RPKM) at different developmental stages starting from E10.5 up to postnatal day 63 (P63). In human hearts, the expression data were provided from the weeks post conception of 4 (4 WPC) up to 19 WPC, as well as postnatal ages including new-born, infant, teenage, young adult, and mid-aged. To assess the possible correlation between birth and modifications in expression of growth factors and cytokines, E18.5 and new-born, and 19 WPC and new-born stages were monitored, in hearts of mice and humans, respectively. Based on the gene expression pattern at birth, we scored each gene with unchanged, or up-, or down-regulated. Finally, a percentage of genes with modified expression pattern at new-born compared to E18.5 and 19 WPC was calculated and represented as a graph. After birth, we noticed that from the entire investigated genes 34% were upregulated, and 34% downregulated, whereas 32% remained unchanged in human and mouse hearts.

2.2.5.2. Antibody array screening

In order to evaluate the protein level of cytokines and growth factors within a tissue lysate, commercially available antibody arrays were used. In this method, pairs of antibodies specific to various target proteins are spotted on a nitrocellulose membrane at defined positions. Upon application of sample, membrane bound antibodies capture epitopes/proteins of interest out of the protein lysate. Later on, unbound proteins are washed away by several wash steps. The membrane is incubated with a cocktail of biotinylated detection antibodies against the pulled-down proteins. Finally, using streptavidin-HRP, together with a chemiluminescent detection system, the density of bound proteins representing their abundance in the lysate is determined.

In this study, to monitor the protein amount of cytokines and growth factors directly after birth compared to shortly before delivery, mouse prenatal hearts at E18.5 and NB18.5 were collected for antibody array screening. The following arrays were used which allowed for studying 129 cytokines and growth factors: proteome profiler TM array mouse XL cytokine (R&D systems, #ARY028) and mouse growth factor array 3 (RayBiotech, #AAM-GF-3-8).

2.2.5.2.1. Cell lysate preparation and protein densitometric analyses for mouse cytokine array

For isolation of total protein extracts from the murine ventricles, snap-frozen perinatal hearts were shortly rinsed in PBS buffer and transferred to 2-ml homogenization tubes containing 5x 2.8 mm, and 12x 1.4 mm ceramic beads (Cole-Parmer GmbH) (Chapter 2.2.5.). To each tube, 190 µl PBS supplemented with phosphatase and protease inhibitors (same as used for western blot), was added. Mechanical tissue disruption was carried out by two homogenization steps at 6300 rpm, for 20 s, with a 30 s break in between (Precellys Evolution homogenizer). To avoid protein degradation, all the experimental steps were performed on ice. Afterwards, each tube was supplemented with Triton-X-100 to a final concentration of 1% (v/v). The samples were shortly next snap frozen in liquid nitrogen and then thawed again. After thawing, the homogenization was repeated, as mentioned above. The generated foam was reduced by short centrifugation at 18407 rcf, for 1 min, using a Micro Centrifuge 5424 (Eppendorf AG). The entire tissue lysate was collected into a fresh 1.5 ml reaction tube. The proteins were separated from cell derbies by centrifugation at 21910 rcf, 5 min, at 4°C. The supernatants and PBS buffer containing inhibitors were stored at -80°C for protein concentration determination as well as further experiments. The in kit suggested protein amount needed for this experiment ranged between 100 to 200 µg (per membrane). Therefore, to use identical protein amounts among the experimental groups, the protein concentration of the lysates was determined using Lowry method (Chapter 2.2.5.2.). Based on the protein concentration and the available lysate volume 170 µg protein per membrane were used for each heart in this study. All the experimental procedures were performed according to the user manual provided by the manufacturer. Briefly, the membranes were labelled and placed in the wells of a provided 4-well multi-dish. The membrane blocking was performed by incubation in 2 ml of blocking buffer per well for 1 h, 24 rpm, at RT. The heart protein

lysates from E18.5 and NB18.5 male mice containing 170 µg total protein were mixed with the provided buffers up to the final volume of 1.5 ml. The blocking buffer was aspirated and 1.5 ml of the corresponding samples were added onto each membrane. The lid of each 4-well dish was closed and the dishes were sealed with parafilm to avoid drying of the membranes. The incubation was proceeded for O/N, at 24 rpm, at 4°C. The following day, to discard unbound proteins, membranes were washed three times with the provided washing buffer each time for 10 min, 24 rpm. Next, 1.5 ml of detection antibody cocktail was prepared and added onto each membrane. After 1 h incubation in biotinylated antibody cocktail solution, the unbound antibodies were washed away using washing buffer, as described above. Subsequently, 2 ml of streptavidin-HRP solution, was incubated on each membrane for 30 min, 24 rpm, at RT. Following three washing steps, the excess washing buffer was aspirated and 2 membranes from each gestational stage (2x E18.5 and 2x NB18.5) were carefully placed on a plastic sheet. Afterwards, the chemiluminescent reaction was performed by pipetting 1 ml of Chemi Reagent mixture onto each membrane. 1 min later, all the four membranes (2x E18.5 and 2x NB18.5) were wrapped in a plastic bag and the air bubbles were removed. Luminescence was detected using a Fusion Solo 6S Imaging system (VILBER Lourmat Deutschland). The densitometric analyses of each cytokine was carried out using Bio-1D software (version: 15.08a, VILBER Lourmat Deutschland). For each cytokine, as well as positive and negative controls, two antibody spots were printed as adjacent pairs on each membrane. Therefore, for each membrane (heart sample) from the densitometric volume of each duplicate a mean value was calculated. Afterwards, the mean value of each cytokine was subtracted from the mean value of the negative controls (or vice versa). The results were normalized to the mean value of the positive controls. The biological sample size and thereby membrane number for each stage was equal to four, meaning that for each cytokine four values at E18.5 and four values at NB18.5 were calculated. Afterwards, from all four values measured for each cytokine concerning E18.5 heart samples, a mean value was calculated. Finally, all eight values (four regarding E18.5, and four concerning NB18.5 heart samples), were separately normalized to the calculated mean value, setting the mean value of E18.5 stage to 1.

2.2.5.2.2. Cell lysate preparation and protein densitometric analyses for mouse growth factor arrays

Hearts of E18.5 and NB18.5 mice were prepared as described. After rinsing in PBS, the hearts were transferred to 2-ml homogenization tubes containing 5x 2.8 mm, and 12x 1.4 mm ceramic beads (Cole-Parmer GmbH). The 2x Lysis buffer provided in the mouse growth factor array kit (RayBiotech #AAM-GF-3-8) was diluted 1:1 with ddH_2O to the final volume of 350 µl for each heart and supplemented with protease and phosphatase inhibitors. 350 µl of lysis buffer mixture was added to each tube and homogenization was carried out using the Precellys Evolution homogenizer (2x 5500 rpm, for 20 s, with 20 s break). The foams were reduced by spinning the tubes down at 18407 rcf, for 1min. To enhance the protein yield, samples were shortly snap frozen in liquid nitrogen. Following thawing at RT, the homogenization step was repeated. Afterwards, the entire solution was transferred into fresh 1.5 reaction tubes, and the centrifugation was performed at 21910 rcf, for 10 min, at 4°C. The supernatant was carefully separated from cell derbies and used for the antibody screening array. The total protein quantity per membrane suggested by the manufacturer was between 50 to 500 µg. Therefore, the total protein concentration was determined using Lowry assay and protein amount for all samples within the experiment was 350 µg. All experimental steps were performed according to the provided user manual (RayBiotech, #AAM-GF-3-8). Briefly, the antibody spotted membranes were labelled with sample IDs and placed in wells of the provided incubation tray. Afterwards, the blocking step was conducted by incubation of membrane in 2 ml of the blocking buffer for 30 min, 24 rpm, at RT. Per membrane, one sample (lysate from one heart) containing 350 µg total protein was diluted in blocking buffer to a final volume of 1 ml. The blocking solutions were aspirated and lysate samples were pipetted onto corresponding membranes. The trays containing samples and membranes were sealed with parafilm and incubation was proceeded for O/N, 24 rpm, at 4°C. The next day, following five washing steps, the incubation in biotinylated antibody cocktail was performed. Here, 1 ml of antibody cocktail solution was added onto each membrane and the incubation was proceeded for 1.5 h, at 24 rpm, at RT. Following five washing steps, an incubation in 2 ml (per well) streptavidin-HRP was carried out for 2 h, at 24 rpm, at RT. The remaining streptavidin-HRP was washed away, using final five washing steps. Afterwards, 4 membranes (2x E18.5 and 2x NB18.5), were placed on a plastic sheet and the chemiluminescent reaction was conducted by pipetting 500 ml of a detection mixture

composed of 1:1 volume of detection buffer C and detection buffer D, onto each membrane. 2 min later, all four membranes (2x E18.5 and 2x NB18.5) were wrapped in a plastic bag and air bubbles were removed. Finally, the light emission was detected using Fusion CCD-Imaging system (VILBER Lourmat Deutschland). The relative intensity of each growth factor was measured as described in the cytokine XL array section (Chapter 2.2.5.2.1.) using Excel and Bio-1D software (version: 15.08a, VILBER Lourmat Deutschland).

2.2.6. Enzyme-Linked Immunosorbent Assay (ELISA)

In order to validate the data of antibody screening arrays, enzyme-linked immunosorbent assays (ELISAs) were performed. An ELISA is an immunoassay which is widely used to quantify levels of a specific protein in a lysate, solution or body fluid. Commercially available ELISAs are usually provided in specific 96-well microplates. Each well of the microplate is pre-coated with identical amounts of a particular antibody which captures a desired antigen/protein in a mixture of proteins within samples, standards, or controls. Next, conjugated detection antibody binds specifically to the captured protein of interest. Following addition of a substrate solution, a signal (depending on the ELISA kit, the generated signal type varies; here a color is generated) is produced the optical density (OD) of which is proportional to the amount of the captured protein in the original sample.

2.2.6.1. Cell lysate preparation for ELISA

To validate the results of the antibody screening arrays, ELISA experiments were performed using mouse hearts at E18.5 and NB18.5 stages. Cytokines and growth factors are often generated in and secreted from the liver and transported to other body parts throughout the blood circulation. Therefore, in addition to heart samples, E18.5 and NB18.5 liver and serum samples were also used to address this question. To prepare protein samples from perinatal hearts and livers, tissues were weighted and lysates were prepared. Each sample was shortly washed in PBS and transferred into 2-ml homogenization tubes supplemented with 5x 2.8 mm, and 12x 1.4 mm ceramic beads (Cole-Parmer GmbH). In order to prepare lysate, the commercially available 2x Lysis buffer from RayBiotech was purchased, showing a high-yield lysis efficiency. Therefore, 2x Lysis buffer (RayBiotech) was diluted 1:1 with ddH_2O to a final volume of 400 µl per

sample and supplemented with protease and phosphatase inhibitors. The lysate preparation was proceeded by adding the lysis solution to each homogenization tube and a homogenization step using Precellys Evolution homogenizer (2x 5500 rpm, for 20 s, with 20 s breaks in between). The foam was reduced by spinning the tubes at 18407 rcf, for 1min. To enhance the protein yield, the homogenization was repeated three times. After a short centrifugation step (to remove the foam), the tubes were incubated for 2 h, at 4°C with gentle agitation at 24 rpm. Afterwards, the lysates were spun down using a mini-centrifuge (Spectrafuge Mini-Centrifuge) and the entire lysates were transferred into fresh 1.5 ml reaction tubes. Following a final centrifugation at 21910 rcf, for 10 min, at 4°C, the supernatants were isolated from the pelleted cell derbies. To avoid freezing and thawing cycles, 100 µl aliquots were prepared and stored at -80°C. In order to monitor the total protein concentration isolated from each heart and liver a Lowry assay was conducted.

2.2.6.2. Optimizing the dilution factor of samples for each ELISA

Prior to an ELISA run, optimal sample dilution must be determined to reveal the most sensitive detection range for an ELISA antibody in combination with the amount of target protein. For each type of tissue lysate or serum sample a dilution factor must be selected such that the sample's OD lies in the range of the standard curve of the respective ELISA. To estimate the starting sample dilution used for optimization, ELISA kit contains a booklet representing a standard curve composed of known standard concentrations and the corresponding ODs. Additionally, starting amounts are often suggested for serum, plasma, or even tissue lysates. To monitor IGF-1 amounts in hearts, livers, and serum samples from E18.5 and NB18.5 mice, an ELISA kit from R&D Systems was purchased. The standard curve provided by the manufacturer ranges from 31 to 2000 pg/ml. Furthermore, the previously determined concentration of IGF-1 in mouse serum using the same kit was reported as 742000 pg/ml. Upon 1:500 dilution of samples, the IGF-1 concentration would be roughly 1484 pg/ml, which is within the standard curve. Thus, the 1:500 dilution was used as a starting dilution for serum and two further dilutions of 1:250 and 1:1000 were also selected for optimization. In addition to serum samples, mouse heart lysate was also reported for the IGF-1 ELISA kit which revealed 3158 pg/ml concentration for IGF-1. Thus, the dilutions of heart tissue lysates such as 1:2, 1:4, and 1:8 would likely lead to the detection of ODs within the standard curve. Since cytokines

and growth factors are often produced in the liver, the following dilution factors were tested for liver lysates: 1:4, 1:8, and 1:16. All procedures were performed according to the user manual provided by the manufacturer. Briefly, all sample dilution series were prepared using the provided dilution buffer up to the final volume of 50 µl. Additionally, standard dilution series were also prepared according to the manual. Into each well 50 µl of a calibrator diluent (Diluent RD5-38) was added. Afterwards, 50 µl of samples, standards and the negative control (lysis solution only) were added into the corresponding wells. The plate was covered with an adhesive strip and incubated for 2 h, at 500 rpm, at RT. The unbound proteins were removed from the wells by four washing steps using 400 µl of washing buffer for each well. Next, the washing solution was removed by inverting the plate and blotting it against clean paper towels. Subsequently, 100 µl of Mouse IGF-1 antibody conjugate was added to each well and the plate was covered by adhesive strip. After incubation in the antibody conjugate for 2 h, at 500 rpm, at RT, the washing steps were repeated (as described above). Later on, 100 µl of substrate solution was added to each well under light protected conditions. After incubation in substrate solution for 30 min (at 500 rpm, at RT), 100 µl of stop solution was added and the OD of each well at 450 nm was determined using a FLUOstar optima plate reader (BMG LabTech). Finally, for each sample type (heart, liver and serum) the dilution factors with ODs located in the middle of the standard curve were selected for further ELISA experiments.

2.2.6.3. ELISA for cytokines and growth factors

Duplicates were prepared for each standard solution, negative control (lysis solution) and samples (i.e., serum and tissue lysates from hearts and livers derived from E18.5 and NB18.5 mice). Thus, the samples were mixed with the provided diluent to the selected dilution factor up to the final volume of 50 µl. The experimental steps were performed according to the manufacturer's instructions and as described above (Chapter 2.2.6.). The measured absorbance (ODs) was imported in an Excel table to calculated the relative amount of cytokines and growth factors at NB18.5 compared to E18.5. Accordingly, the mean values of the measured ODs for each sample duplicate were calculated. Next, the mean value of the blanks' ODs (dilution solution) was subtracted from the mean OD value of the lysis solutions (negative control), and was used as a correction factor for heart and liver sample measures. Additionally, using Excel software, a standard curve was generated by plotting the concentrations of standard dilutions against the mean value of

their corresponding OD values. Consequently, from the standard curve, a linear equation was generated, out of which sample concentrations were calculated based on their OD. Upon multiplying the concentration of each sample by the respective dilution factors, the final concentration of the protein in each sample was determined. The protein concentration from liver and heart samples were normalized to their corresponding total protein concentration. Finally, in order to determine the variation in growth factor and cytokine levels, the mean value per group was calculated, related to the mean value of the E18.5 measures and represented as fold change variations.

2.2.7. Transcriptional analysis via Real-time qPCR

2.2.7.1. RNA isolation

In order to purify total RNA including messenger (mRNA), ribosomal (rRNA) and transfer (tRNA) RNA from murine myocardial tissues, the RNeasy® Plus Mini Kit (Qiagen, #74134) was used. In this method, a cell lysate containing total RNA is prepared using chemical and mechanical disruption simultaneously. The chemical cell disruption is carried out using the guanidine-isothiocyanate-containing buffer RLT plus. In addition, the RLT buffer allows for denaturation of proteins and DNA. The RLT buffer is furthermore supplemented with ß-ME to the final concentration of 1% (v/v). ß-ME is a reducing agent which inactivates RNases by irreversible destruction of their native conformation ensuring isolation of intact RNA. Furthermore, to optimize the lysate preparation, a mechanical disruption was performed via homogenization. Therefore, five 2.8 mm and twelve 1.4 mm ceramic beads (Cole-Parmer GmbH) were transferred into RNase free 2-ml homogenization tubes supplemented with 350 µl RLT/ß-ME solution. Snap frozen whole neonatal murine hearts were transferred to each tube followed by homogenization (2x 5500 rpm, for 20 s, with a 30 s break in a Precellys® 24 homogenizer). The entire lysate was transferred into RNase free 1.5-ml reaction tubes and the RNA containing solution was separated from cell derbies by centrifugation at 18407 rcf, for 5 min, at RT. Afterwards, the supernatant was collected and used for RNA isolation using the user manual provided by the RNeasy® Mini kit (Qiagen, #74134). Furthermore, to get rid of genomic DNA, an RNase-Free DNase Set (Qiagen, #79254) was used, where genomic DNA is directly digested on the RNA purification columns. Thus, the DNase I

provided by the kit was directly added to the RNeasy column and the incubation was carried out for 15 min, at RT. The digested DNA was next removed from the column via several washing steps. Purified RNA bound to the RNeasy column was eluted applying 30 µl of RNase-free HPLC ddH_2O followed by centrifugation at 14463 rcf (Eppendorf, Centrifuge 5418), for 1 min. The column flow through was collected for RNA concentration measurement and stored at -80°C for future use.

2.2.7.2. RNA concentration measurement and cDNA synthesis

Isolated RNA has to be reverse-transcribed into more stable complementary DNA (cDNA), for which 0.9 µg of total RNA was used. Hence, the RNA concentration was determined using a NanoDrop spectrophotometer (NP-80, IMPLEN GmbH) according to the manufacturer's instructions. The NanoDrop measures OD at 260 nm and thereby calculates the RNA concentration. During the RNA isolation step, the RNA elution from the RNeasy column was carried out using RNase-free HPLC ddH_2O. Therefore, the same water was used as blank. Afterwards, concentrations of isolated RNA samples were measured by applying 1.5 µl sample onto the NanoDrop. The RNA samples with OD_{260}/OD_{280} and OD_{260}/OD_{230} equal to 2.0±0.1 showed the optimum quality and therefore were used for cDNA synthesis. Thus, in 8-well PCR strips the RNA volume corresponding to 0.9 µg was diluted in RNase-free water up to a total volume of 10 µl. In order to denature secondary structures of nucleic acids, the solution was supplemented with 2 µl of 50 µM random hexamer primer and 4 µl of 2.5 mM dNTPs stock solutions, and incubated for 5 min at 70°C in a thermal cycler. After denaturation, 2 µl of 10x reverse transcriptase reaction buffer, 0.5 µl of 40 U/µl RibiLock® ribonuclease inhibitor (Thermo Fisher Scientific) and 1 µl of 200 U/µl M-MuLV reverse transcriptase (New England BioLabs) were added to each tube to reach the final reaction volume of 20 µl. Samples were incubated in a thermocycler (Thermo Fisher 4375786 Veriti™ 96-WellPCR Thermocycler) for 10 min at 25°C, and for 60 min at 42°C, for primer annealing and cDNA synthesis, respectively. Finally, to inactivate the reverse transcriptase enzyme, the tubes were incubated for 10 min, at 90°C. The cDNA was diluted 1:4 in ddH_2O and stored at -20°C.

2.2.7.3. Primer design for quantitative real time PCR

In order to design primers for transcriptional analysis by quantitative real time PCR (RT-qPCR), the Primer-BLAST online tool provided by National Center for Biotechnology Information (NCBI) was used. The mouse RNA reference sequence for the gene of interest was selected using the gene data base provided by the NCBI Pubmed tool. The accession number of the gene/transcript was used in the NCBI Primer-BLAST online tool. For designing the primers, the following criteria was considered: primer length (from 18 to 26 bp), PCR product size (between 70-200 bp), primer melting temperature (60°C), and GC content (>50%), as well as the lowest probability values for self-annealing and hairpin formation (monitored via NCBI Primer-BLAST), no primer binding over an exon-exon junction, and separation of primer pairs on genomic DNA by at least one intron (longer than 1kb). Among the primer pairs displayed by the NCBI Primer-BLAST tool, those matching most of the mentioned criteria were selected for RT-qPCR experiments and were ordered from Eurofins Genomics.

2.2.7.4. Optimizing primers for RT-qPCR

In order to determine the optimal annealing temperature, the selected primer pairs were used for a gradient PCR experiment. This is a normal PCR (as described before in Chapter 2.2.2.3. and Table 13), except that 6 different annealing temperatures of 56, 58, 60, 62, 64, and 66°C were applied. Therefore, either 1 µl of cardiac cDNA template or ddH_2O (serving as a negative control) was used in the PCR reaction mixture for the gradient PCR (Table 16). The PCR products were visualized using agarose gel electrophoresis (Chapter 2.2.2.4.). Finally, the temperature at which only one single PCR-product (with the expected product size) was observed on the gel, was selected as annealing temperature for further primer optimization.

Table 16. PCR reaction mixture for gradient PCR

components	Final Concentration	Volume [µl]
ddH2O	-	19.4
10× PCR buffer	1x	2.5
5 µM forward primer	0.1 µM	0.5
5 µM reverse primer	0.1 µM	0.5
2.5 mM dNTPs	0.1 mM	1

5 U/µl Taq polymerase	0.02 U/µl	0.1
cDNA	-	1
Total Volume	-	25

The selected annealing temperature was used to evaluate the optimal primer concentration for RT-qPCR experiments, assessment of which was based on a melt curve and PCR efficiency. Therefore, RT-qPCR experiments were performed using SYBR®Green dye (BioRad Laboratories, #1725272). After each PCR cycle new PCR products are generated to which the SYBR®Green dye binds. The SYBR®Green dye preferentially intercalates with double stranded, but not single stranded DNA. In its DNA-intercalated state absorbs light at 497 nm wave length and emits a green light at 520 nm. The intensity of the emitted light correlates with the DNA amount present in the reaction mixture. Through the exponential amplification of cDNA, the measured light intensity after each elongation step also increases exponentially. Accordingly, the relative quantification of the expression of the target gene is defined by the target gene, normalized to a ubiquitously expressed reference gene (the so-called housekeeper). For this purpose, the PCR cycle of threshold (C_T) is first determined where the measured light intensity enters the exponential phase. The C_T is proportional to the amount of template cDNA and thereby indirectly to the mRNA of interest in the sample. Accordingly, the earlier the cycle threshold is reached, the higher are the RNA copies of the desired gene in the sample. To find out the optimal primer concentration, three different stock (not final) concentrations were prepared from each primer pair: 1 µM, 5 µM and 10 µM. For each primer concentration, a RT-qPCR run with a cDNA dilution series including 1:1, 1:2, 1:4, 1:8, 1:16 (diluted in ddH_2O) was performed. Therefore, the RT-qPCR reaction mixture (Table 18) was prepared using SsoAdvanced™ Universal SYBR®Green Supermix (BioRad Laboratories) which contains polymerase, dNTPs, PCR-buffer and SYBR®Green dye. After supplementation of each well of a 96-well microplate with 19 µl of the reaction mixture, 1 µl of template cDNA was added. The microplate was then sealed with an adhesive strip and the solution was mixed by vortexing for 30 s. To spin down the solution, the plate was centrifuged for 30 s at 500 xg, at RT using a Mini Plate Spinner MPS 1000 centrifuge. The RT-qPCR experiment was run, using a StepOnePlus™ Real-Time PCR System (Applied Biosystem) and the PCR program shown in Table 17.

Table 17. Setup of a RT-qPCR run.

Step	Temperature [°C]	Time [s]	Cycle number
Initial denaturation	95	30	1x
Denaturation	95	10	40x
Annealing and elongation	Primer dependent	60	
Melting curve			1x

The run was terminated after a melt curve analysis. For each sample a fluorescence threshold was set above background signal within the exponential phase of the PCR amplification curve. Furthermore, based on the dilution series of the cDNA, the efficiency of the RT-qPCR was determined, which is needed for selection of the optimal primer concentration. Theoretically, it is expected that within the cDNA dilution series, the C_T value is increased by 1 with each increasing dilution, which leads to a PCR efficiency of 100% (i.e., doubling of the PCR product with each cycle). Thus, PCR efficiencies between 90% to 110% and a correlation coefficient along the dilution series larger than 0.99 were accepted. To monitor the primer specificity, the melt curve was analyzed. Detection of one single peak determines one single PCR product dissociating during the melting event. To sum up, the primer concentrations giving PCR efficiencies between 90% to 110% and a correlation coefficient of larger than 0.99, with a single-peaked melt curve, were selected for further RT-qPCR experiments.

Table 18. The reaction mixture for a RT-qPCR test run for each concentration of primers and the final primer concentrations

Components	Volume [µl]
ddH2O	6.2
forward primer	1.4
reverse primer	1.4
2x SYBR®Green	10
Template (cDNA or ddH_2O)	1
∑	20

Stock Concentration [µM]	Final Concentration [nM]
1 →	70
5 →	350
10 →	700

2.2.7.5. Gene expression analyses by RT-qPCR

Following the determination of optimal primer criteria, the relative gene expression analyses using RT-qPCR was performed. Thus, RNA was isolated from murine perinatal hearts and reverse-transcribed to cDNA (as described in Chapter 2.2.7.2.). Using a specific primer pair, a desired gene was amplified from cDNA templates and quantified using SYBR®Green RT-qPCR. The sample size was equal to five, meaning five cDNA samples obtained from five hearts at E18.5 and five hearts at NB18.5. For each cDNA sample triplicates runs were performed using primer pairs for the gene of interest as well as for a housekeeping gene (*Polr2A*). Additionally, as negative controls, instead of cDNA sample, ddH_2O was used as template (known as none-template control, NTC). Therefore, per well of a 96-well plate, 19 µl of RT-qPCR reaction mixture was prepared as described before (Table 18), and together with 1 µl cDNA template, it was applied into the respective well. After sealing the plate with an adhesive strip, the RT-qPCR experiment was run, using a StepOnePlus™ Real-Time PCR System as mentioned before. After the run, the C_T values were used to quantify the relative gene expression differences among groups of E18.5 and NB18.5 hearts via the $\Delta\Delta C_T$ method (Rao *et al*., 2013; Schmittgen *et al*., 2008).

2.2.8. *In vitro* studies using neonatal mouse cardiomyocytes

In order to assess the possible involvement of cytokines and growth factors in cell cycle regulation of neonatal mouse cardiomyocytes (CMs), *in vitro* experiments were carried out. Therefore, neonatal mouse hearts were isolated and dissociated mechanically and enzymatically to single cells.

2.2.8.1. Coating the culture flasks and chamber slides with fibronectin

Primary CMs rely on extracellular matrix proteins to adhere to cell culture dishes and survive longer culture periods. Thus, plates, coverslips and chamber slides were coated prior to adding cell suspension using fibronectin (Sigma Aldrich, #F1141-5MG) which is an important extra-cellular matrix (ECM) protein in the neonatal heart mediating cell-matrix interaction. Established concentration of fibronectin (i.e., 0.025 mg/ml from 1 mg/ml stock solution) was prepared by diluting fibronectin in sterile PBS (as listed below

in Table 19). Specific volumes of fibronectin solution were added to each growth culture flask or well. Following O/N incubation, under gentle agitation at 24 rpm, at 37°C, coating was carried out. The next day, plates were sealed with parafilm and stored for up to one week, at 4°C. Shortly before seeding cells, the fibronectin solution was discarded and the cells were transferred onto the pre-coated surfaces.

Table 19. The fibronectin coating conditions

Type of culture flask	Fibronectin volume per well [µl]	PBS volume per well [µl]
6-well plate	20	780
8-well chamber slide	5	195
12-well plate	7.5	292.5

2.2.8.2. Preparation of primary cardiomyocytes from the new-born mouse heart

In order to isolate primary cardiac myocytes, hearts from newly delivered mice were isolated (NB18.5 or NB19.5). Thus, the pups were sacrificed via decapitation, the thoracic cavities were opened and the hearts were transferred into a petri dish containing ice cold 1x PBS. Under an SZX7 stereo microscope (Olympus), the atria were removed, and the ventricles were stored on ice in PBS. Two enzyme mixtures were prepared according to the Neonatal Heart Dissociation Kit (Miltenyi Biotec, #130-098-373. Shortly before use, enzyme solution I and II (as provided by manufacturer) were mixed and the entire 2.5 ml enzyme solution was added to a gentleMACS™ C tube (Miltenyi Biotec). The isolated ventricles were transferred to the C tube and submerged in the enzyme solution. The murine cardiac cells were dissociated using a gentleMACS™ Octo Dissociator with Heaters (Miltenyi Biotec). Therefore, the C tube was inverted and installed in the Dissociator and after placing a heating cap on the tube the dissociation was performed using the preinstalled program for neonatal mouse heart dissociation (i.e., *37_mr_NHDK1)*. In the meantime, a culture medium for neonatal CMs were prepared as listed below and pre-warmed in a water bath at 37°C. After the run was terminated, cell isolation was continued under a laminar flow hood suitable for cell culture experiments. In order to remove the undigested cell clumps and tissue debris, the cell suspension needs to be passed through a strainer. Accordingly, to the cell suspension 7.5 ml of pre-warmed

neonatal CM incubation medium (as described below) was added and the mixture was passed through a MACS SmartStrainer (70 µm pore size) placed on a 50-ml falcon tube. Another 7.5 ml of medium was added to the C tube to harvest remaining cells and filtered through the SmartStrainer. After washing the SmartStrainer with 5 ml of medium, the filtered cells were centrifuged at 600 xg, for 5 min, at RT. The supernatant was carefully discarded and the cells were resuspended in 5 ml of medium. Cell number per ml of medium was counted using a DeNovix CellDrop cell counter. To exclude dead cells, cell viability was assessed using Trypan Blue staining. The living cells do not take up the dye, while dead cells turn blue. Thus, 20 µl of cell suspension was mixed with 20 µl Trypan Blue (1:1) and 10 µl of the mixture was loaded to the cell counter. Next, the program Trypan Blue was selected and after focusing onto the appropriate focal plane, the cell count was carried out by selection of the count option appeared on the display. The counter determines the number of dead and life cells per ml, and the latter is used for calculation of cell suspension volumes needed for seeding. The cell suspension volume corresponding to the appropriate cell number (living cells per cm2; listed in Table 20) was mixed with pre-warmed neonatal CMs culture medium and transferred to fibronectin pre-coated culture flasks. Finally, the cells were cultured for O/N, 5% CO_2, at 37°C. The following day, cultured cells were monitor for several factors including morphology, contractility, confluency, dead cells, and contamination.

Table 20. Details about the needed cell number and medium per well of each culture flask type.

Materials	**Area per well [cm^2]**	**Living cells per well**	**Medium volume per well**
6-well plate	9.6	7.2 x 10^5	2 ml
8-well chamber slide	0.8	0.6 x 10^5	0.5 ml

2.2.8.3. General culture conditions for neonatal mouse cardiomyocytes

Neonatal mouse cardiomyocytes were incubated in a specific culture medium to maintain their rather immature differentiation state and support their normal physiological conditions. To avoid bacterial contamination the medium was supplemented with antibiotics like penicillin and streptomycin. Additionally, as an antioxidant molecule, ascorbic acid was added to the culture medium. To avoid overgrowth of non-myocytes, as well as excessive hypertrophic growth in CMs, the serum added to the culture medium

must not contain high amounts of growth factors. Therefore, horse serum was used, which contains less growth factors compared to the commonly used fetal calf serum (FCS). Accordingly, to enhance cellular viability in the absence of growth factors as well as maintain the CMs in their differentiation state, Insulin-Transferrin-Selenium (ITS) was added to the culture medium. Additionally, the ITS is shown to reduce the serum supplementation requirement in adherent cells. In order to monitor the impact of treatment of primary CMs with certain growth factors and cytokines, a Neonatal CMs treatment culture medium was used where the horse serum was substituted with a low concentration of FCS (0.5%). FCS as a supplement of cells and tissues in culture media, is essential for cell attachment, growth, proliferation, and survival. To avoid over-stimulation of CM hypertrophic growth and non-myocyte proliferative overgrowth, only 0.5% FCS was used in the culture media upon parallel growth factor and cytokine treatment (Engel *et al*., 2005; Nguyen *et al*., 2012).

2.2.8.4. Cytokine and growth factor treatment for stimulating cardiomyocyte cell cycle activity

Selected cytokines and growth factors are used to monitor their possible involvement in cell cycle regulation of primary neonatal CMs under *in vitro* conditions. In order to assess cell cycle activity following treatments, the percentage of CMs that have completed an S phase of the cell cycle was monitored by BrdU incorporation. Additionally, the activation of the growth regulating signal transduction pathways upon growth factor and cytokine treatment was validated by western blot experiment. The starting concentration of the selected cytokines and growth factors was determined by literature review using previous studies showing an effect on proliferation in cultured cells. Additionally, one concentration lower (1/2) and one higher (2x) than the suggested concentration in the literatures, were chosen. For instance, the suggested optimal concentration for the positive control FGF1 to enhance cell cycle activity in cardiac myocytes was 50 ng/ml (Engel *et al*., 2005). Therefore, the concentrations for primary CM treatment used in this study were 25, 50, and 100 ng/ml FGF1. In addition, 10% FCS was used as another positive control to apply a maximum growth stimulus. The recombinant proteins Angptl3 (R and D system, #136-AN-050) and PDGFAA (Sigma Aldrich, #SRP3228-10UG) were all delivered as lyophilized powders and were reconstituted according to the manufacturer instructions. The solvent itself was used as a negative control for treating cells. Prior to

CMs treatment, depending on the purpose of the experiment cells were seeded on fibronectin coated chamber slides or 6-well plates, respectively. The following day, the treatment culture media were prepared by adding the recombinant cytokines and growth factors as well as controls (positive and negative) to neonatal CMs treatment medium (Table 5). Moreover, to assess BrdU incorporation, BrdU was added to the culture media at a final concentration of 10 µM. Prior to treatment, culture medium was carefully discarded, the seeded primary CMs were rinsed twice with sterile pre-warmed PBS and subsequently incubated with the prepared treatment media. The treatment was performed by 24 h incubation, with 5% CO_2, at 37°C. Subsequently, the 6-well plates were used for protein isolation and western blot analyses as described before (Chapter 2.2.4.1.1.). In order to detect incorporated BrdU, the chamber slides were used for IF experiments (Chapter 2.2.8.4.1.).

2.2.8.4.1. Immunofluorescence antibody staining for incorporated BrdU in primary CMs

Bromodeoxyuridine (BrdU) is added to culture medium as a thymidine analogue. While replicating DNA in the S phase of the cell cycle, the BrdU is incorporated into the newly synthesized DNA. This integrated BrdU is detected by IF staining using an antibody against BrdU. After cell treatment was performed, the medium was aspirated and cells were washed twice for 5 min in PBS, at 24 rpm, at RT. Subsequently, fixation was carried out by incubation of cells in ice-cold 70% EtOH, for 5 min, at RT. Prior to immuno-detection, the cells are required to undergo a pre-treatment step using 2 M HCl incubation to denature the DNA and unmask the BrdU epitopes. Therefore, cells were washed three times for 5 min in PBS, at 24 rpm, at RT and incubated with 2 M HCl, at 24 rpm, for 30 min, at RT. After another wash step, blocking was performed by RT incubation for 1.5 h in 5% (v/v) normal goat serum (NGS) diluted in antibody solution-IF. Afterwards, the blocking solution was discarded and 200 µl of the primary AB mixture (i.e., anti-Actinin and Anti-BrdU) was added to each well (140 µl for chamber slides). In order to distinguish between CMs and non-myocytes a primary AB against α-Actinin (a sarcomeric protein) was used which stains CMs. The chamber slides were sealed with parafilm and incubation was conducted at 24 rpm, for O/N, at 4°C. The following day, after three steps of washing in PBS, incubation in secondary AB was carried out. Therefore, 200 µl of the secondary AB mixture (DAPI, Anti-Mouse Alexa-488, and Anti-Rat Alexa-555) was added to each

well and the incubation was proceeded for 2 h, at 24 rpm, at RT in the dark. Following three wash steps in PBS, the chambered-coverslip attached to the slide was removed carefully. The excess liquid was discarded and onto each well area 5 µl of ProLong® Gold mounting medium was added. Next, the cells were covered with coverslip and stored under light protected conditions, for O/N, at RT. Finally, the next day the slides were used for microscopic imaging using IF microscopic analyses (Axio Observer Fluorescence Microscope, Carl Zeiss Microscopy), using N-Achroplan 10x/0,25 Ph1 M27, and Zen 2.3 pro software. Per well, twenty snaps randomly from various parts were taken und used for analyses. The rate of CMs that had undergone an S phase was determined for each treatment and control by counting the number of nuclei (DAPI) stained for both BrdU and α-Actinin (CMs), related to the total CM number (nuclei positive for α-Actinin but not BrdU) given in percent. Accordingly, total DAPI counts as well as BrdU exhibiting nuclei were counted automatically using Zen 3.8 desk with Image analysis toolkit. However, the number of non-myocytes together with BrdU signals in CMs were counted manually using Zen 2.3. lite. The row data were transferred in Excel (Excel v16.72) and the percentages of CM nuclei and non-myocytes exhibiting BrdU staining were calculated, separately.

2.2.9. Statistical analyses

Graphical presentation of data was carried out using mean values ± standard error of the mean (SEM) by Microsoft® Excel v16.72 (for bar graphs) and Graphpad Prism v9.5.1. software (for scatter plots). Statistical analyses were performed using SPSS v29.0.0.0 software. Accordingly, normal distribution of data sets was evaluated using Shapiro-Wilk test (sample sizes smaller than 50). Homogeneity of variances between groups was evaluated by Levene's test. Depending on the number of study groups, the normally distributed data with homogenous variances were either examined with unpaired two-sided student's *t*-test or one-way analysis of variance (ANOVA). Whereas the *t*-test was performed comparing two study groups (E18.5 vs. NB18.5), for more than two study groups (E17.5, E18.5, NB18.5 and NB18.5+1), ANOVA was conducted. Based on the homogeneity of variances, different post-hoc tests were performed upon ANOVA including Tukey's for homogenous variances and Games-Howell for unequal variances. In the case of non-normal data distributions, non-parametric analyses were performed.

Therefore, differences between two study groups which were not normally distributed were assessed by Mann-Whitney test, while the differences among multiple groups which were not normally distributed was evaluated by Kruskal-Wallis test including pairwise comparison of groups. *p*-values less than 0.05 were considered as statistically significant and the respective groups were labelled by * ($p<0.05$), ** ($p<0.01$), *** ($p<0.001$), and **** ($p<0.0001$).

Using *t*-test while comparing a huge number of proteins (i.e., 111 cytokines studied in cytokine arrays) can lead to statistical false positive results. Therefore, in order to avoid the false positive results, False Discovery Rates (FDR) were calculated. Accordingly, for each cytokine the normalized densitometry values were compared between the E18.5 and NB18.5 group and a *P*-value was generated using the *t*-test in SPSS. Using Excel, the cytokines and their respective measured *P*-values were inserted. Afterwards, the cytokines were arranged based on their *P*-values from lowest to highest *P*-values (Figure X1). In a new column, to each cytokine a number was given from one to 111 (since 111 cytokines were studied using cytokine arrays) (Figure X2). In a new Excel column, the q-value for each cytokine was calculated. However, prior to q-value calculation for all cytokines, the q-value of the cytokine with the highest *P*-value was defined as 1. Next, in the q-value column at the position of penultimate cytokine (here 110), the following equation was typed (Figure X3). Consequently, the generated formula was dragged from position 110 and dropped to the first cytokine (the one with the lowest *P*-value) (Figure X4).

q-value = MIN(*P*-value of the cytokine*total cytokine number/cytokine given number;q-value of the following cytokine)

Finally, following FDR analyses, the cytokines showing q-values less than 0.05, were selected for further analyses.

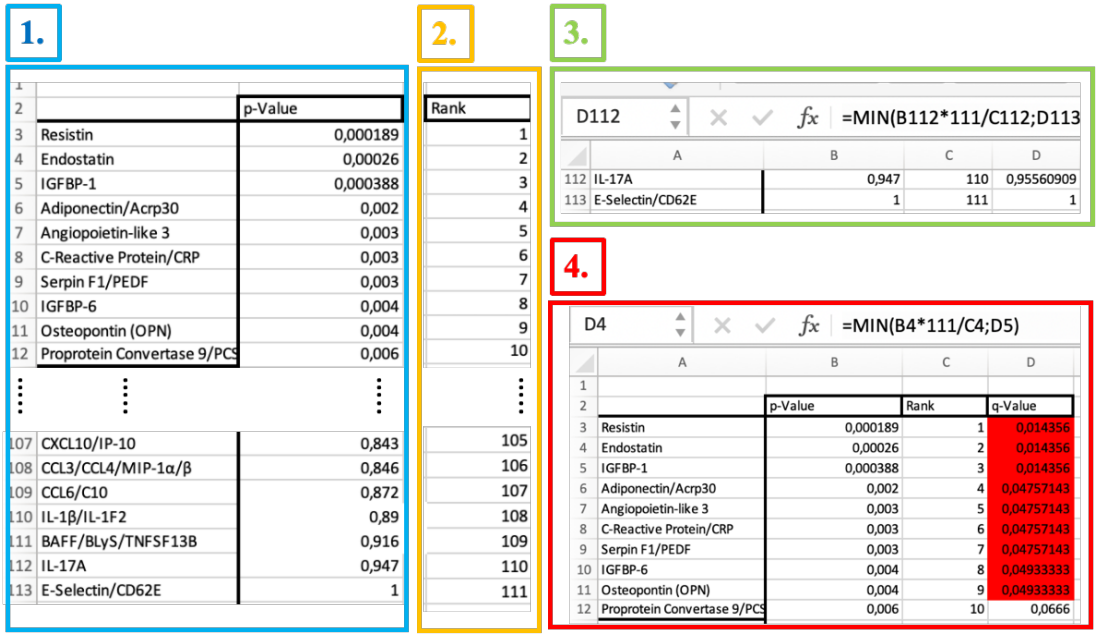

		p-Value	Rank
3	Resistin	0,000189	1
4	Endostatin	0,00026	2
5	IGFBP-1	0,000388	3
6	Adiponectin/Acrp30	0,002	4
7	Angiopoietin-like 3	0,003	5
8	C-Reactive Protein/CRP	0,003	6
9	Serpin F1/PEDF	0,003	7
10	IGFBP-6	0,004	8
11	Osteopontin (OPN)	0,004	9
12	Proprotein Convertase 9/PCS	0,006	10
107	CXCL10/IP-10	0,843	105
108	CCL3/CCL4/MIP-1α/β	0,846	106
109	CCL6/C10	0,872	107
110	IL-1β/IL-1F2	0,89	108
111	BAFF/BLyS/TNFSF13B	0,916	109
112	IL-17A	0,947	110
113	E-Selectin/CD62E	1	111

		A	B	C	D
112	IL-17A	0,947	110	0,95560909
113	E-Selectin/CD62E	1	111	1

		p-Value	Rank	q-Value
3	Resistin	0,000189	1	0,014356
4	Endostatin	0,00026	2	0,014356
5	IGFBP-1	0,000388	3	0,014356
6	Adiponectin/Acrp30	0,002	4	0,04757143
7	Angiopoietin-like 3	0,003	5	0,04757143
8	C-Reactive Protein/CRP	0,003	6	0,04757143
9	Serpin F1/PEDF	0,003	7	0,04757143
10	IGFBP-6	0,004	8	0,04933333
11	Osteopontin (OPN)	0,004	9	0,04933333
12	Proprotein Convertase 9/PCS	0,006	10	0,0666

Figure X. Illustration of False Discovery Rate (FDR) measurement using Excel. 1) Cytokines were arranged in Excel from the lowest to the highest p-value. **2)** The cytokines were ranked based on the p-value (1 to 111). **3)** In new column, we defined a q-value of one (position D113), for the cytokine with the largest p-value. The formula represented in the box was generated at the position of the penultimate cytokine (position D112). **4)** The generated formula was copied in the q-value column for the remaining cytokines and the q-values were generated. q-value < 0.05 was determined as significant, represented in red.

3. Results

3.1. Investigation of cell cycle activity in the mouse myocardium around birth

Previous studies have highlighted that within the first week after birth in mice, the proliferation rate in CMs is reduced continuously. Moreover, from the postnatal day 7 (P7) on, the murine CMs are almost unable to proliferate. If the separation from the intrauterine surroundings would promote the CM cell cycle arrest, it would mean that humans delivered preterm would have reduced CM number, thereby potentially limited heart function compared to the term born individuals. Therefore, a deep understanding about the onset of CM cell cycle regulation upon birth, would be beneficial for preterm-born humans. Moreover, this understanding provides an essential orientation point for monitoring factors involved in postnatal cell cycle regulation in cardiac myocytes. In this study, we aimed to evaluate the cell cycle activity and proliferation rate in both CMs and non-myocytes in the mouse myocardium at two consecutive late embryonic stages (E17.5 and E18.5), immediately after birth (NB18.5 and NB19.5), one day after delivery (NB18.5+1 and NB19.5+1), and 48 h after birth (NB19.5+2). In this context, factors including the gestational ages and sex, were strictly controlled. Additionally, all analytical steps were performed in a blinded manner, ensuring that the investigator conducting the analyses was unaware of the gestational age and sex of studied mice.

3.1.1. Declined rate of Ki67 positive cardiac cells immediately after birth in male mice

In order to determine the overall cell cycle activity in cardiac cells, immunofluorescence staining was performed on heart paraffin sections using an antibody against Ki67 (Figure 6). Ki67 is a protein, which is expressed at all stages of the cell cycle except for G0 (where cells are inactive with respect to cell cycle progression). Hence, cells that display immunofluorescence signals following a Ki67 antibody staining demonstrate an active cell cycle (Figure 6A).

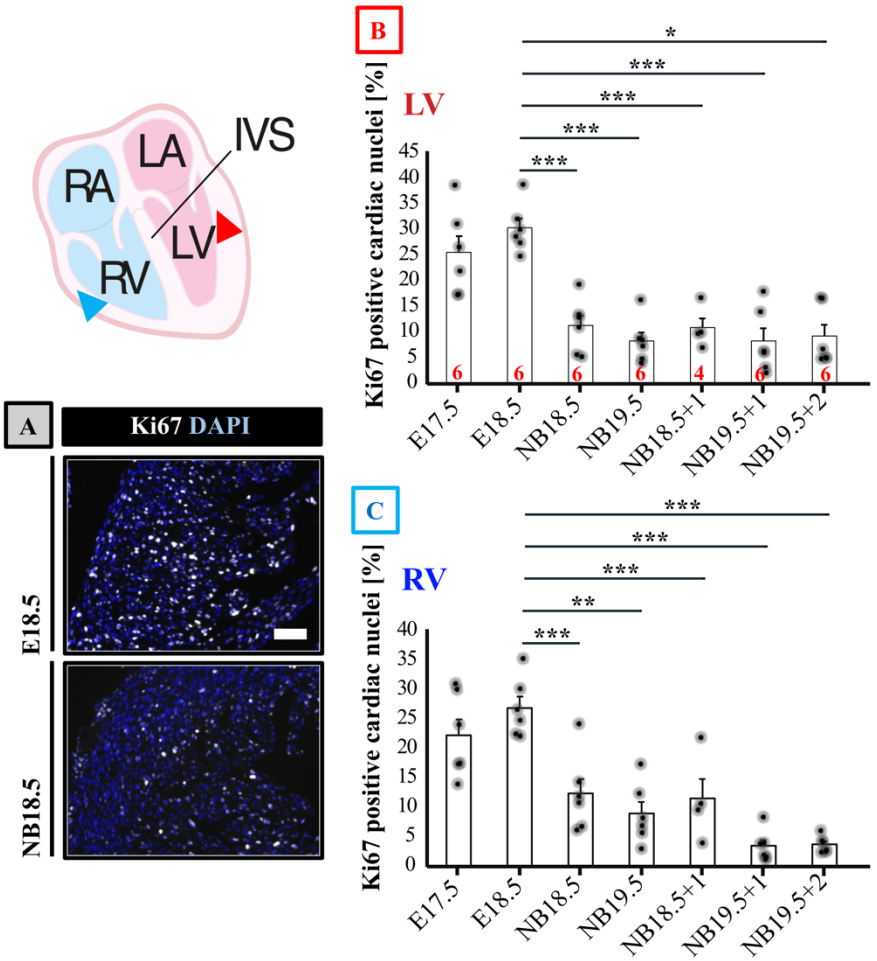

Figure 6. Reduced cell cycle activity immediately after birth in the ventricular myocardium of male mice. Investigation of perinatal cell cycle activity in murine ventricular myocardium via immunofluorescence antibody staining against Ki67. **A)** Representative immunofluorescence images of comparable regions of the LV in E18.5 vs. NB18.5 heart sections. Ki67 is shown in white, whereas the nuclei are represented in blue (stained with DAPI). The scale bar is 50 µm. **B-C)** Graphs represent the percentage of cardiac nuclei exhibiting cell cycle activity (i.e., positive for Ki67) in the left ventricle (LV) (B) and right ventricle (RV) (**C**) at seven represented consecutive stages around birth. In both ventricular compartments, cell cycle activity drops directly after birth (at NB18.5 and NB19.5). However, cell cycle activity remained unchanged at one and two days after birth (compared to birth). The numbers shown in red (B) represent the sample size n. LV: Left ventricle, RV: Right ventricle, E: Embryonic stage, NB: Newborn, NB18.5+1 and NB19.5+1: Samples were collected at 24 h after birth, NB19.5+2: Animals were born at day 19.5 and kept for 48 h with mother and then the samples were collected. The colours of the triangles in the heart animation (top-left) are identical to the colours of the graphs corresponding the analysed ventricular regions (B and C). The results are illustrated as mean values ± SEM, each data point represents one mouse heart. Statistical significance among groups was assessed by one-way ANOVA. *: $P<0.05$, **: $P<0.01$, ***: $P<0.001$.

Our immunofluorescence (IF) findings employing a Ki67 antibody revealed that at 25.8% of ventricular cardiac nuclei at left ventricle (LV), 33.2% at interventricular septum (IVS), and 22.5% at right ventricle (RV) exhibited cell cycle activity at the fetal E17.5 stage. Moreover, comparing two late fetal stages (E17.5 and E18.5), no statistically significant modifications in the cardiac nuclei demonstrating a cell cycle activity were recorded. Notably, immediately after exposure to an extrauterine environment (at NB18.5), the proportion of cardiac nuclei actively engaged in the cell cycle was reduced significantly

to 11.5% at LV, 16.7% at IVS, and 12.5% at RV, compared to E18.5 (P<0.01). Moreover, comparing NB18.5 and NB19.5, the percentage of nuclei exhibiting a cell cycle activity remained statistically unchanged in all three investigated ventricular regions. Nonetheless, comparing NB18.5 and NB19.5 hearts with one (at NB18.5+1 and NB19.5+1) and two further postnatal days, the cell cycle activity demonstrated a steady state (in average ~6%) in all three heart compartments (LV, RV, and IVS) of the murine ventricular myocardium (Figure 6B-C; Supplementary Figure 1). Consequently, these findings revealed an immediate impact of birth on postnatal cell cycle activity in entire ventricular cardiac cells irrespective to the animal's gestational age at delivery. It is essential to mention that in this experiment we did not differentiate between myocardial cell types. Therefore, we cannot make any conclusions about CM at this stage. Additionally, using the Ki67 and DAPI IF analyses, we did not investigate the cardiac cells but nuclei, given that CM can be binucleated or polyploid.

3.1.2. Reduction of cardiomyocyte mitosis rates within the early postnatal period in male and female mice

Alongside Ki67 staining, to evaluate the proliferation dynamics in the myocardium throughout the perinatal lifespan of mice, phosphorylated Histone H3 (pHH3) immunostaining can be conducted. In the late G2 phase of cell cycle, the DNA protein Histone H3 is phosphorylated at serine-10 residue, which promotes the DNA condensation and cell-cycle progression. From the late anaphase to early telophase (parts of mitosis), the Histone H3 dephosphorylation occurs. Therefore, via IF staining against the pHH3, the mitotically active cells can be stained. Our next objective was to investigate the mitosis dynamics in CMs using perinatal mouse heart sections. Notably, in order to distinguish between CMs and non-myocytes, in our team we developed an IF method using Caveolin3 (Cav3) and Wheat Germ Agglutinin (WGA) staining. Cav3 is a membrane protein expressed in CMs and skeletal muscles. Therefore, its immunostaining using heart sections, allows for CMs detection. However, factors including signals from close focal planes, heart section preparation, and cellular 3-dimensional orientations, limit the CMs differentiation from non-myocytes, using Cav3 staining alone. Therefore, to overcome this issue, we used Cav3 in a combination with another membrane staining called WGA. The WGA stains the cellular membrane of mammals. Accordingly, the

entire cardiac cell populations were stained with WGA (in green), whereas only CMs displayed an additional staining for Cav3 (in red).

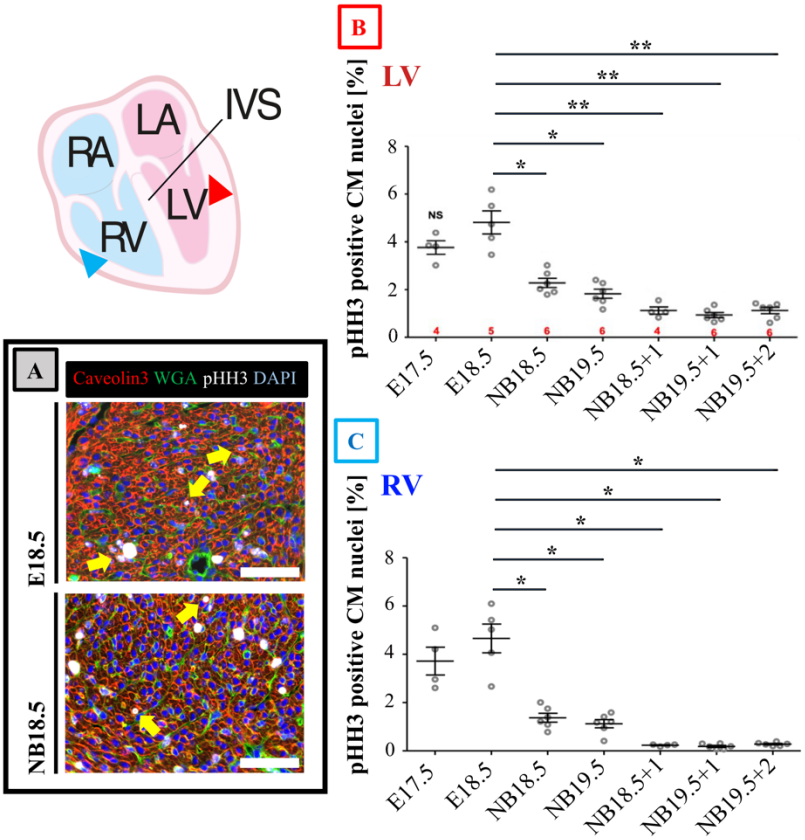

Figure 7. Declined mitosis rate immediately after birth in the ventricular CMs of male mice. Investigation of perinatal mitosis in murine ventricular myocardium via immunofluorescence antibody staining against pHH3 and Caveolin 3. **A)** Representative IF images of comparable regions of the LV in perinatal heart sections obtained from male mice. pHH3 is represented in white, whereas the nuclei are stained in blue (using DAPI), CMs in red and green (but dominantly red), and non-myocytes in green. The yellow arrows highlight examples of CMs in mitosis. The scale bar is 50 µm. **B-C)** Graphs represent the percentage of CM nuclei exhibiting mitosis activity (i.e., positive for pHH3) in the left ventricle (LV) (B) and right ventricle (RV) (**C**) at seven represented consecutive stages around birth. In both ventricular compartments, mitosis rate is reduced shortly after birth (at NB18.5 and NB19.5). Moreover, mitosis rate in CMs is further reduced at one day after birth at NB18.5+1 and NB19.5+1(compared to birth). However, the number of mitotically active CM nuclei remained unchanged at NB19.5+2 compared to one day after birth. The numbers shown in red (B) represent the sample size n. LV: Left ventricle, RV: Right ventricle, E: Embryonic stage, NB: Newborn, NB18.5+1 and NB19.5+1: Samples were collected at 24 h after birth, NB19.5+2: Animals were born at day 19.5 and the housing by mother was conducted for 48 h and then the samples were collected. The colours of the triangles in the heart animation (top-left) are identical to the colours of the graphs corresponding the analysed ventricular regions (B and C). The results are illustrated as mean values ± SEM, each data point represents one mouse heart. Statistical significance among groups was assessed by one-way ANOVA. *: $P<0.05$, **: $P<0.01$.

In parallel, employing a co-staining against pHH3, the CMs and non-myocytes undergoing mitosis were detected. Consequently, the cells exhibiting nuclear pHH3 signals and green but no red membrane staining corresponded to non-myocytes active in mitosis (Figure 7A). Furthermore, the pHH3 positive cells which show green and red membrane staining represented CMs engaged in mitosis (Figure 7A). In contrast to the

Results

Ki67 data described above, we investigated the perinatal mitosis dynamics in CMs, in particular.

Our IF findings using pHH3 staining on male mouse heart sections unveiled that at E17.5, in all three ventricular regions, including LV, RV and IVS, the percentage of CMs exhibiting pHH3 signals was between 3.72% and 4.2% (Figure 7B and 7C, and Supplementary Figure 2). Notably, comparing E18.5 to E17.5 heart paraffin slices prepared from male individuals, the proportion of mitotically active CM nuclei revealed no statistically significant variation. However, shortly after an exposure to the extrauterine environment (i.e., at NB18.5), this percentage declined noticeably to 2.3% in LV, to 2% in IVS, and 1.4% in RV. Comparing NB18.5 and NB19.5 outcomes, the rate of CM exhibiting mitosis followed a steady pattern. It is essential to mention that at NB18.5 and NB19.5 the samples were collected immediately after delivery, however the gestational ages of animals at birth were variable. In this context, comparing these two stages, revealed that not the gestational age, but the separation from an intrauterine environment promoted the reduced mitotic activity in CMs. Interestingly, following one additional day after birth (i.e., at NB18.5+1), the percentage of CMs active in mitosis was reduced further to 1.1% in LV, to 0.65% in IVS, and 0.24% in RV of male mice LV, IVS, and RV (compared to NB18.5). No changes in proportion of mitotically active CMs at NB18.5+1 and NB19.5+1 was noted in male mice LV, IVS, and RV (Figure 7B and 7C, and Supplementary Figure 2). Moreover, following 48 h after birth, the mitosis rate in CMs remained unchanged at NB19.5+2 compared to NB19.5+1. Taken together, comparing our Ki67 and pHH3 data, our analyses concluded following findings for the first time:

1. The cell cycle arrest in CMs and cardiac cells is not a planned mechanism (based on our E18.5 vs. E17.5 data).
2. Immediately after an exposure to an extrauterine surrounding the cell cycle activity is remarkably declined (E18.5 vs. NB18.5 and NB19.5).
3. The birth promotes the cell cycle withdrawal in such an irreversible manner (comparing NB18.5 and NB19.5 with NB18.5+1, NB19.5+1, and NB19.5+2 data).

It needs to be mentioned that in our Ki67 and pHH3 experiments, the heart samples at NB18.5+1 and NB19.5+2 were obtained from the littermates of only one litter, which could impact any conclusions. Therefore, to overcome this uncertainty and to validate our data, we repeated the pHH3 immunostaining. This time we only analysed three key stages such as E18.5, NB18.5, and NB18.5+1, and for each stage the investigated littermates

were delivered from at least two litters. Additionally, the investigation was conducted using samples from both male and female mice (Figure 8, 9, and 10).

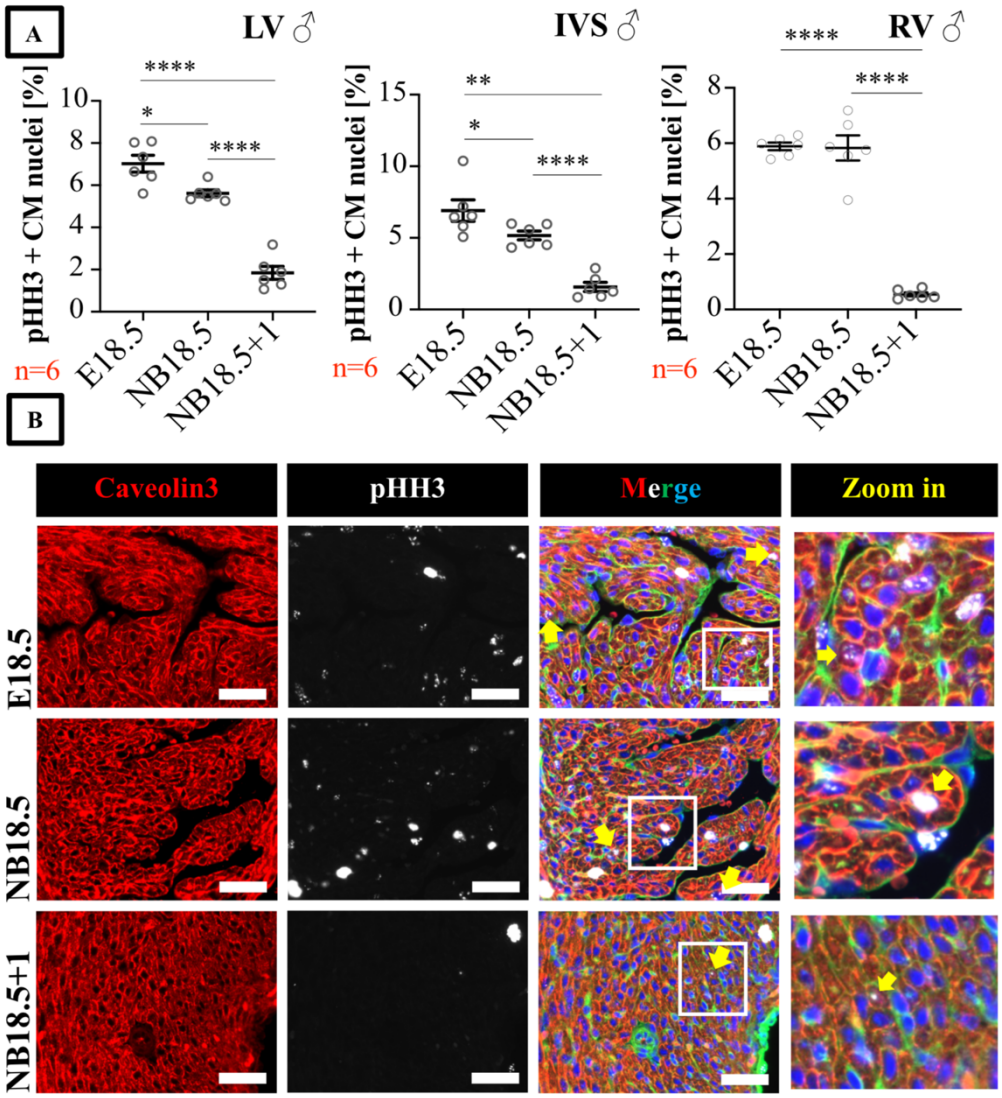

Figure 8. Declined rate of CMs exhibiting mitotic activity after birth in ventricular myocardium of male mice. Investigation of perinatal mitosis in murine ventricular myocardium via IF antibody staining against pHH3 and caveolin-3. **A)** Graphs demonstrate the percentage of CMs active in mitosis in the right ventricle (RV), interventricular septum (IVS), and left ventricle (LV), at three consecutive stages around birth. In LV and IVS myocardium, the mitosis rate in CMs was reduced directly after birth. Moreover, at NB18.5+1 the mitosis rate was reduced further in LV and IVS. In contrast, in RV myocardium the number of CMs active in the mitosis stage, was unchanged immediately after birth but decreased between NB18.5 and NB18.5+1. The red numbers represent the sample sizes. RV: Right ventricle, LV: Left ventricle, IVS: Interventricular septum. The results show the mean values ± SEM. Statistical significance among groups was determined by one-way ANOVA. *: $P<0.05$, **: $P<0.01$, ****: $P<0.0001$. **B)** Representative IF images of comparable regions of the RV in perinatal heart sections obtained from male mice. pHH3 is represented in white, whereas the nuclei are stained in blue (using DAPI), CMs in red and green (but dominantly represented in red), and non-myocytes only in green. The yellow arrows highlight examples of CMs in mitosis. The scale bar is 50 µm. The white box in merge image, represents the magnified area illustrated in zoom-in part.

Results

Our validation IF findings using pHH3 staining on male mouse heart sections unveiled that at E18.5, in all three ventricular components including LV, RV and IVS, the percentage of CMs exhibiting pHH3 signals was between 6 and 7% (Figure 8A).

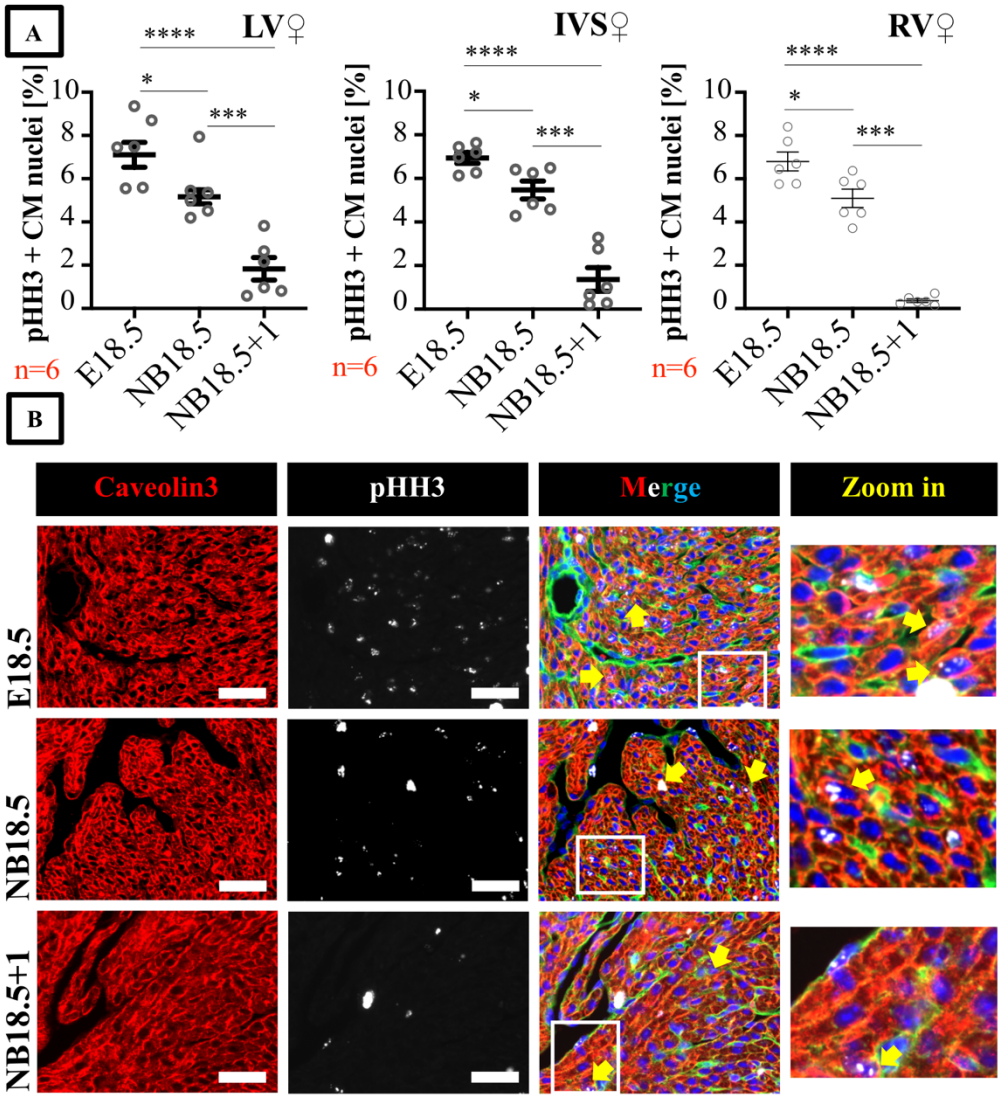

Figure 9. Immediate decline in mitosis rates after birth in ventricular CMs of female mice. Investigation of perinatal mitosis in murine female ventricular myocardium via IF antibody staining against pHH3 and Caveolin 3. **A)** Graphs represent the percentage of CM nuclei in mitosis in three compartments of the ventricular myocardium, at three consecutive stages around birth. In RV, LV and IVS, the mitosis rate in CMs dropped shortly after birth when comparing fetal (E18.5) and neonatal (NB18.5) hearts. Moreover, one day after birth the mitosis rate is further reduced when comparing stage NB18.5 and NB18.5+1. The numbers shown in red, represent the sample sizes. RV: Right ventricle, LV: Left ventricle. IVS: Interventricular septum. The results exhibit the mean values ± SEM. To assess the statistical significance among groups one-way ANOVA was performed. *: $P<0.05$, ***: $P<0.001$, ****: $P<0.0001$. **B)** Illustration of comparable regions of the LV within the perinatal heart sections isolated from female mice. The pHH3 is represented in white, whereas the nuclei are shown in blue (DAPI), CMs in red and green (dominantly in red), and non-myocytes in only green. The yellow arrow highlights the CMs in their mitosis state. The scale bar (demonstrated in white) is 50 µm. The white box in merge image, demonstrates the magnified region illustrated in zoom-in part.

However, similar to our preliminary pHH3 findings, we noticed declined counts of CM nuclei exhibiting a mitosis activity immediately after delivery at NB18.5. Briefly, shortly after an exposure to the extrauterine environment (i.e., at NB18.5), this percentage declined noticeably to ~5% in LV and IVS compared to E18.5. Following one additional day after birth (i.e., at NB18.5+1), the percentage of CMs active in mitosis was reduced further to ~1.5% in male mouse LV and IVS (Figure 8A). In contrast to LV and IVS, the number of CMs stained for pHH3 demonstrated a delayed reduction in the RV myocardium of the male murine hearts following birth. Accordingly, the CM mitosis rate remained constant (6%) in the RV of male mice immediately after delivery compared to the fetal E18.5 stage. A drop in the CM mitosis rate was eventually observed between NB18.5 and NB18.5+1 in male mouse RV (Figure 8). In this context, the proportion of mitotic CMs at NB18.5+1 decelerated remarkably from 6% (at NB18.5) to 0.5% (Figure 8A). Consequently, following our validation pHH3 immunostaining, we were able to highlight the essential influence of delivery on the reduced mitosis rate in CMs of male mice.

Consistent with the findings in males, in ventricular myocardium of female mice at fetal stage E18.5, approximately 7% of CMs exhibited activity in the mitosis stage of the cell cycle (Figure 9A). However, in contrast to results in males, in females immediately after birth at NB18.5, the number of CMs exhibiting pHH3 signals was significantly reduced in all three ventricular compartments (LV, IVS, and RV) compared to fetal stages. In males this was only observed in our initial pHH3 findings, as well as in the validation IF staining in LV and IVS regions, but not RV (see Figure 7 and 8). Accordingly, comparing NB18.5 with E18.5 stages in females, the mitosis rate in CMs declined noticeably from ~7% to ~5% following delivery. One additional day after birth (i.e., at NB18.5+1), the mitosis rate was decreased further to 1.8%, 1.4% and 0.4%, in LV, IVS, and RV of murine female hearts, respectively (Figure 9A). In conclusion, in the course of our IF outcomes against pHH3, we revealed for the first time that an exposure to an extrauterine surrounding is involved in induction of immediate decrease in the number of mitotically active CMs in the ventricular myocardium of male and female mice.

3.1.3. Decreased mitosis rate in non-myocytes in the early postnatal period of male and female mouse hearts

Beside the mitosis rate in CM nuclei, we investigated the proportion of non-myocytes exhibiting a mitotic activity in all three compartments of the male and female ventricular myocardium at E18.5, NB18.5, and NB18.5+1 stages using the pHH3-validation staining snaps.

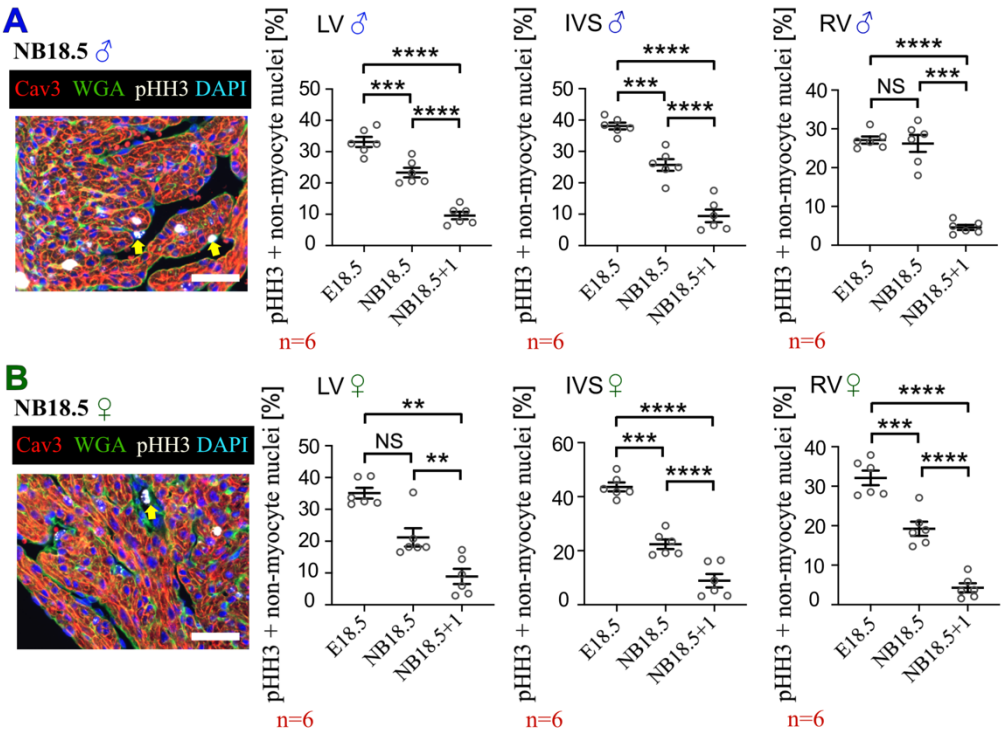

Figure 10. Decreased number of non-myocytes active in mitosis shortly after birth in LV and IVS of male and female mice. The mitosis rate during the perinatal period was analysed in murine ventricular myocardium via IF antibody staining against pHH3. **A)** Data concerning the representative IF image and graphs related to male mice. **B)** Image and graphs concerning the female mice. A and B-left) Representative images of RV regions with identical stages (NB18.5) in perinatal male (A) and female (B) heart sections. The pHH3 is represented in white, while the nuclei are shown in blue (DAPI), CMs in red and green (yet dominantly red), and non-myocytes in only green (no red staining). The yellow arrows pointing towards the non-myocytes in their mitosis state. The scale bar (demonstrated in white) is 50 µm. The graphs corresponding to each sex, were represented with identical colour code as the one in A and B (either green or blue). Graphs demonstrate the proportion of non-myocytes with mitosis activity in all three parts of male mouse ventricular myocardium, at three consecutive stages around birth. In LV and IVS of male mice, the mitosis rate in non-myocytes was decreased directly after birth. Moreover, at NB18.5+1 the mitosis rate was reduced further. Nonetheless, in RV the mitosis reduction in non-myocytes was observed primarily between NB18.5 and NB18.5+1. The red numbers represent the sample size (A). In female mice, the mitosis rate in non-myocytes in all three studied regions, was decreased immediately after birth (at NB18.5 compared to E18.5). Comparing NB18.5+1 and NB18.5, this rate was reduced significantly further at NB18.5+1 (B). RV: Right ventricle, LV: Left ventricle. IVS: Interventricular septum, Cav3: Caveolin 3. The results exhibit the mean values ± SEM. Statistical significance among groups was determined by one-way ANOVA. **: $P<0.01$, ***: $P<0.001$, ****: $P<0.0001$.

Our pHH3 analyses concerning non-myocytes unveiled that the proportion of non-myocytes demonstrating a mitosis activity was 33.1% in LV, 38.1% in IVS, and 27.1% in RV of male mice at final embryonic age (i.e., E18.5). In agreement with mitotically active

CM data, this percentage in non-myocytes was significantly reduced in LV and IVS region shortly after a separation from an intrauterine surrounding. Specifically, compared to E18.5, the rates of mitotically active non-myocyte were reduced significantly to 23.3% in LV, and to 25.7% in IVS at NB18.5 (Figure 10A). Furthermore, comparing stages NB18.5 and NB18.5+1, we observed a further reduction in the mitosis rate in non-myocytes in the LV and IVS regions of the male mice. Accordingly, at NB18.5+1 the percentage of mitotic non-myocytes located in LV and IVS, was declined to 9.6% and 9.4%, respectively. Similar to our CM findings, the number of non-myocytes exhibiting a staining for pHH3 followed a delayed reduction in RV myocardium. Hence, of non-myocytes localized in RV of male hearts, 27.1% at E18.5, and 26.2% at NB18.5 demonstrated mitotic activity. However, following one additional day of exposure to the extrauterine environment (NB18.5+1), the proportion of mitotically active non-myocytes declined remarkably to 4.6% in RV of male mice, compared to E18.5 and NB18.5 (Figure 10A).

Via pHH3 staining on heart slices prepared from female mice, we noticed that at the gestational age of E18.5, 35.1% of non-myocytes located in LV, 43.6% in IVS, and 32.1% in RV, exhibited a pHH3 staining. Moreover, immediately after birth at NB18.5, this percentage was significantly reduced in all three investigated ventricular regions. Briefly, at NB18.5 the rate of non-myocytes demonstrating a mitotic activity was reduced to 21.2% in LV, 22.4% in IVS, and 19.2% in RV, compared to before delivery. Comparing NB18.5+1 and NB18.5, this percentage reduced noticeably further to 8.9%, 8.9%, and 4.3%, in LV, IVS, and RV at NB18.5+1, respectively (Figure 10B).

In summary, according to our IF findings, cell cycle activity was noticeably reduced immediately after delivery in male mouse hearts. Moreover, the with one exception for RV, the percentage of CM and non-myocyte nuclei exhibiting an activity in mitosis, decelerated remarkably briefly after a separation from the intrauterine environment in both male and female mice. 24 h after birth, the mitosis rate in CMs and non-myocytes declined noticeably in heart sections obtained from male and female mice at NB18.5+1 compared to NB18.5. Collectively our data underline the influence of birth on the early postnatal cell cycle withdrawal in mouse hearts, irrespective of animal gender. Our next objective was to investigate the underlying mechanism behind the immediate postnatal proliferation arrest observed in mouse hearts.

3.2. Investigation of the activity of cardiac growth-regulating signalling pathways and expression of cell cycle regulators following birth

Cell cycle activity and proliferation in cardiac myocytes is regulated by diverse factors including expression of cell cycle regulating genes, metabolic state, and a variety of signalling pathways regulating cell growth (Chapter 1.1.4.1.). Since the cardiac cell cycle drops immediately after birth in mice (Chapter 3.1.), we primarily aimed at investigating potential alterations in the expression of cell cycle regulators in combination with changes in the activity of cardiac growth regulating pathways following an exposure to the extrauterine environment. Indeed, preliminary unpublished western blot data from our group suggested that the activities of mechanistic target of rapamycin (mTOR) and mitogen-activated protein kinase (MAPK-Kinase) signalling pathways were significantly reduced in mouse ventricular myocardium of neonatal compared to fetal hearts (Chapter 1.1.6.). In this context, our objective was to study the impact of birth on the expression of cell cycle regulators and the activity of growth regulating signalling pathways. Therefore, we performed western blot (WB) experiments, IF antibody staining, and gene expression analyses (RT-qPCR) using mouse hearts at perinatal stages such as E18.5 and NB18.5.

3.2.1. Reduced activity of AKT/mTOR and MAPK-kinase signalling directly after birth in male mouse hearts

As a signalling pathway involved in the regulation of cell growth and proliferation, the MAPK-kinase signalling pathway is composed of a series of phosphorylation steps. An interaction between extracellular molecules (i.e., growth factors) and tyrosine kinase membrane receptors, induces the MAPK-kinase signalling pathway. Following a set of serine/threonine phosphorylation the cell growth and proliferation is promoted (Malarkey *et al*., 1995). Accordingly, to monitor a possible effect of birth on the activity of MAPK-kinase signalling, WB experiments were conducted using proteins isolated from total mouse hearts at stage E18.5 and NB18.5, in a gender dependent manner. The activity of signalling pathways was primarily monitored by investigating the phosphorylation level of downstream targets including MAPK-kinases p38, p44 and p42 (also referred to as Erk1 and 2) (Figure 11). Our WB results indicated that directly after birth, the phosphorylation of Erk1 (p44) was almost three times lower than this before birth,

whereas Erk2 (p42) phosphorylation remained unchanged following delivery compared to E18.5 (Figure 11A and 11B). Interestingly, comparing NB18.5 and E18.5 female mouse heart samples, no significant changes in the phosphorylation of p44 and p42 were observed immediately after birth (Figure 11C and 11D). Moreover, after birth the phosphorylation state of p38 MAP-kinase declined to ~50% of its value observed at E18.5 in both male and female mouse ventricular myocardium (Figure 11).

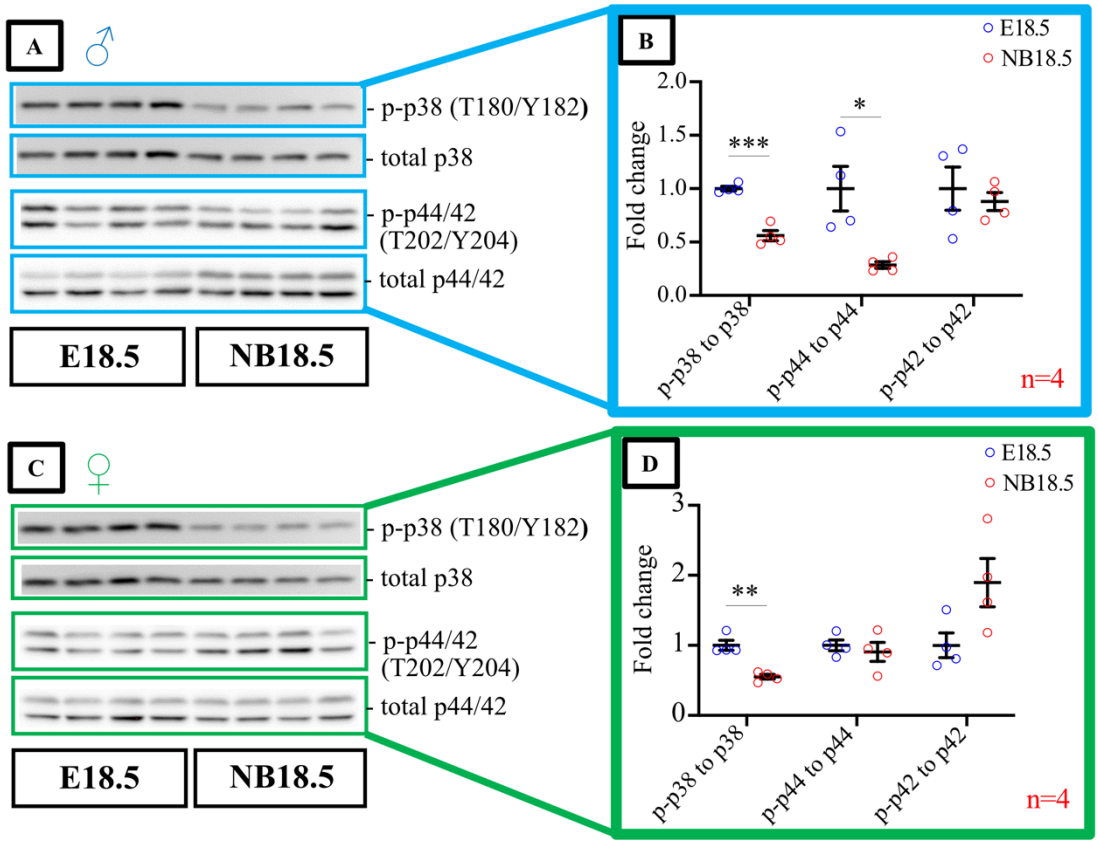

Figure 11. Drop in phosphorylation of p38 and p44 in ventricular myocardium of male mice directly after birth. The activity of MAPK-kinase was monitored by measuring the phosphorylation intensity using WB experiments. **A)** and **C)** WB using whole heart protein extracts from E18.5 and NB18.5 male (A) and female (C) mice. The phosphorylated form of p44/42 (at threonine 202 and tyrosine 204) and p38 (at threonine 180 and tyrosine 182), and their total protein levels were illustrated in blue (male) and green (female) boxes. **B)** (male) and **D)** (female) WB quantifications were carried out by normalizing the phosphorylated to the total protein band intensity. The results were related to the E18.5 data and were represented as fold change. Data exhibited a significant reduction in p44, and p38 phosphorylation, shortly after delivery in male mouse hearts. However, in female hearts only the p38 phosphorylation state was reduced immediately after birth at NB18.5 compared to E18.5. The number shown in red represents the sample size. The results were illustrated as the mean values ± SEM. Statistical significance among groups was assessed by unpaired 2-tailed student *t*-test using SPSS. *: $P<0.05$, **: $P<0.01$, ***: $P<0.001$.

Results

Another key signalling pathway involved in the regulation of cell growth, proliferation and protein synthesis involves the kinase AKT (also known as protein kinase B (PKB)).

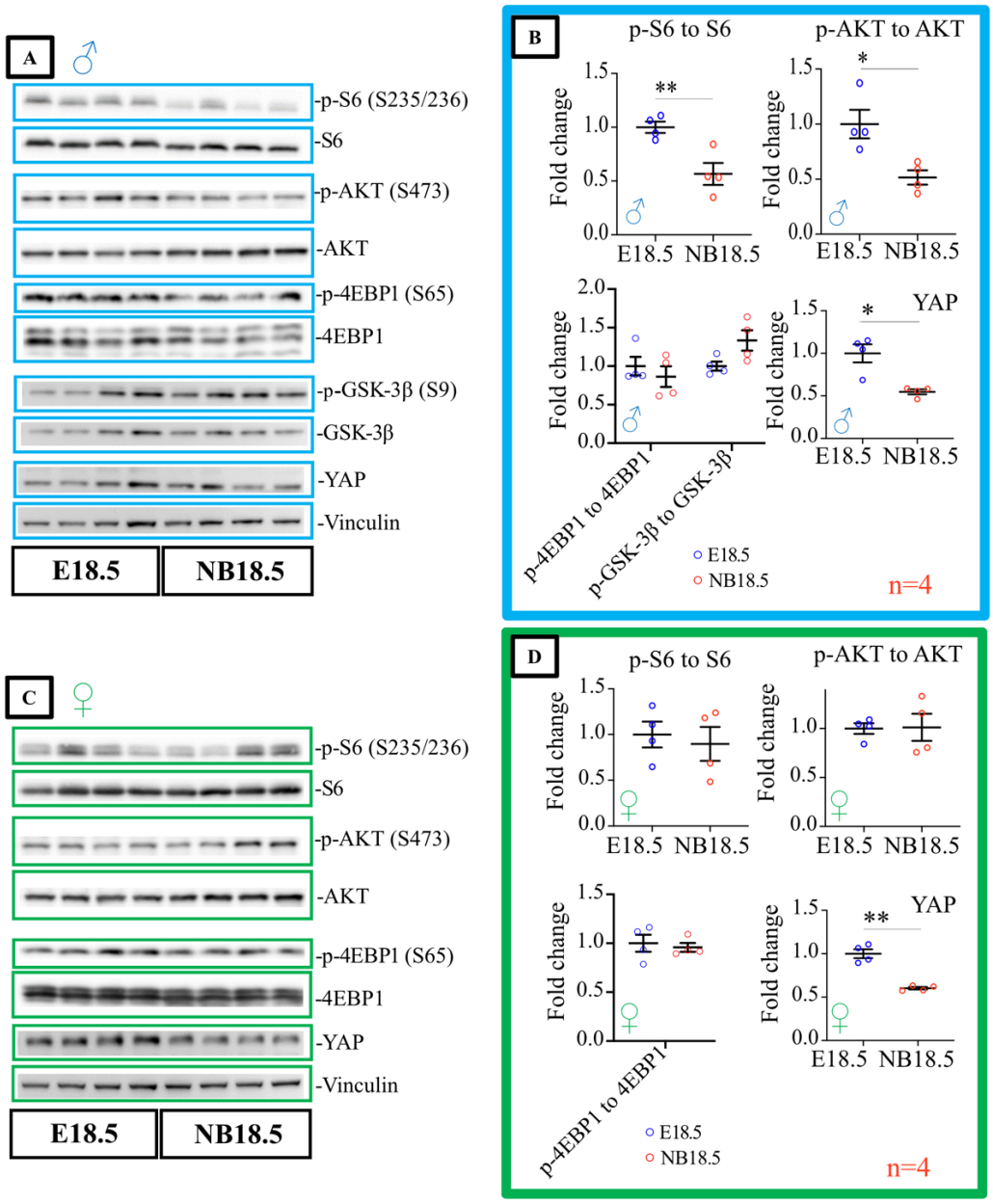

Figure 12. Drop in phosphorylation of S6 and AKT, and YAP total level in ventricular myocardium of male mice directly after birth. The activity of AKT, mTORC1 (S6 and 4EBP1) and Hippo (YAP total) was monitored by measuring the phosphorylation and total protein intensity using WB experiments. **A)** and **C)** WB using whole heart protein extracts from E18.5 and NB18.5 male (A) and female (C) mice. The phosphorylated form of S6 (at serine 235 and 236), AKT (at serine 473), 4EBP1 (at serine 65), GSK-3β (at serine 9), and their total protein levels, together with YAP total and Vinculin (house keeper) were represented in blue (male) and green (female) boxes. **B) (**male**)** and **D) (**female**)** WB quantifications were carried out by normalizing the phosphorylated to the total protein band intensity, or total protein to vinculin (in case of YAP). The results were normalized to the E18.5 data and were represented as fold change. Data exhibited a significant reduction in S6 and AKT phosphorylation, and YAP protein levels shortly after delivery in male mouse hearts (B). However, in females only the YAP level was decreased at NB18.5 vs. E18.5 (D). The red numbers show the sample size. The results were illustrated as the mean values ± SEM. Statistical significance among groups was assessed by unpaired 2-tailed student *t*-test using SPSS. *: $P<0.05$, **: $P<0.01$.

Results

Various factors such as nutrients, as well as growth factors including insulin, Insulin-like growth factor 1 (IGF-1), Platelet-derived growth factor (PDGF) and Epidermal growth factor (EGF) promote AKT activation (Li *et al*., 2011; Reiss *et al*., 1996). Consequently, our next objective was to investigate the potential impact of birth on the activity of AKT and its downstream targets including GSK-3β, 4EBP1, and S6 in hearts obtained from male and female mice at E18.5 and NB18.5, using WB analyses.

Via WB analyses we revealed that the phosphorylation of AKT and S6, was decreased by the factor of two (0.5-fold change) in the ventricular myocardium of male mice immediately after birth, compared to the final fetal stage. However, AKT and S6 phosphorylation remained unchanged following delivery in comparison to E18.5 stage in hearts of females (Figure 12). Furthermore, the phosphorylation state of 4EBP1 in both gender and GSK-3β in male mouse hearts was unaltered in the perinatal period (Figure 12B and 12D). Notably, the p-GSK-3β level in female murine hearts (at NB18.5 vs. E18.5) was not assessed due to technical issues; which needs to be elucidated in future. Taken together, we noticed that the activity of AKT and S6 dropped remarkably in male hearts briefly after a separation from an intrauterine surrounding, whereas in female hearts these remained unchanged following birth compared to the E18.5 stage.

The Hippo signalling pathway is involved in the regulation of size and growth of various organs, as well as controlling cellular outcomes such as apoptosis, differentiation, and proliferation (reviewed by Mia and Singh, 2019). As a consequence of an activation of the Hippo pathway, a downstream target known as the transcriptional coactivator YAP undergoes phosphorylation, resulting in its inactivation (reviewed by Mia and Singh, 2019). YAP knock-out mice have been shown to develop myocardial hypoplasia and embryonic lethality, whereas CM-specific YAP overexpression results in CM proliferation in adult mice (Xin *et al*., 2013). Accordingly, YAP is a master regulator of CM proliferation in the heart. Thus, performing WB experiments we investigated the Hippo signalling pathway by analysing phosphorylation and total protein levels of YAP using male and female murine hearts at stage E18.5 and NB18.5. In both female and male hearts, the phosphorylation level of YAP exhibited no significant changes after birth compared to fetal stages (Supplementary Figure 3). Nonetheless, the total YAP protein amount was decreased shortly after birth compared to E18.5, in both sexes. Accordingly, the YAP level declined to ~0.5-fold in mouse ventricular myocardium at NB18.5 compared to E18.5 (Figure 12).

Finally, it has been concluded that bone morphogenetic protein 7 (BMP7) signalling pathway is involved in regulation of postnatal cardiac growth (Yang *et al*., 2023). As a consequence of BMP7 and its receptor interaction, p38 as well as SMAD1 become phosphorylated, whereas YAP get dephosphorylated. This leads to YAP, p-SMAD1, and p-p38 nuclear localization, and finally CM proliferation. However, BMP7 signalling inhibition attenuates the p38 and SMAD1 phosphorylation, while it promotes YAP phosphorylation. Consequently, the nuclear localization of YAP, p38, and SMAD1 is suppressed, leading to CM maturation as well as CM proliferation arrest (Yang *et al*., 2023).

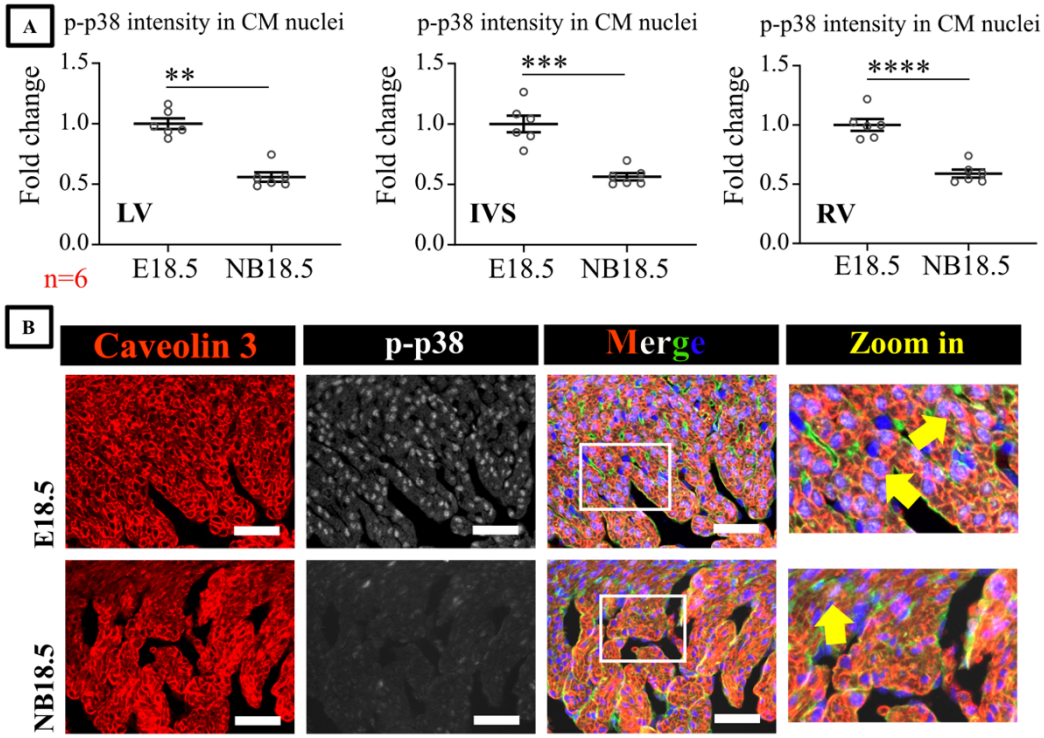

Figure 13. Immediate decline in p-p38 level in CM nuclei after birth in ventricular CMs of male mice. Investigation of perinatal p-p38 nuclear level in murine male ventricular CMs via IF antibody staining against p-p38, WGA, and Caveolin 3. **A)** Graphs represent the fold changes of CM nuclear intensities for p-p38, at NB18.5 vs. E18.5. In all three investigate ventricular regions the p-p38 nuclear intensity in CMs dropped significantly shortly after birth compared to E18.5. The numbers shown in red, represent the sample sizes. RV: Right ventricle, LV: Left ventricle. IVS: Interventricular septum. The results exhibit the mean values ± SEM. To assess the statistical significance among groups unpaired 2-tailed student *t*-test using SPSS was performed. **: $P<0.01$, ***: $P<0.001$, ****: $P<0.0001$. **B)** Illustration of comparable regions of the LV within the perinatal heart sections isolated from male mice. The p-p38 is represented in white, whereas the nuclei are shown in blue (DAPI), CMs in red and green (dominantly in red), and non-myocytes in only green. The yellow arrow highlights the CM nuclei exhibiting p-p38 signals. The scale bar (demonstrated in white) is 50 µm. The white box in merge image, demonstrates the magnified region illustrated in zoom-in part.

Interestingly, using WB analyses we demonstrated that both YAP level and p-p38 degree was remarkably declined briefly after delivery in whole heart lysate obtained from male and female mice. In this context, in order to monitor the degree of p-p38 nuclear

localization in CMs we performed IF antibody staining against p-p38, Cav3, and WGA (Figure 13) using male heart sections, at E18.5 and NB18.5 stages. Using ImageJ, the nuclear intensity of p-p38 in CM in particular, were measured and normalized to E18.5 data.

Interestingly, in agreement with the study performed by Yang and colleagues and our pHH3 and Ki67 outcomes, we observed that concomitant with the birth-dependent reduction in cell cycle activity in CMs the nuclear p-p38 signals declined in CMs immediately after birth compared to E18.5 (Figure 13).

Collectively, our WB findings concluded that the activity of p38 and the level of YAP were decreased remarkably shortly after delivery, in mouse hearts isolated from both sexes. Notably, the activity of BMP7 signalling (YAP level and nuclear p-p38 signals), as well as Erk1, AKT, and S6 activities revealed a significant drop in the male mouse hearts immediately after birth compared to before delivery. Nonetheless, these factors (except for p-p38 and total YAP) exhibited no significant alterations in their activities at NB18.5 vs. E18.5 in female murine hearts.

3.2.2. Protein levels of D-type Cyclins decline immediately after birth in male and female mouse hearts

Cell cycle progression depends on the expression level of cell cycle promoting factors (such as various cyclins and cyclin-dependent kinases) and cell cycle inhibitors (such as p21/Cip1 and p27/Kip1). In cells revealing no G1 to S activity, the tumour suppressor protein retinoblastoma (Rb) interacts and thereby suppresses E2F transcription factors. However, in cells exhibiting a G1 to S progression, the Rb is phosphorylated by cyclin-dependent kinases CDK4 and CDK6. Consequently, the phosphorylated Rb is dissociated from E2F, leading to expression of the gene regulated by E2F which are essential for DNA replication. Indeed, the CDK4 and CDK6 are activated by their binding partners namely D-type Cyclins (Bartek *et al.*, 1996). Nonetheless, CDK/Cyclins are inhibited by various proteins among which p21 and p27 can be mentioned (reviewed by Abukhdeir and Park 2008).

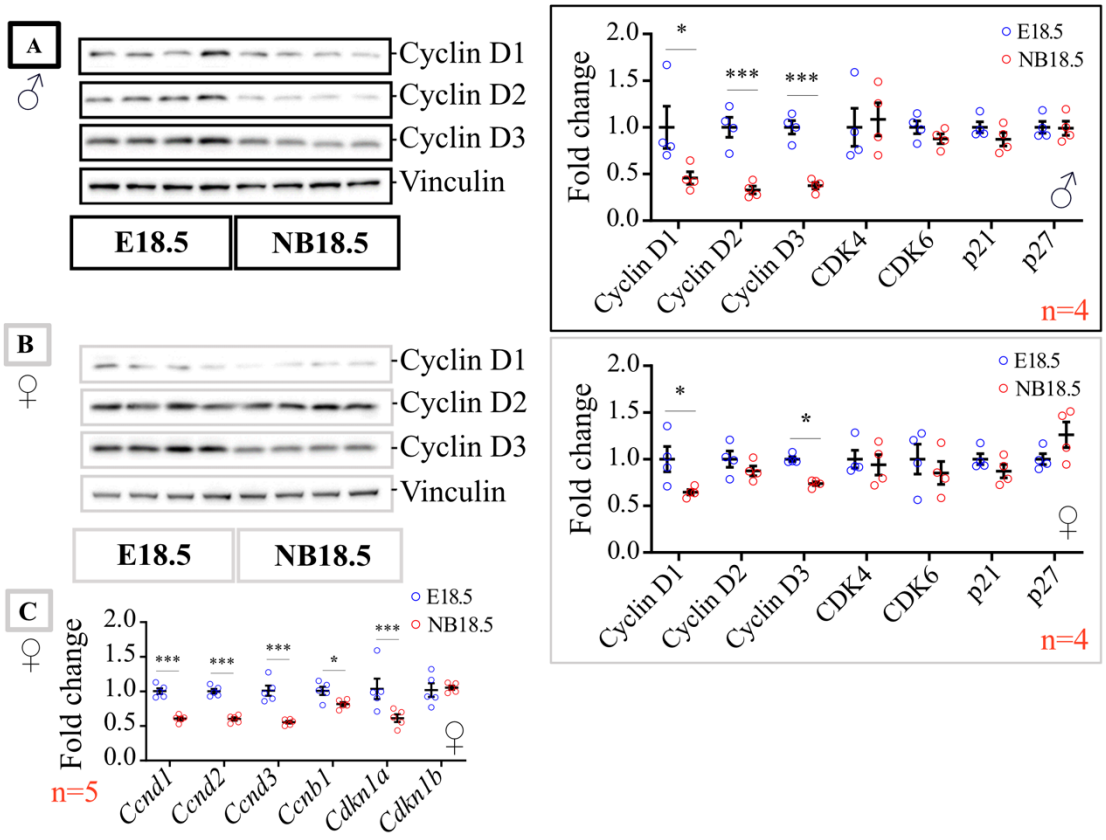

Figure 14. RNA and protein expression of cell cycle regulating genes in male and female mouse hearts before and after birth. The perinatal expression of cell cycle regulators was examined by WB and RT-qPCR experiments. **A)** and **B) Left:** Illustration of WB using whole heart protein extracts obtained from E18.5 and NB18.5 male (A) and female (B) mice. **Right**: WB densitometric quantifications: The intensity of each analyzed protein band was normalized to a housekeeper (Vinculin) intensity. To analyze protein expression after birth compared to fetal stages, the measures were related to the mean value of the E18.5 hearts. **A)** WB experiments using heart samples isolated from male mice: Among the studied cell cycle regulators, only D-type Cyclins revealed a noticeable reduction directly after birth. **B)** WB analyses in female mouse hearts showed a birth-related reduction in Cyclin D1 and D3. **C)** RT-qPCR experiments using RNA isolated from female murine hearts, showed reduced expression of all studied cell cycle regulators after birth, except for *Cdkn1b* (encoding p27*)*. The red numbers represent the n. The results were demonstrated as the mean values ± SEM. In order to determine the sstatistical significance among groups unpaired 2-tailed student *t*-test was conducted using SPSS. *: $P<0.05$, ***: $P<0.001$.

Thus, to assess the availability of cell cycle regulators upon birth, WB and RT-qPCR experiments were performed using female and male mouse hearts at stage E18.5 and NB18.5. Immediately after birth, protein levels of all members of the D-type Cyclin family (i.e., Cyclin D1, D2 and D3) were decreased significantly compared to the fetal stage in male mouse hearts. Accordingly, our WB results revealed that Cyclin D1 was reduced to 0.46 (fold change), Cyclin D2 to 0.32, and Cyclin D3 to 0.37 at NB18.5 compared to E18.5 in male mouse hearts (Figure 14A). However, no birth-related changes in the protein amounts of other examined cell cycle regulators including CDK4 and

CDK6, as well as p21 and p27 (cyclin dependent kinase inhibitors), were evident in male murine hearts (Figure 14A).

Similar to males, using female mouse hearts our WB analysed showed that protein expression of CDK4, CDK6, p21, and p27 was unchanged immediately after birth compared to fetal stages (Figure 14B). Moreover, Cyclin D2 levels showed no significant variations shortly after birth compared to the fetal heart (E18.5) in female hearts. Nonetheless, similar to male mouse hearts, the Cyclin D1 and Cyclin D3 levels dropped significantly immediately after birth vs. E18.5 in females. At NB18.5, Cyclin D1 was reduced to 0.64 and Cyclin D2 to 0.74 (fold change) compared to E18.5 (Figure 14B).

In order to analyse the expression pattern of cell cycle regulators following an exposure to an extrauterine environment on the transcriptional level, a set of RT-qPCR experiments were carried out using RNA isolated from female mouse hearts at E18.5 and NB18.5. With the exception of *Cdkn1b* (encoding p27), all the analysed cell cycle regulators revealed noticeable declines in their expression patterns at the RNA level shortly after birth (at NB18.5) compared to E18.5, in female murine hearts (Figure 14C). Accordingly, immediately after birth the expression of *Ccnd1* (Cyclin D1) dropped to 0.61 (fold change), *Ccnd2* (Cyclin D2) to 0.60, *Ccnd3* (Cyclin D3) to 0.55, *Ccnb1* (Cyclin B1) to 0.81, and *Cdkn1a* (p21) to 0.61 compared to E18.5. Notably, due to lacking heart samples isolated from male mice at E18.5 and NB18.5, we did not conduct the RT-qPCR analyses studying the mentioned genes; which needs to be investigated in future. Nonetheless, at the protein level, we concluded that immediately after an exposure to an extrauterine environment the availabilities of D-type Cyclins in hearts isolated from male and female mice were decreased, compared to before delivery, revealing the importance of birth on activities of cell cycle regulators.

3.2.3. Reduced number of cardiomyocytes exhibiting Cyclin D3 expression directly after birth in mouse hearts

To validate the WB findings regarding reduced expression of D-type cyclins in the heart immediately after birth, we conducted IF antibody staining experiments on male and female hearts at E18.5 vs. NB18.5. Among our type-D Cyclin antibodies, the Cyclin D1 and Cyclin D3 were suitable for IF staining on paraffin sections. Hence, we initially assessed Cyclin D3 expression in the entire myocardial cell population (including CM

nuclei) and in cardiac myocyte nuclei in particular. Accordingly, the number of CMs nuclei stained positive for MEF2A/C exhibiting co-localization with Cyclin D3 signals was quantified and represented as percentage of the total cardiac nuclei (Figure 15).

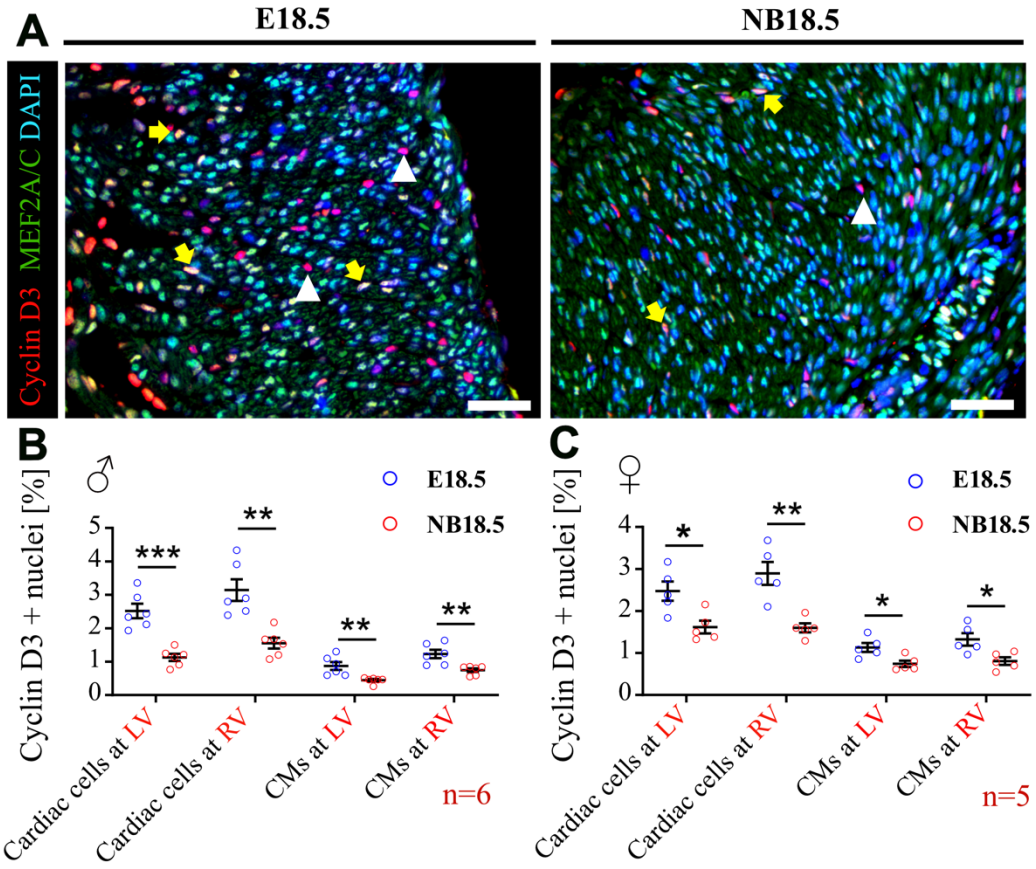

Figure 15. Reduced proportion of Cyclin D3 expressing cardiac cells and CMs shortly after birth in LV and RV of male and female mice. The perinatal Cyclin D3 expression was analysed in LV and RV myocardium via IF antibody staining. **A)** An illustration of IF staining in LV of male mice at E18.5 vs. NB18.5. Cyclin D3 was stained in red, CM nuclei in green (MEF2A/C), and all nuclei in blue (DAPI). The yellow arrows point out CM nuclei expressing Cyclin D3, whereas the white arrowheads show non-myocytes exhibiting Cyclin D3 signals. **B)** and **C)** Illustrations of the percentages of Cyclin D3 positive nuclei among all cardiac cells and Cyclin D3 positive CM nuclei co-stained with MEF2A/C in both male (B) and female (C) mice in both LV and RV. IF findings showed an immediate birth-related significant reduction of Cyclin D3 signals in all cardiac cells and CMs in both genders. The sample size was equal to 6. The scale bar was 50 µm. RV: Right ventricle, LV: Left ventricle. The Cyclin D3 proportions were represented as the mean values ± SEM. Statistical significance among groups was assessed by unpaired 2-tailed student *t*-test using SPSS. *: $P<0.05$, **: $P<0.01$, ***: $P<0.001$.

Our IF staining experiments on mouse heart paraffin sections revealed that regardless of murine gender, the percentage of Cyclin D3 signals in CM nuclei and total cardiac nuclei were decreased shortly after birth in both LV and RV. Specifically, in the LV myocardium of male hearts, the Cyclin D3 proportion at NB18.5 was reduced from 2.5% observed at E18.5 to 1% in all cardiac cells, and from 0.9% to 0.4% in CMs. Moreover, immediately after delivery in RV myocardium this percentage was significantly decreased from 3.1% to 1.5% in all cardiac cells and from 1.2% to 0.7% in CMs compared to E18.5 (Figure

15B). Similarly, in females the Cyclin D3 signals in both ventricular regions were reduced shortly after birth compared to before delivery. Accordingly, in LV myocardium of female mice at NB18.5, the number of Cyclin D3 signals exhibited a significant drop from 2.5% at E18.5 to 1.6% in all cardiac cells, and 1.1% to 0.7% in CMs. Furthermore, in RV myocardium of female mice, the number of cells demonstrating Cyclin D3 signals declined from 2.9% to 1.6% in all cardiac cells and from 1.3% to 0.8% in cardiac myocytes compared to before birth (Figure 15C). Consequently, our IF findings reflected the WB outcomes where the Cyclin D3 levels in murine ventricular myocardium exhibited noticeable reduction immediately after birth, irrespective of the gender of the studied animals. However, alongside Cyclin D3 signals in total cardiac cells (both CMs and non-myocytes), using IF experiments we were able to monitor the Cyclin D3 expression in CM nuclei in particular.

3.3. Studying the potential role of the metabolic switch from glycolysis to fatty acid oxidation in early postnatal cell cycle arrest in the heart

As a potential factor influencing the proliferative decline in postnatal CMs immediately after birth (as observed in our IF findings; see Chapter 3.1.1. and 3.1.2.), the metabolic switch from glycolysis to fatty acid oxidation might be involved. In embryonic and fetal hearts, the major portion of cellular energy in the form of adenosine triphosphate (ATP) is generated by anaerobic glycolysis (Lopaschuk *et al.*, 2010; Makinde *et al.*, 1997). Compared to prenatal hearts, the glycolysis rate in rabbit myocardium at postnatal day 7 is reduced. In murine CMs, the proliferation rate declines continuously at P7 such that the adult CMs are almost not capable to proliferate (Lopaschuk *et al.*, 1991; Porrello *et al.*, 2013). Interestingly, in adult mouse hearts the ectopic expression of pyruvate kinase muscle isozyme 2 (PKM2, as a glycolysis enzyme) promoted the cell cycle activity in CMs following a myocardial infarction (Magadum *et al.*, 2020). Furthermore, as a byproduct of oxidative metabolism, the reactive oxygen species (ROS) can be mentioned, which is increased within the first postnatal week in mouse hearts concurrent by postnatal cell cycle arrest in CMs (Puente *et al*., 2014). It has been concluded that ROS inhibition leads to enhanced postnatal proliferation ability window in murine CMs (Puente *et al*., 2014). Collectively, there is a correlation between the metabolic switch and the postnatal

cell cycle withdrawal in mammals. In this context, in order to examine a potential involvement of the metabolic switch in the immediate postnatal proliferation decline in cardiomyocytes, we conducted WB, RT-qPCR, and IF experiments using perinatal mouse hearts.

3.3.1. Reduced RNA expression but mainly normal protein levels of glycolytic enzymes in the heart immediately after birth

To monitor whether the immediate postnatal cell cycle arrest observed in CMs and non-myocytes, might be a consequence of reduced glycolysis, we studied the dynamics of the expression patterns of glycolysis-involved enzymes. Thus, RT-qPCR and WB experiments were conducted on mouse hearts at E18.5, NB18.5 and NB18.5+1.

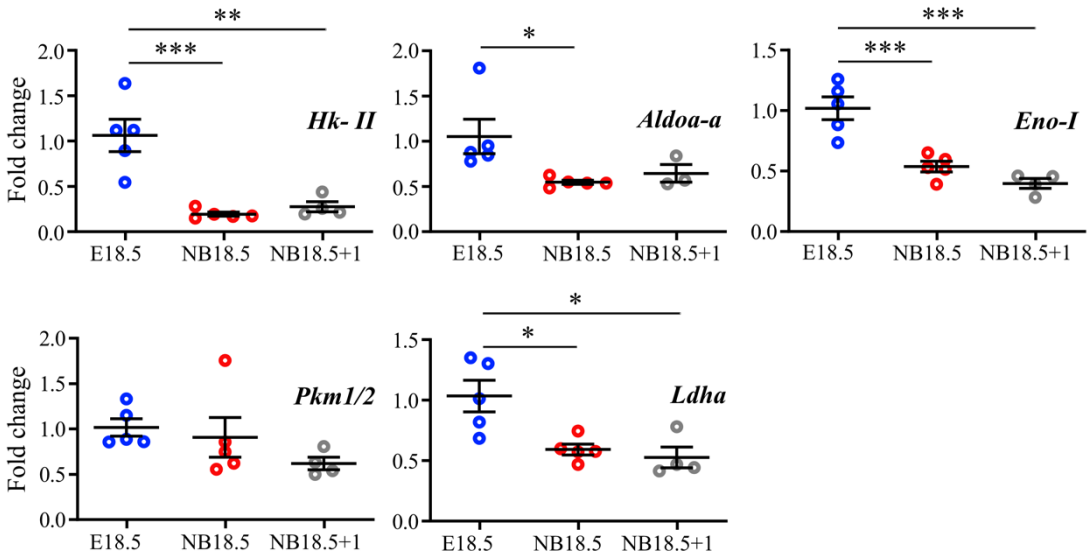

Figure 16. An immediate birth-dependant reduction in expression of glycolysis-involved enzymes in ventricular myocardium of female mice. The glycolysis decline upon delivery was assessed via RT-qPCR expression analyses of glycolysis-involved enzymes on female mouse hearts at E18.5 to NB18.5+1. Graphs illustrate quantifications of fold changes of gene levels in hearts at birth and one day after birth compared to E18.5. Except for *Pyruvatekinase-M* (*PKM* or *Pyruvate kinase muscle*), the remaining investigated genes revealed a noticeable birth-related reduction in their RNA levels compared to before delivery. The sample size was five in E18.5 and NB18.5, and four in NB18.5+1. The results represent the mean values ± SEM. Statistical significance between groups was monitored by one-way ANOVA. *: $P<0.05$, **: $P<0.01$, ***: $P<0.001$.

The RT-qPCR results revealed that shortly after exposure to the extrauterine environment, the RNA expression pattern of genes encoding glycolysis enzymes including *Hexokinase II* (*Hk-II*), *Aldolase-a* (*Aldoa*), *Enolase I* (*Eno-I*), and *Lactatedehydrogenase A* (*Ldha*) showed a significant reduction compared to the fetal stage at E18.5. Accordingly, at

NB18.5 in female hearts the expression of *Hk-II* was reduced to 0.2, *Aldoa* to 0.5, *Eno-I* to 0.6, and *LDHA* to 0.6 when related to E18.5 hearts. Nonetheless, after one additional postnatal day (i.e., at NB18.5+1), no further expression changes in the mentioned genes were observed compared to NB18.5. The *Pyruvatekinase muscle* (*Pkm1/2*) gene, however, followed no birth-related changes in its expression pattern in female murine hearts (Figure 16).

To confirm the RNA expression data at the protein levels, WB analyses with protein lysates from perinatal hearts were performed.

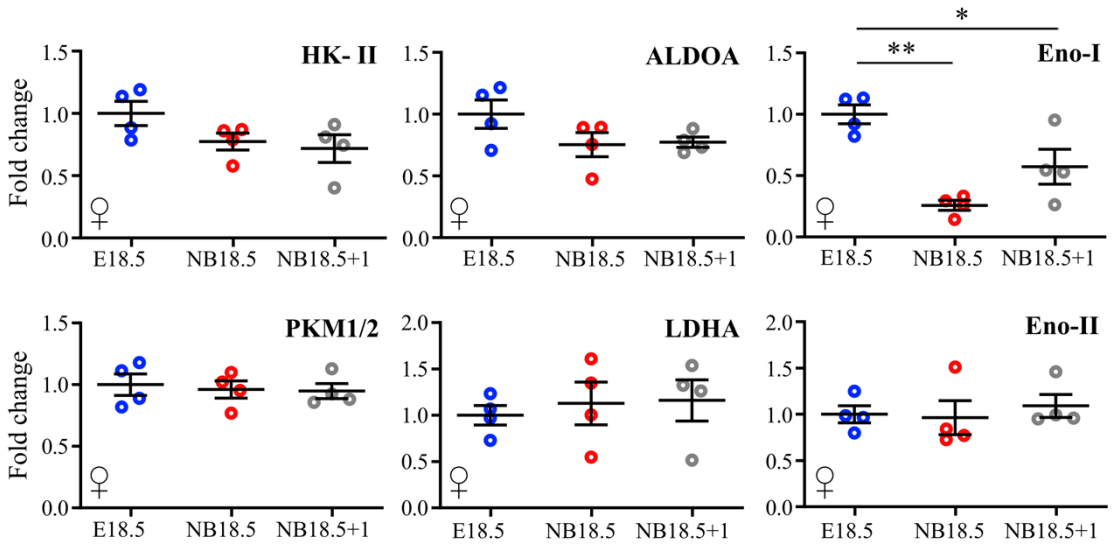

Figure 17. An immediate birth-dependant decline in Eno-I level in ventricular myocardium of female mice. The glycolysis reduction following birth was assessed via WB experiments against glycolysis-involved proteins on female mouse hearts at E18.5 to NB18.5+1. Graphs represent quantifications of fold changes of protein levels in hearts at birth and one day after birth compared to E18.5. Only enolase 1 (Eno-I) exhibited a noticeable birth-related reduction in its level compared to before delivery. The sample size was equal to four. The results are represented as the mean values ± SEM. Statistical significance between groups was monitored by one-way ANOVA. *: $P<0.05$, **: $P<0.01$.

With the exception of enolase-I (Eno-I), protein expression did not align with the results obtained in RT-qPCR experiments. WB results unveiled that among the six evaluated proteins engaged in glycolysis such as Hexokinase II (Hk-II), Aldolase-A (ALDOA), Pyruvatekinase muscle (PKM1/2), Lactate dehydrogenase A (LDHA), and enolase-II (Eno-II), only Eno-I showed a reduction in its protein levels shortly after birth in comparison to E18.5. The Eno-I protein level was reduced to 0.26 (fold change) at NB18.5 vs. E18.5 in female mouse hearts. Moreover, following one additional postnatal day, this value slightly increased to 0.57-fold change compared to NB18.5. However, no statistical significance was detected between Eno-I protein levels at NB18.5 and

NB18.5+1 female mouse hearts. Unlike Eno-I, the remaining glycolytic enzymes studied exhibited no statistically significant variations in their perinatal protein levels (Figure 17). Notably, due to limited heart samples, the experiments in this Chapter were only conducted using heart sample obtained from female individuals. It still needs to be investigated whether in hearts isolated from male mice the same pattern would be observed. Nonetheless, comparing our RT-qPCR together with WB we noticed that to a huge content, at the protein level the glycolysis-regulating enzymes' content remained unmodified following delivery compared to E18.5, meaning that the observed cell cycle reduction in CMs (Chapters 3.1.1. and 3.1.2.) would not be as a consequence of energy switch immediately after birth.

3.3.2. Examining a potential role of oxidative DNA damage in early postnatal cardiomyocyte cell cycle arrest

In contrast to the prenatal mouse life span, in the oxygen-rich postnatal environment more than 95% of ATP is produced by glucose and fatty acid oxidation in mitochondria (Doenst *et al*., 2013). As a consequence of fatty acid oxidation higher amounts of ATP are generated which is essential for the elevated postnatal mechanical and contractile demands of the heart. However, as a by-product of the mitochondrial respiratory chain, ROS is generated which leads to oxidative DNA, lipid and protein damage in cells. Indeed, modifications such as ROS inhibition has been linked to elevate the postnatal proliferation window of CMs in mice, revealing the impact of ROS on CM cell cycle arrest (Puente *et al*., 2014). Accordingly, it is yet to be uncovered, whether the immediate birth-related cell cycle arrest observed in our pHH3 and Ki67 IF experiments (Chapters 3.1.1. and 3.1.2.) would be due to oxidative DNA damage. Additionally, in order to counteract the harmful effects of ROS, cells have developed defence mechanisms such as various antioxidant enzymes to maintain redox homeostasis (Tsutsui *et al*., 2009). Consequently, observing changes in antioxidant enzyme expression levels in the perinatal heart, can indirectly give hints about potential connections between postnatal oxidative stress and the immediate cardiomyocyte cell cycle arrest.

3.3.3. Steady levels of DNA damage in cardiomyocytes of perinatal male mice

Following an oxidative damage, proteins, nucleic acids, DNA, or lipids, are harmed. Accordingly, as a consequence of oxidized base, single- or even double-strand breaks the cell cycle withdrawal is induced (Puente *et al.*, 2014). One of the most common DNA damages induced by ROS, is oxidation of guanine base. Consequently, the guanine is conversed to 8′-Oxo-7,8-dihydroguanine (Kanvah *et al.*, 2010). Thus, to examine a possible birth-related increase in DNA damage leading to the cell cycle exist (Chapters 3.1.1. and 3.1.2.) in mouse cardiac myocytes, an oxidative DNA modification was quantified using IF antibody staining against 8′-Oxo-7,8-dihydroguanine (8-Oxo-G). Moreover, in order to study DNA damage specifically in CM nuclei they were stained using an antibody against MEF2A/C. Consequently, in LV, IVS, and RV of male mouse heart sections, the 8-Oxo-G signal intensities in MEF2A/C positive nuclei were quantified and the results were related to the fetal E18.5 mean value. Finally, the changes of 8-Oxo-G signals in CM nuclei at stage E18.5, NB18.5 and NB18.5+1 were presented (Figure 18).

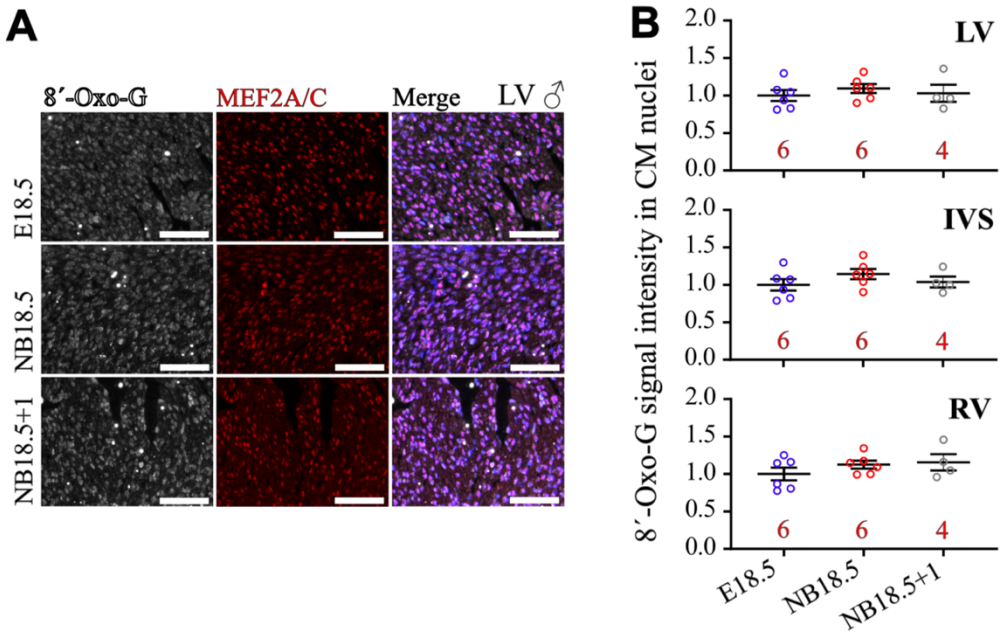

Figure 18. Unaltered oxidative DNA damage within the immediate postnatal period in CM nuclei of male mice in LV, IVS, and RV. The oxidative damage of DNA in CMs was quantified via IF antibody staining on male mouse paraffin sections at E18.5, NB18.5, and NB18.5+1. **A)** Representative IF staining images in the LV myocardium of male mice at three perinatal stages. The 8-Oxo-G was stained in white, CM nuclei in red (by MEF2A/C), and nuclei in blue (DAPI). The scale bar demonstrated in white had a length of 50 µm. **B)** Quantifications of 8-Oxo-G signal intensity in CM nuclei showed no significant variations in the degree of cardiac myocyte DNA damage during a period immediately after birth in all three ventricular parts of male mice. The numbers represented in red reveal the sample sizes. RV: Right ventricle, LV: Left ventricle, IVS: Interventricular septum. The findings are illustrated as the mean values ± SEM. Among the studied groups, the statistical significance was assessed by one-way ANOVA.

Comparing fetal CMs (E18.5) with postnatal CMs directly (NB18.5) and one day after birth (NB18.5+1) revealed that no significant changes in the intensity of 8′-Oxo-G nuclear signals (in CM nuclei) were observed at LV, IVS, and RV of male mouse hearts (Figure 18B). In conclusion, it can be mentioned that the immediate birth-relevant cell cycle withdrawal in CM nuclei cannot be as a result of an oxidative damage to DNA.

3.3.4. Unaltered protein expression of antioxidant enzymes and proteins immediately after birth in female mouse hearts

To scavenge reactive oxygen species generated along the mitochondrial respiratory chain (such as superoxide anions and hydroxyl radicals) and protect the cell from oxidative damage, a variety of antioxidant enzymes and proteins are available (Lei *et al.*, 2016; Puente *et al.*, 2014). Based on the study performed by Puente and colleagues, to investigate the endogenous antioxidant response during the early postnatal stages from P1 to P7, it is suggested to investigate the levels of various antioxidant enzymes. Assuming that the oxidative stress would act as the main inducer of the birth-dependant cell cycle arrest observed in CMs (Chapters 3.1.1. and 3.1.2.), an increase in the level of antioxidant enzymes in a birth-dependent pattern would be expected.

Here, using antibodies against antioxidant enzymes and proteins such as superoxide dismutase 2 (SOD2), and thioredoxin 2 (TRX2), the cellular response to variations in oxidative stress during the perinatal period in mouse hearts was indirectly assessed. Moreover, a family of antioxidant and redox signalling proteins peroxiredoxins (PRDX) can be named. Upon prolonged exposure to oxidative stress, the PRDX proteins are hyperoxidized and thereby form PRDX-SO_3 (Schröder *et al*., 2008). Therefore, postnatal acceleration in PRDX-SO_3 level indicates the increased oxidative stress. Indeed, comparing protein levels of antioxidative proteins as well as PRDX-SO_3 immediately after birth compared to fetal stages at E18.5, we observed no statistically significant alterations in their level around birth in female mouse hearts (Figure 19). Due to limited heart samples isolated from male mice, we did not investigate these factors in male mouse hearts, which needs to be analysed in future. However, taken together, based on our 8-Oxo-G IF findings, together with SOD2, TRX2, and PRDX-SO_3 WB outcomes, the birth-

relevant cell cycle exit in CM nuclei cannot be as a consequence of the oxidative stress immediately after birth.

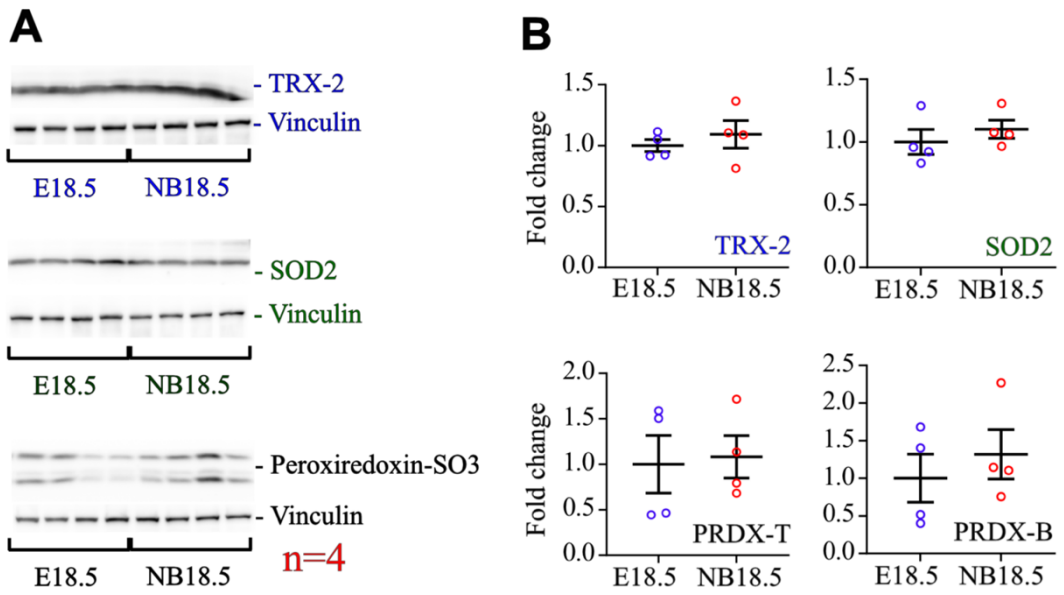

Figure 19. Unchanged levels of antioxidative enzymes shortly after birth in ventricular myocardium of female mice. The oxidative damage was indirectly assessed via WB experiments against antioxidative enzymes and the level of hyper-oxidation on female mouse hearts at E18.5 and NB18.5. **A)** WB membranes at two demonstrated perinatal stages are illustrated. The housekeeper was vinculin. The used housekeeper for each screen was highlighted with the same colour codes. **B)** Quantification of a fold change of antioxidative proteins and PRDX-SO_3 levels in hearts at E18.5 and NB18.5, showed no significant variations in the level of the investigated factors immediately after birth compared to before delivery. The red number represents the sample size. The graphs for each membrane were demonstrated in an identical colour code. In PRDX-SO3 graphs, the T stands for the top band, whereas the B stands for bottom band. The results reveal the mean values ± SEM. Statistical significance among groups was conducted by unpaired 2-tailed student *t*-test using SPSS.

3.4. Investigation of possible alterations in the availability of cytokines and growth factors following an exposure to an extrauterine environment in mouse hearts

According to our IF findings we unveiled for the first time that shortly after a separation from an intrauterine surrounding the cell cycle activity in CM nuclei declines remarkably in both male and female ventricular myocardium (Chapter 3.1.2.). In order to elucidate the mechanism underlying the birth-associated declined proliferation rate, we investigated the potential DNA damage in CM nuclei. However, via our IF and WB experiments we excluded any oxidative DNA modifications within the very early postnatal life period, therefore unlikely to cause the early phase of CM cell cycle arrest even though it is certainly relevant at later stages. However, our WB, RT-qPCR and IF

outcomes concerning cell cycle regulators and pathways' activities together with the previous studies, highlight the potential involvement of cytokines and growth factors in the early-postnatal cell cycle regulation. In this context, we hypothesised that the changes in supplementation of cytokines and growth factors to the heart after birth could be involved in the immediate postanal cell cycle arrest of CMs and non-myocytes shown above (see Chapters 3.1.1., 3.1.2., and 3.1.3.).

3.4.1. Birth-related variations in RNA expression of cytokines and growth factors in mouse and human hearts via *in silico* analyses

Initially, prior to any experimental analysis using hearts isolated from mice, to confirm altered growth factor and cytokine expression following birth, an *in silico* screening was performed. A study performed by Cardoso-Moreira and the team serves as a useful tool to monitor the genome wide developmental RNA expression profile (reachable under: https://apps.kaessmannlab.org/evodevoapp/). Accordingly, developmental gene expression profiles can be plotted in seven organs including brain, cerebellum, heart, kidney, liver, ovary, and testis in several mammalian species such as human, mouse, rat and rabbit. RNA expression patterns of 161 cytokines and growth factors derived from a "Mouse Genome Informatics" database with the Gene Ontology ID: 0008083, demonstrating a cell growth and proliferation function, were investigated in perinatal mouse hearts at E18.5 and P0, as well as human hearts at 19 weeks post-conception (19 WPC) and at birth. According to the factor expression levels at birth, the factors were scored as increased, unchanged, and decreased. Finally, the proportion of factors either increased, decreased or unchanged following birth was calculated as percentage. Our *in silico* screening results indicated that among 161 studied growth factors and cytokines, 68% revealed an alteration in their transcriptome profile after birth compared to E18.5. Whereas 34% of analysed genes demonstrated an elevated expression following birth, 34% of genes exhibited a lower expression rate after birth in the mouse hearts. Nonetheless, 32% of the cytokine and growth factor genes revealed no alteration in their expression pattern at birth compared to E18.5. In humans, 69% of the investigated factors revealed an alteration in their expression pattern at birth. Specifically, 28% of the genes demonstrated an elevation in their transcriptome level, while the expression pattern of 41% exhibited a reduction after delivery compared to 19 WPC. Taken together, via our *in*

silico screening we indicated that both in human and mouse hearts, the expression pattern of over 60% out of 161 studied cytokines and growth factors revealed a modification following birth.

3.4.2. Altered availability of 11 cytokines and growth factors immediately after compared to shortly before birth in male mouse hearts

In this part of the study, based on our hypothesis as well as our *in silico* data, our objective was to investigate the protein levels of 129 cytokines and growth factors in the mouse heart immediately after birth compared to fetal stage E18.5. Therefore, we performed proteomics analyses utilizing two antibody-array screening kits for cytokines (111) and growth factors (30), separately. To assess the potential effect of the extrauterine environment on growth factors and cytokine availability, tissue lysates were prepared from whole male mouse hearts at stage E18.5 and NB18.5. Depending on the kit 4 to 8 membranes are provided (4 membranes for the cytokine kit and 8 membranes for the growth factor kit). On each membrane pairs of antibodies against various cytokines and growth factors, as well as negative and positive controls, are spotted. Per each membrane one sample consisting of the lysate from one whole heart with specific total protein concentration was prepared. Following application of the sample on the membrane, the proteins of interest are captured by the membrane-bound antibodies on defined spots. In followings, the bound proteins are labelled by biotinylated antibodies. Finally, using streptavidin-HRP and a chemiluminescent detection system, the density of the pulled-down proteins in the protein lysate is determined (Chapter 2.2.5.2., Figure 20).

Unlike the *in silico* screening outcomes, where 68% of the analysed growth factors and cytokines demonstrated birth-related altered RNA expression pattern (Chapter 3.4.1.), our antibody-array screening results showed that protein levels of 21% of factors were either increased or decreased immediately after birth at NB18.5 compared to E18.5. The cytokine-array used in this study, was designed to capture 111 cytokines and growth factors originating from mice. Our array screening revealed that the availability of 10 factors was increased significantly following birth compared to E18.5. In addition, 15 factors showed a significant reduction in their protein level in male mouse hearts at NB18.5 vs. E18.5 (Supplementary Table 1). The growth factor array had a capacity for

detecting 30 growth factors, among which 12 factors were also included in the cytokine-array. Consequently, out of 30 analysed growth factors only two including Insulin-like growth factor-1 (IGF-1) and Platelet-derived growth factor AA (PDGFAA) revealed a noticeable reduction in their availability shortly after birth compared to E18.5. In this instance, the postnatal (NB18.5) IGF-1 level was reduced to 0.5 (fold change) and PDGFAA to 0.67 of the values observed in E18.5 male murine hearts (Figure 20B). Both kits shared 11 antibody pairs against identical growth factors and cytokines including, Amphiregulin, EGF, G-CSF, GM-CSF, HGF, IGFBP3, IGFBP6, IL-2, IL-7, M-CSF, and PDGFBB. Notably, except for IGFBP6, all the remaining factor in both kits revealed identical patterns in their levels at NB18.5 vs. E18.5. Specifically, the level of all ten factors remained intact following birth in male mouse hearts compared to E18.5 stage, revealing the sensitivity and reproductivity of both kits.

To avoid false positive results during statistical analyses by using multiple pairwise comparisons on the cytokine array data (111 cytokines and growth factors), a false discovery rate (FDR) was calculated. Here, for each cytokine a q-value was generated, as described in the materials and methods (Chapter 2.2.9.).

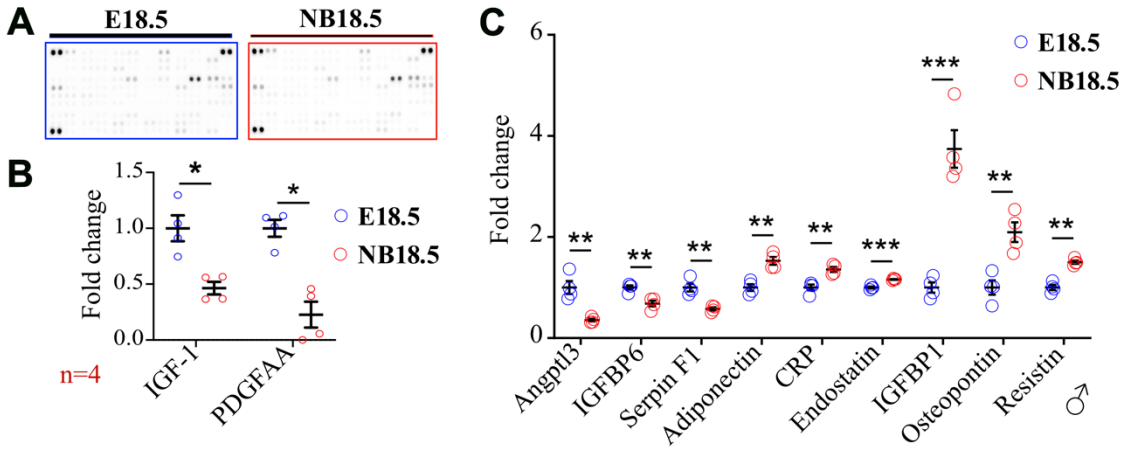

Figure 20. Significant alterations in protein levels of 11 cytokines and growth factors immediately after birth in hearts obtained from male mice. The proteomics analyses were carried out using male mouse whole heart lysate at E18.5 vs. NB18.5, applied on antibody-arrays thereby detecting a total of 129 growth factors and cytokines. **A)** An illustration of antibody-array membranes at stage E18.5 and NB18.5 (cytokine-array). On each membrane pairs of antibodies against each growth factor and cytokine were printed on specific spots. The growth factors and cytokines are specifically pulled-down via spotted antibodies at specific places. Later on, the attached proteins are biotinylated and using streptavidin-HRP and chemiluminescent detection, the signals related to each factor are detected and analysed. The duplicate dots represent the signals related to each analysed growth factor. The signal intensity correlates with the protein amount within the tissue lysate. **B)** and **C)** Fold changes of growth factors and cytokines in the heart shortly after birth (red dots) in comparison to E18.5. The sample size for each stage was four, which is demonstrated in red. The results reveal the mean values ± SEM. Using SPSS, the statistical significance among groups was determined by unpaired 2-tailed student *t*-test. *: $P<0.05$, **: $P<0.01$, ***.

The factors with q-values lower than 0.05 were considered as statistically significant and used for further analyses. Following FDR, out of the initial 25 factors altered after birth, 9 revealed significant changes in NB18.5 male hearts compared to E18.5 (Figure 20C). Accordingly, shortly after birth in mouse hearts, the protein level of Angiopoietin-like 3 (Angptl3) was decreased to 0.35, Insulin-like growth factor-binding protein 6 (IGFBP6) to 0.68, and Serpin F1 to 0.58 (fold change) of their values observed in E18.5 hearts. In contrast, the protein level of Adiponectin was elevated to 1.53, C-Reactive Protein (CRP) to 1.36, Endostatin to 1.16, Insulin-like growth factor-binding protein 1 (IGFBP1) to 3.74, Osteopontin to 2.09, and Resistin to 1.50 after birth in NB18.5 hearts isolated from male mice compared to stage E18.5 (Figure 20C). Collectively, via antibody-array screening we revealed that at protein level the availabilities of eleven cytokines and growth factors such as Adiponectin, Angptl3, CRP, Endostatin, IGF-1, IGFBP1, IGFBP6, Osteopontin, PDGFAA, Serpin-F1, and Resisitin, were modified remarkably in male mouse hearts shortly after birth compared to the E18.5 stage.

3.4.3. Validation of antibody-array findings via Enzyme-linked Immunosorbent Assay (ELISA) experiments

Using antibody-array screenings together with FDR analyses we identified 9 cytokines and 2 additional growth factors that exhibited a noticeable variation in their levels in mouse hearts following a brief separation from an intrauterine environment. In parallel, we have already revealed that shortly after birth the activity of cell cycle in CMs, together with the level of cell cycle regulators, and the activity of MAPK-Kinase, AKT, and S6 signalling pathways in murine ventricular myocardium were reduced significantly. Indeed, except for Serpin F1, all the other growth factors and cytokines were reported to be either involved in either positive or negative regulations of MAPK-kinase, AKT, and mTOR pathways, cell cycle regulator (i.e., Cyclin D1) expression, cardiac cell populations' proliferation, or angiogenesis. Interestingly, their mode of involvement (i.e., positive or negative) in the regulation of pathways or proliferation, correlates with their availabilities assessed via our array screenings (Chapter 3.4.2.). For instance, via antibody-array screening we reported that IGF-1 level in mouse hearts were reduced to 0.6-fold compared to E18.5 (Chapter 3.4.2.). It has been mentioned that in mouse hearts at P2, exogenous thyroid hormone treatment led to increased levels of IGF-1. Moreover,

following an interaction between IGF-1 with the receptor IGF-1R, the Erk1/2 phosphorylation (T202/Y204) is promoted, leading to stimulation of CM proliferation (Bogush *et al*., 2020). Taken together, concurrent with the previous studies, it seems that the availability of the identified cytokines and growth factors following delivery would influence the CM cell cycle activity. Accordingly, our initial objective was to verify our array screening outcomes using sensitive Enzyme-linked Immunosorbent Assay (ELISA) experiments. Moreover, cytokines and growth factors are not necessarily expressed in CMs (hearts). Nonetheless, different cell types express various cytokines and growth factors. The expressed factors can be transported to the heart through the blood circulation. For example, as an essential organ in which the IGF-1 is synthesized, liver can be mentioned. The expressed IGF-1 is later transported to the target organs, thereby influencing the growth of the organs. Additionally, some growth factors and cytokines are synthesized in placenta and via the blood circulations the fetus is supplemented with the factors. Therefore, our next aim was to investigate the origin of the identified cytokine and growth factors. In this context, we investigated the levels of cytokines and growth factors in heart, serum, and liver samples obtained from mice at E18.5 and NB18.5, together with the serum samples isolated from pregnant and nonpregnant, as well as E18.5 and NB18.5 mice.

3.4.3.1. ELISA validation of Adiponectin, Angptl3, IGF-1, IGFBP1, IGFBP6, and PDGFAA protein levels in perinatal male mouse hearts

Previously, using the antibody-array screenings for mouse growth factors, we found that two factors, including IGF-1 and PDGFAA, showed a birth-related decline in their availabilities in male mouse hearts. Accordingly, in order to validate the array data with an independent method, we performed a set of sensitive ELISA experiments using heart samples at E18.5 and NB18.5. Moreover, in order to monitor whether the cytokine and growth factor levels within the perinatal stages (E18.5 and NB18.5) would be regulated in hearts, or regulated in other organs and thereby the heart supplementation with the factors would be influenced, another ELISA experiments were conducted using liver and serum samples obtained from mice at E18.5 and NB18.5.

Evaluating ELISA results, we noticed that shortly after birth, the level of IGF-1 was significantly reduced in heart, liver and serum samples compared to E18.5. Here, the IGF-

1 level in NB18.5 hearts was reduced to 0.6, in serum to 0.7, and in livers to 0.7 (fold change) in comparison with their level at stage E18.5 in male mice (Figure 21B). Interestingly, via our independent-antibody-array screening, we noticed that the IGF-1 level was also declined by almost 0.5-fold directly after birth compared to E18.5 (Figure 20B). After delivery, ELISA validation using male mouse heart lysates revealed a significant reduction of 0.8-fold in the PDGFAA levels compared to the fetal stage. However, in contrast to heart samples, in serum of male mice no significant changes in the availability of PDGFAA were observed directly after birth in relation to E18.5 (Figure 21A). Notably, due to pre-experimental ELISA analyses using PDGFAA ELISA kit, we had limited free ELISA wells. Therefore, we did not assess the PDGFAA levels in liver samples, which needs to be addressed in future studies.

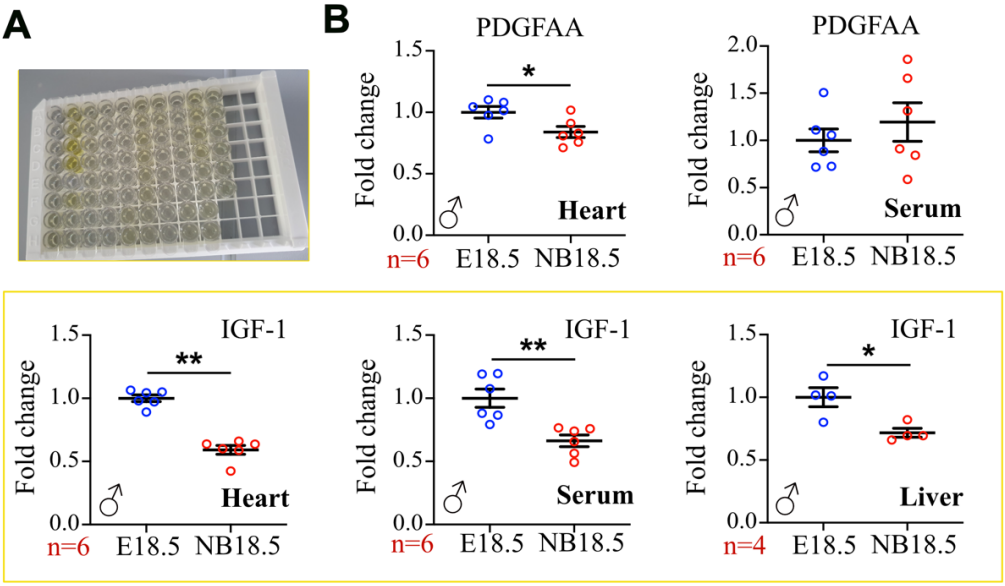

Figure 21. Noticeable reduction in the availability of IGF-1 and PDGFAA immediately after birth in heart samples isolated from male mice using ELISA. The ELISA experiments were carried out using heart and liver lysates, as well as serum samples isolated from male individuals at E18.5 vs. NB18.5. **A)** An illustration of a complete ELISA set for IGF-1 detection composed of duplicates of standards, NC, and heart, serum and liver samples at two mentioned stages. The colour intensity correlates with the epitope concentration within the applied protein pool samples. Graphs represented in yellow show protein levels of IGF-1 after birth (NB18.5) compared to E18.5 in male mouse hearts, serum and livers, which revealed a significant reduction in IGF-1 level in a birth-dependant fashion. **B)** ELISA detection of PDGFAA in NB18.5 vs. E18.5 heart and serum samples showed a birth-related decline in PDGFAA levels only in the mouse hearts. In contrast, the PDGFAA level in serum showed no variations after compared to before birth. The numbers shown in red represent the sample size. The results are illustrated as mean values ± SEM. Statistical significance among groups was assessed by unpaired 2-tailed student *t*-test using SPSS. *: $P<0.05$, **: $P<0.01$.

Collectively, using ELISA experiments, we confirmed our antibody-array screening outcomes concerning IGF-1 and PDGFAA using perinatal mouse hearts. Moreover, comparing E18.5 and NB18.5 stages, we noticed that in agreement with the heart outcomes, the IGF-1 level in serum and liver samples was decreased remarkably

immediately after birth compared to E18.5. With this regard, one reason for this birth-relevant reduced cardiac level of IGF-1 would be the declined IGF-1 synthesis in liver following birth, and thereby decreased IGF-1 heart supplementation. Another reason would be that immediately after a separation of an intrauterine surrounding, the placental IGF-1 supplementation of fetus would be removed, leading to reduced levels of IGF-1 in hearts and livers. Notably, comparing the serum and heart ELISA findings against PDGFAA, we noticed that only in heart samples the birth influenced negatively the PDGFAA levels. In this context, this can be speculated that the organ in which PDGFAA is synthesized, as well as the PDGFAA target organ would be heart.

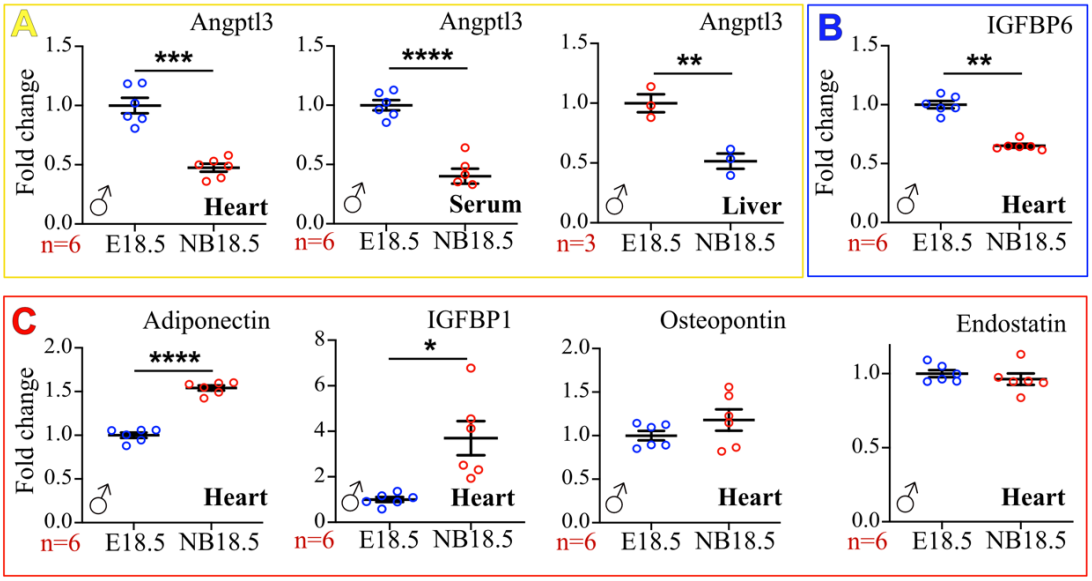

Figure 22. Immediate changes in protein levels of Angptl3, IGFBP6, Adiponectin, and IGFBP1 shortly after birth in male mouse hearts. ELISA experiments were performed using heart and liver lysates, as well as serum samples obtained from male mice at E18.5 and NB18.5. **A)** Shortly after delivery (i.e., at NB18.5) the availability of Angptl3 exhibited significant reduction in heart, serum, and liver samples of male mice compared to the fetal stage E18.5. **B)** At NB18.5, the level of IGFBP6 in heart lysates of male mice was decreased in comparison with shortly before delivery. **C)** ELISA analyses conveyed that Adiponectin and IGFBP1 protein levels exhibited significant reductions in hearts obtained from male mice at NB18.5 compared to the fetal stage E18.5. However, Osteopontin and Endostatin demonstrated no changes in their levels around birth in male mouse heart samples. The numbers shown in red represent the number of mice. The results are represented as the mean values ± SEM. To perform statistical analyses SPSS software was utilized and the statistical significance among groups was measured by unpaired 2-tailed student *t*-test. *: $P<0.05$, **: $P<0.01$, ****: $P<0.0001$.

In order to validate the results of our cytokine antibody-array screening using male mouse hearts, we performed ELISA experiments for Angptl3, IGFBP6, Adiponectin, IGFBP1, Osteopontin, and Endostatin (Figure 22). Similar to the array data, the Angptl3 ELISA analyses revealed a significant decline in postnatal levels (i.e., NB18.5) of Angptl3 compared to E18.5 in all samples. In detail, shortly after an exposure to the extrauterine environment, the Angptl3 level in male mouse hearts was reduced to 0.47-fold compared

to before birth at E18.5. Moreover, compared to the E18.5 samples, at NB18.5 the Angptl3 levels in serum were significantly reduced to 0.4 and in livers to 0.5 (fold change) (Figure 22A). Using ELISA for IGFBP6, we observed noticeable reductions of IGFBP6 levels in NB18.5 heart (0.65-fold) and serum (0.4-fold) samples compared to shortly before birth (i.e., E18.5) (Figure 22B, and Supplementary Figure 4A). However, the IGFBP6 level in male mouse liver samples followed no birth-related changes when comparing NB18.5 and E18.5 stages (Supplementary Figure 4).

Having conducted the antibody-array screening, we also performed ELISA validation for cytokines with significantly increased levels in the heart after birth (Figure 22). Therefore, we validated the availability of Adiponectin, IGFBP1, Osteopontin, and Endostatin at stage E18.5 and NB18.5 in heart, liver and serum. Indeed, comparing the levels of Adiponectin and IGFBP1 in male mouse heart, serum and liver samples at NB18.5 vs. E18.5 using ELISA analyses, we noticed significant elevations in their postnatal levels in all three studied sample types (Figure 22C, and Supplementary Figure 4C and 4D). Hence, after a short-term exposure to an extrauterine surrounding the availability of Adiponectin in male mouse samples was increased by a factor of 1.5 in heart lysates, 3.1-fold in serum, and factor of 3.3 in liver samples, compared to shortly before birth (Figure 22C, and Supplementary Figure 4C). Moreover, shortly after birth (at NB18.5) the IGFBP1 levels were significantly increased compared to E18.5, reaching 3.7 (fold change) in hearts, 5.1 in serum, and 3.3 in livers of male mice (Figure 22C, and Supplementary Figure 4D). Our antibody-array screening results using heart lysates from male mice concluded significant elevations in protein amounts of Endostatin and Osteopontin by the factors of 1.2 and 2.1, respectively, in the heart after birth (Figure 20). Nonetheless, no significant changes in their levels were observed in NB18.5 vs E18.5 male murine hearts using ELISA experiments (Figure 22C). Furthermore, our ELISA findings showed that in the serum of male mice at NB18.5 Endostatin levels declined after birth to 0.67 compared to E18.5 (Supplementary Figure 4B). Additionally, similar to ELISA results in the heart, in the liver no changes in Endostatin level were detected at NB18.5 compared to E18.5 (Supplementary Figure 4B). In contrast to Endostatin, Osteopontin availability in serum and liver were increased significantly following birth, such that the postnatal Osteopontin levels were increased to 1.39 (fold change) in serum and 1.75 in livers compared to the E18.5 stage (Supplementary Figure 4E). In conclusion, following ELISA validation with the exception of Endostatin and Osteopontin, we were able to validate the proteomics data for all tested cytokines and growth factors derived

from the antibody array screen in male mouse hearts. Moreover, in general we concluded that the perinatal availability of the factors in hearts, serum, and livers samples followed the identical pattern.

3.4.3.2. Similar changes in perinatal serum levels of Angptl3, IGF-1, and IGFBP6 in females compared to males

Previously we noticed that 11 cytokines and growth factors revealed identical availability pattern in the heart, serum, and liver samples obtained from male mice at NB18.5 vs. E18.5. Accordingly, we arose up with two hypotheses:

1. The organ supplementation with the factors would be modified after birth compared to before birth; which could be as a secondary consequence of the loss of placental influence.
2. The expression pattern of the identified growth factors and cytokines within the organ would be modified following delivery.

It is still elusive, how the levels of the identified factors in heart, serum, and liver samples isolated from female mice would be regulated following birth. Assuming that the placental supplementation of hearts would be essential in the availability of growth factors and cytokines after birth (either placental factor inhibition or placental factor synthesis), the level of factors in serum sample isolated from the female perinatal mice would have identical pattern, as what observed in male mice. Therefore, our next objective was to investigate how the cytokine and growth factor levels in serum isolated from female E18.5 and NB18.5 would be. Notably, we investigated the factors that revealed a decline in their level following birth. Consistent with findings in males, in females at NB18.5 there was a significant drop in serum levels of Angptl3, IGF-1, and IGFBP6 compared to E18.5. Specifically, Angptl3 level was reduced to 0.6, IGF-1 level decreased to 0.65, and IGFBP6 level dropped to 0.4 of their concentrations at E18.5 in ELISA experiments (Figure 23A). However, in contrast to males (Figure 21B), the PDGFAA level at NB18.5 was significantly elevated to 1.4 of its level observed at E18.5 in females (Figure 23A).

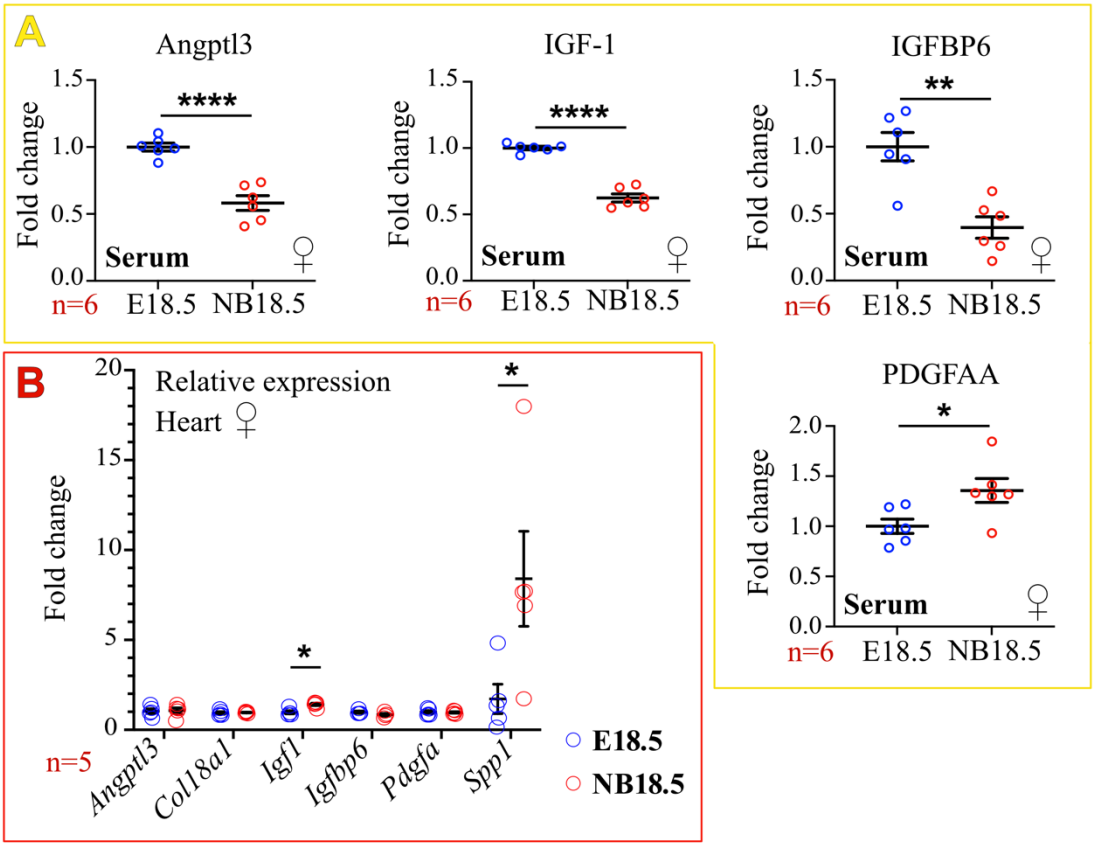

Figure 23. Birth-dependent changes in protein levels of Angptl3, IGF-1, IGFBP6, and PDGFAA in female mouse serum samples. ELISA and RT-qPCR analyses were performed using serum or heart samples, respectively, isolated from female mice at E18.5 and NB18.5. **A)** ELISA analyses showed that levels of Angptl3, IGF-1, and IGFBP6 in serum obtained from female mice were significantly reduced directly after birth compared to the fetal stage, while the PDGFAA availability was elevated immediately after delivery in the female mouse serum. **B)** RT-qPCR analyses using RNA from female mouse hearts are represented. Following birth, the expression of *Igf1* and *Spp1* (coding for Osteopontin) in hearts of female mice was significantly increased compared to the fetal stage E18.5, whereas the expression pattern of the remaining investigated factors was unchanged following birth. The numbers shown in red represent the number of studied mice. The results are illustrated as mean values ± SEM. Statistical significance among groups was assessed by unpaired 2-tailed student *t*-test using SPSS. *: $P<0.05$, **: $P<0.01$, ****: $P<0.0001$.

Moreover, in order to study the expression patterns of growth factors and cytokines at RNA level in mouse hearts, we designed primers for all selected 10 cytokines and growth factors. However, due to limited RNA samples isolated form female mouse hearts, as well as technical issues concerning the primer optimization step, it was not possible to conduct RT-qPCR experiment using primer pairs against all cytokines and growth factors. Furthermore, due to lack of heart samples from male mice, the RT-qPCR was not carried out using male mouse hearts; which has to be performed in future. Unlike proteomics results from male mouse hearts using antibody arrays and ELISA analyses, at the RNA level the expression of *Angptl3*, *Col18a1* (encoding Endostatin), *Igfbp6*, and *Pdgfa* remained constant around birth in female mouse hearts (Figure 23B). Nonetheless, immediately after an exposure to the extrauterine environment the *Igf1* and *Spp1*

(encoding Osteopontin) RNA expression was significantly increased in female mouse hearts compared to the fetal stage. In particular, at NB18.5 the *Igf1* RNA level was elevated to 1.4 and *Spp1* to 8.0 (with huge variability) of their levels observed at E18.5 (Figure 23B). Notably, due to post-transcriptional modifications, any conclusions based on RT-qPCR experiments without proteomic analyses would not be logical. Nonetheless, collectively our RT-qPCR and ELISA findings using the serum samples (male and female) of perinatal mice, it is very probable that the placental supplementation of heart would be as main factor in the modifications in the factor level, since the level of the studied factors (Angptl3, IGF-1, and IGFBP6) in serum of both sexes were identified. Additionally, in female mouse hearts, the RNA levels of these factors were almost intact following birth, which would emphasize on the ectopic supplementation of heart with the factors.

3.4.3.3. Comparison of selected growth factors and cytokines in the serum of pregnant versus non-pregnant female as well as perinatal mice

After conducting ELISA validation on heart, liver and serum samples obtained from perinatal mice, we largely confirmed the antibody-array screening results obtained from heart samples of male mice. In general, among the studied growth factors and cytokines almost all followed a similar pattern in their postnatal levels in all three sample types (i.e., heart, serum, and liver), when comparing NB18.5 to E18.5. Consequently, based on our ELISA findings on male and female animals and the RT-qPCR outcomes using female heart samples, we hypothesized that the serum availability acts as an essential parameter in the factors' supplementation to peripheral organs including the heart. Therefore, we next aimed to address the question whether mice are provided with the growth factors and cytokines identified in this study through the blood circulation of their mothers within the fetal life span. With this regard, we specifically focused on the factors that exhibited a noticeable decline in their levels after birth in the heart compared to shortly before delivery. Therefore, we performed a set of ELISA experiments comparing the levels of Angptl3, IGF-1, IGFBP6, and PDGFAA in serum samples obtained from pregnant (pregnancy days including 13, 14, and 18), and non-pregnant adult females, and perinatal male and female mice.

Our ELISA investigations concluded that the serum levels of all four analysed growth factors and cytokines followed a similar pattern between E18.5 and NB18.5 in male and female mice (Figure 23 and Figure 24). It is noteworthy that the serum findings

concerning female fetal and neonatal mice represented in this chapter, are the same data discussed in the previous chapter (3.4.3.2.). In the serum samples isolated from pregnant and non-pregnant adult female mice, Angptl3 levels were noticeably lower than in fetal and neonatal mice (Figure 24A). Notably, at E18.5 the Angptl3 level in mouse serum demonstrated its highest value among the analysed samples, reaching three times higher levels than those observed in both pregnant and non-pregnant females. After delivery at NB18.5, the Angptl3 serum level declined significantly compared to E18.5. Nonetheless, its concentration was still 1.5-fold higher than that detected in serum samples obtained from pregnant and non-pregnant adult females (Figure 24A). Nevertheless, comparing pregnant with non-pregnant female mice, no significant changes in the Angptl3 level in serum was identified. In this regard, it could be possible that the fetus would be able to express and synthesize Angptl3 itself to achieve sufficient serum levels. Additionally, it is very probable that the heart would not necessarily be supplemented mainly by placental Angptl3 level.

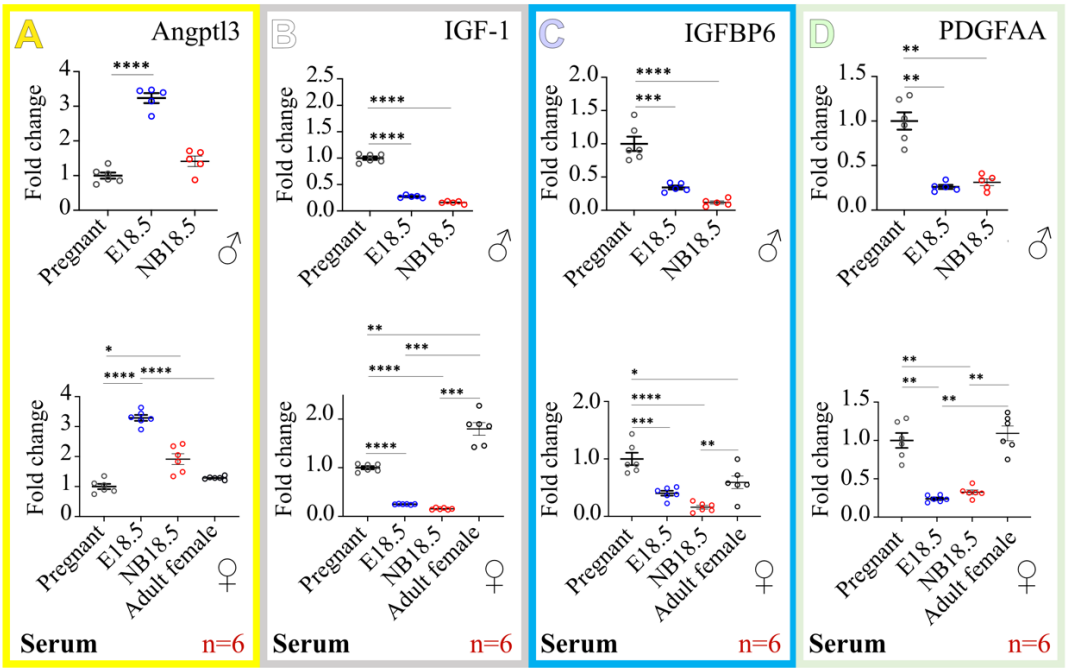

Figure 24. Serum levels of selected growth factors and cytokines in pregnant mice compared to non-pregnant females as well as fetal and neonatal mice. ELISA experiments were carried out using serum samples from pregnant females, E18.5 and NB18.5 mice (both sexes), and adult non-pregnant female mice. **A)** The graphs represent the ELISA data for Angptl3, **B)** IGF-1, **C)** IGFBP6, and **D)** PDGFAA detection. The row on top reveals the data corresponding to male perinatal mice, while the bottom row represents the findings related to the serum samples isolated from female perinatal mice. The graphs for each factor were illustrated with the identical colour code of the frame. For each growth factor and cytokine only one ELISA kit was used using male or female serum samples, as well as pregnant and non-pregnant adult female mice, The number illustrated in red is the sample size n for all female individuals. However, the n for male perinatal animals was 5. The results show the mean values ± SEM. Statistical significance among groups was conveyed by one-way ANOVA. *: P<0.05, **: P<0.01, ***: P<0.001, ****: P<0.0001.

Interestingly and in contrast to Angptl3, all other studied factors including IGF-1, IGFBP6, and PDGFAA exhibited noticeably higher levels (almost 2- to 5-fold) in the serum of pregnant and none-pregnant female mice when compared to fetal and neonatal mice. Comparing serum samples isolated from pregnant compared to both E18.5 and NB18.5 (male and female) mice, we noticed lower concentrations of IGF-1. Specifically, in E18.5 mice the IGF-1 level was reduced by the factor of 0.26 of what was observed in pregnant females. A further decline was observed in the IGF-1 levels in NB18.5 mouse serum samples to 0.15 in comparison to pregnant mice. However, the non-pregnant female mice exhibited 1.8-fold higher concentration of IGF-1 in their serum than pregnant females (Figure 24B). In conclusion, lower serum levels of IGF-1 in samples obtained from fetal and neonatal mice compared to adult (pregnant or non-pregnant) does not necessarily stand for the placental supplementation of hearts with IGF-1 at E18.5. As a consequence of a separation from an intrauterine environment, the IGF-1 level in serum of neonatal mice declined compared to o E18.5.

In case of IGFBP6, its level in the serum samples obtained from pregnant animals was almost 2.8 times higher than in fetal E18.5 mice (0.4-fold change in female, and 0.34-fold change in male E18.5 serum) (Figure 24C). As described before exposure to an extrauterine environment led to a further decrease in IGFBP6 levels, reaching 0.16-fold change in NB18.5 female and 0.12-fold change in NB18.5 male animals compared to pregnant females. Later in life, the concentrations of IGFBP6 revealed a significant elevation in the serum of adult female animals (from 0.16- to 0.6-fold) compared to neonatal females. In addition, the level of IGFBP6 in the serum of pregnant mice is almost twice of that observed in adult non-pregnant females (Figure C). In conclusion, it can be pointed out that during pregnancy the IGFBP6 level increases in the serum of the mother (comparing pregnant and non-pregnant mice). Following a maternal supplementation and through the placenta, the fetal hearts are provided with IGFBP6. Finally, immediately after birth and upon the terminated placental supplementation, the IGFBP6 level in neonatal mice decreased, and the remaining IGFBP6 level was produced in the hearts or livers of the neonates.

PDGFAA concentrations in the serum samples of E18.5 female and male mice were much lower than the values observed in pregnant mice (Figure 24D). In this respect, PDGFAA level are reduced to 0.24-fold in E18.5 females and 0.26-fold in E18.5 males in comparison to its level detected in pregnant female mouse serum. Although shortly after birth the PDGFAA levels in the serum of male mice remained unchanged, in NB18.5

females PDGFAA concentrations were slightly elevated by a factor of 1.3 compared to E18.5 (with the $P<0.05$, not mentioned in the graph). Moreover, unlike IGF-1 and IGFBP6, the PDGFAA availability in the serum isolated from adult females were not influenced by pregnancy (Figure 24D). Consequently, according to our experiments, we cannot demonstrate the origin of the factors (i.e., PDGFAA).

Consequently, having evaluated the antibody-array screening data in combination with ELISA and RT-qPCR investigations, we noticed that expression and protein levels of certain cytokines and growth factors changed in serum and hearts in the immediate perinatal period. Additionally, assessing IGF-1, IGFBP6, and PDGFAA levels in serum samples obtained from pregnant females versus perinatal mice, we noticed higher concentrations of these factors in pregnant animals compared to fetal and neonatal serum samples. In this context, it is very probable that during the prenatal period, the embryo and foetus might be supplemented with maternally derived factors by exchange via the placenta. Notably, assuming that this maternal supplementation idea would make sense, we would expect that the levels of these factors in serum sample obtained from pregnant female mice would be higher than in non-pregnant individuals. Accordingly, we only observed the mentioned conditions in IGFBP6. Once again, in order to investigate the expression patterns of the growth factors such as Angptl3, IGF-1, IGFBP6, and PDGFAA following birth in mouse hearts we performed RT-qPCR analyses in female mouse hearts (Figure 23B). However due to limited number of heart samples isolated from male mice, we did not assess the expression patterns of the mentioned genes in fetal and neonatal male mouse hearts. In addition to our RT-qPCR results, we analysed the transcriptome levels of the Angptl3, IGF-1, IGFBP6, and PDGFAA proteins in mouse hearts (no gender related differentiation) at E18.5 and birth (P0) represented by Cardoso-Moreira and the team (reachable under: https://apps.kaessmannlab.org/evodevoapp/) (Figure 25). Accordingly, we searched for the Reads Per Kilobase per Million mapped reads (RPKM), corresponding to each sequenced transcript for each selected cytokine and growth factor in mouse hearts at E18.5 and P0 (represented by Cardoso-Moreira, *in silico* analyses). For each factor, the single RPKM data were normalized to the RPKM data corresponding the E18.5 mouse hearts, and thereby the data were represented as a fold change compared to the E18.5 (Figure 25). In agreement with our RT-qPCR outcomes using female hearts (Figure 23B), our *in silico* data revealed that the after birth the expression patterns of *Igfbp6* and *Pdgfa* remained unchanged in mouse hearts. Moreover, the *Igf1* expression level was significantly increased in mouse hearts after birth compared to E18.5 (RT-qPCR

and *in silico*; Figure 23B and 25). Notably, we did not note any statistically remarkable modifications in expression of *Angptl3* in female mouse hearts after birth compared to E18.5. Nonetheless, the *in silico* findings revealed a noticeable elevation in the *Angptl3* transcript level by the factor of 4.5-fold change after birth compared to E18.5 (Figure 25). Collectively, transcriptome analyses revealed that the mentioned factors were expressed in mouse hearts. Furthermore, following delivery the expressions of the *Angptl3*, *Igf1*, *Igfbp6*, and *Pdgfa* in mouse hearts were either enhanced or remained unchanged. However, at the protein levels, we noticed that the factors' levels were reduced remarkably briefly after a disconnection from the intrauterine environment in neonatal mouse hearts compared to the fetal mice. With these regards, it is very probable that in fetal life span, in addition to the maternal supplementation the factors are synthesized in mouse heart, liver or any other organs and thereby supplement the heart.

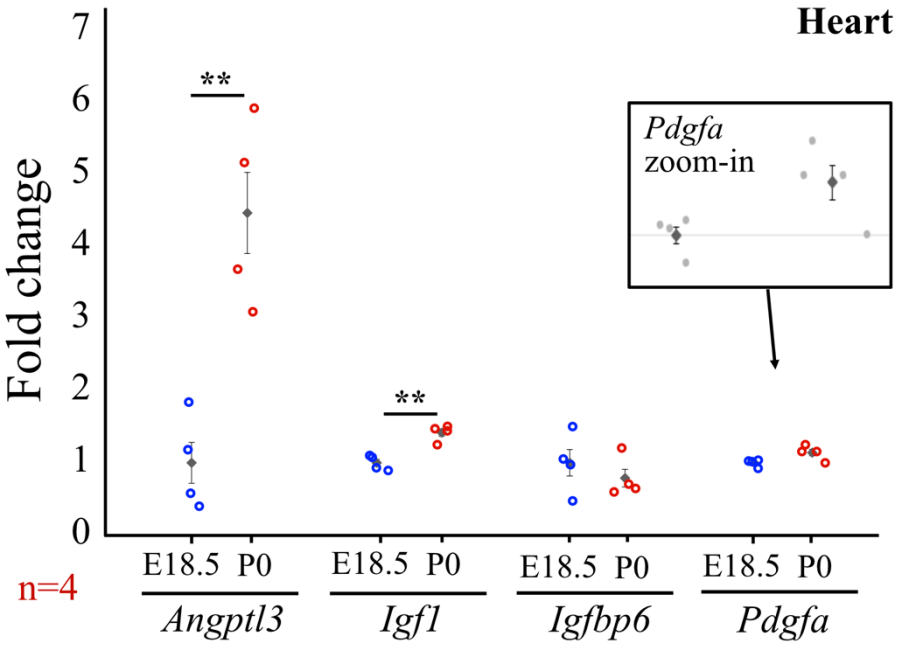

Figure 25. Expression levels of selected growth factors and cytokines in fetal and neonatal mouse hearts assessed by *in silico* analyses. *In silico* investigations based on the row transcription data consisting of RPKM (Reads Per Kilobase per Million) provided by Cardoso-Moreira and colleagues. The graph represents the fold change of the transcriptomes (RPKM) of the *Angptl3*, *Igf1*, *Igfbp6*, and *Pdgfa* in mouse hearts at E18.5 and P0 (birth). For each stage four RPKM values were represented. Each single data was normalized to the mean value of the E18.5, and thereby the data were represented as a fold change of E18.5. Following birth, the expression levels of *Angptl3* and *Igf1*were increased in mouse hearts, whereas the *Igfbp6* and *Pdgfa* transcriptome levels remained unchanged in mouse hearts at P0 compared to E18.5. The zoom-in represents the distribution of *Pdgfa* single data. The results show the mean values ± SEM. Statistical significance among groups was conveyed by one-way ANOVA. **: P<0.01.

3.5. Stimulation of cell cycle activity in neonatal mouse cardiac myocytes with selected growth factors and cytokines *in vitro*

As outlined in Chapter 3.1., within the first week after birth in mice the cell cycle activity in CMs declines in such a way that adult CMs are unable to proliferate. Using Ki67 and pHH3 IF experiments this study showed that immediately after a disconnection from an intrauterine environment, the cell cycle in cardiac cells including CMs was reduced compared to the fetal stage (Chapter 3.1.). Concomitant with the cell cycle arrest, growth signalling together with cell cycle regulators (i.e., type-D Cyclins) were reduced immediately after birth (Chapter 3.2.). With this respect, following our antibody array screen, we identified 11 growth factors with altered levels immediately after birth which are possible candidates to be involved in perinatal CM cell cycle regulation. Accordingly, for subsequent *in vitro* studies, we initially focused on those factors which exhibited a drop immediately after birth including Angptl3, IGF-1, IGFBP6, and PDGFAA. Accordingly, we attempted to induce cell cycle activity by incubating the selected factors on neonatal mouse primary CMs under *in vitro* conditions. Since IGF-1 has already been investigated, revealing that enhanced IGF-1 level in mouse hearts following a thyroid hormone treatment, promoted cell cycle activity in CMs (Bogush *et al*., 2020), we excluded it from *in vitro* experiments. A biding partner for Angptl3, is integrin receptors $\alpha_v\beta_3$ (using the GeneCards human gene data base, (reachable under: https://www.genecards.org/cgi-bin/carddisp.pl?gene=IGFBP6) (Camenisch *et al.*, 2002). It has been reported that the integrin receptors $\alpha_v\beta_3$ regulate the cardiac growth by regulating the activation of AKT, mTOR, and GSK-3ß in hearts (reviewed by Lal *et al.*, 2009). Moreover, in adult CMs the ectopic activity of integrins enhanced the mitosis incidence after a myocardium infarction (Chen *et al*., 2017; Kühn *et al*., 2007). In rat corneal assay also, Angptl3/integrin receptors $\alpha_v\beta_3$ interaction promoted the angiogenesis via MAPK and AKT activation (Camenisch *et al.*, 2002). Additionally, concomitant with our findings regarding the birth-relevant declined cell cycle activity in CM nuclei, our RT-qPCR findings on mouse hearts, as well as ELISA and antibody-array screening results demonstrate a significant reduction of Angptl3 levels in various samples immediately after birth. In human hearts the single cell data (reachable under: https://www.proteinatlas.org/ENSG00000197461-PDGFA/single+cell+type) revealed that the *PDGFA* is expressed in various cardiac cell populations. Moreover, following our RT-qPCR and the *in silico* analyses (Figure 23B and 25), it can be concluded the *Pdgfa*

is expressed in fetal and neonatal mouse hearts, as well. In humans, the PDGFAA treatment has stablished the proliferation in arterial smooth muscle cells through AKT, and p44/p42 activation (Li *et al*., 2011). Indeed, its levels in male mouse hearts at NB18.5 were remarkably decreased compared to its level observed in fetal male mouse hearts. Moreover, concurrent with the immediate birth-related cell cycle drop in CMs (Figure 12, 13, and 14), the activity of AKT and Erk1/2 in male hearts at NB18.5 were reduced in a birth-related manner when compared to fetal hearts. With these regards, we selected Angptl3 and PDGFAA for treatment of primary neonatal mouse CMs to investigate their potential to induce cell cycle activity. Notably, the IGFBP6, as well as the remaining cytokines and growth factors revealing an elevation in level in neonatal mouse hearts compared to E18.5, will be investigated in future.

3.5.3. The BrdU-incorporation incidence in primary CM nuclei was enhanced following a treatment with 100 ng/ml PDGFAA, whereas the 200 ng/ml Angptl3 did not influence the BrdU incorporation in CMs

In this study, we initially unveiled that briefly after delivery the cell cycle activity in murine cardiac cells including CM and non-myocytes nuclei reduced remarkably compared to fetal stages (E17.5 and E18.5). Moreover, following one day after birth compared to shortly after delivery, the cell cycle activity in CM nuclei decelerated further (Chapter 3.1.), highlighting the influence of a separation from an intrauterine surrounding on the cell cycle withdrawal. Concurrent with the birth-dependant cell cycle decline in CM nuclei, we unveiled that 11 cytokines and growth factors exhibited a variation in their availability at NB18.5 hearts compared to E18.5. In this context, our final objective was to accelerate the cell cycle rate in primary CMs by treating them with the selected factors that demonstrated a reduction in their level in mouse hearts briefly after birth (i.e., Angptl3 and PDGFAA).

Initially, we aimed at investigating the optimal concentrations of Angptl3 and PDGFAA for the treatment of primary CMs. In this context, we searched for the *in vitro* studies conducted not only on CMs but also on other cell types using the mentioned factors. The suggested doses of Angptl3 in various studies, were totally divers, ranging from 50 to 500 ng/ml, and 2.2 to 60 µg/ml (Camenisch *et al*., 2002; Dai *et al*., 2015). However, we

primarily selected the 100 and 200 ng/ml (based on the suggested 50-500 ng/ml range) concentrations of Angptl3 for our *in vitro* experiments.

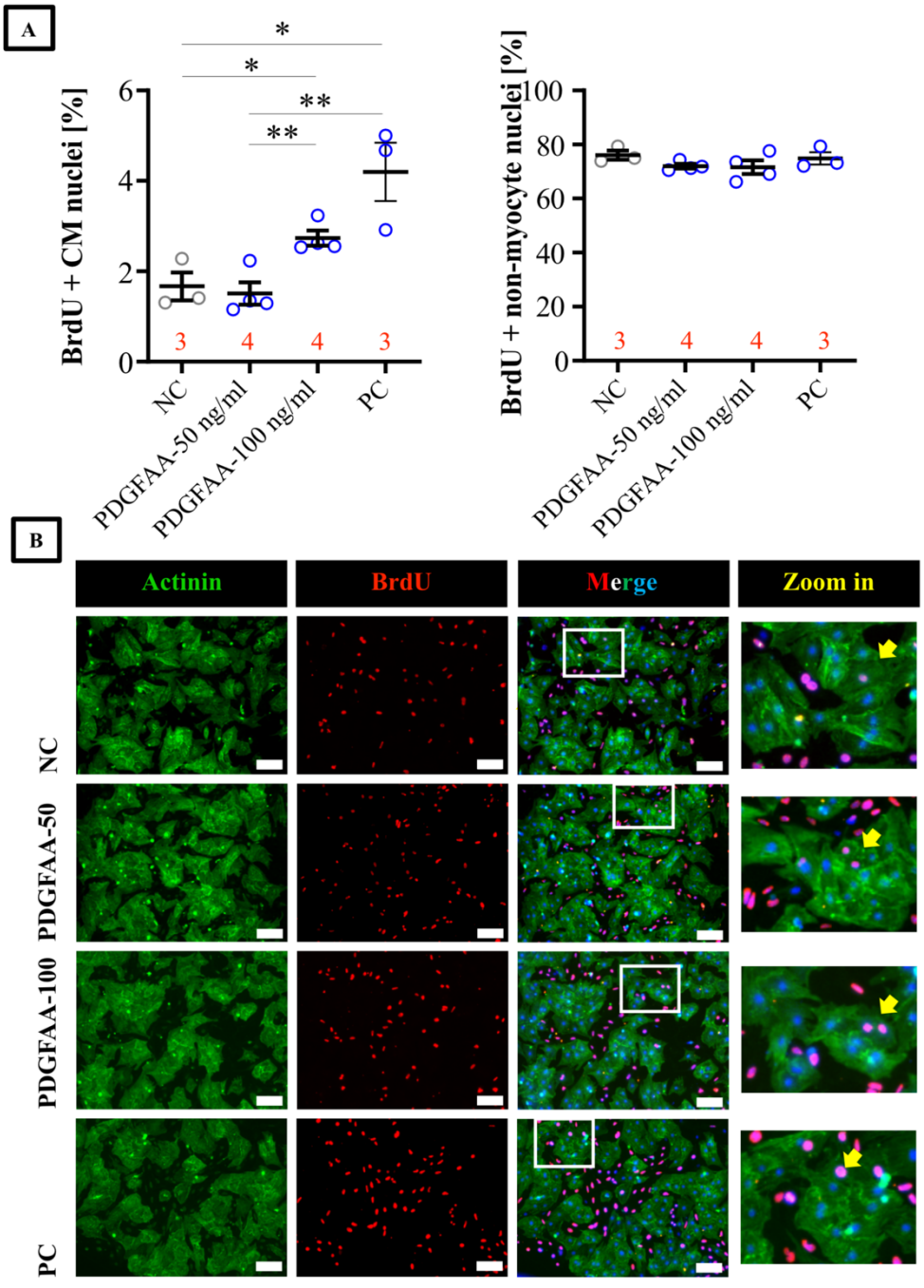

Figure 26. Increased incidence of BrdU incorporation in CM nuclei after a treatment of primary CMs with 100 ng/ml PDGFAA and 10% FCS. The BrdU rate in isolated CM and non-myocyte nuclei was measured via IF antibody staining against BrdU and Actinin. **A)** Graphs represent the proportion of CM (on left) and non-myocyte (on right) nuclei exhibiting a BrdU staining after treatment with either NC (10 mM acetic acid), 50 or 100 ng/ml PDGFAA, and PC (10% FCS). Red numbers in graphs represent the number of repeated experiments. Following treatments with 100 ng/ml PGDFAA and 10%FCS, the BrdU rate in CM nuclei enhanced remarkably compared to the treatment with NC and 50 ng/ml PDGFAA. NC: Negative control, PC: Positive control. Statistical significance among groups was conveyed by one-way ANOVA using SPSS. *: P<0.05, **: *P*<0.01. **B)** Illustration of comparable regions from wells corresponding the treatments. The nuclei are shown in blue (DAPI). The CMs were stained by Actinin and are represented in green. Moreover, the BrdU incorporation was stained in red. The yellow arrow highlights the CM nuclei exhibiting BrdU signals. The scale bar (demonstrated in white) is 100 µm. The white box in merge image, demonstrates the magnified region illustrated in zoom-in part.

The PDGFAA in return, was tested only in ng/ml concentrations. In a study performed on human valve endothelial cells, the consumed concentration of PDGFAA to induce phosphorylation of AKT was reported to be 50 ng/ml (Moore *et al*., 2021). With this regard, we assessed 50 and 100 ng/ml concentrations of PDGFAA.

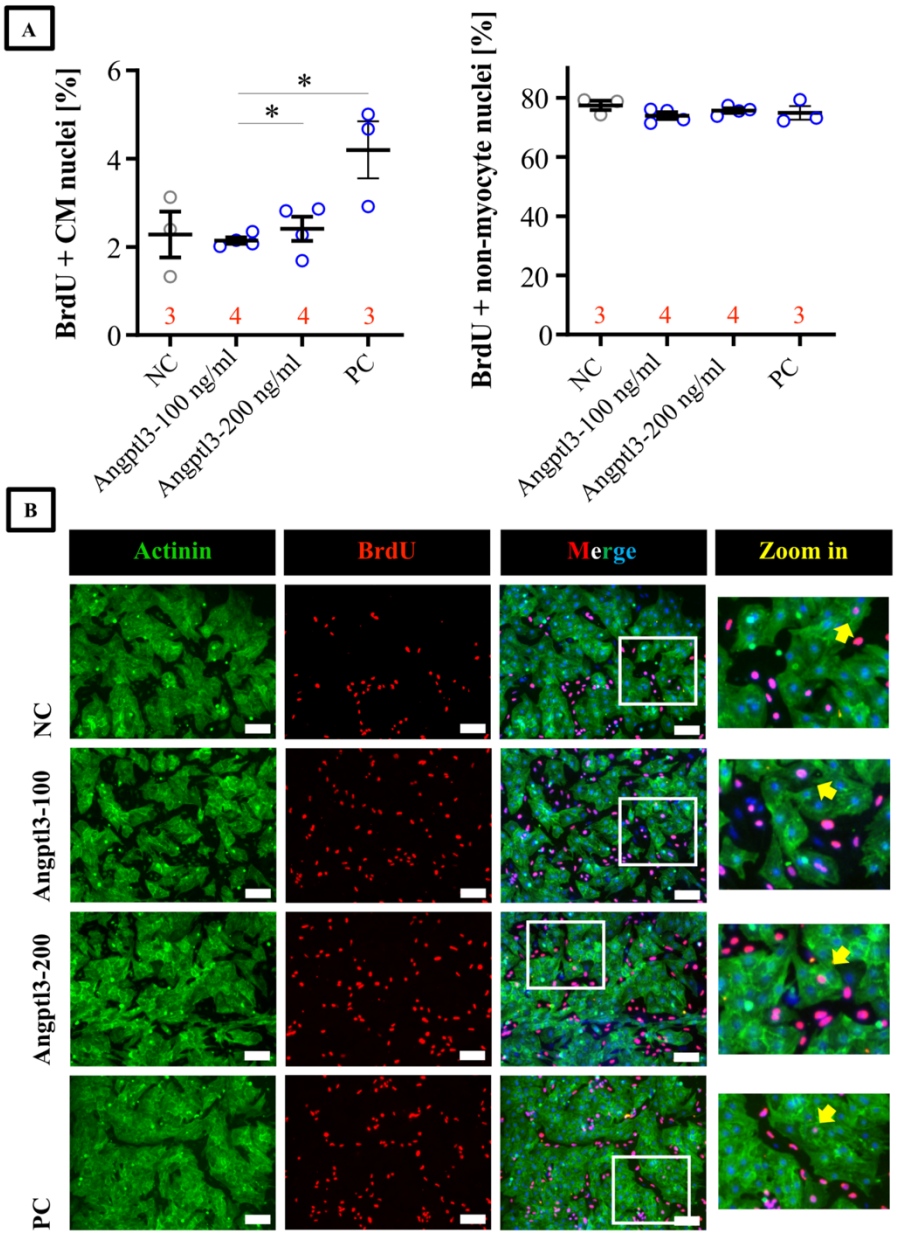

Figure 27. The rate of BrdU incorporation in CM nuclei was increased after a supplementation with 10% FCS. The BrdU rate in isolated CM and non-myocyte nuclei was measured via IF antibody staining against BrdU and Actinin. **A)** The graphs represent the proportion of CM nuclei (on left), and non-myocytes (on right) demonstrating an activity in S-phase after a treatment with either NC (PBS), 100 or 200 ng/ml Angptl3, and PC (10% FCS). Numbers in graphs (in red) represent the number of repeated experiments. 24h after a treatment with 10%FCS, the BrdU rate in CM nuclei enhanced remarkably compared to the treatment with NC, 100 ng/ml and 200 ng/ml Angptl3. NC: Negative control, PC: Positive control. Via one-way ANOVA using SPSS, the statistical significance among the groups, was determined. *: $P<0.05$. **B)** Illustration of comparable regions from wells belonging toeach treatment set-up. The nuclei are stained in blue (DAPI). The CMs were stained by Actinin and shown in green. Furthermore, the BrdU incorporation was stained in red. The yellow arrow points to the CM nuclei exhibiting BrdU signals. The white scale bar is 100 µm. The white box in merge image, represents the magnified region illustrated in zoom-in part.

Results

Accordingly, we isolated primary CMs from neonatal mouse hearts, and treated them for 24 h with the mentioned concentrations of two factors. Moreover, the factors were delivered as a lyophilized powder which were reconstituted in the solutions suggested by the manufacturers. Therefore, the negative control (NC) proportion of the primary CMs were treated with the medium containing only the reconstitution solution. Additionally, as a positive control, a group of cells was treated using a medium containing 10% fetal calf serum (FCS). 24 h after the incubation in the treatment medium, the IF antibody staining was carried out. Accordingly, the proportion of CMs and non-myocytes exhibiting an activity in S-phase of the cell cycle were represented as the rate of BrdU and Actinin double-stained nuclei (for CMs), as well as the rate of single BrdU-stained nuclei (non-myocytes) (Figure 26). Via IF antibody staining, we observed that 1.7% of the total primary CM nuclei exhibited a BrdU incorporation following 24 h of the treatment with the medium containing reconstitution solvent (10 mM acetic acid), in NC group. Moreover, 24 h after the incubation with the medium containing 50 ng/ml PDGFAA, the proportion of BrdU stained CM nuclei did not change noticeably compared to the NC. Accordingly, 1.5% of the entire investigated CM nuclei exhibited the BrdU signals. Interestingly, increased treatment dosage of PDGFAA to 100 ng/ml, enhanced the rate of BrdU-positive CM nuclei significantly to 2.7%, compared to NC, and 50 ng/ml PDGFAA groups. Moreover, following a treatment in 10% FCS, the rate of S-phase active CM nuclei increased remarkably to 4.2%, compared to NC and 50 ng/ml PDGFAA groups (Figure 26A). The nonmyocytes in return exhibited no treatment-related modifications in their S-phase activity. With this respect, the proportion of non-myocyte nuclei stained for the BrdU was 75.7% in NC, 72% in 50 ng/ml PDGFAA, 71.6% in 100 ng/ml PDGFAA, and 73.6% in PC (10% FCS) groups (Figure 26A). Consequently, due to our IF staining on primary CMs, we noticed that 100 ng/ml PDGFAA enhanced the S-phase activity rate in CM nuclei. However, to reach the value observed following a 10% FCS treatment, a higher concentration of PDGFAA such as 200 ng/ml would be suggested.

Since the delivered Angptl3 was suggested to be dissolved in phosphate-buffered saline (PBS) (the cell culture grade). Therefore, the NC cellular populations were treated with the treatment medium containing PBS. Notably, since the treatments of neonatal CMs with PDGFAA and Angptl3, were performed simultaneously, therefore, only one PC group (n equal to 4) for both treatment sets, was studied. Our IF findings revealed that 2.5% of the total CMs nuclei revealed a S-phase activity following 24 h of incubation in medium supplemented with PBS, in the NC group. Moreover, following treatments with

100 or 200 ng/ml Angptl3 no statistically significant variations were observed in the rate of CM nuclei exhibiting BrdU staining, compared to the NC group. Briefly, the proportion of CM nuclei stained for incorporated BrdU was 2.1% in 100 ng/ml Angptl3 treatment set, and 2.4% in 200 ng/ml Angptl3 group. Furthermore, the rate of CM nuclei with a S-phase activity was enhanced to 4.2% after 24 of incubation of the cells in the treatment medium containing 10% FCS, compared to the other studied groups. Notably, no statistically significant changes in BrdU incorporation rate in CM nuclei treated in both control groups such as NC and PC were noted (Figure 27A). Similar to PDGFAA treatment sets, the Angptl3 treatment, and its corresponding NC (PBS containing medium) and PC (10% FCS), did not influence the rate of S-phase active non-myocytes. Accordingly, the proportion of non-myocytes exhibiting a staining for the incorporated BrdU was 77.8% in NC (PBS), 74% in 100 ng/ml Angptl3, 75.6% in 200 ng/ml Angptl3, and 73.6% in PC (10% FCS) groups (Figure 27A). Consequently, following IF staining experiments on primary CMs isolated form neonatal mouse hearts, we noticed no modifications in BrdU incorporation rate in CM and non-myocytes following treatments with 100 ng/ml or 200 ng/ml Angptl3.

3.5.4. An incubation of cultured primary mouse CMs with 200 ng/ml Angptl3 significantly enhanced the P70S6K1 and S6 activity and Cyclin D2 level

Via our BrdU-incorporation analyses, we revealed that an incubation of cultured primary CMs isolated form neonatal mice, did not influence the cell cycle activity in both CMs and nonmyocytes (Figure 27). However, in order to monitor the influence of the Angptl3 on CMs at molecular level, we performed WB analyses using mouse primary CMs. Therefore, the CMs were treated for 24 h with PBS (corresponding NC), or 200 ng/ml Angptl3, or 10% FCS (PC), and finally the cell lysates were used for WB experiments. In this respect, we assessed the influence of Angptl3 on the activity of mTORC1, AKT, and MAPK-Kinase, as well as the level of Cyclin D2 in cultured primary CMs. It is essential to mention that due to the technical issues, we were not successful visualizing and thereby detecting the total protein bands. In this respect, we normalized the intensity of the phosphorylated forms to the Vinculin intensity. Single results were normalized to

the mean value of the NC and data were represented as the fold change of NC (Figure 28).

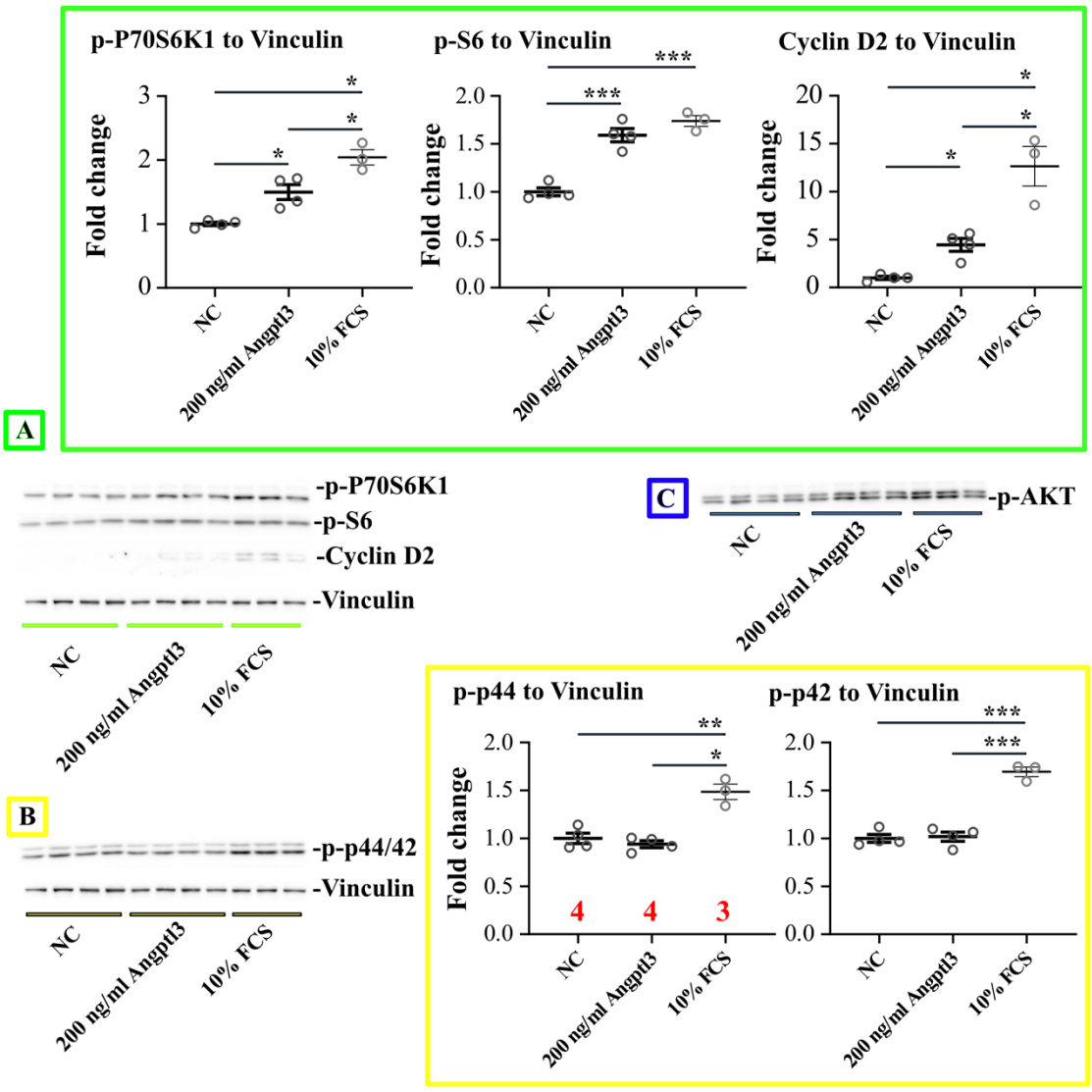

Figure 28. The P70S6K1, S6, and AKT activity and Cyclin D2 was enhanced primary CMs following a supplementation with 200 ng/ml Angptl3. The activity of AKT, mTORC1 (S6 and P70S6K1) and MAPK-kinase (p44/42) was monitored by measuring the phosphorylation and Vinculin (housekeeper) intensity using WB experiments. **A), B)**, and **C)** WB using whole protein extracts obtained from cultured primary mouse neonatal CMs following 24-hours of incubation with either PBC (NC), or 200 ng/ml Angptl3, or 10% FCS (PC). **A)** The phosphorylated form of S6 (at serine 235 and 236), P70S6K1 (at threonine 389), and Cyclin D2 with Vinculin levels were represented (labelled in green). **B)** The phosphorylated stated of p44/42 (at Thr202/204), and the related Vinculin level were demonstrated in yellow. **C)** AKT phosphorylation (at serine 473), and Vinculin (house keeper) levels were represented in blue. Each blot was demonstrated and the corresponding graphs, were demonstrated in identical colour codes. WB quantifications were carried out by normalizing the phosphorylated or total protein to the vinculin band intensity. The results were normalized to the NC data and were represented as fold change. Data exhibited a significant elevation in S6, P70S6K1, and AKT phosphorylation, as well as Cyclin D2 level as a consequence of a treatment of the primary CMs with 200 ng/ml Angptl3, and 10% FCS compared to NC (A and C). Notably, the Angptl3 treatment did not influenced the p44/42 activity, whereas the 10% FCS treatment accelerated the activity of p44/42 (B). The red numbers show the sample size. The results were illustrated as the mean values ± SEM. Statistical significance among groups was conveyed by one-way ANOVA. *: P<0.05, **: P<0.01, ***: P<0.001.

Results

Our WB data revealed that following a treatment of primary CMs with 200 ng/ml of Angptl3, the activity of P70S6K1 enhanced remarkably to 1.5-fold compared to what observed in NC (Figure 28A). Moreover, in PC the phosphorylated state of P70S6K1 was twice of that observed in NC. In addition, both Angptl3 and 10% FCS treatments significantly increased the S6 activity and the Cyclin D2 level in primary mouse CMs in comparison to the NC. Accordingly, S6 activity was significantly enhanced 1.6-fold and the Cyclin D2 level was noticeably increased 4.5-fold in CMs as a consequence of an incubation in Angptl3. Moreover, the S6 activity was 1.7-fold and the Cyclin D2 level was 12.6-fold greater in PC than in NC. It is essential to mention that since the p-AKT-corresponding band (the lower in Figure 28C) was too close to p-P70S6K1 band, we were not able to measure the intensity of the p-AKT. Nonetheless, only by considering the blot, it seems that both Angptl3 and 10%FCS treatments increased the p-AKT level in primary CMs. Additionally, our data revealed that although the Angptl3 incubation did not influence the p44/42 activity, an 10% FCS treatment enhanced the p44/42 phosphorylation degree to almost 1.5-fold compared to NC and 200 ng/ml Angptl3 (Figure 28B).

Consequently, our data revealed that following a treatment with 200 ng/ml Angptl3, the activity of mTORC1 (S6 and P70S6K1) and AKT, as well as level of Cyclin D2 in cultured primary CMs were increased significantly. However, the Angptl3 treatment did not show any impact on the activity of MAPK-kinase (p44/42). Collectively, these data suggest that the investigated Angptl3 doses might be too low to induce any cell cycle activity, however, at molecular levels this low dose promoted the activity of cardiac growth-regulating pathways.

4. Discussion

4.1. Preterm birth and the role of the extrauterine environment for cardiomyocyte proliferation in mammalian organisms

During the embryonic life period, cardiac growth is mainly regulated by cardiomyocyte (CM) proliferation. In the course of the early postnatal stage, following the gradual transition from hyperplastic to hypertrophic growth, the proliferation rate is continuously decelerated in mice (Chapter 1.1.4.1.; Hirai *et al*., 2016; Porrello *et al*., 2011; Soonpaa *et al*., 1996). Interestingly, ^{14}C dating and stereology analyses in human hearts provided evidences for a constant CM number from birth until the age of 80 years, as well as a continuous reduction of CM turnover throughout life (Bergmann *et al*., 2015), all together emphasizing the role of birth for the postnatal proliferation exit in CMs. The latter raises attention about the hearts of humans delivered preterm. Assuming that birth and exposure to an extrauterine environment might act as the main inducer of the postnatal cell cycle arrest in CMs, individuals delivered preterm might exhibit reduced CM numbers, and thereby impaired heart functions compared to humans born at term. The estimation of CM numbers in pre-mature delivered humans is almost impossible due to the limiting factors, such as ethical reasons as well as lack of materials. Notably, there is almost no complete set of materials from identical cardiac regions obtained from healthy term-born and preterm-delivered humans with no signs of complications or various congenital diseases. However, to investigate the impact of premature birth on factors like CM maturation, cardiac function and structure, multiple follow-up studies have been conducted on adult human hearts (Bensley *et al*., 2018; Carr *et al.*, 2017; Crump *et al*., 2019; Lewanddowski *et al*., 2013; Ueda *et al*., 2014).

Bensley *et al*. (2018) used hearts samples obtained at prenatal autopsies of 16 preterm infants (delivered 23 to 36 gestation weeks) to investigate the influence of preterm delivery on structure of myocardium and development of CMs in humans, who died after birth. The control group in return, was composed of tissue samples collected from 37 stillborn infants with identical gestational age (20 to 40 gestation weeks) to preterm-delivered infants. Via immunohistochemical staining for Ki67, they reported that in almost all preterm hearts, the proportion of cardiac cells exhibiting a Ki67 staining was reported to be lower than 0.5%. Notably, the cardiac proliferation rate at the identical gestational age was greater in control compared to preterm infants. For instance, while

the proportion of cardiac cells with a cell cycle activity at gestational week 27 was reported to be almost 2% in control group, in preterm hearts this rate was almost 0.4% (Bensley *et al*.,2018). Furthermore, the factors such as nucleation and polyploidy states of the CMs within the entire investigated stages was reported to be identical. Collectively, Bensley and team (2018) noted a reduced cell cycle activity in preterm-born human infants compared to the stillborn infants with similar gestational age. Notably, the major limitations concerning the control group, was that they analyzed post-mortem myocardium from stillborn infants which might influence the results. Nonetheless, the reduced cardiac cell proliferation rate observed in human premature-delivered cardiac tissue, would indirectly hint to possible reduced total numbers of CMs in preterm group (Bensley *et al*., 2018).

Lewanddowski *et al*. (2013), studied the influence of preterm delivery on left ventricular structure and function in humans. They noted that following a preterm birth, the left ventricular mass was enhanced in young adults delivered preterm in comparison to preterm-born adults. Furthermore, they observed a significant drop in systolic and diastolic cardiac function parameters as a consequence of preterm birth in young adults compared to the term-delivered group (Chapter 1.1.5.1.). In addition, Lewanddowski *et al*., Huckstep and team (2018), compared the cardiac function in preterm and term-delivered humans. Indeed, their findings revealed that following increased sport intensity the ejection fraction and the peak systolic longitudinal strain declined significantly in preterm groups compared to term individuals. Therefore, they concluded a preterm-delivery associated reduction in exercise capacity in human hearts (Chapter 1.1.5.1.).

In 2017 Carr *et al.*, investigated a correlation between a preterm delivery and increased incidence of heart failure in early adulthood. They reported a negative correlation between gestational age and the risks for heart failure. Specifically, while no risk of heart failure was noted in young adults delivered between 32 to 36 weeks, the incidence rate ratio in extremely preterm born group (<28 weeks) was 17.0, and in very preterm delivered humans (28 to 31 weeks) was 3.58 (Chapter 1.1.5.1.). In another study conducted by Crump *et al*. (2019), an association between premature delivery and a possible enhanced risk of ischemic heart disease in adult humans, was investigated. Indeed, their findings suggested a reverse correlation between gestational age and the relative risk of ischemic heart disease. Accordingly, compared to full-term birth, the preterm delivery (<37 weeks) was associated with 53% increased relative risks, whereas the relative risk of ischemic heart disease in the early-term birth (37-38 weeks) was 19% (Chapter 1.1.5.1.).

Discussion

Collectively, the findings of the Carr *et al.* (2017) and Crump *et al*. (2019), suggest an association between preterm delivery and increased risks of heart failure and ischemic heart disease later in adulthood.

As a leading cause of neonatal death globally in children (<5-year-old), 5% to 14% of all live births qualify as pre-term birth (<37 weeks of gestation) yearly (Blencowe *et al.*, 2013; Lee *et al*., 2013). Moreover, according to WHO (2023), in 2020 13.4 million infants were delivered premature, accounting for 10% of all born babies. In this context, a deep insight into the relationship between premature birth and the molecular mechanism regulating postnatal cardiomyocyte proliferation can be highly beneficial for individuals born preterm.

Unfortunately, ethical reasons limit studies of preterm delivery and its direct consequences for the human heart. Additionally, biobanks provide biopsies or cardiac tissue samples of individuals with multiple disorders which restrict any conclusions concerning the regulation of birth-related cell cycle activity in CMs. Moreover, the biobank samples include the autopsies of infants died as a result of premature delivery (Bensley *et al*., 2018). In addition, it is not possible to get access to cardiac biopsies from healthy infants with identical gestational age to the premature-delivered humans, limiting the control group. In this context, the access to the autopsies of stillborn infants is only possible, which might influence the study outcomes. Moreover, utilizing an appropriate animal model to assess the impact of preterm delivery on CM number is challenging as well. Various factors including gestational time, the intrauterine environment, litter size, precociality or atriciality at birth, and growth rates after delivery, might considerably influence postnatal cardiac growth and development (Velayutham *et al.*, 2019).

Moreover, in large mammalian organisms the understanding about the time point, at which the CM proliferation capacity is lost, is not well-established yet. In sheep, the cell cycle withdrawal seems to take place before delivery. For example, it has been demonstrated that in sheep prior to birth, the myocyte number was decreased (Jonker *et al*., 2015). In premature-born lambs (at 128 gestational day) the CM number, cross-sectional area and proliferation rate were reported to be unchanged in comparison to term-delivered lambs (150 gestational age) (Lê *et al*., 2020). According to the previous investigations conducted in sheep, the premature delivery was associated with unchanged CM total number in left ventricle and intraventricular septum, elevated deposition of collagen, reduced right ventricular wall thickness, and decreased peak systolic blood flow in the pulmonary artery comparted to term-born group (Bensley *et al*., 2010; Mrocki *et*

al., 2018) (Chapter 1.1.5.2.). Interestingly, due to the findings of Jonker and colleagues (2015), the binucleation in sheep CMs initiated at gestational age 95, and proceeds to increase continuously. Furthermore, at E125, 20% of entire CMs were reported to be binucleated. Paralleled by increased nucleation, the proliferation rate in CMs reported to be reduced in sheep. Briefly, the proportion of CMs active in cell cycle dropped from 8% at E95 in LV, to 2.5% at E135 in LV. Collectively, the sheep seem to be an appropriate model to study preterm delivery. However, to study the influence of premature-birth on CM cell cycle activity, it seems to be more appealing to investigate the infants at E95 (before the nucleation is developed). Notably, due to huge gestational age (95 to 150 gestational age), the animal housing condition (need more space than small mammals), animal size, sexual maturity (4 to 8 months), number of offspring per pregnancy (1 to 2), frequency of pregnancy (1 per year), it was not possible to study preterm conditions using sheep hearts in the short doctoral investigation period. In addition, using sheep to investigate the upstream factors influencing the birth-related cell cycle regulation in CMs, does not seem to be meaningful; since the CM maturation and cell cycle withdrawal initiates earlier than term.

It has been concluded that across species the timing and patterns of nucleation and ploidy are not identical (Velayutham *et al.*, 2019). In contrast to large mammals, in mice the developmental proliferation dynamics have been studied extensively. Due to the short sexual maturity (6-8 weeks), gestational duration (3 weeks), and large litter size (7 to 10 offspring), as well as well-established animal housing conditions and options for genetical manipulation, *Mus musculus* is widely used as model to study heart development and the pathogenesis of congenital heart disease (Finn, 1963; Velayutham *et al.*, 2019). However, studying preterm birth using mice is limited. The gestational time of mice lasts between 18 and 20 days (Murray *et al.*, 2010). Additionally, similar to other rodents, mice are altricial organism (Loctin *et al*., 1983; Velayutham *et al.*, 2019). Consequently, following cesarean section, a delivery before term birth in mice will reduce the offspring survival (Loctin *et al*., 1983; McCarthy *et al*., 2018). In this regard, our main objective was to study the influence of birth on postnatal cardiomyocyte cell cycle regulation in mouse hearts, rather than studying the impact of preterm delivery.

4.1.1. Shortly after exposure to an extrauterine environment cell cycle activity significantly declined in mouse hearts

Previously, studies conducted on mice have reported a significant reduction in the number of CMs in S-phase within the early postnatal life period. Briefly, from P1 to P14, the proportion of CMs with an activity in cell cycle was noted to be continuously reduced such that from P14 on almost no new CMs are generated (Alkass *et al*., 2015; Soonpaa *et al*., 1996). Remarkably, beginning from P1 the incidence of binucleation in murine CMs was enhanced gradually which led to the binucleation of 60-70% of mouse CMs at P14 (Alkass *et al*., 2015). Indeed, CMs exhibiting a proliferation capability are dominantly mononucleated and diploid (Windmueller *et al.*, 2020). Following an isolation and characterization of mononucleated and binucleated CMs at E18.5, P7 and adult mice, Windmueller *et al.* (2020) revealed that the genes essential for G1/S phase transition were turned off in binucleated CMs at P7 compared to E18.5 mono- and binucleated CMs as well as P7 mononucleated CMs. Notably, their outcomes suggested an E2F/Rb network as a central regulator of binucleation induction in P7 CMs. Collectively, their data suggested a correlation between nucleation state and declined cell cycle activity in CMs. In another study performed by Patterson and team (2017), it was concluded that concomitant with increased nucleation or ploidy during the first week after birth in mouse CMs, the Tnni3k protein was enhanced. Moreover, a transgenic mouse lacking Tnni3k revealed the accelerated EdU incorporation leading to CM proliferation. In addition, the *Tnni3k* knock-down accelerated the number of mononucleated diploid CMs. Taken together, these findings suggest the reverse correlation between nucleation and ploidy state and cell cycle activity.

Stereological analyses performed on mice, revealed that from P11 on, the total number of murine CMs, remained unchanged (2.6×10^6 cells) (Chapter 1.1.4.1.; Alkass *et al*., 2015). Moreover, in humans, from birth to the age of 80-year-old, the total number of CMs were reported to remain constant (i.e., approximately 3×10^9) (Bergmann *et al*., 2015). Collectively, the studies performed in mice and humans (Chapter 1.1.4.1. and 1.1.4.3.) highlighted the influence of delivery on proliferation arrest in CMs as well as total CM number. In this thesis our main objective was to elucidate the immediate impact of a separation from an intrauterine environment on the cell cycle activity in CMs. Therefore, an understanding about exact time point at which the cell cycle withdrawal in CMs initiates facilitates us to unveil the molecular mechanism underlying this arrest. In this

context, we initially investigated the dynamics of cell cycle activity at the precisely-defined perinatal stages starting from two final embryonic stages, birth and early postnatal age in mouse hearts. It is essential to mention that in the entire experimental analyses, we investigated the influence of animal sex in cell cycle activity and regulation. Moreover, to address the immediate influence of a separation from an intrauterine surrounding, we studied hearts from mice at fetal stage E18.5 (isolation by cesarean section) and neonatal stage NB18.5 (directly after birth), sharing identical gestational ages. However, only NB18.5 individuals were shortly exposed to the extrauterine surroundings. In this regard, comparing E18.5 and NB18.5 hearts, facilitates studying the immediate influence of birth on postnatal CM proliferation and cell cycle regulation. Moreover, in order to investigate whether the cell cycle arrest in CMs would be programmed and might be dependent on the gestational age of the animal rather than any environmental impacts, we compared the cell cycle activity in CMs at E17.5 and E18.5. Interestingly, comparing E17.5 and E18.5 stages, we observed no changes in the mitotic rates in CMs or non-myocytes (pHH3 staining, Chapter 3.1., Figures 7 to 10), as well as cell cycle activity in cardiac cells (Ki67 results, Chapter 3.1., Figure 6) of male mouse hearts. These data revealed that the cell cycle arrest in CMs did not initiate before birth. Notably, we observed a decline in cell cycle activity in cardiac cells (Ki67 staining), as well as a significant reduction in mitosis rates in CMs and non-myocytes (pHH3 staining) in LV, IVS and RV myocardium of male mice immediately after birth (i.e., E18.5 compared to NB18.5; Figure 7). The mitosis rate in CMs and non-myocytes exhibited a further noticeable decline following one additional day after birth (i.e., NB18.5 compared to NB18.5+1; Figure 7). It is essential to mention that in order to validate our IF data, we repeated the IF staining in male mouse hearts. Accordingly, with an exception for RV we observed the similar findings concerning the dynamics of perinatal mitosis activity in LV and IVS of the male mouse hearts. However, the percentage of CMs and non-myocytes exhibiting a mitosis activity in the RV of male mice declined initially only at NB18.5+1 compared to E18.5 and NB18.5. Interestingly, in contrast to male mice, in female murine hearts, the mitosis rate in CMs and non-myocytes revealed similar reduction dynamics in all three ventricular parts (LV, IVS, and RV). Notably, according to multiple reasons such as unreliable IF staining in RV as well as lower total cardiac cell numbers in the RV than the remaining ventricular parts, any small variations might lead to huge differences in percentage of cardiac cells showing an activity in cell cycle. In this context, it is very likely that there is no difference between the sexes concerning the prenatal cell cycle activity in CMs. Taken together, we unveiled

that immediately after an exposure to an extrauterine environment, the cell cycle activity in mouse CMs and non-myocytes reduced significantly compared to the fetal stage with the identical gestational age. In a study conducted by Hirai and colleagues (Hirai *et al.*, 2016), the dynamic of cell cycle activity in CMs during mouse development from E10.5 to E18.5, at birth (P0) and at postnatal days P1, P5, and P10 was assessed. Accordingly, they used a special transgenic mouse line. In these mice, under a CM-specific promoter the Cyclin A2 was expressed in a combination with green fluorescence protein (GFP). Accordingly, using an IF antibody staining for GFP, the Cyclin A2 exhibiting CMs will be detected and studied. Interestingly, in agreement to our pHH3 results, they noticed that compared to E18.5 the percentage of Cyclin A2 exhibiting CMs was reduced significantly in LV, IVS, and RV after birth. In brief, at P0 compared to E18.5 CM cell cycle activity dropped from 12.5% to 9% in LV, from 11% to 7% in IVS, and from 11% to 4.5% in RV. However, unlike in our study, the animal gender was not considered. Hence, a gender-related difference in cell cycle activity in RV myocardium following birth was not reported. In addition, it is not clear whether the gestational age at P0 would stand for birth on day 18.5,19.5, or 20.5, since natural birth can occur over a period of three gestational days in mice (Murray *et al.*, 2010). Moreover, in their study as well as previous studies the gestational age was only related to monitoring the vaginal plague. However, in our team we tightly controlled the gestational age, by only an overnight mating procedure (Chapter 2.2.1.). Yet, it is noteworthy that consistent with our pHH3 findings, Hirai and colleagues noticed a declined rate of CMs exhibiting a progression from G1 to M after birth. Indeed, comparing P1 with P0, they also observed a further decline at P1 (Hirai *et al.*, 2016).

In addition to determine cell cycle activity with Ki67 and pHH3, we performed IF experiments on perinatal heart sections using an antibody against Cyclin D3 which is involved in positive regulation of G1 to S transition. In order to identify CMs, we used an antibody against myocyte enhancer factor 2 (MEF2) which is a transcription factor expressed in CMs. It has been reported that MEF2 is also expressed in vascular smooth muscle cells. Nonetheless, in neonatal smooth muscle cells, the MEF2 level is relatively lower compared to CMs (Paddock *et al.*, 2021). Prior to experiments using MEF2, we conducted multiple IF test analyses and observed no staining for MEF2 in other cardiac cell types including endothelial cells, fibroblasts, and smooth muscle cells. This reveals the specificity of our MEF2 antibody in detection of CMs. Therefore, following double staining of MEF2 and Cyclin D3, we quantified the proportion of Cyclin D3 expressing

CMs and cardiac cells. We indeed observed a noticeable decline in Cyclin D3 signals in CM nuclei and cardiac cells in LV and RV regions of male and female mice immediately after delivery (Figure 15). Collectively, our Cyclin D3-IF outcomes revealed that briefly after birth, the rate of cardiac cells as well as CMs demonstrating a Cyclin D3 staining declined remarkably in male and female mouse hearts.

In summary, our data emphasize an immediate influence of the separation from the intrauterine surroundings on cardiomyocyte cell cycle withdrawal in murine hearts. Whether our results utilizing mouse hearts could be transferred to humans needs to be discussed. As previously mentioned, in sheep and humans as large mammalian organisms binucleation and polyploidy, respectively, take place in late gestation (Burrell et al., 2003; Jonker *et al.*, 2015; Mollova *et al*., 2013). Therefore, investigating a potential birth-associated cell cycle arrest in CMs using humans and sheep, might not be supportive. Moreover, the consequence of a termination of fetal development close to the term time might not have the identical outcomes on cardiomyocyte cell cycle activity compared to mice (Chapter 1.1.5.2.).

Respective to our IF data, we were next eager to identify the molecular mechanism underlying the rapid birth-related cell cycle arrest in murine cardiomyocytes. In general, multiple factors have been concluded to be involved in the regulation of proliferation in CMs including cell cycle regulators and signaling pathways, as well as energy metabolism (glycolysis vs. fatty acid oxidation) and oxygen availability (hypoxia vs. hyperoxia) (Chapter 1.1.4.1.).

4.1.2. Immediately after delivery the expression of Cyclin D1 and D3 decreased in the ventricular myocardium of male and female mice

To determine the molecular mechanism underlying the rapid cell-cycle arrest immediately after birth, we initially investigated the expression of cell cycle regulators and the activity of various signaling pathways associated with cardiac growth and proliferation in perinatal hearts of male and female mice.

The proliferation withdrawal in CMs is accompanied by increased levels of cell cycle inhibitors and a reduction in positive cell cycle regulators after birth. Briefly, while the negative cell cycle regulators such as $p21^{Cip1}$, $p27^{Kip1}$, and Retinoblastoma (RB) are upregulated, the cell cycle promoting factors including Cyclins, Cyclin-dependent

kinases, and E2F are downregulated in the mouse heart after birth (Ikenishi *et al*., 2012; Yuan *et al*., 2017). Indeed, in the study performed by Soonpaa and coworkers, WB analyses for diverse cell cycle regulators were performed using mouse hearts isolated from various developmental stages starting from E12.5 to adulthood. Their results show that expression of Cyclin D1 and D3, as well as phosphorylated RB (indicating Rb inactivation and therefore cell cycle progression) at neonatal stages (P1 to P10) were reduced compared to embryonic samples. However, CDK4 protein levels remained unchanged in neonatal P1 to P10 hearts compared to embryonic hearts (Soonpaa *et al.*, 1996). Notably, when interpreting the WB findings performed by Soonpaa and colleagues some uncertainties arise. In brief, the biological sample size in WB experiment, was not mentioned; however, considering the represented blots the samples size seemed to be equal to 1. Moreover, no housekeeping proteins or loading controls on the membrane were shown. In this context, any meaningful conclusions about the data concerning closely related or consecutive developmental stages might be limited, as the normalization to housekeeping or any total protein intensity is essential. In our study, to explore the rapid effect of the extrauterine environment on expression of cell cycle regulators in murine myocardium, we performed multiple WB experiments according to the following standards: the exact gestation of mice was determined, the sample size was set to 4 mice per stage and/or gender, the signal intensity of detected bands was measured and normalized to a housekeeper or loading control, the experiments were validated at least twice (technical replicate), and a potential influence of animal gender was considered. Notably, our WB findings demonstrated that the protein level of the analyzed cell cycle inhibitors p21 and p27, as well as the level of cyclin dependent kinases CDK4 and CDK6 irrespective of gender remained unchanged shortly after birth (i.e., NB18.5) compared to fetal stages (i.e., E18.5) (Figure 14). Interestingly, according to the WB analyses performed by Soonpaa *et al*. (1996) the CDK4 level remained unchanged between E18.5 and P1. However, unlike the study performed by Soonpaa and colleagues where a postnatal reduction in Cyclin D1 and Cyclin D3 expression was first noticeable at P7, we were able to show a statistically significant reduction immediately after birth in heart samples obtained from both genders (Figure 14). In addition to our WB findings, our IF staining for MEF2 and Cyclin D3, confirmed a birth-related reduction in Cyclin D3 level in cardiac cells. Additionally, in CMs the Cyclin D3 level was reduced immediately after a separation from an intrauterine surrounding (Figure 15). Paralleled by our IF and WB findings, via our RT-qPCR studies using female mouse hearts, we

observed at the RNA level the expression of *Ccnd1, Ccnd2*, and *Ccnd3* together with *Cdkn1a* (p21) was remarkably reduced in mouse hearts shortly after birth compared to E18.5. Nonetheless, at protein level only the Cyclin D1 and Cyclin D3 levels were decreased in a birth-dependent manner. These variations between RT-qPCR and WB outcomes could be as a consequence of post-transcriptional modification. In 1997, Soonpaa and colleagues investigating the influence of CM-specific overexpression of Cyclin D1 on myocardial development in mice, initially reported that in non-transgenic mouse hearts the Cyclin D1, Cyclin D3, CDK4, and PCNA demonstrated their highest levels in E15.5 hearts (WB analyses). Furthermore, at P1 the protein levels of these proteins were remarkably declined compared to E15.5 hearts. Indeed, the lowest protein levels were reported in adult mouse hearts. Moreover, the CM-specific overexpression of Cyclin D1, in addition to Cyclin D1 protein level, accelerated the CDK4, and PCNA protein levels in adult murine hearts. Additionally, DNA synthesis as well as, the number of CM nuclei and the ratio of heart weight to body weight in adult hearts were enhanced (Soonpaa *et al*., 1997). Collectively, their outcomes highlight the influence of Cyclin D1 overexpression in cell cycle progression together with a possible hypertrophy, ploidy and multinucleation in adult transgenic hearts. Furthermore, according to their results, the Cyclin D1 overexpression in CMs did not influence the Cyclin D3 level in mouse hearts in adulthood. In this context, it seems that the Cyclin tape-D functions promoting the DNA synthesis, might be independent from each other.

Remarkably, in contrast to the other D-type Cyclins, our WB findings unveiled an immediate change in the postnatal protein levels of Cyclin D2 in a gender-specific fashion. Although the Cyclin D2 level in male mouse hearts revealed a noticeable decline immediately after birth, in females this level was unchanged in the perinatal period (Figure 14). In a study conducted by Pasumarthi and coworkers (2005), CM-specific overexpression of *Ccnd2* (coding for Cyclin D2) was reported to induce a persisted cell cycle activity (DNA synthesis) and infarct regression in injured hearts of adult mice (Pasumarthi *et al.*, 2005). In human induced pluripotent stem cell (hiPSC) derived CMs, Cyclin D2 overexpression has been proven to trigger cell cycle progression and telomerase activity. As a result, there was a noticeable increase in the number of engrafted cells following transplantation in murine infarcts (Zhu * *et al.*, 2018). Comparing our pHH3 IF results and Cyclin D2 (WB) data in female mice with the mentioned studies, it can be speculated that in female individuals the unchanged Cyclin D2 level shortly after birth might be associated with an increase in polyploidy in CMs of females (compared to

males) but not complete proliferation including cell division. In a study performed by Busk *et al*. (2005), the viral overexpression of Cyclin D2 was induced in rat CMs under *in vitro* conditions. They revealed that the Cyclin D2 overexpression promoted DNA synthesis and CM proliferation. Furthermore, they noticed that the Cyclin D2 mechanism of action was as a consequence of activation of CDK4/6, phosphorylation of retina blastoma, and downregulation of P21 and P27. Accordingly, they concluded that the Cyclin D2 inhibited hypertrophy by downregulation of p27 (Busk *et al*., 2005). Notably, in our WB findings, we concluded no alteration in p21 and p27 level following birth (NB18.5 vs E18.5) in both male and female hearts, on one hand. On the other hand, the pHH3 rate in CMs of male and female mice was dropped noticeably after birth compared to E18.5. However, the Cyclin D2 level remained unchanged in female heart following birth. Collectively, this unchanged Cyclin D2 level in female hearts, does not seem to influence the proliferation rate in CMs of female mice. Importantly, the Cyclin tape-D activity has been concluded to be involved in left ventricular hypertrophy in rat hearts (Busk *et al*., 2002). Taken together, comparing the Soonpaa *et al*. (1997) findings (concerning independent function of Cyclin Type-Ds) and the knowledge of involvement of Cyclin type-D in hypertrophy promotion, would mean that the unchanged Cyclin D2 level (NB18.5 vs. E18.5) in female mouse hearts would lead to cardiac hypertrophy in female mouse hearts compared to male heats. In this context, it needs to be elucidated whether the unchanged Cyclin D2 level female hearts following birth, would promote CM hypertrophy or not.

It is essential to point out that in this study we mainly looked at D-type cyclins. However, there are many more cyclins and cell cycle regulators that are needed to be investigated. Therefore, an “omics-approach” or single cell RNA Seq using E18.5 and NB18.5 hearts might be helpful in the future to get an overview of changes in the perinatal cell cycle transcriptome

4.1.3. Activities of AKT/mTOR and MAP-kinase signaling were reduced in hearts of male but not female mice shortly after delivery

The cell cycle in CMs is orchestrated by a variety of signal transduction pathways including, among others, MAPK-kinase, PI3K/AKT, mTORC1, Wnt/ß-catenin, and Hippo/YAP (Witman *et al*., 2020; Chapter 1.1.4.1.2.). We aimed to investigate any

modifications in the activity of these pathways following birth. Usually, following an interaction between an extracellular signaling molecule (such as growth factors or cytokines) and a membrane integral receptor the signaling pathways get activated. This activity is associated with multiple consecutive phosphorylation steps of the intracellular pathway components. Finally, as a result of a nuclear localization of a pathway's member, the expression pattern of a set of genes is altered. Commonly, the activity of signaling pathways is determined by multiple experiments: WB analyses to determine the activity (phosphorylation state) of their components, RT-qPCR experiments to assess the RNA expression level of their target genes, and IF analyses to monitor the intensity or/and localization of the active form of their members in specific cell populations.

Following an activity of the insulin-like growth factor 1(IGF-1), the core signaling protein AKT is activated, which was concluded to enhance the heart size following CM proliferation (Reiss *et al*., 1996). As a target of AKT, glycogen synthase kinase 3β (GSK-3β) can be pointed out. AKT-induced GSK-3β deactivation, leads to the β-Catenin nuclear localization promoting the expression of genes essential for cell cycle progression. Collectively this leads to CM proliferation in mice during development (Xin *et al*., 2011). Another target for AKT activity is mechanistic target of rapamycin (mTORC1) signaling pathway. Sufficient availabilities of nutrients and growth factors activate mTOR signaling pathway. As a result, protein biosynthesis takes place which is essential for cell growth or proliferation (Ma and Blenis, 2009; Paltzer *et al*., 2023; Chapter 1.1.4.1.2.). Prenatal inhibition of mTORC1 in mice has been reported to cause a significant reduction in heart weight, in left ventricular dimension, and in cardiac output at birth. Additionally, prenatal mTORC1 inhibition reduces the number of CMs in adulthood compared to controls (Hennig *et al.*, 2017). In another investigation conveyed by Zhang *et al*. (2014), a muscle-specific mTOR knockout in mice was analyzed, in which the transgenic mice survived both fetal and perinatal development. However, they investigators observed that the transgenic mice exhibited the phenotypes such as severe postnatal growth retardation, cardio myopathy, and premature death. Interestingly, at cellular level the number of CMs in transgenic mice was lower than control group. Moreover, the mTOR knockout remarkably decreased the activity (phosphorylation degree) of S6 and AKT (Zhang *et al*., 2014). Collectively, these studies reveal the essential role of mTOR in CM function and heart development. In agreement with our IF findings concerning reduced rate of Ki67 and pHH3 immediately after birth (compared to E18.5) in mouse CMs and cardiac cells, unpublished WB experiments conducted by Drenckhahn and colleagues revealed that the

activities of all studied members of mTORC1 including p70S6K, S6, and 4EBP1, as well as AKT were declined significantly after birth (Figure 1.1.6.). Accordingly, these findings emphasize the impact of the postnatal environment on AKT and mTORC1 signaling pathways as well as CMs cell cycle activity. We further elucidated a possible correlation between birth and the activity of AKT in male and female perinatal hearts. As a result of a growth stimulus, the kinase AKT is activated, leading to regulation of multiple cellular functions including growth, proliferation, metabolism and survival (Liang and Slingerland, 2003). Multiple studies have shown a role for AKT in CM cell cycle regulation (e.g., G1/S transition), among which activation of Cyclin D1 and CDK2, inhibition of p27, and regulation of mTOR activity, as well as inhibition of GSK-3ß, can be pointed out (Liang and Slingerland, 2003). Studying the activity of mTORC1 and AKT in perinatal hearts, we noticed a remarkable drop in the phosphorylation of S6 and AKT (phosphorylation site Ser473) rapidly after birth in the hearts isolated from male mice. In contrast, our WB data in females demonstrated that the S6 and AKT activities were unchanged immediately after birth (Figures 12). Although the cell cycle in female CMs was decreased in briefly after birth in comparison to shortly after birth, the activity of AKT and S6 remained unchanged in mouse hearts. Whether this unchanged AKT and S6 activity in female hearts would lead to increased ploidy or hypertrophic growth needs to be addressed in future studies.

As another cardiac growth-mediating pathway, MAP-kinase activity was assessed. While p38 MAP-kinase acts mainly as a negative regulator of CM proliferation (Engel *et al*., 2005), the p42 and p44 MAP-kinases (Erk1/2) promote proliferation and growth (Carrasco *et al.*, 2014; Cohen, 1965; Ek *et al*., 1982; Kasuga *et al*., 1982). In murine myocardium, 70% of total p42/p44 amount devotes to p42 (Lips *et al*., 2004). CM-specific knock-out of p42 in adult mouse hearts has been proven not to affect heart development. Moreover, it has been concluded that p42 is essential for adaptive hypertrophic remodeling in the adult heart as a response to pathological conditions (Ulm *et al*., 2014). Deletion of p44 in mouse embryonic fibroblasts has proven to decelerate the proliferation rate (Voisin *et al*., 2010). It has been shown that the constitutive knockout of p42 is embryonic lethaldue to multiple disorders including craniofacial (lack of tongue and shortened maxilla) and cardiovascular (ventricular septal defects and persistent truncus arteriosus) malformations (Frémin *et al.*, 2015). However, over-expression of p44, in turn, has been reported to fully reverse the embryonic and placental mouse defects associated with complete absence of p42 (Frémin *et al.*, 2015). The studies performed by

Voisin *et al*. and Frémin *et al*. could indicate a specific role of p44 in the regulation of CM proliferation. In addition to the mentioned findings, due to a study performed by Strash *et al*. (2021), a lentiviral-induced constitutively active expression of Erbb2 in hiPSC-CMs and neonatal rat ventricular myocytes (NRVMs), was reported to promote the CM proliferation under *in vitro* conditions. However, this Erbb2-promoted CM proliferation was suppressed as a consequence of treatment of cells with Erk1/2 inhibitors. In this respect, they highlighted the essential role of Erbb2/Erk(1/2) activity in CM proliferation, acting as a potential mechanism for cardiac regeneration. In our study, using WB analyses we noticed that in hearts of male mice immediately after birth, the phosphorylation of p44 was noticeably reduced compared to the fetal stage E18.5. However, in hearts obtained from female mice, p44 and p42 activity followed no birth-related changes compared to fetal stage (E18.5). Moreover, since the Erk1/2 is predominantly reported to promote the CM hypertrophy in mammalian hearts. Therefore, it seemed that the unchanged Erk1/2 level following birth in female observed in our WB experiments, could lead to CM hypertrophy rather than unchanged CMs proliferation in females (Gilbert *et al*., 2021; Wang, 2007). Collectively, concomitant the reduced cell cycle activity briefly after birth, our WB data revealed that briefly after a separation from an intrauterine surrounding, the levels of cell cycle positive regulators (Cyclin type-D) as well as the activity of AKT, S6, and Erk signaling pathways in mouse hearts declined remarkably at NB18.5 in comparison to E18.5.

Conversely to p42/p44, the p38 mitogen-activated protein kinase (p38) is associated with proliferation arrest in various cell types (Engel *et al*., 2005). The expression of genes involved in mitosis such as Cyclin A and Cyclin B is regulated by p38 (Engel *et al*., 2005; Pasumarthi and Field 2002). In brief, using SB203580, a particular p38α and p38β inhibitor, on neonatal rat CMs was concluded to coincide with increased expression pattern of Cyclin A2, cdc2a, and Cyclin B. Therefore, it was concluded that the p38 is involved in regulation of genes essential for mitosis in CMs (Engel *et al*., 2005). In contrast, the over-expression as well as activation of p38 have been associated with declined proliferation and BrdU incorporation in fetal CMs (Engel *et al*., 2005). Furthermore, the CM-specific conditional knockout of p38α in neonatal rat CMs and its pharmacological inhibition in adult CMs have promoted mitosis rate and increased cytokinesis, respectively (Engel *et al*., 2005). Accordingly, we aimed to address the question, whether p38 might play a role in the immediate postnatal cell cycle arrest in murine CMs. Moreover, Engel and co-workers using rat hearts, assessed the

developmental dynamics of p38 activity from E12.5 to E21.5, as well as at P2 and adulthood. In this context, the level of phosphorylated p38 at P2 was slightly higher than at E21.5 (Engel *et al*., 2005). Yet based on their study, it is elusive which pattern the activity of p38 immediately after birth would follow. Regarding the perinatal proliferation analyses conducted in this study, and the previously reported role of p38 in CMs cell cycle arrest, it would be expected to observe higher activity of p38 after birth compared to fetal hearts. Surprisingly, WB analyses on ventricular myocardium isolated from male and female mice revealed a reduction in phosphorylation of p38 within a few hours after birth compared with E18.5 (Figure 11). Additionally, we performed IF experiments using phospho-p38 and Cav3 antibodies in combination with WGA and DAPI staining on heart paraffin sections obtained from perinatal male animals. Indeed, directly after birth (i.e., NB18.5) we observed a significant decline in the intensity of p-p38 signals in CMs in LV, IVS, and RV myocardium compared with E18.5 (Figure 13). Consequently, based on our WB and IF results, it can be speculated that the postnatal CM cell cycle arrest cannot be explained by increased p38 activity, on one hand. On the other hand, the immediate reduction in p38 activity shortly after birth could be involved in sustaining a certain level of proliferative ability in mouse hearts at NB18.5, which would otherwise be more drastically reduced. In another study performed by Yokota and team (2020), a CM-specific p38α/β double knockout was induced in mice. Interestingly, their findings demonstrated that the postnatal level of p-p38 (active form) was greater in RV than LV obtained from non-transgenic mice at P1, P3 and P7. Moreover, in the transgenic mice as a consequence of CM-specific p38α/β knockout, the RV-specific enlargement initiating from P1 to 1-month-old age. In addition, only in RV, the p38α/β knockout enhanced the rate of CM nuclei exhibiting pHH3 staining compared to the control group with identical gestational age. Nonetheless, the p38α/β knockout was concluded to induce no cell cycle activity in murine left ventricular CMs. Accordingly, these data show that p38-mediated cardiac growth and CM proliferation are chamber-specific (i.e., RV) and p-p38 is induced in RV but not LV shortly after birth at P1. In this context, the birth-dependent reduced in activity of p38 (our data) might mainly sustain the CM proliferation ability in RV.

4.1.4. Levels of YAP a member of Hippo signaling were decreased in mouse hearts directly after birth

The Hippo signaling pathway is involved in regulation of organ size, apoptosis, differentiation, and proliferation in several tissues and organs (Guo *et al*., 2020; Heallen *et al*, 2011; Heallen *et al*, 2013; Lin *et al*., 2016; Wang *et al*., 2018; Chapter 1.1.4.1.2.). Various studies on Hippo signaling pathway activity and its role on cardiac regeneration and CM proliferation have been performed. In 2012, Von Gise and colleagues to assess the role of the transcriptional co-activator YAP1in regulation of cardiac hypertrophy and proliferation, used two transgenic mouse models in which the YAP1 gain or loss of function was induced in CMs, in particular. In the CMs isolated from the WT mice, the YAP1 level was higher at E17.5 than in P3 and 1.5-month-old mice. The CM-specific YAP1deletion in mice was reported to cause myocardial hypoplasia as well as embryonic lethality. In this context, although the cell cycle activity (conducted by pHH3 IF and EdU incorporation) was reduced following YAP1 knockout compared to control mice at E16.5, the apoptosis rate in CMs was not influenced by CM-specific YAP1 loss of function (Von Gise *et al*., 2012). Moreover, assessing the CM number, they concluded a declined total CM number due to YAP1 knockout. Notably, they reported no association between YAP1 loss of function and the CM hypertrophic growth. The YAP1 gain of function induced in primary rat CMs (isolated at E16.5) in return, accelerated the CM cell cycle activity compared to the control CMs. In addition to the fetal CMs, the rat CMs isolated from hearts at P4 were investigated. Accordingly, the YAP1 overexpression in P4 cultured CMs, enhanced the cell cycle activity under *in vitro* conditions. Specifically, in contrast to control group exhibiting rare cell cycle activity, in the P4 CMs with YAP1 gain of function, 31% of CMs revealed a BrdU labeling, 2.7% stained for pHH3, and 2.1% exhibited AuroraB signals (Von Gise *et al*., 2012). It is noteworthy to mention that following a CM-specific overexpression of YAP under *in vivo* conditions in mice, they noted cardiomegaly in transgenic mice at E15.5, which was as a consequence of enhance cell cycle activity in CMs. Importantly, the postnatal YAP1 overexpression in CMs, stimulated the CM proliferation in transgenic mice at P15 (Von Gise *et al.*, 2012). Collectively, these data highlight the influence of YAP1 on stimulation of cell cycle activity in CMs. In 2011, Heallen *et al*. in order to investigate the possible involvement of Hippo pathway in mammalian heart size, studied a transgenic mouse model in which the upstream activator of LATS1/2 called *Salvador* (*Salv*), was knocked out in CMs. In

this regard, they reported that following CM-specific *Salv* knockout, the phosphorylation state of YAP was dropped compared to control mouse hearts at E9.5. Moreover, the transgenic mice at P2, survived, but they revealed cardiomegaly, as a result of CM proliferation (Heallen *et al*., 2011). YAP is reported to regulate the activity of several cardiac growth mediating pathways. For instance, the YAP/TEAD1 complex associates with nuclear ß-catenin, a downstream effector of the Wnt pathway (Heallen *et al*., 2011). In addition, one of the YAP target genes is *Pik3cb* whose expression leads to activation of the PI3K/AKT pathway in heart (Lin *et al.*, 2015). In order to unveil a possible role of the Hippo pathway in the postnatal CM cell cycle arrest we performed WB analyses on YAP in perinatal mouse hearts. Interestingly, in agreement with our proliferation analyses, WB results revealed a significant reduction in YAP protein levels rapidly after delivery in hearts isolated from male and female mice (Figure 12). In this context, it is possible that increased Hippo activity resulting in reduced YAP levels after birth, might be involved in the immediate postnatal cell cycle reduction in murine hearts. Apart from YAP we attempted to monitor the activity of MST1/2 as well as the level of LATS1/2 in perinatal mouse hearts. Nonetheless, our experiments were not successful, due to weak or unspecific bands. Therefore, in future studies, following WB and IF experiments the activity and level of other Hippo members need to be investigated. Notably, as a YAP transcriptional target gene*, Ccnb1* can be mentioned (Di Agostino *et al*., 2016). Interestingly, via RT-qPCR experiments using RNA isolated from mouse hearts at E18.5 and NB18.5, our data demonstrated that coincidence with reduced YAP total level, the expression of *Ccnb1* was declined in mouse hearts shortly after birth compared to E18.5 (Figure 14). Taken together, these findings together with the previous studies' outcomes might hint to the possible association of YAP in the birth-dependent cell cycle drop in mouse CMs and cardiac cells.

4.1.4.1. Bone morphogenetic protein 7 role in CM cell cycle regulation

In addition to the already mentioned signaling pathways, bone morphogenetic protein 7 (BMP7) is involved in regulating CM proliferation and cell cycle activity (Yang *et al*., 2023). The Yang et al. (2023), assessing the postnatal levels of an adipokine called omentin-1 revealed that concomitant with cell cycle arrest in CMs, the omentin-1 protein level elevated significantly at P14 mouse hearts compared to P1, P4 and P7 hearts. Thus, in order to investigate the role of omentin-1 in the mouse hearts, the global omentin-1 knockout was investigated. They noticed that compared to the wild type mice, the

omentin-1 knockout in P14 mouse CMs promoted a reduction in the area and width, whereas this knockout accelerated CM total number and cell cycle activity (Yang *et al*., 2023). Moreover, following a treatment of primary rat neonatal CMs with omentin-1, they noticed that the CMs became rod-shaped and matured. Furthermore, the omentin-1 induced cell cycle arrest in primary neonatal rat CMs. Next, they investigated the molecular mechanism underling the omentin-1-promoted CM cell cycle arrest and maturation. In this context, they noticed that the omentin-1 by blocking the BMP7 signaling pathway, promoted CM cell cycle withdrawal, as well as maturation. Accordingly, they described the BMP7 signaling in CMs in absent and present of omentin-1. In the absent of omentin-1, BMP7 (extracellular factor) binds to an integral membrane receptor ACTRIIB and Type I receptor, and then activates intracellular signal transduction. Accordingly, this interaction promotes activation of SMAD1 and p38 MAP-Kinase, on one hand. On the other hand, inactivates the YAP. Consequently, as a result of nuclear translocation of inactivated YAP, and activated SMAD and p38 CM proliferation is induced (Yang *et al*., 2023). However, in P14 mice, the enhanced level of Omentin-1 in heart and serum, inhibits BMP7. Moreover, inhibition of BMP7 leads to the suppression of p38 and SMAD1 phosphorylation, and promotion of YAP phosphorylation (thereby leading to YAP degradation). Consequently, cell cycle activity in CMs is disturbed (Yang *et al.*, 2023). Interestingly, in agreement with the data of Yang and colleagues, using IF staining we noticed a remarkable drop in nuclear localization of p-p38 in male murine CMs immediately after birth vs. E18.5 (Figure 13). Additionally, rapidly after birth compared to fetal stages, our WB findings concluded a noticeable declined of p-p38 and total YAP levels in the hearts of male and female mice. Accordingly, it is possible that the suppression of the BMP7 signal transduction pathways might contribute to the early postnatal cell cycle withdrawal in CMs. In this regard, in order to investigate whether an inhibition in BMP7 signaling pathway would lead to the birth-dependent cell cycle regulation in CMs, the co-immunofluorescence antibody staining with YAP, p-SMAD1, and p-p38 can be used to monitor their simultaneous nuclear localization in E18.5 mouse CMs. Moreover, *in vivo* experiments can be performed administrating omentin-1 in pregnant mice at various embryonic stages and thereby assess the activity of BMP7 signaling concerning the fetal CM cell cycle activity. On the other hand, the omentin-1 inhibitors can be administrated in adult mice (*in vivo*) to monitor the possible induction of a CM cell cycle activity.

4.1.4.2. The association of the regulation of signaling pathways with mouse sex

Previously, our results concerning the activity of AKT/mTOR, and MAPK-kinase signaling highlighted a possible involvement of gender in the regulation of cardiac growth in mice during the perinatal period. The possible involvement of female sex hormones in regulating the activity of growth promoting signaling pathway has previously been proposed (Haynes *et al*., 2003). Following a diffusion with the plasma membrane, the estrogen is able to form complexes with cytosolic and nuclear estrogen receptor (ER), interacting with chromatin and thereby regulating gene expression. In addition, the estrogen is also able to bind to ER located on the plasma membrane (reviewed by dos Santos *et al*., 2014). In previous studies, it has been noted that the estrogen regulated the activation of tyrosine kinase c-Src in breast cancer cells (MCF-7) (Migliaccio *et al*., 1993; Migliaccio *et al*., 1996). Moreover, a treatment of human endothelial cells (*in vitro*) was concluded to induce PI3K and AKT activation in a c-Src-dependent manner (Haynes *et al*., 2003). Additionally, the estrogen/ER interaction in vascular cells was reported to promote signal transduction cascades such as PI3K/AKT, Erk1/2, c-Jun NH2-terminal kinase (JNK), and p38 (Haynes *et al*., 2000; Wu *et al*., 2011). It is essential to mention that the postnatal estradiol concentrations are initially detectable at P7 in female mice (Bell, 2018; Dutta *et al*., 2014; Mannan and O'Shaughnessy, 1988). In this respect, the unchanged birth-relevant cardiac growth mediating signaling pathways' activity in female mouse hearts would not be as a result of estrogen activity. Nonetheless, estrogen receptor activation even in the absence of estrogens or other agonists has been proposed (Bennesch & Picard, 2015; Maggi, 2011; Vrtačnik *et al.*, 2014). Interestingly, genes that are regulated by the activation of estrogen receptor α include insulin-like growth factor-1 (IGF-1), IGF-1-receptor, and Cyclin D1 (Fujimoto *et al.*, 2004; Marino *et al*., 2002). Using ELISA experiments we revealed that in the serum obtained from female perinatal mice, the IGF-1 concentration was reduced immediately after birth. At the protein level, unfortunately due to lack of samples, we were not able to investigate the IGF-1 level in the female mouse hearts at E18.5 and NB18.5. Nonetheless, using RT-qPCR experiments on mouse hearts, we noticed that briefly after birth compared to the fetal stage E18.5, the *Igf1* RNA expression was increased noticeably in female mice (Figure 23). Notably, this uncertainty arises whether the enhanced transcriptome level would lead to increased protein level of IGF-1 in hearts of female mice at NB18.5 vs. E18.5; which needs to be addressed in future

studies. Furthermore, *Igf1* RNA expression is probably regulated by a multitude of transcription factors such that estrogen receptor activation might not be involved at all. However, to monitor the possible influence of ER on IGF-1 induced AKT/mTOR and MAP-kinase activity, the conditional knockout mice can be generated. With this regard, the expression of IGF-1, as well as activity of IGF-1-promoted mentioned signaling pathway, and rate of cell cycle activity in mouse CMs immediately after birth can be monitored.

In 2020, an investigation carried out by Sakamoto a team highlighted a role for estrogen-related receptor (ERR) signaling in the cardiac maturation. In their investigations, they generated a mouse model in which the expression level of ERRα and γ in murine hearts were reduced after birth. Accordingly, they noted that at five weeks after birth, compared to the control groups, the ERRα/γ knockdown was associated with cardiac dysfunction, mitochondrial structural abnormalities, decreased left ventricular (LV) fractional shortening, and accelerated LV end-diastolic and end-systolic volume measurements (Sakamoto *et al*., 2020). Moreover, they revealed that during the postnatal life, ERRγ inhibited the expression of the genes involved in the early developmental stages and non-cardiac lineages. The CM-specific ERRα/γ knockout during the fetal stages, revealed that at E17.5 the left ventricular wall was thinner in transgene groups than in control mouse hearts. Furthermore, the ventricular wall of the ERRα/γ knockout mice exhibited a non-compaction phenotype. The mitochondria were smaller and less developed following fetal ERRα/γ knockout compared to control hearts. Collectively, their data point out the influence of ERR signaling in the postnatal cardiac maturation (Sakamoto *et al*., 2020). Nonetheless, it yet needs to be assessed whether the ERR signaling in female and male mice would induce identical outcomes in cardiac maturation or not. Moreover, since the ERR knockout was coincidence with thinner ventricular wall, therefore, to investigate the mechanism underling it the cell cycle activity and apoptosis experiments in CMs following ERRα/γ knockout needs to be performed.

In male mice, within hours after delivery, the testosterone level was reported to be relatively high, which was comparable to almost 50% of its level in adults. However, 24 after birth serum testosterone level decreased remarkably to 20% of its concentration in adult mice. (Corbier *et al*., 1992; Poling and Kauffman, 2012). It is essential to mention that the exogenous elevation in testosterone level was concomitant with enhanced cardiac hypertrophy. Investigating the molecular mechanism underling the testosterone action, Altamirano and team (2009), noticed that following treatment of cultured neonatal rat

CMs, the phosphorylation degree of mTORC1 members such as mTOR (Ser2448), S6K1 (Thr389), and 4EBP1 (Ser65), was accelerated compared to untreated condition (Altamirano *et al*., 2009). It has been concluded that the mTORC1 is regulated by Erk1/2 and AKT (reviewed by Proud, 2004). Therefore, to assess the influence of testosterone on Erk1/2 and AKT, Altamirano *et al*. (2009) treated the rat neonatal CMs with testosterone. Accordingly, they demonstrated that the testosterone treatment elevated the phosphorylation of Erk1/2 and AKT. Next, using inhibitors for Erk1/2 and AKT prior to the testosterone treatment, they noticed that the although the AKT inhibition revealed no specific effect. The testosterone-promoted S6K1 phosphorylation was suppressed following Erk1/2 inhibition (Altamirano *et al*., 2009). In this context, they concluded that Erk1/2 was the upstream factor of testosterone-induced mTORC1 activation. Additionally, assessing the CM size, they revealed that following a testosterone treatment the CM size was enhanced, demonstrating the testosterone-promoted cardiac hypertrophy. Concerning the high serum concentration of testosterone level in male mice within the 24 hours after birth, we would expect that activity of Erk1/2, and 4EBP1 would be elevated in male mouse heart at NB18.5 compared to E18.5. Notably, our data suggested that the activity of p42 (Erk2) and 4EBP1 in male mouse heart remained unchanged following birth compared to E18.5 (Figure 11 and 12). Yet, we cannot conclude that the unchanged activity of Erk1/2, and 4EBP1 would be a result of high testosterone levels in serum of male mice. Moreover, in female mouse hearts at NB18.5, the activity of Erk1/2, and 4EBP1 was not noticeably changed compared to E18.5 hearts (Figure 11 and 12). Collectively, it is not likely that testosterone might influence the activity of all investigated cardiac growth mediating pathways following birth.

Taken together, our data revealed that immediately after a separation from an intrauterine environment, the cell cycle activity in mouse CMs declined dramatically compared to E18.5. Indeed, investigating the upstream regulators of this declined-cell cycle activity, we observed a drop in the activity of MAP-kinase, AKT, and YAP, together with a decrease in levels of positive cell cycle regulators such as Cyclin type-D. In this respect, it seems that the postnatal CM cell cycle exit might be a result of variation in activity of cardiac growth-regulating signaling pathways and the levels of cell cycle positive regulators. However, it is noteworthy that cell cycle activity and proliferation in CMs, are not regulated by only one factor or one specific pathway. Instead, the orchestrated cooperation and interaction of multiple signaling molecules and intracellular signaling pathways together regulate cell cycle activity in CMs. This also involves multiple

environmental players and other endogenous factors such as metabolism (glucose versus fatty acids), nutrients, oxygen levels (hypoxia versus hyperoxia), mechanical load, hormones (thyroid hormones or glucocorticoids), innervation (sympathetic/ß-adrenergic stimulation), the immune system (macrophage and monocyte invasion) (Chapter 1.1.4.1.). In this context, it is essential to investigate, whether within the hours after birth, the factors such as metabolic switch, oxidative stress, as well as oxidative DNA damage would promote the cell cycle arrest in CMs or not.

4.1.5. No correlation between the perinatal CM cell cycle arrest and expression of glycolytic enzymes, oxidative DNA damage and antioxidant enzyme levels

Another possible factor promoting postnatal proliferation exit in CMs is the transition from glycolysis to fatty acid oxidation. As already pointed out (Chapter 1.1.4.1.3.), concurrent with the proliferation-arrest at P7 in mouse CMs, the glycolysis rate in the heart at this stage was reported to decrease remarkably such that less than 10% of cardiac ATP was produced following glycolysis (Lopaschuk *et al*., 1991; Postic *et al.*, 1994). Moreover, comparing P1 and P7 mouse hearts, Puente *et al*. (2014) reported a noticeable drop in 68.7% of glycolysis-relevant enzymes and remarkable acceleration in over 80% of mitochondrial Krebs cycle and fatty acid β oxidation-associated enzymes at P7. In another study, it has been noted that as a consequence of metabolic switch to mitochondrial fatty acid oxidation, the CMs switched from proliferative to non-proliferative and terminally differentiated types (Chung *et al*., 2007). Additionally, in cells exhibiting a proliferation ability such as hematopoietic cells as well as CM progenitor, the glycolysis rate together with lactate production was reported to be considerably high (Bauer *et al*., 2004; Chung *et al*., 2007). Collectively, these studies suggest an association between glycolysis and the proliferation ability in various cells (i.e., CMs). It is crucial to mention that in contrast to mammalian organisms, the adult zebrafish has already revealed a regeneration ability following amputation of 20% of the apex (Poss *et al*., 2002). In this regard, the regeneration was promoted by CM proliferation coincident with no scar formations (Poss *et al*., 2002). Using zebrafish, Honkoop and colleagues (2019), investigated the processes orchestrating the CM proliferation following an injury. Therefore, after cryoinjury in adult zebrafish hearts, they collected the border zone CMs

which possess a proliferation ability, as well as the non-proliferative remote CMs. Interestingly, following a single-cell RNA sequencing, they noticed a very distinct gene expression pattern in proliferative CMs obtained from the border zone, compared to the non-proliferative remote ones (Honkoop *et al*., 2019). The border zone CMs exhibited a remarkable drop in mitochondrial genes and activity, on one hand. On the other hand, the glycolysis genes as well as the glucose uptake were enhanced in the proliferative border zone CMs compared to non-proliferative remote ones. Collectively, they suggested that the proliferation ability of CMs would be promoted by the glycolysis pattern during the cardiac regeneration (Honkoop *et al*., 2019). One of the glycolysis enzymes is pyruvate kinase isoenzyme 2 (PKM2). Administration of PKM2 mRNA in the infarcted region of adult mouse hearts promoted CM division, improved cardiac function and reduced scar size (Magadum *et al*., 2020). Notably, whether shortly after birth a possible modification in glycolysis rate parallels the birth-related cell cycle exit in the heart is still not clear. Using RT-qPCR on hearts obtained from mice at E18.5, NB18.5, and NB18.5+1, we noticed that immediately after birth the expression pattern of genes encoding for glycolysis-involved enzymes including *Hexokinase II*, *Aldolase-a*, *Enolase I*, and *Lactatedehydrogenase A*, was remarkably decreased compared to E18.5. Moreover, 24 hours after birth (i.e., NB18.5+1), we noticed no significant changes in expression pattern of the glycolysis-associated enzymes compared to NB18.5 mouse hearts (Figure 16). However, at protein level via WB experiments, except for Enolase I, we detected no significant changes in the protein levels of all studied glycolysis enzymes after birth compared to fetal stages (Figure 17). Our data, suggest only an indirect indication that glycolysis might not change in the immediate perinatal period. Nonetheless, we did not prove any functional activity of glycolysis-involved enzymes. This requires more experimental approaches.

In the oxygen-rich postnatal surroundings, as a consequence of mitochondrial oxidative phosphorylation, reactive oxygen species (ROS) are produced (Cadenas and Davies, 2000; Turrens, 2003). ROS causes oxidative damage to DNA and other macromolecules such as lipids and proteins, suppressing cellular proliferation (Puente *et al*., 2014). In human-induced pluripotent stem cell-derived CMs, the DNA damage was concluded to promote a DNA-damage response. Moreover, following single cell screening and chromatin stat analyses, Pettianto and team (2021) concluded that the polyploidization in CMs (hiPSC-CMs) was promoted by factors including accelerated the fatty acid oxidative metabolism, DNA-damage response, and p53 activation. Comparing RNA-seq data

obtained from the CM nuclei obtained from fetal and adult human hearts, the Pettianto *et al*. (2021) observed that only the expression of Cyclins involved in G2/M transition such as *CCNB1* and *CCNB2* was decreased in adult hearts, whereas the *CCND1* and *CCND2* (G1/S) expressions did not change among adult and fetal hearts. Their data were in agreement with the understanding that human CMs possess a DNA synthesis ability, and not mitosis (Bergmann *et al*., 2009). Moreover, comparing the Cyclin B1-adundant CMs with polyploid-abundant CMs, they reported that in Cyclin B1-abundant group, the levels of genes involved in regulation of mitosis, cell cycle, and proliferation was significantly high. Nevertheless, the genes involved in p53 signaling and myofibril assembly were accelerated in polyploid-abundant CMs. Indeed, using gene set enrichment analysis (GSEA) using polyploid-abundant clusters, they identified *GADD45B* and *CDKN1A* which were upregulated by ROS and p53 activation, together with the genes related to p53-regulated DNA damage-induction. Finally, they concluded that the CM polyploidy was associated with p53-dependent DNA damage response (Pettinato *et al*., 2021). In adult and neonatal CMs ROS inhibition was concluded to stimulate proliferation (Bae *et al*., 2021). Indeed, Puente and colleagues unveiled that at P4, and P7, the ROS level in murine CMs was gradually increased compared to P1 mouse hearts. Furthermore, paralleled by cell cycle arrest in CMs at P7, they noticed detectable nuclear signals for oxidative DNA modification using 8-oxo-7,8-dihydroguanine (8′-Oxo-G) IF staining (detecting the oxidative damage to DNA; Chapter 1.1.4.1.3.), demonstrating the influence of DNA oxidative modification on proliferation arrest (Puente *et al*., 2014). Additionally, postnatal hypoxia or pharmacological ROS neutralization was reported to enhance the postnatal CM proliferation ability and extend the postnatal window of hyperplastic growth in mice (Puente *et al*., 2014). In contrast, hyperoxia reduces CM proliferation after birth and shortens the hyperplastic time window (Puente *et al*., 2014). Taken together, there is a correlation between ROS generation and the postnatal cell cycle arrest in CMs. Nevertheless, it is not clear whether ROS mediated oxidative DNA damage would induce the birth-dependent proliferation arrest in CMs already on the first postnatal day. To assess this, we performed IF experiments studying nuclear 8-Oxo-G signals in CMs of perinatal hearts. Assuming that oxidative stress would promote cell cycle withdrawal, we would expect that the degree of oxidative DNA damage increases immediately after birth in murine hearts compared to fetal stages. Nonetheless, based on 8-Oxo-G IF findings we observed no changes in oxidative DNA damage in CMs between E18.5 and NB18.5 hearts (Figure 18).

Notably, in order to protect the cells from the oxidative damages induced by ROS and maintain redox homeostasis, antioxidant proteins and enzymes are expressed to scavenge ROS. The imbalance between ROS and the antioxidant system leads to oxidative stress, causing DNA, lipid and protein damages (reviewed by Lei *et al*., 2016). In order to measure a potential involvement of oxidative stress in the induction of immediate postnatal cell cycle arrest in CMs, the expression of antioxidant enzymes can be measured. Examples for antioxidant enzymes include superoxide dismutase (SOD), catalase, peroxiredoxin (PRDX), and thioredoxin (TRX). The SOD enzymes catalyze the dismutation of O^{-}_{2} (a ROS molecule) into O_2 and H_2O_2 (Halliwell and Gutteridge, 1986). Furthermore, as a mechanism of catalase and PRDX action, the H_2O_2 is converted to harmless H_2O and O_2. The ectopic SOD and PRDX overexpression in rabbit and mice, respectively, was demonstrated to reduce infarct size, and suppress maladaptive left ventricular remodeling and heart failure in infarcted hearts (Li *et al.*, 2001; Matsushima *et al*., 2006). To investigate the consequences of oxidative stress indirectly, we analyzed the expression of antioxidant enzymes and proteins at NB18.5 vs. E18.5 in mouse hearts. Notably, in agreement with our 8-Oxo-G IF findings, we observed no altered levels of antioxidant enzymes, as well as the hyperoxidized form of PRDX (PRDX-SO_3) in heart samples immediately after birth (Figure 19). Collectively, we concluded no correlation between the immediate cell cycle withdrawal observed shortly after birth, and both the oxidative stress and the metabolic switch. Notably, to further assess the possible role of ROS in immediate CM cell cycle arrest after birth, the directly ROS levels can be detected in perinatal hearts. Furthermore, oxidative protein or lipid damage must be investigated in the perinatal heart.

Taken together, among the possible factors promoting the cell cycle withdrawal in postnatal CM, the cell cycle regulators and the cardiac growth-mediating signaling pathways seem to be the most appealing candidates; since their level and activity were remarkably reduced in mouse hearts at NB18.5 compared to E18.5. Therefore, our next objective was to uncover the upstream factors regulating the signaling pathways following birth in mouse hearts.

4.1.6. The availabilities of eleven growth factors and cytokines were significantly altered in mouse hearts after birth

In contrast to oxidative stress, findings regarding growth promoting signaling pathways and cell cycle regulators exhibited declines in activities of cardiac growth regulating pathways together with D-type Cyclin expression in a birth-related manner (Figure 14 and 15). To some extents, the activity of these pathways and the cell cycle regulators is mediated by cytokines and growth factors. If cytokines and growth factors would regulate the rapid postnatal cell cycle arrest in CMs following birth, it would be expected that they exhibit an alteration in their availability shortly after delivery. Indeed, via *in silico* analyses we reported changes in expression patterns of 68% of 161 studied growth factors and cytokines in murine hearts at birth compared to E18.5 (Chapter 3.4.1.). Consequently, we hypothesized that shortly after a separation from the intrauterine environment the early cell cycle arrest in CMs might be promoted due to altered cytokine and growth factors availability. The identification of the respective factors involved could offer beneficial applications for preterm-born humans as well as heart regeneration.

It is crucial to emphasize that transcriptomic data underlying the *in silico* findings do not necessarily give any hints about the protein levels of the respective cytokines and growth factors. Therefore, we aimed at uncovering the availability of 129 cytokines and growth factors at the protein level at NB18.5 vs. E18.5 mouse hearts. In order to evaluate the *in silico* findings, we performed antibody-array screening experiments using whole heart samples obtained from male mice at E18.5 and NB18.5. Interestingly, we observed noticeable changes in availabilities of 27 cytokines and growth factors at the protein level directly after birth in mouse hearts. Following FDR, 11 cytokines exhibited a significant change in their protein level in the heart directly after compared to before birth. For the ELISA validation we selected the factors which aligned with our findings regarding expression of cell cycle regulators, activity of signaling pathways, and cell cycle activity obtained from WB and IF experiments. The selected factors have been reported to exhibit involvement in AKT, MAPK-Kinase, and mTOR pathway activity, as well as regulation of proliferation and angiogenesis. According to the literature research together with ELISA experiments using serum, heart, and liver samples obtained from mouse hearts we, selected 10 growth factors and cytokines. In mouse heart samples the level of Angptl3, IGF-1, IGFBP-6, and PDGFAA was decreased, whereas the level of

Adiponectin, CPR, Endostatin, IGFBP-1, Osteopontin, and Resistin was increased significantly (Figure 20).

IGF-1

Searching for potential binding of the identified factors using the GeneCards human gene database, we noticed that Angptl3, Osteopontin, and IGF-1 shared common binding partners interacting with integrin receptors. Interestingly, the integrin receptors have been reported to be involved in activation of AKT, mTOR, and GSK-3ß in hearts, thereby regulating cardiac growth (reviewed by Lal *et al.*, 2009). In injured adult myocardium, the activity of integrins and PI3K have been reported to promote mitosis in CMs after myocardial infarction (Chen *et al*., 2017; Kühn *et al*., 2007). Immediately after birth, we noticed that the level of the growth factor IGF-1 was reduced in mouse hearts compared to E18.5 hearts. Cardiac overexpression of IGF-1 in mice has been proven to induce proliferation, on one hand. On the other hand, the IGF-1 overexpression inhibited cell death, ventricular dilation remodeling, and cardiac hypertrophy after infarction in mice (Li *et al.*, 1997). Using a transgenic mouse model, in which the CM-specific expression of IGF-1 was initiated at P1, Reiss and team (1996), revealed that, from P75, the heart weight to body weight ratio in transgenic mice was greater than in the control group. Moreover, at P45, P75, and P210 days the CM number in transgenic mice were reported to be significantly higher than in control mice. In addition, although the mouse CM numbers in control groups remained unchanged. However, in transgenic mice the CM number increased from P45 to P210 day (Reiss *et al*., 1996). Collectively, it seems that the birth-relevant reduced level of IGF-1 might act as one of the factors influencing the postnatal cardiac cell cycle arrest in mouse hearts. Another growth factor exhibiting a significant reduction in its level following delivery is IGFBP6. Interestingly, our ELISA outcomes investigating the serum samples obtained from neonatal (female and male) mice, as well as adult pregnant and non-pregnant female mice, we noticed that among all investigated factors such as Angptl3, IGF-1, IGFBP6, and PDGFAA, only IGFBP6 seemed to supply the fetal mice through the maternal serum (Figure 24). In this context, it is essential to investigate the potential involvement of the IGFBP6 in cell cycle activity in any cardiac cell types.

IGFBP6

The mechanism of IGFBP6 action in heart, is still elusive. However, GeneCards data reveal that it interacts with IGF2 (GeneCards; reachable under: https://www.genecards.org/cgi-bin/carddisp.pl?gene=IGFBP6). As a consequence of ligand (i.e., IGF-1 or IGF2) binding, IGF-1R can activate MAPK-kinase and AKT/PI3K signaling pathways leading to proliferation induction in CMs (Bogush *et al*., 2020; Díaz Del Moral *et al*., 2021). It has been reported that there was a correlation between IGF-1, IGF-2, and IGF-binding proteins (IGFBPs) with vascular smooth muscle cells (VSMCs) (Wang *et al.*, 2012; Wu *et al*., 2020). In a study performed by Wang, Z. and colleagues (2020), IGFBP6 knockdown in primary cultured human VSMCs, resulted in declined proliferation rate compared to the control group. Moreover, they noted that the IGFBP6 knockdown promoted downregulation in Cyclin E/CDK2, and inhibition in centrosome replication. Furthermore, comparing the humans' normal great saphenous vein (NV) and varicose great saphenous vein (VV) samples, they unveiled that the both IGFBP6 and the Ki67 were remarkably greater in VV compared to NV. Collectively, they concluded that the IGFBP6 was involved in promotion of VSMC proliferation and varicosity progression in humans (Wang, Z. *et al*., 2020). In our study, in comparison to E18.5, we noticed that immediately after birth concomitant with declined birth-dependent cell cycle activity in CMs and non-myocytes, the IGFBP6 level in mouse heart and serum samples reduced significantly (Figure 23 and Supplementary Figure 4). Therefore, it is essential to investigate the possible involvement of IGFBP6 in promotion of cell cycle activity in mouse heart.

Angptl3

One of the identified growth factors and cytokines exhibiting a declined availability in mouse heart, serum, and liver samples shortly after birth, was Angiopoietin-like 3 (Angptl3) (Figure 22), which has been reported to promote angiogenesis (Camenisch *et al*., 2002; Luo *et al*., 2018). According to the bioinformatics data using "The Human Protein Atlas", in humans, the *ANGPTL3* is largely expressed in hepatocytes, hinting that it might originate from liver rather than expressed in hearts (reachable under: https://www.proteinatlas.org/ENSG00000132855-ANGPTL3/single+cell+type).

Camenisch *et al*. (2002), revealed that the ANGPTL3 interacted with integrin receptor $\alpha_v\beta_3$ on human microvascular vein endothelial cells (HMVECs) (*in vitro*). As a consequence of ANGPTL3/integrin activity, they noticed enhanced activity of MAPK and

AKT in HMVECs. Moreover, they observed that the ANGPTL3 interaction promoted the migration of HMVECs. Under *in vivo* situations, following ANGPTL3 treatment of rat corneas via hydron pellet implantation, they concluded promotion of angiogenesis (Camenisch et al., 2002). Multiple studies have concluded an association of ANGPTL3 with occurrence and development of cancers (Jiang *et al*., 2019; Koyama *et al*., 2015; Zhao *et al.*, 2019). In 2022, Zhong and team, investigated the role ANGPTL3 in cervical cancer (CC). They indeed revealed that the ANGPTL3 expression level was greater in cultured human CC cells than the control normal cervical cells. Moreover, ANGPTL3 knockdown in cultured HeLa cells was reported to reduce the cell proliferation, invasion and migration. In addition, they reported a reduction in levels of integrin receptors $\alpha_v\beta_3$ paralleled by ANGPTL3 knockdown. Taken together, they concluded that the ANGPTL3 promotes the proliferation in CC cells by regulating integrin receptors $\alpha_v\beta_3$ (Zhong *et al*., 2022). It is not clear whether the reduced cardiac cell cycle activity briefly after birth, might be as a result of reduced accessibility of postnatal mouse hearts to the Angptl3; which needs to be studies in future. In a study performed by Wu *et al*. (2023), via single cell approaches using cardiac cells isolated from neonatal and adult zebrafish together with regeneration studies, a role for Angptl4 to induce the proliferation in CMs and cardiac regeneration was reported. They reported that during the heart regeneration in zebrafish at the site of cryoinjury, the Angptl4 was detectable in Epicardium-derived cells (EPDC) (Wu et al., 2023). In adult zebrafish, the CM-specific upregulation of Angptl4 was reported to reduce the scar size noticeably compared to control group at 30 days after cryoinjury. Moreover, they reported that the Angptl4-associated heart regeneration in zebrafish was promoted by activation of Tie2 and Erk1/2 signaling. Moreover, increasing doses of Angptl4 was reported to enhance the cell cycle activity in cultured primary rat neonatal CMs through activation of Erk1/2. In addition, using viral infection they induced the Angptl4 upregulation in adult mouse hearts, and two weeks after induction of MI, they reported an enhanced cell cycle activity (investigated by Ki67 and Aurora B IF staining) in CMs and improved cardiac function in adult mouse hearts induced by Angptl4 treatment compared to the control group. Collectively, they concluded an ability of adult mammalian heart to regenerate following an Angptl4-induced MAPK-kinase signaling, coincided with the promotion in CM proliferation.

PDGFAA

Our ELISA and antibody array screening approaches, revealed that briefly after birth the level of PDGFAA was significantly lower in the hearts obtained from mice at NB18.5 than in E18.5 (Figure 21). The human heart single cell data (https://www.proteinatlas.org/ENSG00000197461-PDGFA/single+cell+type), demonstrated that the *PDGFA* in humans was expressed in the cardiac cell populations such as CMs, endothelial cells, smooth muscle cells and fibroblast. PDGFAA has been concluded to bind to the PDGFRA receptor (again a classical receptor tyrosine kinase) (Heldin *et al*., 1998), and thereby induces the activations of AKT and MAPK-kinase pathways (Li *et al*., 2011). The influence of PDGF on human arterial smooth muscle cells (SMCs), was studied by Li *et al*. (2011). Following an incubation of cultured SMCs with PDGFAA, they reported a significant increase in the rate of BrdU incorporation in arterial SMCs. Moreover, in the arterial SMCs, they revealed that as a consequence of phosphorylation of PDGFRA by PDGFAA, the PDGFRA became activated. Consequently, the PDGFAA treatment enhanced the activity of Erk1/2 and AKT in arterial SMCs, on one hand. On the other hand, it reduced the level of p27 in arterial SMCs compared to the control groups. Collectively, their data suggested an PDGFAA-promoted cell cycle activity in human arterial SMCs (Li *et al*., 2011). In 2016, Gallini and colleagues, assessing the *in-situ* localization of PDGFRA, revealed that the PDGFRA was localized in the interstitium of the ventricular myocardium. Moreover, comparing the mouse fetal hearts with postnatal and adult hearts, they revealed that the PDGFRA was highly expressed at E17.5 and reduced in ventricular myocardium of mice at P0. Furthermore, they reported that the CM-specific overexpression of short and long forms of *Pdgfa* (initiating from P0), promoted an increase in the heart size at P27. Additionally, within two months after delivery all transgenic mice did not survive. The CM-specific overexpression of *Pdgfa* caused reduced capillary density and enhanced fibrosis and collagen accumulation in adult mouse hearts. They concluded that PDGFAA promoted the cardiac fibrosis in the adult mice (Gallini *et al*., 2016). In their experiments a long-term *Pdgfa* overexpression was investigated. It would be interesting to monitor how the influence of a short-term CM-specific *Pdgfa* overexpression on CMs would be. In addition, it would be interesting to elucidate, whether an overexpression of *Pdgfa* in other cardiac cell types (rather than CMs) would influence the CM growth and proliferation or not.

In order to address our hypothesis regarding the maternal supplementation of factors through placenta, we investigated the origin of PDGFAA via ELISA experiments using serum samples of female adult mice (pregnant or non-pregnant) and perinatal mice. However, we were not able to demonstrate the origin of PDGFAA (Figure 24). We observed that the serum levels of PDGFAA were higher in samples obtained from pregnant mice than this in perinatal individuals. Additionally, the PDGFAA levels between the fetal and neonatal murine serum did not change (following birth). Consequently, two scenarios could be speculated:

1. Comparing the PDGFAA level in mouse hearts (decreased in a birth-related pattern), and its level in serum of pregnant vs. E18.5, it is possible that in additional to placental supplementation of fetal hearts with PDGFAA, the PDGFAA is locally produced in hearts. However, after the loss of maternal supplementation of hearts with PDGFAA, the neonatal hearts rely only on their own PDGFAA expression.
2. Comparing heart and perinatal serum patterns of PDGFAA, it is very probable that the placental PDGFAA supplementation would not directly influence its level in hearts. However, it could be probable that an upstream placental cytokine or growth factor would promote the local PDGFAA upregulation in the heart of fetal mice. Therefore, after birth, the loss of that factor reduced the cardiac levels of PDGFAA in E18.5 mouse hearts.

Which of the two scenarios may be close to the reality, need to be addressed in future studies.

It is noteworthy to mention that in this doctoral thesis we mainly focused on the factors exhibiting a reduction in their availability in mouse hearts after birth.

Taken together, according to the previous studies, it is very likely that the factor exhibiting a drop in their availability in a birth-dependent manner in mouse hearts, might be involved in regulation of AKT, Erk1/2, and mTORC1 signaling pathway in mouse perinatal hearts. Moreover, these studies as well as our proteomics approaches, the identified growth factors and cytokines seem to be involved in the regulation of cell cycle activity in mouse hearts following birth.

4.1.6.1. Association of the growth factors and cytokines exhibiting an increased level in mouse hearts following birth in cell cycle regulation

In contrast to Angptl3, IGF-1, IGFBP6, and PDGFAA, following ELISA and antibody-array screening approaches, we revealed that the growth factors and cytokines including

Adiponectin, IGFBP1, CRP, Osteopontin, and Resistin demonstrated a remarkable increase in their cardiac level in mouse heart and serum samples at NB18.5 compared to E18.5 (Figure 20). Due to lacking time in this doctoral thesis, we mainly focused on only Angptl3, IGF-1, IGFBP6, and PDGFAA. However, it is essential to investigate the possible involvement of the remaining identified factors in cell cycle regulation. According to our ELISA data, we noticed identical perinatal patterns in the level of the factors (specifically those with elevated postnatal levels) in heart, serum, and liver samples. In this regard, we speculated it is very possible that These factors would be synthesized in liver, and transported to the heart after birth. As a consequence of the heart supplementation by these factors either have positive or negative influence on the cell cycle activity summarized in two following scenarios:

1. The cardiac cells would be able to conserve their minimal proliferation ability.
2. The increased levels of these factors, would be a main reason for the birth-associated declined cell cycle activity in cardiac cell types.

With this regard, this uncertainty about the positive or negative involvement of the factors such as Adiponectin, IGFBP1, CRP, Osteopontin, and Resistin in proliferation regulation in CMs, needs to be investigated.

Adiponectin

Adiponectin was one of the identified factors exhibiting an increase in its level following birth in mouse hearts. Dadson *et al*. (2015), investigated influence of adiponectin knockout in mouse hearts following an increase in pressure overload at P0. Initially, they observed that in the control group, the established pressure overload induced at P0 by transverse aortic banding, promoted increased CM hypertrophy, and heart weight to tibia length ratio at P7 to P28. However, the CM hypertrophy in Adiponectin-null mice were initially observed at P28. An incubation of primary CMs with adiponectin, enhanced p38 activity, as well as increased the activation of the transcription factor MEF2. Collectively, they reported that as a consequence of increased pressure overload, the adiponectin-induced activation of MEF2 was associated with CMs hypertrophy and thereby enhanced heart size (Dadson *et al*., 2015). In this context, it seems that the birth-relevant acceleration in adiponectin level in mouse heart (observed in our study), might promote the CM hypertrophy immediately after birth. In vascular smooth muscle cells (VSMCs), the influence of Adiponectin in cell proliferation has been studied by Zhang *et al.* (2015). Following treatment of VSMCs with adiponectin, they concluded a decrease in

proliferation rate of cultured VSMCs compared to the control group. Moreover, investigating the molecular mechanism underling the Adiponectin-induced cell cycle arrest in VSMCs, they concluded that the Adiponectin treatment reduced the proliferation rate by suppressing the activity of Ras, Raf and Erk1/2 signaling pathway.

IGFBP1

According to the human-single cell data (https://www.proteinatlas.org/ENSG00000146678-IGFBP1/single+cell+type) the *IGFBP1* is mainly expressed in liver (hepatocytes). As member of IGF-binding proteins, the IGFBP1 interacts with IGF-1 or IGF-2 and thereby modulates the activity of IGFs. In 2007, Sun studied the role of IGFBP-1 overexpression in mouse cardiac structure at the perinatal ages. He reported that the in both transgenic and wild type mice, the ventricular wall thickness in LV, IVS, and RV was elevated from E14.5 to E17.5. After birth, while in the wild type group the wall thickness was reported to be elevated until 24 weeks, in the transgenic mice the ventricular wall thickness postnatally was accelerated only until 4 weeks. Consequently, he reported that by 24 weeks, the wall of LV was remarkably thinner in the mice overexpressing IGFBP1 compared to the control group. Prenatally, he reported that the ratio of LV weight to body weight was remarkably higher in transgenic mice than this in wild type mice. Nonetheless, postnatally, the LV weight to body weight ratio was reported to drop in transgenic mice. However, this ratio remained unchanged in wild type mice from E17.5 and P7. Additionally, having investigated the CM size, he revealed that the CM size in transgenic mice was 29% larger compared to wild type mice. At E17.5 the proliferation rate in CMs of the transgenic mice was 25% lower than the wild type group. He concluded that the upregulation of IGFBP1 in mice coincided with the enhanced heart weight to body weight rate which was caused by cardiac hypertrophy rather than the cardiac hyperplasia (University of Toronto, 2007). In agreement with the Sun's findings, it is very likely that immediately after delivery the enhanced IGFBP1 level in mouse hearts observed in our experiments, might be associated with reduced CM proliferation and increased cardiac hypertrophy. This needs to be investigated in future.

CRP

As another identified factors demonstrating enhanced level in mouse heart, C-reactive protein (CRP) can be pointed out, which in humans is mainly expressed in hepatocytes (liver) (https://www.proteinatlas.org/ENSG00000132693-CRP/single+cell+type). The

CRP has been associated with cardiovascular diseases (Gortney and Sanders, 2007). In 2011, in a study conducted by Choi and colleagues to assess the influence of CRP on cardiac cell cycle regulation, using H9C2 cardiac myocytes originated from embryonic rat hearts. Initially, following a flow cytometry analysis, they concluded that the CRP treatment enhanced the rate of cells active in G1, whereas it reduced the rate of cells exhibiting an activity in S and M phases compared to the control group. They concluded that the CRP promoted the G0/G1 arrest H9C2 cells. Furthermore, the H9C2 cells were incubated with different concentrations of CRP for 24 h, and the protein levels of cell cycle regulators were assessed. Accordingly, they revealed that as a consequence of a treatment of H9C2 cells with 50 µg/ml of CRP, the levels of CDK2, CDK4, CDK6, and Cyclin D1 was noticeably reduced compared to the control group. In addition, assessing the activity of p53 as a main regulation of cell cycle withdrawal, they reported that the CRP treatment enhanced the phosphorylation state of p53 and elevated the level of p21. To undercover the upstream factor regulating p53, they mentioned that the CRP treatment elevated the activity of Erk1/2. Interestingly, as a consequence of pharmacological Erk1/2 inhibition, the CRP-promoted p53 activation and p21 accumulation were suppressed. Collectively, they reported that the CRP protein promoted cell cycle exit in H9C2 cells by activating p53 (Choi *et al*., 2011).

Osteopontin

In the course of our ELISA and antibody-array approaches, we concluded a remarkable elevation in the level of Osteopontin (OPN) in mouse heart shortly after birth in comparison to E18.5 (Figure 20). In humans, the major source of OPN is reported to be macrophages (Shirakawa and Sano, 2021; Trueblood *et a*l., 2001). In 2001, the role of OPN in left ventricular remodeling following a LAD ligation, was investigated by Trueblood and team using OPN-knockout (OPN-KO) mice. In control and OPN-KO and control adult mouse hearts after a myocardial infarction (induced by LAD ligation), the OPN expression was shown to be elevated at the infarct zone. They reported that the LV volume to heart weight ratio was larger in OPN-KO mice than in wild type, whereas the myocyte length in OPN-KO mice was remarkably lower than in the wild type group following LAD ligation. They reported a compensatory hypertrophy in the wild type mouse hearts after MI. Interestingly, one month after LAD ligation, at the remote and infarct areas the collagen level was significantly lower (almost undetectable) in the OPN-lacking mice compared to the control group.

Collectively, they concluded an exaggerated LV dilation and declined collagen level in the adult mouse heart after LAD promoted by OPN knockout (Trueblood *et a*l., 2001). In adult rat cardiac endothelial cells, the OPN was reported to be upregulated following an Ang II-promoted activity of Erk1/2 pathway (Xie *et al*., 2001).

Resistin

According to the data represented by human single cell databank (https://www.proteinatlas.org/ENSG00000104918-RETN/single+cell+type),in human the *RETN* (Resistin) is highly expressed in macrophages. Kim et al. (2008), revealed that the Resistin was expressed in heart and caused the cardiac hypertrophy. A viral *Retn*-upregulation in the cultured neonatal rat ventricular myocytes (NRVM), was reported to increase the surface area of NRVM compared to the control NRVM. Furthermore, the Resistin upregulation in NRVM, enhanced the activity of Erk1/2 and p38. They concluded that the Resistin upregulation in CMs, promoted the cardiac hypertrophy via activation of MAPK-kinase signaling pathway. Notably, via our proteomics outcomes we revealed a birth-relevant increase in the cardiac level of Resistin compared to E18.5 hearts (Figure 20). It seems that this postnatally elevated Resistin level might promote cardiac hypertrophy immediately after birth.

Taken together, it is very likely that the identified factors exhibiting an increased level in NB18.5 mouse hearts, might dominantly be associated with reduced postnatal cell cycle activity and increased cardiac hypertrophy. Since the investigation time during this doctoral thesis was limited, we concentrated mainly on the factors with reduced availability in the mouse hearts at NB18.5 compared to E18.5 such as Angptl3, IGF-1, IGFBP6, and PDGFAA. Our objective was to assess the source of these four factors using serum and liver samples obtained from perinatal mice, as well as serum samples isolated from perinatal (male and female) together with female adult pregnant and non-pregnant mice. Based on quantitative analyses, it is not possible to make any conclusion about the origin of the factors, since the factors are not only expressed in heart or liver. However, concerning our data, it seems that during the fetal life span the heart would be supplemented by maternal IGFBP6, since the serum level of IGFBP6 was larger in pregnant mice than in adult female and fetal mice. Moreover, following a maternal separation, the IGFBP6 in the serum samples obtained from NB18.5 mice decrease compared to E18.5. Yet, we need more detailed-experiments to navigate the origin of these identified factor, which will be described in the Outlook chapter (Chapter 4.2.). Our

final aim was to incubate the cultured primary CMs with the identified factors in order to promote the cell cycle activity. Since the IGF-1 is well-investigated (Bogush *et al*., 2020), we focused on the remaining three factors: Angptl3, IGFBP6, and PDGFAA.

4.1.7. Primary neonatal mouse CM treatment with Angptl3 and PDGFAA

Concurrent with postnatal cell cycle arrest, we identified four cytokines and growth factors whose levels significantly declined immediately after birth, Angptl3, IGF-1, IGFBP6, and PDGFAA. Indeed, all these factors have been concluded to regulate cell growth or proliferation through activation of MAPK-kinase and AKT/PI3K pathways. Our objective was to induce cell cycle activity and possibly proliferation in murine neonatal CMs under *in vitro* conditions by treatment with IGF-1, IGFBP6, Angptl3, and PDGFAA.

4.1.7.1. Angptl3 incubation

Little is known about Angptl3 and its role in CMs. However, it has been speculated about a potential role of Angptl3 to improve the proangiogenic ability of endothelial progenitor cells (following an interaction with integrin receptors $\alpha_v\beta_3$ (Luo *et al.*, 2018). Previous studies mentioned the involvement of Angptl3 in activation of integrin receptors $\alpha_v\beta_3$, and thereby the angiogenesis via MAPK and AKT activation (Camenisch *et al.*, 2002). In agreement to our findings concerning the reduced cell cycle activity in CMs and declined activity of AKT and Erk1/2 immediately after birth, our proteomics analyses revealed that the Angptl3 level in the mouse heart, serum and liver samples reduced following birth compared to E18.5. In order to investigate the influence of Angptl3 in the promotion of cell cycle activity in CMs, we selected Angptl3 for our *in vitro* analyses.

It has been demonstrated that primary CMs obtained from neonatal mice exhibit a relatively low cell activity (<3.5%) (Jiang *et al*., 2022). Following Angptl3 treatment (100 ng/ml and 200 ng/ml), we observed no variations in the percentage of BrdU positive CM nuclei compared to the negative control (0.5% FCS). However, an incubation of the CMs with 10% FCS (as positive control or PC), noticeably enhanced the cell cycle activity in CMs (almost 4%), compared to the treated groups. It is essential to mention that in our experiments, the CM confluency was relatively high, which might lead to contact-inhibition and reduced or unchanged cell cycle activity in CMs. A study conducted by

Camenisch and colleagues has demonstrated that increasing the Angptl3 concentration when treating human microvascular vein endothelial cells (HMVEC), promoted cell migration through integrin receptors $\alpha_v\beta$ activity (Camenisch *et al.*, 2002). However, in our investigations, we did not find any modifications in the rate of non-myocytes exhibiting an activity in S-phase of the cell cycle following Angptl3 treatment. In contrast to Camenisch and colleagues, we did not specifically distinguish between non-myocyte cell types, which might explain this variation between our outcomes. The Angptl3 concentration inducing integrin signaling was reported 6.6 µg/ml (Camenisch et al., 2002), being 33 times higher than the concentration we used in our experimental setup. Our ELISA experiments revealed that the Angptl3 concentration in serum isolated from NB18.5 mice was almost ~224 ng/ml, whereas in E18.5 this value was ~558 ng/ml. Therefore, in order to induce cell cycle activity in CMs, higher concentrations of the Angptl3 could be tested in future studies. Using WB experiments, we noticed a significantly increased expression of Cyclin D2, as well as enhanced phosphorylation degrees of AKT and mTORC1 levels in primary CMs following treatment with 200 ng/ml Angptl3 compared to NC (Figure 28A and C). However, the MAPK-kinase (p44/42) activity was not influenced by Angptl3 treatment (Figure 28B). It is not very likely that potential influence of the Angptl3 in CM growth regulation would be as a consequence of MAPK-kinase activity. Nonetheless, it seems that the Angptl3 influenced the AKT and mTORC1 activity and Cyclin D2 level in primary CMs. Moreover, it has been already concluded that following an overexpression of type-D Cyclins in injured adult mouse hearts, increased CM cell cycle activity (S-phase activity) and reduced the infarct size (Pasumarthi *et al*., 2005; Soonpaa *et al*, 1997). It seems that the investigated level of Angptl3 in our study was too low to induce the cell cycle activity in CMs, whereas at molecular levels even low levels of it enhanced the expression level of Cyclin D. In future studies in vitro experiments with higher Angptl3 doses need to be performed.

4.1.7.2. PDGFAA treatment

According to the single cell data, the PDGFAA is expressed in CMs, SMCs, FBs, and ECs (Chapter 4.1.5.). Moreover, paralleled by the birth-associated cell cycle arrest in mouse CMs and non-myocytes, our ELISA experiments unveiled that PDGFAA level in mouse heart was lower in NB18.5 hearts than in E18.5. Notably, PDGFAA was reported to be associated in cellular proliferation by activating AKT and Erk1/2 signaling (Li *et*

al., 2011). We selected PDGFAA for our *in vitro* experiments. PDGFAA has demonstrated high affinity to PDGFRα. The receptor PDGFRα is expressed in cardiomyocyte progenitors. It is elusive whether it would be involved in myocardial repair after an injury in adult hearts (reviewed by Kalra *et al.*, 2021).

Taken together, it seems that the PDGFAA can potentially serve as promising candidates to enhance proliferation rates in primary neonatal CMs. After 24 h treatment with 50 ng/ml PDGFAA we observed that the BrdU incorporation rate in neonatal CM nuclei was reduced from 2.2% to 1.6% (compared to the negative control), without reaching statistical significance. A higher concentration of PDGFAA (100 ng/ml) significantly increased the rate of BrdU exhibiting CM nuclei to 2.74% (compared to both NC and the 50 ng/ml PDGFAA-treated cells). Stimulating arterial smooth muscle cells in human arterial SMCs by PDGFAA, Li *et al*. (2011) reported that the BrdU incorporation in these cells increased significantly by the factor of 10 after treatment with 50 ng/ml PDGFAA for 48 h (Li *et al*., 2011). In our *in vitro* experiments, we noticed no noticeable variations in BrdU incorporation using this concentration in non-myocytes (Figure 26) in comparison to the NC. One reason for this reduction is that in contrast to the study performed by Li *et al*., our PDGFAA incubation time was shorter (24 h instead of 48 h) (Li *et al*., 2011). In our study we only investigated the total cardiac non-myocyte cell populations, irrespective to their type (including all cardiac SMCs, ECs, and FBs), which might explain this variation. Whether increasing the PDGFAA treatment period to 48 h would lead to an elevation in CM and non-myocyte proliferation rates needs to be examined. In future the cell-specific response to the PDGFAA can be assessed. In addition to the already mentioned factors, the confluency of the cultured cells was relatively high (more than 90%), which can highlight the influence of contact inhibition on cell cycle activity.

Taken together, PDGFAA seems to be able to promote CM proliferation. We revealed that PDGFAA treatment promoted the cell cycle activity in CMs. However, it needs to be investigated whether this cell cycle activity might lead to proliferation, or hypertrophy, multinucleation or even polyploidy.

4.2. Outlook and conclusion

4.2.1. Determination of cardiac hypertrophy, polyploidy, and nucleation

Following our WB findings, we noticed that the activity of AKT, S6, Erk1/2 in female mouse hearts remained unchanged at NB18.5 compared to E18.5, whereas in male mouse hearts these reduced significantly immediately after birth. In both sexes the cell cycle activity following birth was reduced in a birth-associated manner. Therefore, we hypothesize that the unchanged activity of signaling pathways in hearts obtained from female mice, would promote the cardiac hypertrophy. Male and female hearts will be isolated, fixed in 4% PFA (for 2 hours at RT) and dissociated to single cells, separately Neonatal Heart Dissociation Kit (#130-098-373) and the gentleMACS™ Octo Dissociator with Heaters (Chapter 2.2.8.2.). Following IF staining and microscopic imaging, the surface area of dissociated CMs will be determined using ZEN 2.3 pro (Image Acquisition) software. Additionally, the size, ploidy and binucleation states of CMs can be determined using fluorescence activated cell sorting (FACS) (Bak *et al*., 2023). Moreover, the cross-sectional area of CMs in tissue sections of perinatal male and female mice will be determined using IF microscopic analyses (Ocsan *et al*., 2013). The WGA co-staining with Caveolin 3, and DAPI staining will be performed and following imaging, the area of CMs with identical orientation will be measured.

4.2.2. Investigation of the influence of sex hormones on CM cell cycle activity

Concerning our AKT, MAPK-Kinase, and mTORC1 findings, together with ELISA experiments for serum levels of cytokines and growth factors, we noticed that although the hearts of both male and female mice are supplemented with similar levels of certain cytokines and growth factors, the activity of the mentioned signaling pathways in the two sexes was not identical. This underlines the potential involvement of the female sex hormone estrogen or the male hormone testosterone. However, according to previous studies, the estrogen level in serum of male and female mice briefly after birth is identical (reviewed by Leffler *et al*., 2018). Whether the estrogen receptors in female animals would exhibit higher affinity to estrogen compared to receptors in males, or the receptor

proportion would be different in each gender needs to be addressed. Moreover, the estrogen receptor α has been reported to exhibit an activity in the absence of estrogen (Bennesch & Picard, 2015; Maggi, 2011; Vrtačnik *et al.*, 2014). Considering the previous findings and our pathway activity analyses, we speculate that in female mice an intrinsic activity of estrogen receptor α would influence the unchanged AKT, MAP-Kinase, and mTORC1 activity immediately after birth compared to fetal stages. Therefore, to investigate a potential participation of estrogen receptor α in CMs, *in vitro* experiments can be performed on primary CMs isolated from male and female mice, separately using Neonatal Heart Dissociation Kit (#130-098-373) and the gentleMACS™ Octo Dissociator with Heaters (Chapter 2.2.8.2.). The primary mouse neonatal CMs can be tittered with various concentrations of sex hormones and thereby the proliferation analyses will be conducted in cellular levels using single cell analysis as well as IF staining using Caveolin 3 (Chapter 2.2.3.4.) (Bak *et al*., 2023). In addition, using siRNAs or CRISPR cas9 method, the estrogen or testosterone receptors can be downregulated in the primary mouse neonatal CMs and the outcomes on the cell cycle activity will be monitored (reviewed by Boettcher and McManus, 2015; Carroll *et al*., 2016). Consequently, based on the results of *in vitro* experiments, the in vivo experiments can be designed, treating the neonatal mice with the selected sex hormones to promote the cell cycle activity. The neonatal mice can be treated with the estrogen or testosterone and their antagonists to investigate their involvement in promotion or inhibition of postnatal cell cycle activity.

4.2.3. Assessment of the influence of BMP7 and Omentin-1on CM proliferation

Based on our p-p38 and YAP findings via IF and WB experiments (Figure 11, 12, and 13; Chapter 3.2.1.), we noticed a decreased nuclear localization of p-p38 in CMs, together with reduced protein levels of p-p38 and YAP in hearts of mice at NB18.5 vs. E18.5. These outcomes were in agreement with the study conveyed by Yang and colleagues, revealing the influence of BMP7 on induction of CM proliferation in mice (Yang *et al.*, 2023). Whether a reduction in the activity of the BMP7 signaling pathway after birth would be concomitant with the early cell cycle withdrawal in CMs needs to be investigated. The reduction of BMP7 pathway activity is promoted by reduced BMP7

level and/or increased amounts of its inhibitor called Omentin-1. Therefore, ELISA experiments will be performed measuring the level of BMP7 and Omentin-1 in serum and hearts of male and female individuals at E18.5 and NB18.5 (Mouse BMP7 kit ELISA, #A76214; Mouse Omentin-1 kit ELISA, #NBP2-81145). Moreover, multiple approaches can be performed to investigate the influence of BMP7 and Omentin-1 on CM cell cycle activity. For instance, the pregnant mice can be injected with Omentin-1 or even another adipokine (i.e., Adiponectin), which might lead to reduced fetal CM proliferation. Fetal hearts will be isolated and following IF and WB approaches the proliferation and the activity of cardiac growth-promoting signaling pathways, will be assessed. In addition, CM-specific Omentin-1 conditional knockdown mouse models can be investigated, in which the Omentin-1 is inhibited in the postnatal hearts. Therefore, Cre/LoxP transgenic mice can be generated in which the Cre-recombinase is expressed under the activity of alpha-myosin heavy chain (alpha-MHC) promoter, and the *Intelectin-1a* (encoding for Omentin-1) gene is found within the *LoxP* sequences, which leads to postnatal knockout of *Intelectin-1a* in CMs (Jones *et al*., 1996; Kim *et al*., 2018). Accordingly, the CM cell cycle activity will be measured. As another approach, using siRNA against Omentin-1, under *in vitro* conditions the cell cycle activity of primary mouse CMs can be investigated.

4.2.4. Navigation of cytokine and growth factor exchange between fetal and maternal blood circulation

Studies have concluded the importance of bidirectional maternal and fetal interaction on the mouse physiology (Cleaton *et al*., 2016; Lopez-Tello *et al*., 2023). Due to our data concerning the birth-related modifications in the availability of the identified factors in NB18.5 mouse hearts, we hypothesized that a separation from maternal supplementations with the factors, would cause the change in the factors' levels in neonatal mouse hearts. According to our experimental setups, it was not possible to reveal the origin of the factors as well as the possible maternal factors' supplementation of the embryonic hearts. Therefore, the multiple experiments need to conducted to address these uncertainties. The GFP-tagged factors can be injected to the mother blood circulation (tail vein), and their possible presence in blood of the fetus can be investigated by ELISA against GFP, or IF staining for GFP using fetal or neonatal mouse heart sections. The possible maternal

factors supplementation of fetus can be assessed. On the other hand, in order to monitor whether the fetal factors might be involved in the maternal blood circulation through placenta, the GFP-tagged factors can be injected to the fetus and the presence in the mother blood circulation can be monitored using ELISA and co-immunoprecipitations (Cleaton *et al*., 2016; Lopez-Tello *et al*., 2023).

The single cell proteomics can be conducted using mouse hearts and organ samples from mice at E18.5 and NB18.5 to monitor the expression level of the factors in a cell-specific manner. Moreover, in the neonatal mice, to investigate whether the liver or heart would be the main organ expressing the factors, the tagged-factors can be expressed under cell-specific promoters (CM-specific or hepatocyte-specific promotors such as alpha-MHC via Cre/LoxP) and their localization and expression level will be assessed later. Assuming that the hepatocytes would be the origin of the factors (i.e., Angptl3, and IGFBP1), the hepatocyte-specific knockout or even hepatocyte-specific expression of the GFP or any tagged forms of the factor can be generated. Assessing the factor's (with or without tag) availability in serum, heart, and even liver, can help to navigate the main source of the factors.

4.2.5. Promotion of CM proliferation by application of PDGFAA in mice

Investigating the growth factors and cytokines exhibiting reduction in their protein levels after birth including Angptl3 and PDGFAA, our data revealed that treatment of neonatal CMs with 100 ng/ml of PDGFAA, significantly enhanced the BrdU incorporation in primary mouse neonatal CMs, compared to the NC. It needs to be assessed whether, this PDGFAA-induced cell cycle activity might lead to CM proliferation or only hypertrophy, nucleation, or polyploidy. Having addressed this uncertainty, the in vivo experiments can be performed to induce the CM proliferation following an injury in adult mouse hearts. Initially the role of postnatal overexpression or administration of PDGFAA on proliferation induction in mouse CMs will be assessed. Therefore, concomitant by cell cycle exit in CM at P14, PDGFAA will be applied to mice peritoneally or intravenous injection at P14, P28, P56, and 1-year-old (Alkass *et al*., 2015; Gombash Lampe *et al*., 2014; Soonpaa *et al*., 1996). Moreover, 24 h, 48 h, and 72 h later, the hearts will be isolated and the proliferation analyses in CMs will be carried out. Assuming that the PDGFAA administration would promote the CM proliferation in postnatal mice, it will

next be used to enhance the regeneration ability of postnatal mouse hearts. Sham and cryoinjury will be induced (size of the injury will be correlated to the body size) in mouse hearts at P0, P4, P7, P14, and adulthood and the mice will be injected with PDGFAA (treated groups), or only DMSO or PBS (negative control) (intravenous injections). 7, 14, 21 and 30 days later, the heart function and structure, as well as the CM morphology and proliferation at the side of injury will be assessed.

4.2.6. *In vitro* experiments using Angptl3

Coincident with declined cell cycle activity in mouse CMs, we observed that the level of Angptl3 was remarkably declined in mouse serum, heart, and liver samples at NB18.5 compared to E18.5. Moreover, it has been reported that Angptl4 and Angptl3 promoted proliferation and angiogenesis (refer to Chapter 4.1.5.). Therefore, we assessed the potential influence of Angptl3 in CM proliferation using *in vitro experiment* performed on cultured primary mouse neonatal CMs. According to our IF and WB outcomes using 200 ng/ml concentration of Angptl3, we revealed that while the Angptl3 did not influence the BrdU-incorporation rate in CMs. However, at molecular levels it enhanced the level of Cyclin D2 and activity of AKT, S6, and P70S6K1. We speculated that the selected Angptl3 concentration might be too low to promote the cell cycle activity in CMs. In future study higher doses of the Angptl3 will be used to induce the cell cycle activity. Assuming that the Angptl3 would induce proliferation in mouse primary CMs, we will later conduct *in vivo* experiments. The P1, P4, P7, and P14 mice can be injected with the identified doses of Angptl3 (through *in vitro* experiments), and thereby the CM proliferation will be investigated as previously mentioned. Next, using LAD ligation in adult mice, and the injection of Angptl3, the cardiac structure and function, as well as CM proliferation, CM total number, and scar size will be assessed at 7, 14, 21, and 30 days after LAD ligation.

4.2.7. *In vitro* experiments using IGFBP6

IGFBP6 was a common factor detected in both the cytokine and the growth factor antibody-array. However, using the growth factor array we noted no change in early postnatal levels, whereas our ELISA and cytokine array data revealed a birth-related drop

in IGFBP6 levels. Interestingly, studies have demonstrated that IGFBP6 is related to cell proliferation. Specifically, an *Igfbp-6* knockdown in vascular smooth muscle cells (VSMCs) inhibits cell proliferation through Cyclin E degradation, causing S-phase arrest (Wang, Z. *et al*., 2020). Another study has concluded that IGFBP6 inhibited proliferation in fibroblasts obtained from palmar fascia by interacting with and suppressing IGF-2 (Raykha *et al.*, 2013). IGF-2 exhibits a high affinity to the receptor IGF-1R and thereby promotes cardiomyocyte proliferation via MAPK-Kinase and AKT signaling pathways (Bogush *et al*., 2020; Díaz Del Moral *et al*., 2021). However, it is unknown whether IGFBP6 in the heart would positively regulate CM proliferation or not. Therefore, *in vitro* experiments will be performed on primary CMs in the future. The CMs will be treated with IGFBP6 for 48 h, and cell cycle and pathway activity will be investigated.

Conclusion

Collectively, in this doctoral thesis we concluded for the first time that the immediate postnatal cell cycle arrest in CMs is not dependent on gestational age, developmental programming or gender. Our data demonstrated a reduced cell cycle activity in CMs rapidly after a separation from the intrauterine environment. Concurrent with this birth-related cell cycle withdrawal, the expression of cell cycle regulating proteins and the activity of growth promoting signaling pathway were declined noticeably in a gender-dependent fashion. We speculated that CMs in female mice might differ in the timing of the perinatal switch from hyperplastic to hypertrophic growth and would initiate hypertrophy earlier compared to males with the same gestational age. The cell cycle regulators and signaling pathways might partially be regulated by cytokines and growth factors whose availability changes in the perinatal heart. Interestingly, we reported that directly after birth the level of 10 cytokines and growth factors was altered in mouse hearts and serum. It is essential to mention that the identified factors are mainly involved in the regulation of MAP-Kinase, AKT, and mTORC1 pathways, supporting their possible involvement in regulation of postnatal cell cycle arrest in CMs. Preliminary *in vitro* results revealed that out of the 10 factors with perinatal changes in the heart, treatment of primary neonatal CMs with PDGFAA might moderately induce cell cycle activity. Future studies need to be conducted to validate our findings and characterize the various growth factors and cytokines in more detail with respect to their potential to

modulate CM cell cycle activity. Assuming that the PDGFAA might indeed promote the proliferation in CMs, it is potential to induce the CMs proliferation in adult mice and humans following an injury. Moreover, since the cardiac function and structure were reported to be influenced in preterm-delivered humans. It is tempting to speculate whether a treatment with PDGFAA would be able to improve the CM total numbers in premature-delivered humans. Thus, our findings could potentially have essential clinical implications for the improvement of life quality of preterm-born humans.

5. Abstract

During the embryonic development, the cardiac growth is mainly promoted by cardiomyocyte proliferation. In mice the cardiomyocyte proliferation declines continuously after birth, such that in adults cardiac myocytes are largely unable to divide. If an exposure to an extrauterine environment induces postanal cell cycle arrest, cardiomyocyte numbers per heart might be reduced following preterm birth compared to term deliveries. This might affect cardiovascular health later in life. Thus, in this thesis, we evaluated the onset of cell cycle withdrawal in mouse hearts in the period immediately after birth. We performed independent immunofluorescence (IF) staining for Ki67, and phospho-Histone H3 together with Caveolin 3 as a cardiomyocyte marker in murine ventricular myocardium at two latest fetal stages (E17.5 and E18.5), shortly after birth (NB18.5 and NB19.5), a day after delivery (NB18.5+1 and NB19.5+1), and two days after birth (NB19.5+2). Both E18.5 and NB18.5 mice share an identical gestational age, however, only the NB18.5 mice were briefly exposed to the extrauterine environment. Thus, comparing E18.5 and NB18.5 hearts allows for the evaluation of the birth influence on cardiac growth regulation. Moreover, in the entire analytical steps, the mouse gestational age and sex were precisely monitored. Our IF data revealed no remarkable variations in the cardiac cell cycle activity between E17.5 and E18.5 stages. Nonetheless, shortly after birth, the cell cycle activity rate (Ki67) in cardiac cells, as well as mitosis rate in cardiomyocyte and non-myocyte (phospho-Histone H3 and Caveolin 3) were noticeably reduced in mouse ventricular myocardium at NB18.5 and NB19.5 compared to E18.5 ($p<0.05$). Comparing the cardiac proliferation rate in NB18.5 and NB19.5 hearts, out data suggested that the cell cycle activity was gender and gestational age-independent. Furthermore, at one day after birth compared to immediately after delivery, the mitosis rate in cardiomyocytes and non-myocytes dropped significantly, whereas the cardiac cell cycle activity remained unchanged during the early postnatal stages. Notably, within the first week after birth factors such as the metabolic switch, oxidative stress and DNA damage, as well as the activity of the cardiac growth regulating signalling pathways and the availability of cell cycle regulators influence the murine postnatal cardiac cell cycle arrest. However, assessing the availability of glycolysis-involved enzymes (HK-II, ALDOA, PKM1/2, LDHA, and Eno-II), levels of antioxidative enzymes (SOD2, TRX2 and hyperoxidized PRDX-SO_3), and the degree of oxidative DNA-damage (using IF

staining for 8′-Oxo-7,8-dihydroguanine and MEF2A/C) in perinatal mouse ventricular myocardium, we observed no noticeable modifications in the level of these factor at NB18.5 compared to E18.5. Thus, it is very unlikely that these factors would be associated in the cell cycle arrest in CMs shortly after birth. Interestingly, via western blot and IF approaches, we revealed that coincidence with the birth-associated cell cycle arrest in CMs, the levels of type-D Cyclins and activity of MAP-kinase, AKT, and mTORC1 were significantly reduced in mouse ventricular myocardium at NB18.5 compared to E18.5. These pathways are partially regulated by growth factors and cytokines. Accordingly, we hypothesized that immediately after a separation from an intrauterine environment, an alteration in the availability of growth factors and cytokines promote the postnatal cardiac cell cycle arrest. Indeed, our *in silico* approaches revealed that out of 161 studied growth factors and cytokines, 68% exhibited an altered RNA expression level in neonatal compared to fetal mouse and human hearts. Via proteomics analyses (antibody-array screenings and ELISA experiments), we unveiled that concomitant with the birth-associated cardiac cell cycle arrest, the level of the growth factors and cytokines including Angptl3, IGF-1, IGFBP6, and PDGFAA declined remarkably, whereas Adiponectin, CRP, IGFBP1, Osteopontin, and Resistin levels were noticeably accelerated in mouse hearts at NB18.5 compared to shortly before delivery (at E18.5). Consequently, to promote the cell cycle activity in cultured primary cardiomyocytes isolated from neonatal mouse hearts, the cells were incubated with either medium (negative control), or Angptl3, or PDGFAA, and thereby the BrdU incorporation rates were assessed. While the Angptl3 treatment did not influence the cell cycle activity in cardiomyocytes, an incubation of primary cardiomyocytes with PDGFAA enhanced the rate of cardiomyocytes exhibiting a BrdU-incorporation to twice its value observed in negative controls. Collectively, it seems that PDGFAA might promote proliferation in cardiomyocyte, which needs to be elucidated in future. In this context, the outcome of this thesis can have beneficial clinical implications in preterm-born humans as well as cardiac regeneration studies in humans.

6. Zusammenfassung

Die Proliferation von Kardiomyozyten während der embryonalen Entwicklung ist ein wesentlicher Bestandteil des kardialen Wachstums. Die Proliferation von Kardiomyozyten nimmt bei Mäusen nach der Geburt kontinuierlich ab, sodass adulte Herzmuskelzellen größtenteils unfähig sind, sich zu teilen. Der genaue Zeitpunkt an dem es zum post-natalen Zellzyklusarrestes der Kardiomyozyten kommt ist bisher nicht bekannt. Außerdem ist unklar wie groß der Einfluss des Gestationsalters und der extrauterinen Umgebung auf den Zellzyklus der Kardiomyozyten ist. Sollte der Zellzyklusarrest unmittelbar nach der Geburt erfolgen, könnte die Kardiomyozyten-Anzahl pro Herz bei Frühgeburtlichkeit im Vergleich zu termingerecht geborenen Säuglingen reduziert sein. Dies könnt zur Folge haben, dass Frühgeborene im Vergleich zu Reifgeborenen im Verlauf ihres Lebens ein erhöhtes Risiko für kardiovaskuläre Erkrankungen haben. Um den genauen Zeitpunkt zu ermitteln, an dem die Kardiomyozyten postnatal aus dem Zellzyklus austreten haben wir murines ventrikuläres Myokard von den zwei letzten fetalen Entwicklungsstadien (E17.5 und E18.5), kurz nach der Geburt (NB18.5 und NB19.5), einen Tag nach der Geburt (NB18.5+1 und NB19.5+1) und zwei Tage nach der Geburt (NB19.5+2) mittels Immunfluoreszenz-Färbungen (IF) für Ki67 und phospho-Histon H3 zusammen mit dem Kardiomyozyten-Marker Caveolin 3 untersucht. E18.5 und NB18.5-Mäuse haben das gleiche Gestationsalter, jedoch waren die NB18.5-Mäuse kurzzeitig der extrauterinen Umgebung ausgesetzt. Daher ermöglicht der Vergleich von E18.5- und NB18.5-Herzen die Bewertung des Einflusses der Geburt auf die Regulation des Herz-Wachstums. Unsere IF-Daten zeigten keine signifikanten Unterschiede in der gesamt zellulären kardialen Zyklusaktivität zwischen den Stadien E17.5 und E18.5. Direkt nach der Geburt verringerte sich die Rate der Zellzyklusaktivität (Ki67) aller kardialer Zellen sowie die Mitoserate der Kardiomyozyten und Nicht-Kardiomyozyten (phospho-Histon H3) signifikant (NB18.5 und NB19.5 im Vergleich zu E18.5: $p<0,05$). Das Geschlecht der Mäuse hatte hierbei keinen Einfluss auf die Zellzyklusaktivität. Des Weiteren verringerte sich die Mitoserate (phospho-Histon H3) der Kardiomyozyten und Nicht-Kardiomyozyten bereits einen Tag nach der Geburt. Die Zellzyklusaktivität (Ki67) blieb während dieses perinatalen Zeitraums unverändert. Es ist bekannt, dass Faktoren wie die Umstellung des Stoffwechsels von Glykolyse zur oxidativen Phosphorylierung, oxidativer Stress, DNA-Schäden, die Aktivität von

Wachstumssignalwegen und die Verfügbarkeit von Zellzyklusregulatoren den postnatalen Kardialen-Zellzyklusarrest bei Mäusen innerhalb der ersten Lebenswoche beeinflussen. Weder die an der Glykolyse beteiligten Enzyme (HK-II, ALDOA, PKM1/2, LDHA und Eno-II) noch Marker für oxidativen Stress (SOD2, TRX2 und hyperoxidierter PRDX-SO3) oder oxidativen DNA-Schaden (8′-Oxo-7,8-Dihydroguanin und MEF2A/C) waren im perinatalen ventrikulären Myokard im Vergleich zu E18.5 Herzen verändert. Diese Faktoren scheinen somit nicht mit dem unmittelbar postnatalen Zellzyklusarrest der Kardiomyozyten in Verbindung zustehen. Wir konnten jedoch beobachten, dass parallel zum perinatalen Zellzyklusarrest die Mengen an Typ-D-Zyklinen, so wie die Aktivität des MAP-Kinase-, AKT- und mTORC1-Signalweges im ventrikulären Myokard signifikant abnahmen. Da Wachstumsfaktoren und Zytokine an der Regulation all dieser Signalwege beteiligt sind, stellten wir die Hypothese auf, dass durch Trennung des maternalen und fetalen Organismus durch die Geburt die Verfügbarkeit von Wachstumsfaktoren und Zytokinen im neonatalen Organismus sinkt und somit der Zellzyklusarrest der Kardiomyozyten ausgelöst wird. Tatsächlich zeigten unsere *In-silico*-Ansätze, dass von 161 untersuchten Wachstumsfaktoren und Zytokinen 68% eine veränderte RNA-Expressionsrate zwischen den neonatalen und fetalen Herzen (human und murin) aufwiesen. Auf Proteinebene konnten wir in einem Antikörper-Array-Screening und mittels ELISA-Experimenten zeigen, dass gleichzeitig mit dem geburtsbedingten Kardiomyozyten-Zellzyklusarrest die Menge an Angptl3, IGF-1, IGFBP6 und PDGFAA, signifikant abnahm, während die Menge an Adiponectin, CRP, IGFBP1, Osteopontin und Resistin in NB18.5 Herzen im Vergleich zu E18.5 deutlich zunahm. Um den Effekt von Angptl3 und PDGFAA auf die Proliferation von Kardiomyozyten zu untersuchen, wurden primäre neonatale murine Kardiomyozyten isoliert, mit Angptl3 oder PDGFAA behandelt und die BrdU-Inkorporationsraten gemessen. Dabei hatte die Angptl3-Behandlung keinen Einfluss auf die Inkorporation von BrdU und somit die Zellzyklusaktivität. PDGFAA hingegen verdoppelte die Rate der Kardiomyozyten, die eine BrdU-Inkorporation aufwiesen, im Vergleich zur Kontrolle.

Zusammenfassend konnte in dieser Arbeit gezeigt werden, dass die Zellzyklusaktivität muriner Kardiomyozyten unmittelbar post-natal abnimmt. Als Ursache hierfür konnten post-natal veränderte Spiegel von Wachstumsfaktoren und Zytokinen, wie beispielsweise die Abnahme von PDGFAA, identifiziert werden

7. List of Abbreviations

A

A	Anterior
AB	Antibody
ALDOA	Aldolase-A
a.m.	Before midday
AMPK	5´-adenosine monophosphate-activated protein kinase
Angptl3	Angiopoietin-like 3
ATP	Adenosine triphosphate
AV	Atrioventricular

B

BMP	Bone morphogenetic protein
bp	Base pair
bpm	beats per minute
BrdU	Bromodeoxyuridine
BVG	Balboventricular groove

C

CANS	Cardiac autonomic nervous system
Cav3	Caveolin 3
CDK	Cyclin-dependent kinase
cDNA	Complementary DNA
CDKI	CDK-inhibitors
CHD	Congenital heart disease
CLB	Cell lysis buffer
CM	Cardiomyocyte
CRP	C-Reactive Protein
C_T	Cycle of threshold
CVDs	Cardiovascular diseases
^{14}C	Carbon-14

D

DC	Detergent compatible
DMSO	Dimethyl Sulfoxide
DNA	Deoxyribonucleic acid
Dpc	Days post coitus

E

E	Embryonic day (E18.5 stands for embryonic day 18.5)
4EBP1	Eukaryotic translation initiation factor 4E
EC	Endothelial cell
ECCs	Endothelial cushion cells
ECL	Enhanced chemiluminescence
ECM	Extracellular matrix

EdU	3[H] thymidine incorporation
EF	Ejection fraction
EGF	Epidermal growth factor
EIF4E	Eukaryotic translation initiation factor 4E
ELISA	Enzyme-Linked Immunosorbent Assay
Eno	Enolase
EPDC	Epicardium-derived cells
ER	Estrogen receptor
ERR	Estrogen-related receptor
EtOH	Ethanol
F	
F	Forward (primer)
FACS	Fluorescence-activated cell sorting
FB	Fibroblast
FCS	Fetal calf serum
FDR	False Discovery Rates
FELASA	Federation of European Laboratory Animal Science Associations
FGF	Fibroblast growth factor
FHF	First heart field
G	
G1	Gap1
G2	Gap2
GFP	Green fluorescence protein
GLUT	Glucose transporter
GO	Gene Ontology
GPCRs	G-protein-coupled receptors
GSEA	Gene set enrichment analysis
GSK-3β	Glycogen synthase kinase-3β
H	
h	hour
Hccs	*X-chromosomal holocytochrome c synthase* gene
HF	Heart failure
HFs	Head folds
HIF-1α	Hypoxia-inducible factor 1α
hiPSCs	Human induced pluripotent stem cell
HK	Hexokinase
HMVECs	Human microvascular vein endothelial cells
H_2O_2	Hydrogen peroxide
HRE	Hypoxia response elements
HRP	Horseradish peroxidase
I	
IF	Immunofluorescence
IGF	Insulin-like growth factor

List of Abbreviations

IGFBP	Insulin-like growth factor binding protein
ITS	Insulin-Transferrin-Selenium
IVS	Interventricular septum
J	
JNK	c-Jun NH2-terminal kinase
K	
KO	Knockout
KD	Knockdown
L	
L	Left
LA	Left atrium
LAD	Left anterior descending coronary artery
LATS1/2	Large-tumor suppressors
LDH	Lactate dehydrogenase
LV	Left ventricle
LVNC	Left ventricular non-compaction
M	
M	Mitosis phase
MAPK	Mitogen-activated protein kinases
B-ME	β-mercaptoethanol
MEF2	Myocyte enhancer factor 2
MeVS	Membranous interventricular septum
MHC	Myosin heavy chain
MI	Myocardial infarction
min	Minute
ML	Midline
mmHg	Millimeter mercury
mRNA	Messenger ribonucleic acid
MST1	Mammalian sterile 20-related 1
MST2	Mammalian sterile 20-related 2
mtDNA	Mitochondrial DNA
mTOR	Mammalian/Mechanistic target of rapamycin
MuVS	Muscular interventricular septum
N	
NB	New born or age at birth (NB18.5: Birth occurrence at day 18.5)
NC	Negative control
NCBI	National Center for Biotechnology Information
NGS	Normal goat serum
NPAT	Nuclear protein coactivator of histone transcription
NPM	Nucleophosmin
NRVMs	Neonatal rat ventricular myocytes
NTC	None-template control
NV	Normal great saphenous vein

List of Abbreviations

O

$^1O_2$	Singlet oxygen
$O2^{\bullet-}$	Superoxide anion
O_3	Ozone
OD	Optical density
3'-OH	Hydroxyl
$OH^{\bullet}$	Hydroxyl ion
O/N	Over night
OPN	Osteopontin
8´-Oxo-G	8-hydroxyguanine

P

P	Posterior
P	Postnatal day
PAA	Poly acrylamide
PBS	Phosphate buffered saline
PC	Positive control
PCR	Polymerase chain reaction
PDGF	Platelet-derived growth factor
PDGFRA	Platelet-derived growth factor receptor A
PDK	Pyruvate dehydrogenase kinase
PFA	Paraformaldehyde
PFK	Phosphofructokinase
PFs	Purkinje fibers
pHH3	Phosphorylated Histone H3
PKM1/2	Pyruvatekinase muscle
p.m.	Past midday
PRDX	Peroxiredoxin
PS	Primitive streak
PTYA	Preterm-delivered young adults

R

R	Right
(R)	Reverse (primer)
RA	Right atrium
Rb	Retinoblastoma
rcf	Relative centrifugal force
RNA	Ribonucleic acid
rRNA	Ribosomal ribonucleic acid
$RO^{\bullet}$	Alkoxyl
ROS	Reactive oxygen species
RPKM	Read Per Kilobase of transcript per Million mapped reads
rpm	Rate per minute
RT	Room temperature
RT-qPCR	Quantitative real-time PCR

List of Abbreviations

RV	Right ventricle
S	
Salv	*Salvador*
S phase	Synthesis phase
SDS	Sodium dodecyl sulphate
SDS-PAGE	Sodium dodecyl sulphate-polyacrylamide gel electrophoresis
SEM	Standard error of the mean
SHF	Second heart field
S6K1	Ribosomal protein S6 kinase
SMC	Smooth muscle cell
SOD	Superoxide dismutase
SR	Sarcoplasmic reticulum
Sry	*Sex determining region of chromosome Y* gene
T	
T_A	Annealing temperature
TAZ	Transcriptional coactivator with PDZ-binding motif
TEAD	TEA domain family member
TnT	Troponin T
tRNA	Transfer ribonucleic acid
TRX	Thioredoxin
TYA	Term-born young adults
U	
UV	Ultraviolet
V	
VSMCs	Vascular smooth muscle cells
VV	Varicose great saphenous vein
W	
WB	Western blot
WGA	Wheat germ agglutinin
WHO	World health organization
wk	Gestational week
WPC	Weeks post conception
Y	
YAP	Yes-associated protein 1

8. List of Figures

Figure……Page number

List of Figures and Tables

9. List of Tables

Table……...Page number

10. References

Abukhdeir, A. M.; Park, B. H. (2008): P21 and P27: Roles in Carcinogenesis and Drug Resistance. In: Expert Reviews in Molecular Medicine 10, P. 1-18. DOI: 10.1017/S1462399408000744.

Ahmad, F.; Soe, S.; White, N.; Johnston, R.; Khan, I.; Liao, J.; Jones, M.; Prabhu, R.; Maconochie, I.; Theobald, P. (2018): Region-Specific Microstructure in the Neonatal Ventricles of a Porcine Model. In: Annals of Biomedical Engineering 46 (12), P. 2162–2176. DOI: 10.1007/s10439-018-2089-4.

Akgul, Y.; Word, R. A.; Ensign, L. M.; Yamaguchi, Y.; Lydon, J.; Hanes, J.; Mahendroo, M. (2014): Hyaluronan in Cervical Epithelia Protects Against Infection-mediated Preterm Birth. In: The Journal of Clinical Investigation 124 (12), P. 5481-5489. DOI: 10.1172/JCI78765.

Alkass, K.; Panula, J.; Westman, M.; Wu, T. D.; Guerquin-Kern, J. L.; Bergmann, O. (2015): No Evidence for Cardiomyocyte Number Expansion in Preadolescent Mice. In: Cell 163 (4), P. 1026-1036. DOI: 10.1016/j.cell.2015.10.035.

Altamirano, F.; Oyarce, C.; Silva, P.; Toyos, M.; Wilson, C.; Lavandero, S.; Uhlén, P.; Estrada, M. (2009): Testosterone induces Cardiomyocyte Hypertrophy through Mammalian Target of Rapamycin Complex 1 Pathway. In: The Journal of Endocrinology 202 (2), P. 299-307. DOI: 10.1677/JOE-09-0044.

American Heart Association (2015): All About Heart Rate (Pulse). 31.07.2015. Retrieved 19.07.2022, <https://www.heart.org/en/health-topics/high-blood-pressure/the-facts-about-high-blood-pressure/all-about-heart-rate-pulse>

Andersen, D. C.; Ganesalingam, S.; Jensen, C. H.; Sheikh, S. P. (2014): Do Neonatal Mouse Hearts regenerate following Heart Apex Resection?. In: Stem Cell Reports 2 (4), P. 406-413. DOI: 10.1016/j.stemcr.2014.02.008.

Anderson, R. H.; Spicer, D. E.; Brown, N. A.; Mohun, T. J. (2014): The Development of Septation in the Four-chambered Heart. In: The Anatomical Record 297 (8), P. 1414–1429. DOI: 10.1002/ar.22949.

Anmann, T.; Varikmaa, M.; Timohhina, N.; Tepp, K.; Shevchuk, I.; Chekulayev, V.; Saks, V.; Kaambre, T. (2014): Formation of Highly Organized Intracellular Structure and Energy Metabolism in Cardiac Muscle Cells during Postnatal Development of Rat Heart. In: Biochimicia et Biophysica Acta. 2014 Aug;1837 (8), P. 1350-1361. DOI: 10.1016/j.bbabio.2014.03.015.

Arai, M.; Suzuki, T.; Nagai, R. (1996): Sarcoplasmic Reticulum Genes are Upregulated in Mild Cardiac Hypertrophy but Downregulated in Severe Cardiac Hypertrophy Induced by Pressure Overload. In: Journal of Molecular and Cellular Cardiology 28 (8), P. 1583-1590. DOI: 10.1006/jmcc.1996.0149.

Arsenescu, G.; Sabău, M.; Roşca, G.; Roşca, S.; Avrigeanu, V. (1978): The Role of Increased Ca^{2+} Influx as a Possible Additional Adaptive Mechanism in Experimental Left Ventricular Hypertrophy. In: Physiology 15 (3), P. 157-160. DOI: (NO)

Asghar, U.; Witkiewicz, A. K.; Turner, N. C.; Knudsen, E. S. (2015): The History and Future of Targeting Cyclin-dependent Kinases in Cancer Therapy. In: Nature Reviews Drug Discovery 14 (2), P. 130–146. DOI: 10.1038/nrd4504.

References

Auchampach, J.; Han, L.; Huang, G. N.; Kühn, B.; Lough, J. W.; O'Meara, C. C.; Payumo, A. Y.; Rosenthal, N. A.; Sucov, H. M.; Yutzey, K. E.; Patterson, M. (2022): Measuring Cardiomyocyte Cell-cycle Ativity and Proliferation in the Age of Heart Regeneration. In: American Journal of Physiology 322 (4), P. 579-596. DOI: 10.1152/ajpheart.00666.2021.

Bae, J.; Salamon, R. J.; Brandt, E. B.; Paltzer, W. G.; Zhang, Z.; Britt, E. C.; Hacker, T. A.; Fan, J.; Mahmoud, A. I. (2021): Malonate Promotes Adult Cardiomyocyte Proliferation and Heart Regeneration. In: Circulation 143 (20), P. 1973-1986. DOI: 10.1161/CIRCULATIONAHA.120.049952.

Bak, S. T.; Harvald, E. B.; Ellman, D. G.; Mathiesen, S. B.; Chen, T.; Fang, S.; Andersen, K. S.; Fenger, C. D.; Burton, M.; Thomassen, M.; Andersen, D. C. (2023): Ploidy-stratified Single Cardiomyocyte Transcriptomics Map Zinc Finger E-Box Binding Homeobox 1 to Underly Cardiomyocyte Proliferation Before Birth. In: Basic Research in Cardiology 118 (1), P. 8-31. DOI: 10.1007/s00395-023-00979-2.

Balasubramanian, S.; Kuppuswamy, D. (2003): RGD-Containing Peptides activate S6K1 through Beta3 Integrin in Adult Cardiac Muscle Cells. In: The Journal of Biological Chemistry 278 (43), P. 42214-42224. DOI: 10.1074/jbc.M303428200.

Bartek, J.; Bartkova, J.; Lukas, J. (1996): The Retinoblastoma Protein Pathway and the Restriction Point. In: Current Opinion in Cell Biology 8 (6), P. 805-814. DOI: 10.1016/s0955-0674(96)80081-0.

Bauer, D. E.; Harris, M. H.; Plas, D. R.; Lum, J. J.; Hammerman, P. S.; Rathmell, J. C.; Riley, J. L.; Thompson, C. B. (2004): Cytokine Stimulation of Aerobic Glycolysis in Hematopoietic Cells exceeds Proliferative Demand. In: FASEB Journal 18 (11), P. 1303-1305. DOI: 10.1096/fj.03-1001fje.

Bell, M. R. (2018): Comparing Postnatal Development of Gonadal Hormones and Associated Social Behaviors in Rats, Mice, and Humans. In: Endocrinology 159 (7), P. 2596-2613. DOI: 10.1210/en.2018-00220.

Bennesch, M. A.; Picard, D. (2015): Minireview: Tipping the Balance: Ligand-independent Activation of Steroid Receptors. In: Molecular Endocrinology 29 (3), P. 349-363. DOI: 10.1210/me.2014-1315.

Bensley, J. G.; Stacy, V. K.; De Matteo, R.; Harding, R.; Black, M. J. (2010): Cardiac Remodelling as a Result of Pre-term Birth: Implications for Future Cardiovascular Disease. In: European Heart Journal 31 (16), P. 2058-2066. DOI: 10.1093/eurheartj/ehq104.

Bensley, J. G.; Moore, L.; De Matteo, R.; Harding, R.; Black, M. J. (2018): Impact of Preterm Birth on the Developing Myocardium of the Neonate. In: Pediatric Research 83 (4), P. 880-888. DOI: 10.1038/pr.2017.324.

Bergmann, O.; Bhardwaj, R. D.; Bernard, S.; Zdunek, S.; Barnabé-Heider, F.; Walsh, S.; Zupicich, J.; Alkass, K.; Buchholz, B. A.; Druid, H.; Jovinge, S.; Frisén, J. (2009): Evidence for Cardiomyocyte Renewal in Humans. In: Science 324 (5923), P. 98-102. DOI: 10.1126/science.1164680.

Bergmann, O.; Zdunek, S.; Felker, A.; Salehpour, M.; Alkass, K.; Bernard, S.; Sjostrom, S. L.; Szewczykowska, M.; Jackowska, T.; Dos Remedios, C.; Malm, T.; Andrä, M.; Jashari, R.; Nyengaard, J. R.; Possnert, G.; Jovinge, S.; Druid, H.; Frisén, J. (2015): Dynamics of Cell Generation and Turnover in the Human Heart. In: Cell 161 (7), P. 1566-1575. DOI: 10.1016/j.cell.2015.05.026.

References

Bersell, K.; Arab, S.; Haring, B.; Kühn, B. (2009): Neuregulin1/ErbB4 Signaling induces Cardiomyocyte Proliferation and Repair of Heart Injury. In: Cell 138 (2), P. 257-270. DOI: 10.1016/j.cell.2009.04.060.

Blencowe, H.; Cousens, S.; Chou, D.; Oestergaard, M.; Say, L.; Moller, A. B.; Kinney, M.; Lawn, J. (2013): Born Too Soon: The Global Epidemiology of 15 Million Preterm Births. In: Reprod Health 10 (Suppl 1), Suppl.: 1-2. DOI: 10.1186/1742-4755-10-S1-S2.

Boettcher, M.; McManus, M. T. (2015): Choosing the Right Tool for the Job: RNAi, TALEN, or CRISPR. In: Molecular Cell 58 (4), P. 575-585. DOI: 10.1016/j.molcel.2015.04.028.

Bogush, N.; Tan, L.; Naib, H.; Faizullabhoy, E.; Calvert, J. W.; Iismaa, S. E.; Gupta, A.; Ramchandran, R.; Martin, D. I. K.; Graham, R. M.; Husain, A.; Naqvi, N. (2020): DUSP5 Expression in Left Ventricular Cardiomyocytes of Young Hearts Regulates Thyroid Hormone (T3)-induced Proliferative ERK1/2 Signaling. In: Scientific Reports 10 (1), P. 21918-21931. DOI: 10.1038/s41598-020-78825-x.

Brodsky, V. Ya.; Sarkisov, D. S.; Arefyeva, A. M.; Panova, N. W.; Gvasava, I. G. (1994): Polyploidy in Cardiac Myocytes of Normal and Hypertrophic Human Hearts; Range of Values. In: Virchows Archive: An International Journal of Pathology 424 (4), P. 429-435. DOI: 10.1007/BF00190566.

Buckingham, M.; Meilhac, S.; Zaffran, S. (2005): Building the Mammalian Heart from Two Sources of Myocardial Cells. In: Nature Reviews Genetics 6 (11), P. 826–835. DOI: 10.1038/nrg1710.

Buettner, G. R. (2011): Superoxide Dismutase in Redox Biology: The Roles of Superoxide and Hydrogen Peroxide. In: Anticancer Agents in Medicinal Chemistry 11 (4), P. 341-346. DOI: 10.2174/187152011795677544.

Burrell, J. H.; Boyn, A. M.; Kumarasamy, V.; Hsieh, A.; Head, S. I.; Lumbers, E. R. (2003): Growth and Maturation of Cardiac Myocytes in Fetal Sheep in the Second Half of Gestation. In: Anatomical Records 274 (2), P. 952-961. DOI: 10.1002/ar.a.10110.

Burton, G. J.; Jauniaux, E. (2011): Oxidative Stress. In: Best Practice and Research 25 (3), P. 287-299. DOI: 10.1016/j.bpobgyn.2010.10.016.

Busk, P. K.; Bartkova, J.; Strøm, C. C.; Wulf-Andersen, L.; Hinrichsen, R.; Christoffersen, T. E.; Latella, L.; Bartek, J.; Haunsø, S.; Sheikh, S. P. (2002): Involvement of Cyclin D Activity in Left Ventricle Hypertrophy in Vivo and in Vitro. In: Cardiovascular Research 56 (1), P. 64-75. DOI: 10.1016/s0008-6363(02)00510-2.

Busk, P. K.; Hinrichsen, R.; Bartkova, J.; Hansen, A. H.; Christoffersen, T. E.; Bartek, J.; Haunsø, S. (2005): Cyclin D2 induces Proliferation of Cardiac Myocytes and represses Hypertrophy. In: Experimental Cell Research 304 (1), P. 149-161. DOI: 10.1016/j.yexcr.2004.10.022.

Cadenas, E.; Davies, K. J. (2000): Mitochondrial Free Radical Generation, Oxidative Stress, and Aging. In: Free Radical Biology & Medicine 29 (4), P. 222-230. DOI: 10.1016/s0891-5849(00)00317-8.

Callus, B. A.; Verhagen, A. M.; Vaux, D. L. (2006): Association of Mammalian Sterile Twenty Kinases, Mst1 and Mst2, with HSalvador via C-Terminal Coiled-Coil Domains, leads to its Stabilization and Phosphorylation. In: Federation of European Biochemical Societies Journal 273 (18), P. 4264-4276. DOI: 10.1111/j.1742-4658.2006.05427.x.

References

Camelliti, P.; Borg, Th. K.; Kohl, P. (2005): Structural and Functional Characterisation of Cardiac Fibroblasts. In: Cardiovascular Research 65 (1), P. 40–51. DOI: 10.1016/j.cardiores.2004.08.020.

Camenisch, G.; Pisabarro, M. T.; Sherman, D.; Kowalski, J.; Nagel, M.; Hass, P.; Xie, M. H.; Gurney, A.; Bodary, S.; Liang, X. H.; Clark, K.; Beresini, M.; Ferrara, N.; Gerber, H. P. (2002): ANGPTL3 Stimulates Endothelial Cell Adhesion and Migration via Integrin Alpha Vbeta 3 and Induces Blood Vessel Formation in Vivo. In: The Journal of Biological Chemistry 277 (19), P. 17281-17290. DOI: 10.1074/jbc.M109768200.

Captur, G.; Wilson, R.; Bennett, M. F.; Luxán, G.; Nasis, A.; de la Pompa, J. L. (2016): Morphogenesis of Myocardial Trabeculae in the Mouse Embryo. In: Journal of Anatomy 229 (2), P. 314–325. DOI: 10.1111/joa.12465.

Cardoso-Moreira, M.; Halbert, J.; Valloton, D.; Velten, B.; Chen, C.; Shao, Y.; Liechti, A.; Ascenção, K.; Rummel, C.; Ovchinnikova, S.; Mazin, P. V.; Xenarios, I.; Harshman, K.; Mort, M.; Cooper, D. N.; Sandi, C.; Soares, M. J.; Ferreira, P. G.; Afonso, S.; Carneiro, M.; Turner, J. M. A.; VandeBerg, J. L.; Fallahshahroudi, A.; Jensen, P.; Behr, R.; Lisgo, S.; Lindsay, S.; Khaitovich, P.; Huber, W.; Baker, J.; Anders, S.; Zhang, Y. E.; Kaessmann, H. (2019): Gene Expression Across Mammalian Organ Development. In: Nature 571 (7766), P. 505-509. DOI: 10.1038/s41586-019-1338-5.

Carr, H.; Cnattingius, S.; Granath, F.; Ludvigsson, J. F.; Edstedt Bonamy, A. K. (2017): Preterm Birth and Risk of Heart Failure Up to Early Adulthood. In: Journal of the American College of Cardiology 69 (21), P. 2634-2642. DOI: 10.1016/j.jacc.2017.03.572.

Carrasco, L.; Cea, P.; Rocco, P.; Peña-Oyarzún, D.; Rivera-Mejias, P.; Sotomayor-Flores, C.; Quiroga, C.; Criollo, A.; Ibarra, C.; Chiong, M.; Lavandero, S. (2014): Role of Heterotrimeric G Protein and Calcium in Cardiomyocyte Hypertrophy induced by IGF-1. In: Journal of Cellular Biochemistry 115 (4), P. 712-720. DOI: 10.1002/jcb.24712.

Carroll, K. J.; Makarewich, C. A.; McAnally, J.; Anderson, D. M.; Zentilin, L.; Liu, N.; Giacca, M.; Bassel-Duby, R.; Olson, E. N. (2016): A Mouse Model for Adult Cardiac-specific Gene Deletion with CRISPR/Cas9. In: Proceeding of the National Academy of Sciences of the United States of America 113(2), P. 338-343. DOI: 10.1073/pnas.1523918113.

Carvalho, B. M. R.; Bassani, R. A.; Franchini, K. G.; Bassani, J. W. M. (2006): Enhanced Calcium Mobilization in Rat Ventricular Myocytes During the Onset of Pressure Overload-induced Hypertrophy. In: American Journal of Physiology. Heart and Circulatory Physiology 291 (4), P.1803-1813. DOI: 10.1152/ajpheart.01345.2005.

Chen, Z.; Indjeian, V. B.; McManus, M.; Wang, L.; Dynlacht, B. D. (2002): CP110, a Cell Cycle-dependent CDK Substrate, regulates Centrosome Duplication in Human Cells. In: Developmental Cell 3 (3), P. 339-350. DOI: 10.1016/s1534-5807(02)00258-7.

Chen, H.; Shi, S.; Acosta, L.; Li, W.; Lu, J.; Bao, S.; Chen, Z.; Yang, Z.; Schneider, M. D.; Chien, K. R.; Conway, S. J.; Yoder, M. C.; Haneline, L. S.; Franco, D.; Shou, W. (2004): BMP10 is Essential for Maintaining Cardiac Growth during Murine Cardiogenesis. In: Development 131 (9), P. 2219-2231. DOI: 10.1242/dev.01094.

Chen, S. N.; Gurha, P.; Lombardi, R.; Ruggiero, A.; Willerson, J. T.; Marian, A. J. (2014): The Hippo Pathway is Activated and is a Causal Mechanism for Adipogenesis in Arrhythmogenic Cardiomyopathy. In: Circulation Research 114 (3), P. 454-468. DOI: 10.1161/CIRCRESAHA.114.302810.

References

Chen, Z.; Xie, J.; Hao, H.; Lin, H.; Wang, L.; Zhang, Y.; Chen, L.; Cao, S.; Huang, X.; Liao, W.; Bin, J.; Liao, Y. (2017): Ablation of Periostin Inhibits Post-Infarction Myocardial Regeneration in Neonatal Mice Mediated by the Phosphatidylinositol 3 Kinase/glycogen Synthase Kinase 3β/cyclin D1 Signalling Pathway. In: Cardiovascular Research 113 (6), P. 620-632. DOI: 10.1093/cvr/cvx001.

Cheng, R. K.; Asai, T.; Tang, H.; Dashoush, N. H.; Kara, R. J.; Costa, K. D.; Naka, Y.; Wu, E. X.; Wolgemuth, D. J.; Chaudhry, H. W. (2007): Cyclin A2 induces Cardiac Regeneration after Myocardial Infarction and prevents Heart Failure. In: Circulation Research 100 (12), P. 1741-1748. DOI: 10.1161/CIRCRESAHA.107.153544.

Chien, K. R.; Domian, I. J.; Parker, K. K. (2008): Cardiogenesis and the Complex Biology of Regenerative Cardiovascular Medicine. In: Science 322 (5907), P. 1494-1497. DOI: 10.1126/science.1163267.

Cho, Y. M.; Kwon, S.; Pak, Y. K.; Seol, H. W.; Choi, Y. M.; Park, D. J.; Park, K. S.; Lee, H. K. (2006): Dynamic Changes in Mitochondrial Biogenesis and Antioxidant Enzymes during the Spontaneous Differentiation of Human Embryonic Stem Cells. In: Biochemical and Biophysical Research Communications 348 (4), P. 1472-1478. DOI: 10.1016/j.bbrc.2006.08.020.

Choi, J. W.; Lee, K. H.; Kim, S. H.; Jin, T.; Lee, B. S.; Oh, J.; Won, H. Y.; Kim, S. Y.; Kang, S. M.; Chung, J. H. (2011): C-Reactive Protein induces p53-mediated Cell Cycle Arrest in H9c2 Cardiac Myocytes. In: Biochemical and Biophysical Research Communications 410 (3), P. 525-530. DOI: 10.1016/j.bbrc.2011.06.016.

Chung, S.; Dzeja, P. P.; Faustino, R. S.; Perez-Terzic, C.; Behfar, A.; Terzic, A. (2007): Mitochondrial Oxidative Metabolism is required for the Cardiac Differentiation of Stem Cells. In: Nature Clinical Practice. Cardiovasc Medicine 4 (1), P. 60-67. DOI: 10.1038/ncpcardio0766.

Cleaton, M. A.; Dent, C. L.; Howard, M.; Corish, J. A.; Gutteridge, I.; Sovio, U.; Gaccioli, F.; Takahashi, N.; Bauer, S. R.; Charnock-Jones, D. S.; Powell, T. L.; Smith, G. C.; Ferguson-Smith, A. C.; Charalambous, M. (2016): Fetus-derived DLK1 is Required for Maternal Metabolic Adaptations to Pegnancy and is Associated with Fetal Growth Restriction. In: Nature Genetics 48 (12), P. 1473-1480. DOI: 10.1038/ng.3699.

Cohen, S. (1965): The Stimulation of Epidermal Proliferation by a Specific Protein (EGF). In: Developmental Biology 12 (3), P. 394-407. DOI: 10.1016/0012-1606(65)90005-9.

Contreras-Ramos, A.; Sánchez-Gómez, C.; García-Romero, H. L.; Cimarosti, L. O. (2008): Normal Development of the Muscular Region of the Interventricular Septum--I. The Significance of the Ventricular Trabeculations. In: Anatomia, Histologia, Embryologia 37 (5), P. 344–351. DOI: 10.1111/j.1439-0264.2008.00852.x.

Corbier, P.; Edwards, D. A.; Roffi ,J. (1992): The Neonatal Testosterone Surge: A Comparative Study. In: Archives Internationales de Physiologie, de Biochimie et de Biophysique 100 (2), P. 127-131. DOI: 10.3109/13813459209035274.

Crump, C.; Howell, E. A.; Stroustrup, A.; McLaughlin, M. A.; Sundquist, J.; Sundquist, K. (2019): Association of Preterm Birth with Risk of Ischemic Heart Disease in Adulthood. In: JAMA Pediatrics 173(8), P. 736-743. DOI: 10.1001/jamapediatrics.2019.1327.

Dadson, K.; Turdi, S.; Hashemi, S.; Zhao, J.; Polidovitch, N.; Beca, S.; Backx, P. H.; McDermott, J. C.; Sweeney, G. (2015): Adiponectin is required for Cardiac MEF2 Activation during Pressure Overload induced Hypertrophy. In: Journal of Molecular and Cellular Cardiology 86, P. 102-109. DOI: 10.1016/j.yjmcc.2015.06.020.

References

Dai, R.; Lin, Y.; Liu, H.; Rao, J.; Zhai, Y.; Zha, X.; Fang, X.; Xu, H. (2015): A Vital Role for Angptl3 in the PAN-Induced Podocyte Loss by Affecting Detachment and Apoptosis in Vitro. In: BMC Nephrology 16 (38), P. 1-10. DOI: 10.1186/s12882-015-0034-4.

Dai, D. F.; Danoviz, M. E.; Wiczer, B.; Laflamme, M. A.; Tian, R. (2017): Mitochondrial Maturation in Human Pluripotent Stem Cell Derived Cardiomyocytes. In: Stem Cells International 2017, P. 5153625-5153634. DOI: 10.1155/2017/5153625.

Darehzereshki, A.; Rubin, N.; Gamba, L.; Kim, J.; Fraser, J.; Huang, Y.; Billings, J.; Mohammadzadeh, R.; Wood, J.; Warburton, D.; Kaartinen, V.; Lien, C. L. (2015): Differential Regenerative Capacity of Neonatal Mouse Hearts after Cryoinjury. In: Developmental Biology 399 (1), P. 91-99. DOI: 10.1016/j.ydbio.2014.12.018.

De Acetis, M.; Notte, A.; Accornero, F.; Selvetella, G.; Brancaccio, M.; Vecchione, C.; Sbroggiò, M.; Collino, F.; Pacchioni, B.; Lanfranchi, G.; Aretini, A.; Ferretti, R.; Maffei, A.; Altruda, F.; Silengo, L.; Tarone, G.; Lembo, G. (2005): Cardiac Overexpression of Melusin protects from Dilated Cardiomyopathy due to Long-Standing Pressure Overload. In: Circulation Research 96 (10), P. 1087-1094. DOI: 10.1161/01.RES.0000168028.36081.e0.

De la Cruz, M.; Gómez, C.; Cayre, R. (1991): The Developmental Components of the Ventricles: Their Significance in Congenital Cardiac Malformations. In: Cardiology in the Young 1 (2), P. 123-128. DOI: 10.1017/S1047951100000238.

Deng, Y.; Pang, A.; Wang, J. H. (2003): Regulation of Mammalian STE20-Like Kinase 2 (MST2) by Protein Phosphorylation/dephosphorylation and Proteolysis. In: The Journal of Biological Biol Chemistry 278 (14), P. 11760-11767. DOI: 10.1074/jbc.M211085200.

DeRuiter, M. C.; Poelmann, R. E.; VanderPlas-de Vries, I.; Mentink, M. M.; Gittenberger-de Groot, A. C. (1992): The Development of the Myocardium and Endocardium in Mouse Embryos. Fusion of Two Heart Tubes? In: Anatomy and Embryology 185 (5), P. 461–473. DOI: 10.1007/BF00174084.

Dettman, R. W.; Denetclaw, W. Jr.; Ordahl, C. P.; Bristow, J. (1998): Common Epicardial Origin of Coronary Vascular Smooth Muscle, Perivascular Fibroblasts, and Intermyocardial Fibroblasts in the Avian Heart. In: Developmental Biology 193 (2), P. 169-181. DOI: 10.1006/dbio.1997.8801.

Dhalla, N. S.; Golfman, L.; Liu, X.; Sasaki, H.; Elimban, V.; Rupp, H. (1999): Subcellular Remodeling and Heart Dysfunction in Cardiac Hypertrophy Due to Pressure Overload. In: Annals of the New York Academy of Sciences 874 (1), P. 100-110. DOI: 10.1111/j.1749-6632.1999.tb09228.x.

Di Agostino, S.; Sorrentino, G.; Ingallina, E.; Valenti, F.; Ferraiuolo, M.; Bicciato, S.; Piazza, S.; Strano, S.; Del Sal, G.; Blandino, G. (2016): YAP enhances the Pro-proliferative Transcriptional Activity of Mutant p53 Proteins. In: EMBO Reports 17 (2), P. 188-201. DOI: 10.15252/embr.201540488.

Díaz Del Moral, S.; Benaouicha, M.; Muñoz-Chápuli, R.; Carmona, R. (2021): The Insulin-like Growth Factor Signalling Pathway in Cardiac Development and Regeneration. In: International Journal of Molecular Sciences 23 (1), P. 234-244. DOI: 10.3390/ijms23010234.

Ding, L.; Cao, J.; Lin, W.; Chen, H.; Xiong, X.; Ao, H.; Yu, M.; Lin, J.; Cui, Q. (2020): The Roles of Cyclin-Dependent Kinases in Cell-Cycle Progression and Therapeutic Strategies in Human Breast Cancer. In: International Journal of Molecular Sciences 21 (6), P. 1960-1987. DOI: 10.3390/ijms21061960.

References

Di Stefano, V.; Giacca, M.; Capogrossi, M. C.; Crescenzi, M.; Martelli, F. (2011): Knockdown of Cyclin-Dependent Kinase Inhibitors induces Cardiomyocyte Re-entry in the Cell Cycle. In: The Journal of Biological Chemistry 286 (10), P. 8644-8654. DOI: 10.1074/jbc.M110.184549.

Doble, B. W.; Woodgett, J. R. (2003): GSK-3: Tricks of the Trade for a Multi-tasking Kinase. In: Journal of Cell Science116 (Pt 7), P. 1175-1186. DOI: 10.1242/jcs.00384.

Doenst, T.; Nguyen, T. D.; Abel, E. D. (2013): Cardiac Metabolism in Heart Failure: Implications Beyond ATP Production. In: Circulation Research 113 (6), P. 709-724. DOI: 10.1161/CIRCRESAHA.113.300376.

Dorn, L. E.; Lawrence, W.; Petrosino, J. M.; Xu, X.; Hund, T. J.; Whitson, B. A.; Stratton, M. S.; Janssen, P. M. L.; Mohler, P. J.; Schlosser, A.; Sorensen, G. L.; Accornero, F. (2021): Microfibrillar-Associated Protein 4 Regulates Stress-Induced Cardiac Remodeling. In: Circulation Research 128 (6), P. 723-737. DOI: 10.1161/CIRCRESAHA.120.317146.

dos Santos, R. L.; da Silva, F. B.; Ribeiro, R. F. Jr.; Stefanon, I. (2014): Sex Hormones in the Cardiovascular System. In: Hormone Molecular Biology and Clinical Investigation 18 (2), P. 89-103. DOI: 10.1515/hmbci-2013-0048.

Drenckhahn, J. D.; Schwarz, Q. P.; Gray, S.; Laskowski, A.; Kiriazis, H.; Ming, Z.; Harvey, R. P.; Du, X. J.; Thorburn, D. R.; Cox, T. C. (2008): Compensatory Growth of Healthy Cardiac Cells in the Presence of Diseased Cells restores Tissue Homeostasis during Heart Development. In: Developmental Cell 15 (4), P. 521-533. DOI: 10.1016/j.devcel.2008.09.005.

Dutta, S.; Mark-Kappeler, C. J.; Hoyer, P. B.; Pepling, M. E. (2014): The Steroid Hormone Environment during Primordial Follicle Formation in Perinatal Mouse Ovaries. In: Biology of Reproduction 91 (3), P. 68-79. DOI: 10.1095/biolreprod.114.119214.

D'Uva, G.; Aharonov, A.; Lauriola, M.; Kain, D.; Yahalom-Ronen, Y.; Carvalho, S.; Weisinger, K.; Bassat, E.; Rajchman, D.; Yifa, O.; Lysenko, M.; Konfino, T.; Hegesh, J.; Brenner, O.; Neeman, M.; Yarden, Y.; Leor, J.; Sarig, R.; Harvey, R. P.; Tzahor, E. (2015): ERBB2 triggers Mammalian Heart Regeneration by Promoting Cardiomyocyte Dedifferentiation and Proliferation. In: Nature Cell Biology 17 (5), P. 627-638. DOI: 10.1038/ncb3149.

Eiby, Y. A.; Lumbers, E. R.; Headrick, J. P.; Lingwood, B. E. (2012): Left Ventricular Output and Aortic Blood Flow in Response to Changes in Preload and Afterload in the Preterm Piglet Heart. In: American Journal of Physiology: Regulatory, Integrative, and Comparative Physiology 303 (7), P. 769-777. DOI: 10.1152/ajpregu.00010.2012.

Eisenberg, L.; Markwald, R. (1995): Molecular Regulation of Atrioventricular Valvuloseptal Morphogenesis. In Circulation Research 77 (1), P. 1–6. DOI: 10.1161/01.RES.77.1.1.

Ek, B.; Westermark, B.; Wasteson, A.; Heldin, C. H. (1982): Stimulation of Tyrosine-Specific Phosphorylation by Platelet-Derived Growth Factor. In: Nature 295 (5848), P. 419-420. DOI: 10.1038/295419a0.

Engel, F. B.; Schebesta, M.; Duong, M. T.; Lu, G.; Ren, S.; Madwed, J. B.; Jiang, H.; Wang, Y.; Keating, M. T. (2005): p38 MAP Kinase Inhibition enables Proliferation of Adult Mammalian Cardiomyocytes. In: Genes and Development 19 (10), P. 1175-1187. DOI: 10.1101/gad.1306705.

Evans, J. L.; Goldfine, I. D.; Maddux, B. A.; Grodsky, G. M. (2003): Are Oxidative Stress-activated Signaling Pathways Mediators of Insulin Resistance and Beta-cell Dysfunction?. In: Diabetes 52 (1), P. 1-8. DOI: 10.2337/diabetes.52.1.1.

References

Fiala, G. J.; Minguet, S. (2018): Caveolin-1: The Unnoticed Player in TCR and BCR Signaling. In: Advances in Immunology 137, P. 83-133. DOI: 10.1016/bs.ai.2017.12.002.

Finn, C. A. (1963): Reproductive Capacity and Litter Size in Mice: Effect of Age and Environment. In: Journal of Reproduction and Fertility 6, P. 205-214. DOI: 10.1530/jrf.0.0060205.

Fisk, H. A.; Winey, M. (2001): The Mouse Mps1p-like Kinase rRgulates Centrosome Duplication. In: Cell 106 (1), P. 95-104. DOI: 10.1016/s0092-8674(01)00411-1.

Franco, D.; Meilhac, S. M.; Christoffels, V. M.; Kispert, A.; Buckingham, M.; Kelly, R.G. (2006): Left and Right Ventricular Contributions to the Formation of the Interventricular Septum in the Mouse Heart. In: Developmental Biology 294 (2), P. 366–375. DOI: 10.1016/j.ydbio.2006.02.045.

Frémin, C.; Saba-El-Leil, M. K.; Lévesque, K.; Ang, S. L.; Meloche, S. (2015): Functional Redundancy of ERK1 and ERK2 MAP Kinases during Development. In: Cell Reports 12 (6), P. 913-921. DOI: 10.1016/j.celrep.2015.07.011.

Fujimoto, N.; Honda, H.; Kitamura, S. (2004): Effects of Environmental Estrogenic Chemicals on AP1 Mediated Transcription with Estrogen Receptors Alpha and Beta. In: The Journal of Steroid Biochemistry and Molecular Biology 88 (1), P. 53-59. DOI: 10.1016/j.jsbmb.2003.10.006.

Galan, J. A.; Avruch, J. (2016): MST1/MST2 Protein Kinases: Regulation and Physiologic Roles. In: Biochemistry 55 (39), P. 5507-5519. DOI: 10.1021/acs.biochem.6b00763.

Gallini, R.; Lindblom, P.; Bondjers, C.; Betsholtz, C.; Andrae, J. (2016): PDGF-A and PDGF-B induces Cardiac Fibrosis in Transgenic Mice. In: Experimental Cell Research 49 (2), P. 282-290. DOI: 10.1016/j.yexcr.2016.10.022.

Gavet, O.; Pines, J. (2010): Progressive Activation of CyclinB1-Cdk1 Coordinates Entry to Mitosis. In: Developmental Cell 18 (4), P. 533–543. DOI: 10.1016/j.devcel.2010.02.013.

Gessner, I.; Krovetz, L. J.; Benson, R. W.; Prystowsky, H.; Stenger, V.; Eitzman, D. V. (1965): Hemodynamic Adaptations in the Newborn Infant. In: Pediatrics 36 (5):752-762. DOI: 10.1542/peds.36.5.752.

Gilbert, C. J.; Longenecker, J. Z.; Accornero, F. (2021): ERK1/2: An Integrator of Signals That Alters Cardiac Homeostasis and Growth. In: Biology 10 (4), P. 346-364. DOI: 10.3390/biology10040346.

Girard, J.; Ferré, P.; Pégorier, J. P.; Duée, P. H. (1992): Adaptations of Glucose and Fatty Acid Metabolism during Perinatal Period and Suckling-weaning Transition. In: Physiological Reviews 72 (2), P. 507-562. DOI: 10.1152/physrev.1992.72.2.507.

Gittenberger-de Groot, A. C.; Bartelings, M. M.; Deruiter, M. C.; Poelmann, R. E. (2005): Basics of Cardiac Development for the Understanding of Congenital Heart Malformations. In: Pediatric Research 57 (2), P. 169–176. DOI: 10.1203/01.PDR.0000148710.69159.61.

Gombash Lampe, S. E.; Kaspar, B. K.; Foust, K. D. (2014): Intravenous Injections in Neonatal Mice. In: Journal of Visualized Experiments 11; (93), P. 52037-52042. DOI: 10.3791/52037.

González-Rosa, J. M.; Sharpe, M.; Field, D.; Soonpaa, M. H.; Field, L. J.; Burns, C. E.; Burns, C. G. (2018): Myocardial Polyploidization Creates a Barrier to Heart Regeneration in Zebrafish. In: Developmental Cell 44 (4), P.433-446. DOI: 10.1016/j.devcel.2018.01.021.

References

Gortney, J. S.; Sanders, R. M. (2007): Impact of C-reactive Protein on Treatment of Patients with Cardiovascular Disease. In: American Journal of Health-System Pharmacy 64 (19), P. 2009-2016. DOI: 10.2146/ajhp060542.

Groves, A. M.; Chiesa, G.; Durighel, G.; Goldring, S. T.; Fitzpatrick, J. A.; Uribe, S.; Razavi, R.; Hajnal, J. V.; Edwards, A. D. (2011): Functional Cardiac MRI in Preterm and Term Newborns. In: Archives of Disease Childhood: Fetal and Neonatal Edition 96 (2), P. 86-91. DOI: 10.1136/adc.2010.189142.

Günthel, M.; Barnett, P.; Christoffels, V. M. (2018): Development, Proliferation, and Growth of the Mammalian Heart. In: Molecular Therapy: The Journal of the American Society of Gene Therapy 26 (7), P. 1599-1609. DOI: 10.1016/j.ymthe.2018.05.022.

Guo, Y.; Pu, W. T. (2020): Cardiomyocyte Maturation: New Phase in Development. In: Circulation Research 126 (8), P. 1086-1106. DOI: 10.1161/CIRCRESAHA.119.315862.

Halliwell, B.; Gutteridge, J. M. (1986): Oxygen Free Radicals and Iron in Relation to Biology and Medicine: some Problems and Concepts. In: Archives of Biochemistry and Biophysics 246 (2), P. 501-514. DOI: 10.1016/0003-9861(86)90305-x.

Hallman, M. (1971): Changes in Mitochondrial Respiratory Chain Proteins during Perinatal Development. Evidence of the Importance of Environmental Oxygen Tension. In: Biochimica et Biophysica Acta 253 (2), P. 360-372. DOI: 10.1016/0005-2728(71)90040-5

Hatem, S. N.; Redheuil, A.; Gandjbakhch, E. (2016): Cardiac Adipose Tissue and Atrial Fibrillation: The Perils of Adiposity. In: Cardiovascular Research 109 (4), P. 502-509. DOI: 10.1093/cvr/cvw001.

Haubner, B. J.; Adamowicz-Brice, M.; Khadayate, S.; Tiefenthaler, V.; Metzler, B.; Aitman, T.; Penninger, J. M. (2012): Complete Cardiac Regeneration in a Mouse Model of Myocardial Infarction. In: Aging 4 (12), P. 966-797. DOI: 10.18632/aging.100526.

Haubner, B. J.; Schneider, J.; Schweigmann, U.; Schuetz, T.; Dichtl, W.; Velik-Salchner, C.; Stein, J. I.; Penninger, J. M. (2016): Functional Recovery of a Human Neonatal Heart After Severe Myocardial Infarction. In: Circulation Research 118 (2), P. 216-221. DOI: 10.1161/CIRCRESAHA.115.307017.

Häuselmann, S. P.; Rosc-Schlüter, B. I.; Lorenz, V.; Plaisance, I.; Brink, M.; Pfister, O.; Kuster, G. M. (2011): β1-Integrin is Up-Regulated via Rac1-Dependent Reactive Oxygen Species as Part of the Hypertrophic Cardiomyocyte Response. In: Free Radical Biology and Medicine 51 (3), P. 609-618. DOI: 10.1016/j.freeradbiomed.2011.05.007.

Hay, N.; Sonenberg, N. (2004): Upstream and Downstream of mTOR. In: Genes and Development 18 (16), P. 1926-1945. DOI: 10.1101/gad.1212704.

Haynes, M. P.; Sinha, D.; Russell, K. S.; Collinge, M.; Fulton, D.; Morales-Ruiz, M.; Sessa, W. C.; Bender, J. R. (2000): Membrane Estrogen Receptor Engagement activates Endothelial Nitric Oxide Synthase via the PI3-kinase-Akt Pathway in Human Endothelial Cells. In: Circulation Research 87 (8), P. 677-682. DOI: 10.1161/01.res.87.8.677.

Haynes, M. P.; Li, L.; Sinha, D.; Russell, K. S.; Hisamoto, K.; Baron, R.; Collinge, M.; Sessa, W. C.; Bender, J. R. (2003): Src Kinase Mediates Phosphatidylinositol 3-kinase/Akt-dependent Rapid Endothelial Nitric-oxide Synthase Activation by Estrogen. In: The Journal of Biological Chemistry 78 (4), P. 2118-2123. DOI: 10.1074/jbc.M210828200.

References

Heallen, T.; Zhang, M.; Wang, J.; Bonilla-Claudio, M.; Klysik, E.; Johnson, R. L.; Martin, J. F. (2011): Hippo Pathway Inhibits Wnt Signaling to Restrain Cardiomyocyte Proliferation and Heart Size. In: Science 332 (6028), P. 458-461. DOI: 10.1126/science.1199010.

Heallen, T.; Morikawa, Y.; Leach, J.; Tao, G.; Willerson, J. T.; Johnson, R. L.; Martin, J. F. (2013): Hippo Signaling Impedes Adult Heart Regeneration. In: Development 140 (23), P. 4683-4690. DOI: 10.1242/dev.102798.

Heallen, T. R.; Kadow, Z. A.; Wang, J.; Martin, J. F. (2020): Determinants of Cardiac Growth and Size. In: Cold Spring Harbor Perspectives in Biology 12 (3), a. 037150. DOI: 10.1101/cshperspect.a037150.

Heldin, C. H.; Ostman, A.; Rönnstrand, L. (1998): Signal Transduction via Platelet-derived Growth Factor Receptors. In: Biochimica et Biophysica Acta 1378 (1), P. 79-113. DOI: 10.1016/s0304-419x(98)00015-8.

Hennig, M.; Fiedler, S.; Jux, Ch.; Thierfelder, L.; Drenckhahn, J. D. (2017): Prenatal Mechanistic Target of Rapamycin Complex 1 (m TORC1) Inhibition by Rapamycin Treatment of Pregnant Mice Causes Intrauterine Growth Restriction and Alters Postnatal Cardiac Growth, Morphology, and Function. Journal of the American Heart Association 6 (8), P. e005506. DOI: 10.1161/JAHA.117.005506.

Hirai, M.; Chen, J.; Evans, S. M. (2016): Tissue-Specific Cell Cycle Indicator Reveals Unexpected Findings for Cardiac Myocyte Proliferation. In: Circulation Research 118 (1), P. 20-28. DOI: 10.1161/CIRCRESAHA.115.307697.

Hirotani, S.; Zhai, P.; Tomita, H.; Galeotti, J.; Marquez, J. P.; Gao, S.; Hong, C.; Yatani, A.; Avila, J.; Sadoshima, J. (2007): Inhibition of Glycogen Synthase Kinase 3beta During Heart Failure is Protective. In: Circulation Research 101 (11), P. 1164-1174. DOI: 10.1161/CIRCRESAHA.107.160614.

Hoeijmakers, J. H. (2009): DNA Damage, Aging, and Cancer. In: The New England Journal of Medicine 361 (15), P. 1475-1485. DOI: 10.1056/NEJMra0804615.

Hoffman, J. I. (1995): Incidence of Congenital Heart Disease: I. Postnatal Incidence. In: Pediatric Cardiology 16 (3), P. 103–113. DOI: 10.1007/BF00801907.

Hoffmann, J. I. E.; Kaplan, S. (2002): The Incidence of Congenital Heart Disease. In: Journal of the American College of Cardiology 39 (12), P. 1890-1900. DOI: 10.1016/S0735-1097(02)01886-7.

Honkoop, H.; de Bakker, D. E.; Aharonov, A.; Kruse, F.; Shakked, A.; Nguyen, P. D.; de Heus ,C.; Garric, L.; Muraro, M. J.; Shoffner, A., Tessadori, F.; Peterson, J. C.; Noort, W.; Bertozzi, A.; Weidinger, G.; Posthuma, G.; Grün, D.; van der Laarse, W. J.; Klumperman, J.; Jaspers, R. T.; Poss, K. D.; van Oudenaarden, A.; Tzahor, E.; Bakkers, J. (2019): Single-cell Analysis uncovers that Metabolic Reprogramming by ErbB2 Signaling is Essential for Cardiomyocyte Proliferation in the Regenerating Heart. In: Elife 23 (8), P. 50163-50189. DOI: 10.7554/eLife.50163.

Huang, Y.; Hickey, R. P.; Yeh, J. L.; Liu, D.; Dadak, A.; Young, L. H.; Johnson, R. S.; Giordano, F. J. (2004): Cardiac Myocyte-Specific HIF-1alpha Deletion alters Vascularization, Energy Availability, Calcium flux, and Contractility in the Normoxic Heart. In: FASEB Journal 18 (10), P. 1138-1140. DOI: 10.1096/fj.04-1510fje.

Huckstep, O. J.; Williamson, W.; Telles, F.; Burchert, H.; Bertagnolli, M.; Herdman, C.; Arnold, L.; Smillie, R.; Mohamed, A.; Boardman, H.; McCormick, K.; Neubauer, S.; Leeson, P.;

References

Lewandowski, A. J. (2018): Physiological Stress Elicits Impaired Left Ventricular Function in Preterm-Born Adults. In: Journal of the American College of Cardiology 71 (12), P. 1347-1356. DOI: 10.1016/j.jacc.2018.01.046.

Ikenishi, A.; Okayama, H.; Iwamoto, N.; Yoshitome, S.; Tane, S.; Nakamura, K.; Obayashi, T.; Hayashi, T.; Takeuchi, T. (2012): Cell Cycle Regulation in Mouse Heart during Embryonic and Postnatal Stages. In: Development Growth & Differentiation 4 (8), P. 731-738. DOI: 10.1111/j.1440-169X.2012.01373.x.

Irasto World Health (2021): Anatomy of the Human Heart. 23.05.2021, Retrieved 19.07.2022, <https://www.irastoworldhealth.com/cardiology/anatomy-of-the-human-heart>.

Iwenofu, O. H.; Lackman, R. D.; Staddon, A. P.; Goodwin, D. G.; Haupt, H. M.; Brooks, J. S. (2008): Phospho-S6 Ribosomal Protein: A Potential New Predictive Sarcoma Marker for Targeted mTOR Therapy. In: Modern Pathology 21 (3), P. 231-237. DOI: 10.1038/modpathol.3800995.

Jiang, S.; Qiu, G. H.; Zhu, N.; Hu, Z. Y.; Liao, D. F.; Qin, L. (2019): ANGPTL3: A Novel Biomarker and Promising Therapeutic Target. In: Journal of Drug Targeting 27 (8), P. 876-884. DOI: 10.1080/1061186X.2019.1566342.

Jiang, F. Q.; Liu, K.; Chen, J. X.; Cao, Y.; Chen, W. Y.; Zhao, W. L.; Song, G. H.; Liang, C. Q.; Zhou, Y. M.; Huang, H. L.; Huang, R. J.; Zhao, H.; Park, K. S.; Ju, Z.; Cai, D.; Qi, X. F. (2022): Mettl3-mediated m^6A Modification of Fgf16 Restricts Cardiomyocyte Proliferation during Heart Regeneration. In: ELife (11), P. 77014-77044. DOI: 10.7554/eLife.77014.

Jones, W. K.; Grupp, I. L.; Doetschman, T.; Grupp, G.; Osinska, H.; Hewett, T. E.; Boivin, G.; Gulick, J.; Ng, W. A.; Robbins, J. (1996): Ablation of the Murine Alpha Myosin Heavy Chain Gene leads to Dosage Effects and Functional Deficits in the Heart. In: The Journal of Clinical Investigations 98 (8), P. 1906-1917. DOI: 10.1172/JCI118992.

Jonker, S. S.; Louey, S.; Giraud, G. D.; Thornburg, K. L.; Faber, J. J. (2015): Timing of Cardiomyocyte Growth, Maturation, and Attrition in Perinatal Sheep. In: Official Publication of the Federation of American Societies for Experimental Biology Journal 29 (10), P. 4346-4357. DOI: 10.1096/fj.15-272013.

Jopling, C.; Sleep, E.; Raya, M.; Martí, M.; Raya, A.; Izpisúa Belmonte, J. C. (2010): Zebrafish Heart Regeneration occurs by Cardiomyocyte Dedifferentiation and Proliferation. In: Nature 464 (7288), P. 606-609. DOI: 10.1038/nature08899.

Judge, S.; Leeuwenburgh, C. (2007): Cardiac Mitochondrial Bioenergetics, Oxidative Stress, and Aging. In: The American Journal of Physiology 292 (6), P. 1983-1992. DOI: 10.1152/ajpcell.00285.2006.

Kalra, K.; Eberhard, J.; Farbehi, N.; Chong, J. J.; Xaymardan, M. (2021): Role of PDGF-A/B Ligands in Cardiac Repair After Myocardial Infarction. Frontiers in Cell and Developmental Biology 9, P. 669188. DOI: 10.3389/fcell.2021.669188.

Kamo, T.; Akazawa, H.; Komuro, I. (2015): Cardiac Nonmyocytes in the Hub of Cardiac Hypertrophy. In: Circulation Research 117 (1), P. 89-98. DOI: 10.1161/CIRCRESAHA.117.305349.

Kanda, M.; Nagai, T. (2018): SSBP1: A Target Molecule for Prevention of Fibrosis. In: International Heart Journal 59 (6), P. 1191-1193. DOI: 10.1536/ihj.18-530.

References

Kanvah, S.; Joseph, J.; Schuster, G. B.; Barnett, R. N.; Cleveland, C. L.; Landman, U. (2010): Oxidation of DNA: Damage to Nucleobases. In: Accounts of Chemical Research 43 (2), P. 280-287. DOI: 10.1021/ar900175a.

Karra, R.; Poss, K. D. (2017): Redirecting Cardiac Growth Mechanisms for Therapeutic Regeneration. In: The Journal of Clinical Investigation 127 (2), P. 427-436. DOI: 10.1172/JCI89786.

Kasai, H.; Nishimura, S. (1984): Hydroxylation of Deoxyguanosine at the C-8 Position by Ascorbic Acid and Other Reducing Agents. In: Nucleic Acids Research 12 (4), P. 2137-2145. DOI: 10.1093/nar/12.4.2137.

Kasuga, M.; Zick, Y.; Blithe, D. L.; Crettaz, M.; Kahn, C. R. (1982): Insulin stimulates Tyrosine Phosphorylation of the Insulin Receptor in a Cell-Free System. In: Nature 298 (5875), P. 667-669. DOI: 10.1038/298667a0. PMID: 6178977.

Kelly, R. G.; Brown, N. A.; Buckingham, M. E. (2001): The Arterial Pole of the Mouse Heart Forms from Fgf10-Expressing Cells in Pharyngeal Mesoderm. In: Developmental Cell 1 (3), P. 435-440. DOI: 10.1016/s1534-5807(01)00040-5.

Kilkenny, C.; Browne, W. J.; Cuthill, I. C.; Emerson, M.; Altman, D. G. (2010): Improving Bioscience Research Reporting: The ARRIVE Guidelines for Reporting Animal Research. In: PLoS Biology 8 (6), P. 1000412-1000416. DOI: 10.1371/journal.pbio.1000412.

Kim, M.; Oh, J. K.; Sakata, S.; Liang, I.; Park, W.; Hajjar, R. J.; Lebeche, D. (2008): Role of Resistin in Cardiac Contractility and Hypertrophy. In: Journal of Molecular and Cellular Cardiology 45 (2), P. 270-280. DOI: 10.1016/j.yjmcc.2008.05.006.

Kim, Y. S.; Jeong, H. Y.; Kim, A. R.; Kim, W. H.; Cho, H.; Um, J.; Seo, Y.; Kang, W. S.; Jin, S. W.; Kim, M. C.; Kim, Y. C.; Jung, D. W.; Williams, D. R.; Ahn, Y. (2016): Natural Product Derivative BIO promotes Recovery after Myocardial Infarction via Unique Modulation of the Cardiac Microenvironment. In: Scientific Reports 11 (6), P. 30726-30738. DOI: 10.1038/srep30726.

Kim, J. Y.; Jeong, H. S.; Chung, T.; Kim, M.; Lee, J. H.; Jung, W. H.; Koo, J. S. (2017): The Value of Phosphohistone H3 as a Proliferation Marker for Evaluating Invasive Breast Cancers: A Comparative Study with Ki67. In: Oncotarget 8 (39), P. 65064-65076. DOI: 10.18632/oncotarget.17775.

Kim, H.; Kim, M.; Im, S. K.; Fang, S. (2018): Mouse Cre-LoxP System: General Principles to determine Tissue-Specific Roles of Target Genes. In: Laboratory Animal Research 34 (4), P. 147-159. DOI: 10.5625/lar.2018.34.4.147.

Kimura, W.; Xiao, F.; Canseco, D. C.; Muralidhar, S.; Thet, S.; Zhang, H. M.; Abderrahman, Y.; Chen, R.; Garcia, J. A.; Shelton, J. M.; Richardson, J. A.; Ashour, A. M.; Asaithamby, A.; Liang, H.; Xing, C.; Lu, Z.; Zhang, C. C.; Sadek, H. A. (2015): Hypoxia Fate Mapping identifies Cycling Cardiomyocytes in the Adult Heart. In: Nature 523 (7559), P. 226-230. DOI: 10.1038/nature14582.

Kisucka, J.; Chauhan, A. K.; Patten, I. S.; Yesilaltay, A.; Neumann, C.; Van Etten, R. A.; Krieger, M.; Wagner, D. D. (2008): Peroxiredoxin1 prevents Excessive Endothelial Activation and Early Atherosclerosis. In: Circulation Research 103 (6), P. 598-605. DOI: 10.1161/CIRCRESAHA.108.174870.

References

Kluckow, M. (2005): Low Systemic Blood Flow and Pathophysiology of the Preterm Transitional Circulation. In: Early Human Development 81 (5), P. 429-437. DOI: 10.1016/j.earlhumdev.2005.03.006.

Koyama, T.; Ogawara, K.; Kasamatsu, A.; Okamoto, A.; Kasama, H.; Minakawa, Y.; Shimada, K.; Yokoe, H.; Shiiba, M.; Tanzawa, H.; Uzawa, K. (2015): ANGPTL3 is a Novel Biomarker as it activates ERK/MAPK Pathway in Oral Cancer. In: Cancer Medicine 4 (5), P. 759-769. DOI: 10.1002/cam4.418.

Krishnan, A.; Sharma, H.; Yuan, D.; Trollope, A. F.; Chilton, L. (2022): The Role of Epicardial Adipose Tissue in the Development of Atrial Fibrillation, Coronary Artery Disease and Chronic Heart Failure in the Context of Obesity and Type 2 Diabetes Mellitus : A Narrative Review. In: Journal of Cardiovascular Development and Disease 9 (7), P. 217-238. DOI: 10.3390/jcdd9070217.

Kühn, B.; del Monte, F.; Hajjar, R. J.; Chang, Y. S.; Lebeche, D.; Arab, S.; Keating, M. T. (2007): Periostin Induces Proliferation of Differentiated Cardiomyocytes and Promotes Cardiac Repair. In: Nature Medicine 13 (8), P. 962-969. DOI: 10.1038/nm1619.

Lal, H.; Verma, S. K.; Foster, D. M.; Golden, H. B.; Reneau, J. C.; Watson, L. E.; Singh, H.; Dostal, D. E. (2009): Integrins and Proximal Signaling Mechanisms in Cardiovascular Disease. In: Frontiers in Bioscience (Landmark Edition) 14 (6), P. 2307-2334. DOI: 10.2741/3381.

Lavine, K. J.; Epelman, S.; Uchida, K.; Weber, K. J.; Nichols, C. G.; Schilling, J. D.; Ornitz, D. M.; Randolph, G. J.; Mann, D. L. (2014): Distinct Macrophage Lineages Contribute to Disparate Patterns of Cardiac Recovery and Remodeling in the Neonatal and Adult Heart. In: Proceedings of the National Academy of Sciences of the United States of America 2111 (45), P. 16029-16034. DOI: 10.1073/pnas.1406508111.

Lê, B.; Dahl, M. J.; Albertine, K. H.; Sutherland, M. R.; Black, M. J. (2020): Preterm Birth with Neonatal Interventions Accelerates Collagen Deposition in the Left Ventricle of Lambs without Affecting Cardiomyocyte Development. In: CJC Open 3 (5), P. 574-584. DOI: 10.1016/j.cjco.2020.12.017.

Lee, A. C.; Katz, J.; Blencowe, H.; Cousens, S.; Kozuki, N.; Vogel, J. P.; Adair, L.; Baqui, A. H.; Bhutta, Z. A.; Caulfield, L. E.; Christian, P.; Clarke, S. E.; Ezzati, M.; Fawzi, W.; Gonzalez, R.; Huybregts, L.; Kariuki, S.; Kolsteren, P.; Lusingu, J.; Marchant, T.; Merialdi, M.; Mongkolchati, A.; Mullany, L. C.; Ndirangu, J.; Newell, M. L.; Nien, J. K.; Osrin, D.; Roberfroid, D.; Rosen, H. E.; Sania, A.; Silveira, M. F.; Tielsch, J.; Vaidya, A.; Willey, B. A.; Lawn, J. E.; Black, R. E.; CHERG SGA-Preterm Birth Working Group (2013): National and Regional Estimates of Term and Preterm Babies Born Small for Gestational Age in 138 Low-income and Middle-income Countries in 2010. In: Lancet Glob Health 1 (1), P. 26-36. DOI: 10.1016/S2214-109X(13)70006-8.

Leffler, J.; Stumblesm, P. A.; Strickland, D. H. (2018): Immunological Processes Driving IgE Sensitisation and Disease Development in Males and Females. In: International Journal of Molecular Sciences 19 (6), P. 1554-1574. DOI: 10.3390/ijms19061554.

Lei, Q. Y.; Zhang, H.; Zhao, B.; Zha, Z. Y.; Bai, F.; Pei, X. H.; Zhao, S.; Xiong, Y.; Guan, K. L. (2008): TAZ promotes Cell Proliferation and Epithelial-Mesenchymal Transition and is inhibited by the Hippo Pathway. In: Molecular and Cellular Biology 28 (7), P. 2426-2436. DOI: 10.1128/MCB.01874-07.

References

Lei, X. G.; Zhu, J. H.; Cheng, W. H.; Bao, Y.; Ho, Y. S.; Reddi, A. R.; Holmgren, A.; Arnér, E. S. (2016): Paradoxical Roles of Antioxidant Enzymes: Basic Mechanisms and Health Implications. In: Physiological Reviews 96 (1), P. 307-364. DOI: 10.1152/physrev.00010.2014.

Lewandowski, A. J.; Augustine, D.; Lamata, P.; Davis, E. F.; Lazdam, M.; Francis, J.; McCormick, K.; Wilkinson, A. R.; Singhal, A.; Lucas, A.; Smith, N. P.; Neubauer, S.; Leeson, P. (2013): Preterm Heart in Adult Life: Cardiovascular Magnetic Resonance Reveals Distinct Differences in Left Ventricular Mass, Geometry, and Function. In: Circulation 127 (2), P. 197-206. DOI: 10.1161/CIRCULATIONAHA.112.126920.

Li, Q.; Li, B.; Wang, X.; Leri, A.; Jana, K. P.; Liu, Y.; Kajstura, J.; Baserga, R.; Anversa, P. (1997): Overexpression of Insulin-like Growth Factor-1 in Mice Protects from Myocyte Death after Infarction, Attenuating Ventricular Dilation, Wall Stress, and Cardiac Hypertrophy. In: Journal of Clinical Investigation 100 (8), P. 1991-1999. DOI: 10.1172/JCI119730.

Li, Q.; Bolli, R.; Qiu, Y.; Tang, X. L.; Guo, Y.; French, B. A. (2001): Gene Therapy with Extracellular Superoxide Dismutase Protects Conscious Rabbits against Myocardial Infarction. In: Circulation 103 (14), P. 1893-1898. DOI: 10.1161/01.cir.103.14.1893.

Li, L.; Blumenthal, D. K.; Terry, C. M.; He, Y.; Carlson, M. L.; Cheung, A. K. (2011): PDGF-induced Proliferation in Human Arterial and Venous Smooth Muscle Cells: Molecular Basis for Differential Effects of PDGF Isoforms. In: Journal of Cellular Biochemistry 112 (1), P. 289-298. DOI: 10.1002/jcb.22924.

Liang, J.; Slingerland, J. M. (2003): Multiple Roles of the PI3K/PKB (Akt) Pathway in Cell Cycle Progression. In: Cell Cycle 2 (4), P. 339-345. DOI: 10.4161/cc.2.4.433.

Liang, Q.; Molkentin, J. D. (2003): Redefining the Roles of P38 and JNK Signaling in Cardiac Hypertrophy: Dichotomy between Cultured Myocytes and Animal Models. In: Journal of Molecular and Cellular Cardiology 35 (12), P. 1385-1394. DOI: 10.1016/j.yjmcc.2003.10.001.

Licile Packard Children's Hospital (2010): *Factors Contributing to Congenital Heart Disease*. 04.07.2010, Retrieved 17.07.2023, < https://web.archive.org/web/20100704183659/http://www.lpch.org/DiseaseHealthInfo/HealthLibrary/cardiac/fcchd.html>

Limas, C. J.; Spier, S. S.; Kahlon, J. (1980): Enhanced Calcium Transport by Sarcoplasmic Reticulum in Mild Cardiac Hypertrophy. In: Journal of Molecular and Cellular Cardiology 12 (10), P. 1103-1116. DOI: 10.1016/0022-2828(80)90035-8.

Lin, Z.; von Gise, A.; Zhou, P.; Gu, F.; Ma, Q.; Jiang, J.; Yau, A. L.; Buck, J. N.; Gouin, K. A.; van Gorp, P. R.; Zhou, B.; Chen, J.; Seidman, J. G.; Wang, D. Z.; Pu, W. T. (2014): Cardiac-specific YAP Activation Improves Cardiac Function and Survival in an Experimental Murine MI Model. In: Circulation Research 115 (3), P. 354-363. DOI: 10.1161/CIRCRESAHA.115.303632.

Lin, Z.; Zhou, P.; von Gise, A.; Gu, F.; Ma, Q.; Chen, J.; Guo, H.; van Gorp, P. R.; Wang, D. Z.; Pu, W. T. (2015): Pi3kcb Links Hippo-YAP and PI3K-AKT Signaling Pathways to Promote Cardiomyocyte Proliferation and Survival. In: Circulation Research 116 (1), P. 35-45. DOI: 10.1161/CIRCRESAHA.115.304457.

Lin, Z.; Guo, H.; Cao, Y.; Zohrabian, S.; Zhou, P.; Ma, Q.; VanDusen, N.; Guo, Y.; Zhang, J.; Stevens, S. M.; Liang, F.; Quan, Q.; van Gorp, P. R.; Li, A.; Dos Remedios, C.; He, A.; Bezzerides, V. J.; Pu, W. T. (2016): Acetylation of VGLL4 Regulates Hippo-YAP Signaling and Postnatal Cardiac Growth. In: Developmental Cell 39 (4), P. 466-479. DOI: 10.1016/j.devcel.2016.09.005.

References

Litviňuková, M.; Talavera-López, C.; Maatz, H. (2020): Cells of the Adult Human Heart. In: Nature 588 (7838), P. 466-472. DOI: 10.1038/s41586-020-2797-4.

Liu, H.; Zhang, C. H.; Ammanamanchi, N.; Suresh, S.; Lewarchik, C.; Rao, K.; Uys, G. M.; Han, L.; Abrial, M.; Yimlamai, D.; Ganapathy, B.; Guillermier, C.; Chen, N.; Khaladkar, M.; Spaethling, J.; Eberwine, J. H.; Kim, J.; Walsh, S.; Choudhury, S.; Little, K.; Francis, K.; Sharma, M.; Viegas, M.; Bais, A.; Kostka, D.; Ding, J.; Bar-Joseph, Z.; Wu, Y.; Yechoor, V.; Moulik, M.; Johnson, J.; Weinberg, J.; Reyes-Múgica, M.; Steinhauser, M. L.; Kühn, B. (2019): Control of Cytokinesis by β-adrenergic Receptors Indicates an Approach for Regulating Cardiomyocyte Endowment. In: Science Translational Medicine 11 (513), P. 6419-6440. DOI: 10.1126/scitranslmed.aaw6419.

Loctin, J.; Delost, P. (1983): Mortality in Premature Mice at Birth and during Neonatal Development. In: Reproduction, Nutrition and Development 23 (2a), P. 293-301. DOI: 10.1051/rnd:19830213.

Lopaschuk, G. D.; Spafford, M. A.; Marsh, D. R. (1991): Glycolysis is Predominant Source of Myocardial ATP Production Immediately after Birth. In: The American Journal of Physiology 261 (6 Pt 2), P. 1698-1705. DOI: 10.1152/ajpheart.1991.261.6.H1698.

Lopaschuk, G. D.; Collins-Nakai, R. L.; Itoi, T. (1992): Developmental Changes in Energy Substrate use by the Heart. In: Cardiovascular Research 26 (12), P. 1172-1180. DOI: 10.1093/cvr/26.12.1172.

Lopaschuk, G. D.; Witters, L. A.; Itoi, T.; Barr, R.; Barr, A. (1994): Acetyl-CoA Carboxylase Involvement in the Rapid Maturation of Fatty Acid Oxidation in the Newborn Rabbit Heart. In: The Journal of Biological Chemistry 269 (41), P. 25871-25878. DOI: 10.1016/S0021-9258(18)47327-9.

Lopaschuk, G. D.; Jaswal, J. S. (2010): Energy Metabolic Phenotype of the Cardiomyocyte during Development, Differentiation, and Postnatal Maturation. In: Journal of Cardiovascular Pharmacology 56 (2), P. 130-140. DOI: 10.1097/FJC.0b013e3181e74a14.

Lopez-Tello, J.; Yong, H. E. J.; Sandovici, I.; Dowsett, G. K. C.; Christoforou, E. R.; Salazar-Petres, E.; Boyland, R.; Napso, T.; Yeo, G. S. H.; Lam, B. Y. H.; Constancia, M.; Sferruzzi-Perri, A. N. (2023): Fetal Manipulation of Maternal Metabolism is a Critical Function of the Imprinted Igf2 Gene. In: Cell Metabolism 35 (7), P. 1195-1208. DOI: 10.1016/j.cmet.2023.06.007.

Lu, J.; Holmgren, A. (2014): The Thioredoxin Antioxidant System. In: Free Radical Biology and Medicine 66, P. 75-87. DOI: 10.1016/j.freeradbiomed.2013.07.036.

Luo, F.; Wu, P.; Chen, J.; Guo, Y.; Wang, J.; Li, X.; Fang, Z. (2018): ANGPTL3 Possibly Promotes Cardiac Angiogenesis through Improving Proangiogenic Ability of Endothelial Progenitor Cells after Myocardial Infarction. In: Lipids Health and Disease 17 (1), P. 184-186. DOI: 10.1186/s12944-018-0835-0.

Lyer, N. V.; Kotch, L. E.; Agani, F.; Leung, S. W.; Laughner, E.; Wenger, R. H.; Gassmann, M.; Gearhart, J. D.; Lawler, A. M.; Yu, A. Y.; Semenza, G. L. (1998): Cellular and Developmental Control of O2 Homeostasis by Hypoxia-Inducible Factor 1 Alpha. In: Genes & Development 12 (2), P. 149-162. DOI: 10.1101/gad.12.2.149.

Ma, T.; Van Tine, B. A.; Wei, Y.; Garrett, M. D.; Nelson, D.; Adams, P. D.; Wang, J.; Qin, J.; Chow, L. T.; Harper, J. W. (2000): Cell Cycle-regulated Phosphorylation of p220(NPAT) by Cyclin E/Cdk2 in Cajal Bodies promotes Histone Gene Transcription. In: Genes and Development 14 (18), P. 2298–2313. DOI: 10.1101/gad.829500.

References

Ma, X. M.; Blenis, J. (2009): Molecular Mechanisms of mTOR-Mediated Translational Control. In: Nature Review. In: Molecular Cell Biology 10 (5), P. 307-318. DOI: 10.1038/nrm2672

Magadum, A.; Singh, N.; Kurian, A. A.; Munir, I.; Mehmood, T.; Brown, K.; Sharkar, M. T. K.; Chepurko, E.; Sassi, Y.; Oh, J. G.; Lee, P.; Santos, C. X. C.; Gaziel-Sovran, A.; Zhang, G.; Cai, C. L.; Kho, C.; Mayr, M.; Shah, A. M.; Hajjar, R. J.; Zangi, L. (2020): Pkm2 Regulates Cardiomyocyte Cell Cycle and Promotes Cardiac Regeneration. In: Circulation 141 (15), P. 1249-1265. DOI: 10.1161/CIRCULATIONAHA.119.043067.

Maggi, A. (2011): Liganded and Unliganded Activation of Estrogen Receptor and Hormone Replacement Therapies. In: Biochimica et Biophysica Acta 1812 (8), P. 1054-1060. DOI: 10.1016/j.bbadis.2011.05.001.

Maillet, M.; van Berlo, J. H.; Molkentin, J. D. (2013): Molecular Basis of Physiological Heart Growth: Fundamental Concepts and New Players. In: Nature Reviews. Molecular Cell Biology 14 (1), P. 38–48. DOI: 10.1038/nrm3495.

Makinde, A. O.; Gamble, J.; Lopaschuk, G. D. (1997): Upregulation of 5'-AMP-Activated Protein Kinase is Responsible for the Increase in Myocardial Fatty Acid Oxidation Rates Following Birth in the Newborn Rabbit. In: Circulation Research 80 (4), P. 482-489. DOI: 10.1161/01.res.80.4.482.

Malarkey, K.; Belham, C. M.; Paul, A.; Graham, A.; McLees, A.; Scott, P. H.; Plevin, R. (1995): The Regulation of Tyrosine Kinase Signalling Pathways by Growth Factor and G-protein-coupled Receptors. In: Biochemical Journal 309 (Pt 2), P. 361-375. DOI: 10.1042/bj3090361.

Mannan, M. A.; O'Shaughnessy, P. J. (1988): Ovarian Steroid Metabolism during Post-natal Development in the Normal Mouse and in the Adult Hypogonadal (hpg) Mouse. In: Journal of Reproduction and Fertility 82 (2), P. 727-734. DOI: 10.1530/jrf.0.0820727.

Marino, M.; Acconcia, F.; Bresciani, F.; Weisz, A.; Trentalance, A. (2002): Distinct Nongenomic Signal Transduction Pathways Controlled by 17beta-estradiol Regulate DNA Synthesis and Cyclin D(1) Gene Transcription in HepG2 Cells. In: Molecular Biology of the Cell 13 (10), P. 3720-3729. DOI: 10.1091/mbc.e02-03-0153.

Marnett, L. J. (2000): Oxyradicals and DNA Damage. In: Carcinogenesis 21 (3), P. 361-370. DOI: 10.1093/carcin/21.3.361.

Marnett, L. J.; Riggins, J. N.; West, J. D. (2003): Endogenous Generation of Reactive Oxidants and Electrophiles and Their Reactions with DNA and Protein. In: The Journal of Clinical Investigation 2003 111 (5), P. 583-593. DOI: 10.1172/JCI18022.

Matsushima, S.; Ide, T.; Yamato, M.; Matsusaka, H.; Hattori, F.; Ikeuchi, M.; Kubota, T.; Sunagawa, K.; Hasegawa, Y.; Kurihara, T.; Oikawa, S.; Kinugawa, S.; Tsutsui, H. (2006): Overexpression of Mitochondrial Peroxiredoxin-3 Prevents Left Ventricular Remodeling and Failure after Myocardial Infarction in Mice. In: Circulation 113 (14), P. 1779-1786. DOI: 10.1161/CIRCULATIONAHA.105.582239.

Mayhew, T. M.; Pharaoh, A.; Austin, A.; Fagan, D. G. (1997): Stereological estimates of Nuclear Number in Human Ventricular Cardiomyocytes Before and after Birth Obtained using Physical Disectors. In: Journal of Anatomy 191 (1), P. 107-115. DOI: 10.1046/j.1469-7580.1997.19110107.x.

McCarthy, R.; Martin-Fairey, C.; Sojka, D. K.; Herzog, E. D.; Jungheim, E. S.; Stout, M. J.; Fay, J. C.; Mahendroo, M.; Reese, J.; Herington, J. L.; Plosa, E. J.; Shelton, E. L.; England, S. K.

(2018): Mouse Models of Preterm Birth: Suggested Assessment and Reporting Guidelines. In: Biology of Reproduction 99 (5), P. 922-937. DOI: 10.1093/biolre/ioy109.

Mc Mullen, J. R.; Jennings, G. L. (2007): Differences Between Pathological and Physiological Cardiac Hypertrophy: Novel Therapeutic Strategies to treat Heart Failure. In: Clinical and Experimental Pharmacology and Physiology 34 (4), P. 255-262. DOI: 10.1111/j.1440-1681.2007.04585.x.

Meilhac, S. M.; Kelly, R. G.; Rocancourt, D.; Eloy-Trinquet, S.; Nicolas, J. F.; Buckingham, M. E. (2003): A Retrospective Clonal Analysis of the Myocardium Reveals two Phases of Clonal Growth in the Developing Mouse Heart. In: Development 130 (16), P. 3877-3889. DOI: 10.1242/dev.00580.

Mia, M. M.; Singh, M. K. (2019): The Hippo Signaling Pathway in Cardiac Development and Diseases. In: Frontiers in Cell and Developmental Biology 7 (211), P. 1-13. DOI: 10.3389/fcell.2019.00211.

Migliaccio, A.; Pagano, M.; Auricchio, F. (1993): Immediate and Transient Stimulation of Protein Tyrosine Phosphorylation by Estradiol in MCF-7 Cells. In: Oncogene 8 (8), P. 2183-2191.

Migliaccio, A.; Di Domenico, M.; Castoria, G.; de Falco, A.; Bontempo, P.; Nola, E.; Auricchio, F. (1996): Tyrosine Kinase/p21ras/MAP-kinase Pathway Activation by Estradiol-receptor Complex in MCF-7 Cells. In: EMBO Journal 15 (6), P. 1292-1300. DOI: 10.1002/j.1460-2075.1996.tb00471.x.

Mikawa, T.; Gourdie, R. G. (1996): Pericardial Mesoderm generates a Population of Coronary Smooth Muscle Cells Migrating into the Heart along with Ingrowth of the Epicardial Organ. In: Developmental Biology 174 (2), P. 221-232. DOI: 10.1006/dbio.1996.0068.

Mohamed, T. M. A.; Ang, Y. S.; Radzinsky, E.; Zhou, P.; Huang, Y.; Elfenbein, A.; Foley, A.; Magnitsky, S.; Srivastava, D. (2018): Regulation of Cell Cycle to Stimulate Adult Cardiomyocyte Proliferation and Cardiac Regeneration. In: Cell 173 (1), P. 104-116.e12. DOI: 10.1016/j.cell.2018.02.014.

Mollova, M.; Bersell, K.; Walsh, S.; Savla, J.; Das, L. T.; Park, S. Y.; Silberstein, L. E.; Dos Remedios, C. G.; Graham, D.; Colan, S.; Kühn, B. (2013): Cardiomyocyte proliferation contributes to heart growth in young humans. In: Proceeding of the National Academy of Sciences of the United States of America 110 (4), P. 1446-1451. DOI: 10.1073/pnas.1214608110.

Moore, K.; Fulmer, D.; Guo, L.; Koren, N.; Glover, J.; Moore, R.; Gensemer, C.; Beck, T.; Morningstar, J.; Stairley, R.; Norris, R. A. (2021): PDGFRα: Expression and Function during Mitral Valve Morphogenesis. In: Journal of Cardiovascular Development and Disease 8 (3), P. 28-41. DOI: 10.3390/jcdd8030028.

Moore-Morris, T.; Cattaneo, P.; Puceat, M.; Evans, S. M. (2016): Origins of Cardiac Fibroblasts. In: Journal of Molecular and Cellular Cardiology 91 (x), P. 1-5. DOI: 10.1016/j.yjmcc.2015.12.031.

Moorman, A.; Webb, S.; Brown, N. A.; Lamers, W.; Anderson, R. H. (2003): Development of the Heart: (1) Formation of the Cardiac Chambers and Arterial Trunks. In: Heart (British Cardiac Society) 89 (7), P. 806–814. DOI: 10.1136/heart.89.7.806.

Moorman, A. F. M.; Christoffels, V. M. (2003): Cardiac Chamber Formation: Development, Genes, and Evolution. In: Physiological Reviews 83 (4), P. 1223–1267. DOI: 10.1152/physrev.00006.2003.

References

Mrocki, M. M.; Nguyen, V. B.; Lombardo, P.; Sutherland, M. R.; Bensley, J. G.; Nitsos, I.; Allison, B. J.; Harding, R.; De Matteo, R.; Schneider, M.; Polglase, G. R.; Black, M. J. (2018): Moderate Preterm Birth affects Right Ventricular Structure and Function and Pulmonary Artery Blood Flow in Adult Sheep. In: Journal of Physiology 596 (23), P. 5965-5975. DOI: 10.1113/JP275654.

Murray, S. A.; Morgan, J. L.; Kane, C.; Sharma, Y.; Heffner, C. S.; Lake, J.; Donahue, L. R. (2010): Mouse Gestation Length is Genetically Determined. In: PLoS One 5 (8), P. 12418-12424. DOI: 10.1371/journal.pone.0012418.

Nakada, Y.; Canseco, D. C.; Thet, S.; Abdisalaam, S.; Asaithamby, A.; Santos, C. X.; Shah, A. M.; Zhang, H.; Faber, J. E.; Kinter, M. T.; Szweda, L. I.; Xing, C.; Hu, Z.; Deberardinis, R. J.; Schiattarella, G.; Hill, J. A.; Oz, O.; Lu, Z.; Zhang, C. C.; Kimura, W.; Sadek, H. A. (2017): Hypoxia induces Heart Regeneration in Adult Mice. In: Nature 541 (7636), P. 222-227. DOI: 10.1038/nature20173.

National Institute of Health (2011): What Are the Signs and Symptoms of Congenital Heart Defects?. 01.07.2011, Retrieved 20.07.2022, https://web.archive.org/web/20150727210816/http://www.nhlbi.nih.gov/health/health-topics/topics/chd/signs

National Institute of Health (2022): What are Congenital Heart Defects?. 24.03.2022, Retrieved 13.07.2023, https://www.nhlbi.nih.gov/health/congenital-heart-defects

Nemoto, S.; Sheng, Z.; Lin, A. (1998): Opposing Effects of Jun Kinase and p38 Mitogen-Activated Protein Kinases on Cardiomyocyte Hypertrophy. In: Molecular and Cellular Biology 18 (6), P. 3518-3526. DOI: 10.1128/MCB.18.6.3518.

Nguyen, P. D.; Hsiao, S. T.; Sivakumaran, P.; Lim, S. Y.; Dilley, R. J. (2012): Enrichment of Neonatal Rat Cardiomyocytes in Primary Culture Facilitates Long-term Maintenance of Contractility in Vitro. In: American Journal of Physiology 303 (12), P. 1220-1228. DOI: 10.1152/ajpcell.00449.2011.

Ocsan RJ, Lai YN, Prabhu KV, Hambly BD, McLachlan CS. (2013): Chronic NG-nitro-l-arginine Methyl Ester (L-NAME) Administration in C57BL/6J Mice induces a Sustained Decrease in c-kit Positive Cells during Development of Cardiac Hypertrophy. In: Journal of Physiology and Pharmacology 64 (6), P. 727-736.

Okuda, M.; Horn, H. F.; Tarapore, P.; Tokuyama, Y.; Smulian, A. G.; Chan, P. K.; Knudsen, E. S.; Hofmann, I. A.; Snyder, J. D.; Bove, K. E. (2000): Nucleophosmin/B23 is a Target of CDK2/cyclin E in Centrosome Duplication. In: Cell 14 (18), P. 127–140. DOI: 10.1016/S0092-8674(00)00093-3.

Olivetti, G.; Cigola, E.; Maestri, R.; Corradi, D.; Lagrasta, C.; Gambert, S. R.; Anversa, P. (1996): Aging, Cardiac Hypertrophy and Ischemic Cardiomyopathy do not Affect the Proportion of Mononucleated and Multinucleated Myocytes in the Human Heart. In: Journal of Molecular Cellular Cardiology 28 (7), P. 1463-1477. DOI: 10.1006/jmcc.1996.0137.

Onimaru, K.; Shoguchi, E.; Kuratani, Sh.; Tanaka, M. (2011): Development and Evolution of the Lateral Plate Mesoderm: Comparative Analysis of Amphioxus and Lamprey with Implications for the Acquisition of Paired Fins. In: Developmental Biology 359 (1), P. 124–136. DOI: 10.1016/j.ydbio.2011.08.003.

References

Owens, G. K.; Kumar, M. S.; Wamhoff, B. R. (2004): Molecular Regulation of Vascular Smooth Muscle Cell Differentiation in Development and Disease. In: Physiological Reviews 84 (3), P. 767-801. DOI: 10.1152/physrev.00041.2003.

Paddock, S. J.; Swift, S. K.; Alencar-Almeida, V.; Kenarsary, A.; Alvarez-Argote, S.; Flinn, M. A.; Patterson, M.; O'Meara, C. C. (2021): IL4Rα Signaling Promotes Neonatal Cardiac Regeneration and Cardiomyocyte Cell Cycle Activity. In: Journal of Molecular and Cellular Cardiology 161, P. 62-74. DOI: 10.1016/j.yjmcc.2021.07.012.

Paltzer, W. G.; Aballo, T. J.; Bae, J.; Hubert, K. A.; Nuttall, D. J.; Perry, C.; Wanless, K. N.; Nahlawi, R.; Ge, Y.; Mahmoud, AI. (2023): mTORC1 Regulates the Metabolic Switch of Postnatal Cardiomyocytes During Regeneration. In: BioRxiv [Preprint] 12.557400, P. 1-32. DOI: 10.1101/2023.09.12.557400.

Parer, J. T. (2008): Fetal Circulation. In: Global Women's Medicine. DOI: 10.3843/GLOWM.10194. Retrieved 22.09.2023, <https://www.glowm.com/section-view/heading/Fetal%20Circulation/item/194>

Pasumarthi, K. B.; Field, L. J. (2002): Cardiomyocyte Cell Cycle Regulation. In: Circulation Research 90 (10), P. 1044-1054. DOI: 10.1161/01.res.0000020201.44772.67.

Pasumarthi, K. B.; Nakajima, H.; Nakajima, H. O.; Soonpaa, M. H.; Field, L. J. (2005): Targeted Expression of Cyclin D2 Results in Cardiomyocyte DNA Synthesis and Infarct Regression in Transgenic Mice. In: Circulation Research 96 (1), P. 110-118. DOI: 10.1161/01.RES.0000152326.91223.4F.

Pasqualini, F. S.; Nesmith, A. P.; Horton, R. E.; Sheehy, S. P.; Parker, K. K. (2016): Mechanotransduction and Metabolism in Cardiomyocyte Microdomains. In: BioMed Research International 2016 (4081638), P. 1-17. DOI: 10.1155/2016/4081638.

Patterson, M.; Barske, L.; Van Handel, B.; Rau, C. D.; Gan, P.; Sharma, A.; Parikh, S.; Denholtz, M.; Huang, Y.; Yamaguchi, Y.; Shen, H.; Allayee, H.; Crump, J. G.; Force, T. I.; Lien, C. L.; Makita, T.; Lusis, A. J.; Kumar, S. R.; Sucov, H. M. (2017): Frequency of Mononuclear Diploid Cardiomyocytes Underlies Natural Variation in Heart Regeneration. In: Nature Genetics 49 (9), P. 1346-1353. DOI: 10.1038/ng.3929.

Pettinato, A. M.; Yoo, D.; VanOudenhove, J.; Chen, Y. S.; Cohn, R.; Ladha, F. A.; Yang, X.; Thakar, K.; Romano, R.; Legere, N.; Meredith, E.; Robson, P.; Regnier, M.; Cotney, J. L.; Murry, C. E.; Hinson, J. T. (2021): Sarcomere Function activates a p53-dependent DNA Damage Response that promotes Polyploidization and limits in Vivo Cell Engraftment. In: Cell Reports 35 (5), P. 109088-109134. DOI: 10.1016/j.celrep.2021.109088.

Piatkowski, T.; Mühlfeld, C.; Borchardt, T.; Braun, T. (2013): Reconstitution of the Myocardium in Regenerating Newt Hearts is preceded by Transient Deposition of Extracellular Matrix Components. In: Stem Cells and Development 22 (13), P. 1921-1931. DOI: 10.1089/scd.2012.0575.

Pinto, A. R.; Ilinykh, A.; Ivey, M. J.; Kuwabara, J. T.; D'Antoni, M. L.; Debuque, R.; Chandran, A.; Wang, L.; Arora, K.; Rosenthal, N. A.; Tallquist, M. D. (2016): Revisiting Cardiac Cellular Composition. In: Circulation Research 118 (3), P. 400-409. DOI: 10.1161/CIRCRESAHA.115.307778.

Piquereau, J.; Novotova, M.; Fortin, D.; Garnier, A.; Ventura-Clapier, R.; Veksler, V.; Joubert, F. (2010): Postnatal Development of Mouse Heart: Formation of Energetic Microdomains. In: The Journal of Physiology 588 (Pt 13), P. 2443-2454. DOI: 10.1113/jphysiol.2010.189670.

References

Pohjoismäki, J. L.; Boettger, T.; Liu, Z.; Goffart, S.; Szibor, M.; Braun, T. (2012): Oxidative Stress during Mitochondrial Biogenesis compromises MtDNA Integrity in Growing Hearts and induces a Global DNA Repair Response. In: Nucleic Acids Research 40 (14), P. 6595-6607. DOI: 10.1093/nar/gks301.

Pohjoismäki, J. L.; Krüger, M.; Al-Furoukh, N.; Lagerstedt, A.; Karhunen, P. J.; Braun, T. (2013): Postnatal Cardiomyocyte Growth and Mitochondrial Reorganization cause Multiple Changes in the Proteome of Human Cardiomyocytes. In: Molecular Biosystems 9 (6), P. 1210-1219. DOI: 10.1039/c3mb25556e.

Poling, M. C.; Kauffman, A. S. (2012): Sexually Dimorphic Testosterone Secretion in Prenatal and Neonatal Mice is Independent of Kisspeptin-Kiss1r and GnRH Signaling. In: Endocrinology 153 (2), P. 782-793. DOI: 10.1210/en.2011-1838.

Polizzotti, B. D.; Ganapathy, B.; Walsh, S.; Choudhury, S.; Ammanamanchi, N.; Bennett, D. G.; dos Remedios, C. G.; Haubner, B. J.; Penninger, J. M.; Kühn, B. (2015): Neuregulin Stimulation of cardiomyocyte Regeneration in Mice and Human Myocardium reveals a Therapeutic Window. In: Science Translational Medicine 7 (281), P. 28-45. DOI: 10.1126/scitranslmed.aaa5171.

Porrello, E. R.; Mahmoud, AI.; Simpson, E.; Hill, J. A.; Richardson, J. A.; Olson, E. N.; Sadek, H. A. (2011): Transient Regenerative Potential of the Neonatal Mouse Heart. In: Science 331 (6020), P. 1078-1080. DOI: 10.1126/science.1200708.

Porrello, E. R.; Mahmoud, AI.; Simpson, E.; Johnson, B. A.; Grinsfelder, D.; Canseco, D.; Mammen, P. P.; Rothermel, B. A.; Olson, E. N.; Sadek, H. A. (2013): Regulation of Neonatal and Adult Mammalian Heart Regeneration by the MiR-15 Family. In: Proceedings of the National Academy of Sciences of the United States of America 110 (1), P. 187-192. DOI: 10.1073/pnas.1208863110.

Porrello, E. R.; Olson, E. N. (2014): A Neonatal Blueprint for Cardiac Regeneration. In: Stem Cell Research 13 (3 Pt B), P. 556-570. DOI: 10.1016/j.scr.2014.06.003.

Poss, K. D.; Wilson, L. G.; Keating, M. T. (2002): Heart Regeneration in Zebrafish. In: Science 298 (5601), P. 2188-2190. DOI: 10.1126/science.1077857.

Postic, C.; Leturque, A.; Printz, R. L.; Maulard, P.; Loizeau, M.; Granner, D. K.; Girard, J. (1994): Development and Regulation of Glucose Transporter and Hexokinase Expression in Rat. In: The American Journal of Physiology 266 (4), P. 548-559. DOI: 10.1152/ajpendo.1994.266.4.E548.

Praskova, M.; Khoklatchev, A.; Ortiz-Vega, S.; Avruch, J. (2004): Regulation of the MST1 Kinase by Autophosphorylation, by the Growth Inhibitory Proteins, RASSF1 and NORE1, and by Ras. In: Biochemical Journal 381 (2), P. 453-462. DOI: 10.1042/BJ20040025.

Puente, B. N.; Kimura, W.; Muralidhar, S. A.; Moon, J.; Amatruda, J. F.; Phelps, K. L.; Grinsfelder, D.; Rothermel, B. A.; Chen, R.; Garcia, J. A.; Santos, C. X.; Thet, S. M.; Mori, E.; Kinter, M. T.; Rindler, P. M.; Zacchigna, S.; Mukherjee, S.; Chen, D. J.; Mahmoud, AI.; Giacca, M.; Rabinovitch, P. S.; Aroumougame, A.; Shah, A. M.; Szweda, L. I.; Sadek, H. A. (2014): The Oxygen-rich Postnatal Environment Induces Cardiomyocyte Cell-cycle Arrest Through DNA Damage Response. In: Cell 157 (3), P. 565-579. DOI: 10.1016/j.cell.2014.03.032.

Proud, C. G. (2004): Ras, PI3-kinase and mTOR Signaling in Cardiac Hypertrophy. In: Cardiovascular Research 63 (3), P. 403-413. DOI: 10.1016/j.cardiores.2004.02.003.

Purcell, N. H.; Wilkins, B. J.; York, A.; Saba-El-Leil, M. K.; Meloche, S.; Robbins, J.; Molkentin, J. D. (2007): Genetic Inhibition of Cardiac ERK1/2 promotes Stress-Induced Apoptosis and Heart Failure but has no Effect on Hypertrophy in Vivo. In: Proceedings of the National Academy of

Sciences of the United States of America 2104 (35), P. 14074-14079. DOI: 10.1073/pnas.0610906104.

Qi, M.; Elion, E. A. (2005): MAP Kinase Pathways. In: Journal of Cell Science 118 (16), P. 3569-3572. DOI: 10.1242/jcs.02470.

Radi, R.; Turrens, J. F.; Chang, L. Y.; Bush, K. M.; Crapo, J. D.; Freeman, B. A. (1991): Detection of Catalase in Rat Heart Mitochondria. In: Journal of Biological Chemistry 266 (32), P. 22028-22034. DOI: 10.1016/S0021-9258(18)54740-2.

Raingeaud, J.; Gupta, S.; Rogers, J. S.; Dickens, M.; Han, J.; Ulevitch, R. J.; Davis, R. J. (1995): Pro-Inflammatory Cytokines and Environmental Stress Cause p38 Mitogen-Activated Protein Kinase Activation by Dual Phosphorylation on Tyrosine and Threonine. In: The Journal of Biological Chemistry 270 (13), P. 7420-7426. DOI: 10.1074/jbc.270.13.7420.

Rao, X.; Huang, X.; Zhou, Z.; Lin, X. (2013): An Improvement of the 2ˆ(-delta delta CT) Method for Quantitative Real-Time Polymerase Chain Reaction Data Analysis. In: Biostatistics, Bioinformatics, and Biomathematics 3 (3), P. 71-85.

Raykha, C.; Crawford, J.; Gan, B. S.; Fu, P.; Bach, L. A.; O'Gorman, D. B. (2013): IGF-II and IGFBP-6 Regulate Cellular Contractility and Proliferation in Dupuytren's Disease. In: Biochimica et Biophysica Acta 1832 (10), P. 1511-1519. DOI: 10.1016/j.bbadis.2013.04.018.

Reiser, P. J.; Portman, M. A.; Ning, X. H.; Schomisch Moravec, C. (2001): Human Cardiac Myosin Heavy Chain Isoforms in Fetal and Failing Adult Atria and Ventricles. In: American Journal of Physiology: Heart and Circulatory Physiology 280 (4), P. 1814-1820. DOI: 10.1152/ajpheart.2001.280.4.H1814.

Reiss, K.; Cheng, W.; Ferber, A.; Kajstura, J.; Li, P.; Li, B.; Olivetti, G.; Homcy, C. J.; Baserga, R.; Anversa, P. (1996): Overexpression of Insulin-Like Growth Factor-1 in the Heart is coupled with Myocyte Proliferation in Transgenic Mice. In: Proceedings of the National Academy of Sciences of the United States of America 93 (16), P. 8630-8635. DOI: 10.1073/pnas.93.16.8630.

Richter, J. D.; Sonenberg, N. (2005): Regulation of Cap-Dependent Translation by eIF4E Inhibitory Proteins. In: Nature 433 (7025), P. 477-480. DOI: 10.1038/nature03205.

Rosenthal, N.; Brown, S. (2007): The Mouse Ascending: Perspectives for Human-disease Models. In: Nature Cell Biology 9 (9), P. 993-999. DOI: 10.1038/ncb437.

Rudolph, A. M.; Drorbaugh, J. E.; Auld, P. A.; Rudolph, A. J.; Nadas, A. S.; Smith, C. A.; Hubbell, J. P. (1961): Studies on the Circulation in the Neonatal Period. The Circulation in the Respiratory Distress Syndrome. In: Pediatrics 27 (4), P. 551-566. DOI: 10.1542/peds.27.4.551.

Rudolph, A. M.; Heymann, M. A. (1970): Circulatory Changes During Growth in the Fetal Lamb. In: Circulation Research 26 (3), P. 289-299. DOI: 10.1161/01.res.26.3.289.

Rudolph, A. M. (1985): Distribution and Regulation of Blood Flow in the Fetal and Neonatal Lamb. In: Circulation Research 57 (6), P. 811-821. DOI: 10.1161/01.res.57.6.811.

Rudolph, A. M. (2000): Myocardial Growth before and after Birth: Clinical Implications. In: Acta Paediatrica 89 (2), P. 129-133. DOI: 10.1080/080352500750028681.

Sakamoto, T.; Matsuura, T. R.; Wan, S.; Ryba, D. M.; Kim, J. U.; Won, K. J.; Lai, L.; Petucci, C.; Petrenko, N.; Musunuru, K.; Vega, R. B.; Kelly, D. P. (2020): A Critical Role for Estrogen-Related Receptor Signaling in Cardiac Maturation. In: Circulation Research 126 (12), P. 1685-1702. DOI: 10.1161/CIRCRESAHA.119.316100.

References

Savolainen, S. M.; Foley, J. F.; Elmore, S. A. (2009): Histology Atlas of the Developing Mouse Heart with Emphasis on E11.5 to E18.5. In: Toxicologic Pathology 37 (4), P. 395–414. DOI: 10.1177/0192623309335060.

Schmittgen, T. D.; Livak, K. J. (2008): Analyzing Real-Time PCR Data by the Comparative C(T) Method. In: Nature Protocols 3 (6), P. 1101-1108. DOI: 10.1038/nprot.2008.73.

Schröder, E.; Brennan, J. P.; Eaton, P. (2008): Cardiac Peroxiredoxins undergo Complex Modifications during Cardiac Oxidant Stress. In: American Journal of Physiology 295 (1), P. 425-433. DOI: 10.1152/ajpheart.00017.2008.

Sedmera, D.; Pexieder, T.; Vuillemin, M.; Thompson, R. P.; Anderson, R. H. (2000): Developmental Patterning of the Myocardium. In: The Anatomical Record 258 (4), P. 319–337. DOI: 10.1002/(SICI)1097-0185(20000401)258:4<319::AID-AR1>3.0.CO;2-O.

Semenza, G. L. (2012): Hypoxia-inducible Factors: Mediators of Cancer Progression and Targets for Cancer Therapy. In: Trends in Pharmacological Sciences 33 (4), P. 207-214. DOI: 10.1016/j.tips.2012.01.005.

Sepasi Tehrani, H.; Moosavi-Movahedi, A. A. (2018): Catalase and its Mysteries. In: Progress in Biophysics and Molecular Biology 140, P. 5-12. DOI: 10.1016/j.pbiomolbio.2018.03.001.

Sever-Chroneos, Z.; Angus, S. P.; Fribourg, A. F.; Wan, H.; Todorov, I.; Knudsen, K. E.; Knudsen, E. S. (2001): Retinoblastoma Tumor Suppressor Protein Signals Through Inhibition of Cyclin-dependent Kinase 2 Activity to disrupt PCNA Function in S Phase. In: Molecular Cell Biology 21 (12), P. 4032–4045. DOI: 10.1128/MCB.21.12.4032-4045.2001.

Sharma, S.; Bhattarai, S.; Ara, H.; Sun, G.; St Clair, D. K.; Bhuiyan, M. S.; Kevil, C.; Watts, M. N.; Dominic, P.; Shimizu, T.; McCarthy, K. J.; Sun, H.; Panchatcharam, M.; Miriyala, S. (2020): SOD2 Deficiency in Cardiomyocytes defines Defective Mitochondrial Bioenergetics as a Cause of Lethal Dilated Cardiomyopathy. In: Redox Biology 37, P. 101740-101753. DOI: 10.1016/j.redox.2020.101740.

Shi, J.; Yang, Y.; Cheng, A.; Xu, G.; He, F. (2020): Metabolism of Vascular Smooth Muscle Cells in Vascular Diseases. In: American Journal of Physiology. Heart Circulatory Physiology 319 (3), P. 613-631. DOI: 10.1152/ajpheart.00220.2020.

Shioi, T.; McMullen, J. R.; Kang, P. M.; Douglas, P. S.; Obata, T.; Franke, T. F.; Cantley, L. C.; Izumo, S. (2002): Akt/protein Kinase B promotes Organ Growth in Transgenic Mice. In: Molecular and Cellular Biology 22 (8), P. 2799-2809. DOI: 10.1128/MCB.22.8.2799-2809.2002.

Shiojima, I.; Walsh, K. (2006): Regulation of Cardiac Growth and Coronary Angiogenesis by the Akt/PKB Signaling Pathway. In: Genes and Development 20 (24), P. 3347-3365. DOI: 10.1101/gad.1492806.

Shirakawa, K.; Sano, M. (2021): Osteopontin in Cardiovascular Diseases. In: Biomolecules 11 (7), P. 1047-1064. DOI: 10.3390/biom11071047.

Soonpaa, M. H.; Kim, K. K.; Pajak, L.; Franklin, M.; Field, L. J. (1996): Cardiomyocyte DNA Synthesis and Binucleation during Murine Development. In: The American Journal of Physiology 271 (5 Pt 2), P. 2183-2189. DOI: 10.1152/ajpheart.1996.271.5.H2183.

Soonpaa, M. H.; Koh, G. Y.; Pajak, L.; Jing, S.; Wang, H.; Franklin, M. T.; Kim, K. K.; Field, L. J. (1997): Cyclin D1 Overexpression promotes Cardiomyocyte DNA Synthesis and Multinucleation in Transgenic Mice. In: The Journal of Clinical Investigation 99 (11), P. 2644-2654. DOI: 10.1172/JCI119453.

References

Spalding, K. L.; Bhardwaj, R. D.; Buchholz, B. A.; Druid, H.; Frisén, J. (2005): Retrospective Birth Dating of Cells in Humans. In: Cell 122 (1), P. 133-143. DOI: 10.1016/j.cell.2005.04.028.

Strash, N.; DeLuca, S.; Janer Carattini, G. L.; Heo, S. C.; Gorsuch, R.; Bursac, N. (2021): Human Erbb2-induced Erk Activity Robustly Stimulates Cycling and Functional Remodeling of Rat and Human Cardiomyocytes. In: Elife. 19 (10), P. 65512-65533. DOI: 10.7554/eLife.65512.

Sturzu, A. C.; Rajarajan, K.; Passer, D.; Plonowska, K.; Riley, A.; Tan, T. C.; Sharma, A.; Xu, A. F.; Engels, M. C.; Feistritzer, R.; Li, G.; Selig, M. K.; Geissler, R.; Robertson, K. D.; Scherrer-Crosbie, M.; Domian, I. J.; Wu, S. M. (2015): Fetal Mammalian Heart Generates a Robust Compensatory Response to Cell Loss. In: Circulation 132 (2), P. 109-121. DOI: 10.1161/CIRCULATIONAHA.114.011490.

Su, H.; Cantrell, A. C.; Zeng, H.; Zhu, S. H.; Chen, J. X. (2021): Emerging Role of Pericytes and Their Secretome in the Heart. In: Cells 10 (3), P. 548- 569. DOI: 10.3390/cells10030548.

The Physics Factbook (2001): *An encyclopedia of scientific essays; Volume of a Human Heart*. 2001, Retrieved 20.07.2022, < https://hypertextbook.com/facts/2001/VitaliyShchupak.shtml>

Thygesen, K.; Alpert, J. S.; White, H. D.; Jaffe, A. S.; Katus, H. A.; Apple, F. S.; Lindahl, B.; Morrow, D. A.; Chaitman, B. A.; Clemmensen, P. M.; Johanson, P.; Hod, H.; Underwood, R.; Bax, J. J.; Bonow, R. O.; Pinto, F.; Gibbons, R. J.; Fox, K. A.; Atar, D.; Newby, L. K.; Galvani, M.; Hamm, C. W.; Uretsky, B. F.; Steg, P. G.; Wijns, W.; Bassand, J. P.; Menasché, P.; Ravkilde, J.; Ohman, E. M.; Antman, E. M.; Wallentin, L. C.; Armstrong, P. W.; Simoons, M. L.; Januzzi, J. L.; Nieminen, M. S.; Gheorghiade, M.; Filippatos, G.; Luepker, R. V.; Fortmann, S. P.; Rosamond, W. D.; Levy, D.; Wood, D.; Smith, S. C.; Hu, D.; Lopez-Sendon, J. L.; Robertson, R. M.; Weaver, D.; Tendera, M.; Bove, A. A.; Parkhomenko, A. N.; Vasilieva, E. J.; Mendis, S.; ESC Committee for Practice Guidelines (CPG). (2012): Third Universal Definition of Myocardial Infarction. In: European Heart Journal 33 (20), P. 2551-2567. DOI: 10.1093/eurheartj/ehs184.

Tian, X.; Hu, T.; Zhang, H.; He, L.; Huang, X.; Liu, Q.; Yu, W.; He, L.; Yang, Z.; Yan, Y.; Yang, X.; Zhong, T. P.; Pu, W. T.; Zhou, B. (2014): Vessel Formation. De Novo Formation of a Distinct Coronary Vascular Population in Neonatal Heart. In: Science 345 (6192), P. 90-94. DOI: 10.1126/science.1251487.

Tran, D. H.; Wang, Z. V. (2019): Glucose Metabolism in Cardiac Hypertrophy and Heart Failure. In: Journal of the American Heart Association 8 (12), P. 12673-12690. DOI: 10.1161/JAHA.119.012673.

Trueblood, N. A.; Xie, Z.; Communal, C.; Sam, F.; Ngoy, S.; Liaw, L.; Jenkins, A. W.; Wang, J.; Sawyer, D. B.; Bing, O. H.; Apstein, C. S.; Colucci, W. S.; Singh, K. (2001): Exaggerated Left Ventricular Dilation and Reduced Collagen Deposition after Myocardial Infarction in Mice Lacking Osteopontin. In: Circulation Research 88 (10), P. 1080-1087. DOI: 10.1161/hh1001.090842.

Tsutsui, H.; Kinugawa, S.; Matsushima, S. (2009): Mitochondrial Oxidative Stress and Dysfunction in Myocardial Remodelling. In: Cardiovascular Research 81 (3), P. 449-456. DOI: 10.1093/cvr/cvn280.

Turrens, J. F. (2003): Mitochondrial Formation of Reactive Oxygen Species. In: The Journal of Physiology 52 (Pt 2), P. 335-344. DOI: 10.1113/jphysiol.2003.049478.

Ueda, P.; Cnattingius, S.; Stephansson, O.; Ingelsson, E.; Ludvigsson, J. F.; Bonamy, A. K. (2014): Cerebrovascular and Ischemic Heart Disease in Young Adults Born Preterm: A

Population-based Swedish Cohort Study. In: European Journal of Epidemiology 29 (4), P. 253-260. DOI: 10.1007/s10654-014-9892-5.

Ulm, S.; Liu, W.; Zi, M.; Tsui, H.; Chowdhury, S. K.; Endo, S.; Satoh, Y.; Prehar, S.; Wang, R.; Cartwright, E. J.; Wang, X. (2014): Targeted Deletion of ERK2 in Cardiomyocytes Attenuates Hypertrophic Response but Provokes Pathological Stress Induced Cardiac Dysfunction. In: Journal of Molecular and Cellular Cardiology 72 (100), P. 104-116. DOI: 10.1016/j.yjmcc.2014.03.002.

University of Toronto (Sun, J.) (2007): The effects of insulin-like growth factor binding protein-1 on pre- and postnatal cardiac morphology and function. Retrieved 18.11.2023, <https://tspace.library.utoronto.ca/bitstream/1807/119801/3/MR27395_OCR.pdf >

Varelas, X. (2014): The Hippo Pathway Effectors TAZ and YAP in Development, Homeostasis and Disease. In: Development 141 (8), P. 1614-1626. DOI: 10.1242/dev.102376.

Velayutham, N.; Agnew, E. J.; Yutzey, K. E. (2019): Postnatal Cardiac Development and Regenerative Potential in Large Mammals. In: Pediatric Cardiology 40 (7), P. 1345-1358. DOI: 10.1007/s00246-019-02163-7.

Voisin, L.; Saba-El-Leil, M. K.; Julien, C.; Frémin, C.; Meloche, S. (2010): Genetic Demonstration of a Redundant Role of Extracellular Signal-regulated Kinase 1 (ERK1) and ERK2 Mitogen-activated Protein Kinases in Promoting Fibroblast Proliferation. In: Molecular and Cellular Biology 30 (12), P. 2918-2932. DOI: 10.1128/MCB.00131-10.

von Gise, A.; Lin, Z.; Schlegelmilch, K.; Honor, L. B.; Pan, G. M.; Buck, J. N.; Ma, Q.; Ishiwata, T.; Zhou, B.; Camargo, F. D.; Pu, W. T. (2012): YAP1, the Nuclear Target of Hippo Signaling, Stimulates Heart Growth through Cardiomyocyte Proliferation but not Hypertrophy. In: Proceeding of the National Academy of Sciences of the United States of America 109 (7), P. 2394-2399. DOI: 10.1073/pnas.1116136109.

Vrselja, A.; Pillow, J. J.; Bensley, J. G.; Ellery, S. J.; Ahmadi-Noorbakhsh, S.; Moss, T. J.; Black, M. J. (2022): Intrauterine Inflammation exacerbates Maladaptive Remodeling of the Immature Myocardium after Preterm Birth in Lambs. In: Pediatric Research 92 (6), P. 1555-1565. DOI: 10.1038/s41390-022-01955-7.

Vrtačnik, P.; Ostanek, B.; Mencej-Bedrač, S.; Marc, J. (2014): The Many Faces of Estrogen Signaling. In: Biochemia Medica (Zagreb) 24 (3), P. 329-342. DOI: 10.11613/BM.2014.035.

Wang, Y.; Huang, S.; Sah, V. P.; Ross, J. Jr.; Brown, J. H.; Han, J.; Chien, K. R. (1998): Cardiac Muscle Cell Hypertrophy and Apoptosis induced by Distinct Members of the p38 Mitogen-Activated Protein Kinase Family. In: The Journal of Biological Chemistry 273 (4), P. 2161-2168. DOI: 10.1074/jbc.273.4.2161.

Wang, Y. (2007): Mitogen-activated Protein Kinases in Heart Development and Diseases. In: Circulation 116 (12), P. 1413-1423. DOI: 10.1161/CIRCULATIONAHA.106.679589.

Wang, J.; Razuvaev, A.; Folkersen, L.; Hedin, E.; Roy, J.; Brismar, K.; Hedin, U. (2012): The Expression of IGFs and IGF Binding Proteins in Human Carotid Atherosclerosis, and the Possible Role of IGF Binding Protein-1 in the Regulation of Smooth Muscle Cell Proliferation. In: Atherosclerosis 220 (1), P. 102-109. DOI: 10.1016/j.atherosclerosis.2011.10.032.

Wang, J.; Liu, S.; Heallen, T.; Martin, J. F. (2018): The Hippo Pathway in the Heart: Pivotal Roles in Development, Disease, and Regeneration. In: Nature Review. Cardiology 15 (11), P. 672-684. DOI: 10.1038/s41569-018-0063-3.

References

Wang, W.; Kang, P. M. (2020): Oxidative Stress and Antioxidant Treatments in Cardiovascular Diseases. In: Antioxidants 9 (12), P. 1292-1316. DOI: 10.3390/antiox9121292.

Wang, Z.; Qi, Y.; Wang, R.; Wu, W.; Li, Z.; Wang, M.; Liu, R.; Zhang, C.; Li, W.; Wang, S. (2020): IGFBP6 Regulates Vascular Smooth Muscle Cell Proliferation and Morphology via Cyclin E-CDK2. In: Journal of Cellular Physiology 235 (12), P. 9538-9556. DOI: 10.1002/jcp.29762.

Windmueller, R.; Leach, J. P.; Babu, A.; Zhou, S.; Morley, M. P.; Wakabayashi, A.; Petrenko, N. B.; Viatour, P.; Morrisey, E. E. (2020): Direct Comparison of Mononucleated and Binucleated Cardiomyocytes Reveals Molecular Mechanisms Underlying Distinct Proliferative Competencies. In: Cell Reports 30 (9), P. 3105-3116. DOI: 10.1016/j.celrep.2020.02.034.

Wiegering, A.; Rüther, U.; Gerhardt, Ch. (2017): The Role of Hedgehog Signalling in the Formation of the Ventricular Septum. In: Journal of Developmental Biology 5 (4), P. 17-30. DOI: 10.3390/jdb5040017.

Witman, N.; Zhou, C.; Grote Beverborg, N.; Sahara, M.; Chien, K. R. (2020): Cardiac Progenitors and Paracrine Mediators in Cardiogenesis and Heart Regeneration. In: Seminars in Cell and Developmental Biology 100, P. 29-51. DOI: 10.1016/j.semcdb.2019.10.011.

Wood, S. M.; Wiesener, M. S.; Yeates, K. M.; Okada, N.; Pugh, C. W.; Maxwell, P. H.; Ratcliffe, P. J. (1998): Selection and analysis of a mutant cell line defective in the hypoxia-inducible factor-1 alpha-subunit (HIF-1alpha). Characterization of hif-1alpha-dependent and -independent hypoxia-inducible gene expression. In: The Journal of Biological Chemistry 273 (14), P. 8360-8368. DOI: 10.1074/jbc.273.14.8360.

World Health Organization (2021): Cardiovascular diseases (CVDs). 11.06.2021, Retrieved 20.07.2022, <https://www.who.int/news-room/fact-sheets/detail/cardiovascular-diseases-(cvds)>

World Health Organization (Mendis, Sh.; Puska, P.; Norrving, B., World Health Organization, World Heart Federation.) (2011): Global atlas on cardiovascular disease prevention and control. Retrieved 20.07.2022, < http://whqlibdoc.who.int/publications/2011/9789241564373_eng.pdf?ua=1>

World Health Organization (2022): Preterm Birth. 14.11.2022, Retrieved 03.01.2023, https://www.who.int/news-room/fact-sheets/detail/preterm-birth

World Health Organization (2023): Preterm Birth. 10.05.2023, Retrieved 25.10.2023, https://www.who.int/news-room/fact-sheets/detail/preterm-birth

Wu, Q.; Chambliss, K.; Umetani, M.; Mineo, C.; Shaul, P. W. (2011): Non-nuclear Estrogen Receptor Signaling in the Endothelium. In: The Journal of Biological Chemistry 86 (17), P. 14737-14743. DOI: 10.1074/jbc.R110.191791.

Wu, B.; Zhang, Z.; Lui, W.; Chen, X.; Wang, Y.; Chamberlain, A. A.; Moreno-Rodriguez, R. A.; Markwald, R. R.; O'Rourke, B. P.; Sharp, D. J.; Zheng, D.; Lenz, J.; Baldwin, H. S.; Chang, C. P.; Zhou, B. (2012): Endocardial Cells form the Coronary Arteries by Angiogenesis through Myocardial-Endocardial VEGF Signaling. In: Cell 151 (5), P. 1083-1096. DOI: 10.1016/j.cell.2012.10.023.

Wu, X.; Zheng, X.; Cheng, J.; Zhang, K.; Ma, C. (2020): LncRNA TUG1 regulates Proliferation and Apoptosis by Regulating MiR-148b/IGF2 Axis in Ox-LDL-stimulated VSMC and HUVEC. In: Life Sciences 243, (8), P. e117287. DOI: 10.1016/j.lfs.2020.117287.

References

Wu, Z.; Shi, Y.; Cui, Y.; Xing, X.; Zhang, L.; Liu, D.; Zhang, Y.; Dong, J.; Jin, L.; Pang, M.; Xiao, R. P.; Zhu, Z.; Xiong, J. W.; Tong, X.; Zhang, Y.; Wang, S.; Tang, F.; Zhang, B. (2023): Single-cell analysis reveals an Angpt4-initiated EPDC-EC-CM cellular coordination cascade during heart regeneration. In: Protein & Cell 14 (5), P. 350-368. DOI: 10.1093/procel/pwac010.

Xie, Z.; Pimental, D. R.; Lohan, S.; Vasertriger, A.; Pligavko, C.; Colucci, W. S.; Singh, K. (2001): Regulation of Angiotensin II-Stimulated Osteopontin Expression in Cardiac Microvascular Endothelial Cells: Role of p42/44 Mitogen-activated Protein Kinase and Reactive Oxygen Species. In: Journal of Cellular Physiologyv188 (1), P. 132-138. DOI: 10.1002/jcp.1104.

Xin, M.; Kim, Y.; Sutherland, L. B.; Qi, X.; McAnally, J.; Schwartz, R. J.; Richardson, J. A.; Bassel-Duby, R.; Olson, E. N. (2011): Regulation of Insulin-like Growth Factor Signaling by Yap governs Cardiomyocyte Proliferation and Embryonic Heart Size. In: Science Signaling 4 (196), P. 70-84. DOI: 10.1126/scisignal.2002278.

Xin, M.; Kim, Y.; Sutherland, L. B.; Murakami, M.; Qi, X.; McAnally, J.; Porrello, E. R.; Mahmoud, A. I.; Tan, W.; Shelton, J. M.; Richardson, J. A.; Sadek, H. A.; Bassel-Duby, R.; Olson, E. N. (2013): Hippo Pathway Effector Yap Promotes Cardiac Regeneration. In: Proceeding of the National Academy of Sciences of the United States of America 110 (34), P. 13839-13844. DOI: 10.1073/pnas.1313192110.

Xu, J. Y.; Lee, Y. K.; Ran, X.; Liao, S. Y.; Yang, J.; Au, K. W.; Lai, W. H.; Esteban, M. A.; Tse, H. F. (2016): Generation of Induced Cardiospheres via Reprogramming of Skin Fibroblasts for Myocardial Regeneration. In: Stem Cells 4 (11), P. 2693-2706. DOI: 10.1002/stem.2438.

Yang, H.; Song, S.; Li, J.; Li, Y.; Feng, J.; Sun, Q.; Qiu, X.; Chen, Z.; Bai, X.; Liu, X.; Lian, H.; Liu, L.; Bai, Y.; Zhang, G.; Nie, Y. (2023): Omentin-1 Drives Cardiomyocyte Cell Cycle Arrest and Metabolic Maturation by Interacting with BMP7. In: Cellular and Molecular Life Sciences 280 (7), P. 186-211. DOI: 10.1007/s00018-023-04829-1.

Ye, L.; D'Agostino, G.; Loo, S. J.; Wang, C. X.; Su, L. P.; Tan, S. H.; Tee, G. Z.; Pua, C. J.; Pena, E. M.; Cheng, R. B.; Chen, W. C.; Abdurrachim, D.; Lalic, J.; Tan, R. S.; Lee, T. H.; Zhang, J.; Cook, S. A. (2018): Early Regenerative Capacity in the Porcine Heart. In: Circulation 138 (24), P. 2798-2808. DOI: 10.1161/CIRCULATIONAHA.117.031542.

Yester, J. W.; Kühn, B. (2017): Mechanisms of Cardiomyocyte Proliferation and Differentiation in Development and Regeneration. In: Current Cardiology Reports 19 (2), P. 13-21. DOI: 10.1007/s11886-017-0826-1.

Yokota, T.; Li, J.; Huang, J.; Xiong, Z.; Zhang, Q.; Chan, T.; Ding, Y.; Rau, C.; Sung, K.; Ren, S.; Kulkarni, R.; Hsiai, T.; Xiao, X.; Touma, M.; Minamisawa, S.; Wang, Y. (2020): P38 Mitogen-activated Protein Kinase regulates Chamber-specific Perinatal Growth in Heart. In: The Journal of Clinical Investigation 30 (10), P. 5287-5301. DOI: 10.1172/JCI135859.

Yuan, X.; Braun, Th. (2017): Multimodal Regulation of Cardiac Myocyte Proliferation. In: Circulation Research 121 (3), P. 293-309. DOI: 10.1161/CIRCRESAHA.117.308428.

Yutzey, K. E. (2017): Cardiomyocyte Proliferation: Teaching an Old Dogma New Tricks. In: Circulation Research 120 (4), P. 627-629. DOI: 10.1161/CIRCRESAHA.116.310058.

Zak, R. (1984): Growth of the heart in health and disease. In: Clinical Cardiology 8 (3), P. 186-666. DOI: 10.1002/clc.4960080313.

Zaffran, S.; Kelly, R. G.; Meilhac, S. M.; Buckingham, M. E.; Brown, N. A. (2004): Right Ventricular Myocardium Derives from the Anterior Heart Field. In: Circulation Research 95 (3), P. 261-268. DOI: 10.1161/01.RES.0000136815.73623.BE.

References

Zeisberg, E. M.; Tarnavski, O.; Zeisberg, M.; Dorfman, A. L.; McMullen, J. R.; Gustafsson, E.; Chandraker, A.; Yuan, X.; Pu, W. T.; Roberts, A. B.; Neilson, E. G.; Sayegh, M. H.; Izumo, S.; Kalluri, R. (2007): Endothelial-to-mesenchymal Transition Contributes to Cardiac Fibrosis. In: Nature Medicine 13(8), P. 952-961. DOI: 10.1038/nm1613.

Zhang, W.; Elimban, V.; Nijjar, M. S.; Gupta, S. K.; Dhalla, N. S. (2003): Role of Mitogen-activated Protein Kinase in Cardiac Hypertrophy and Heart Failure. In: Experimental and Clinical Cardiology 8 (4), P. 173-183.

Zhang, W.; Chen, H.; Qu, X.; Chang, C. P.; Shou, W. (2013): Molecular Mechanism of Ventricular Trabeculation/Compaction and the Pathogenesis of the Left Ventricular Noncompaction Cardiomyopathy (LVNC). In: American Journal of Medical Genetics 163 (3), P. 144-156. DOI: 10.1002/ajmg.c.31369.

Zhang, P.; Shan, T.; Liang, X.; Deng, C.; Kuang, S. (2014): Mammalian Target of Rapamycin is Essential for Cardiomyocyte Survival and Heart Development in Mice. In: Biochemical and Biophysical Research Communication s452 (1), P. 53-59. DOI: 10.1016/j.bbrc.2014.08.046.

Zhang, W.; Shu, C.; Li, Q.; Li, M.; Li, X. (2015): Adiponectin affects Vascular Smooth Muscle Cell Proliferation and Apoptosis through Modulation of the Mitofusin-2-mediated Ras-Raf-Erk1/2 Signaling Pathway. In: Molecular Medicine Reports12 (3), P. 4703-4707. DOI: 10.3892/mmr.2015.3899.

Zhao, B.; Wei, X.; Li, W.; Udan, R. S.; Yang, Q.; Kim, J.; Xie, J.; Ikenoue, T.; Yu, J.; Li, L.; Zheng, P.; Ye, K.; Chinnaiyan, A.; Halder, G.; Lai, Z. C.; Guan, K. L. (2007): Inactivation of YAP Oncoprotein by the Hippo Pathway is involved in Cell Contact Inhibition and Tissue Growth Control. In: Genes & Development 21 (21), P. 2747-2761. DOI: 10.1101/gad.1602907.

Zhao, T.; Liang, X.; Chen, J.; Bao, Y.; Wang, A.; Gan, X.; Lu, X.; Wang, L. (2019): ANGPTL3 inhibits Renal Cell Carcinoma Metastasis by Inhibiting VASP Phosphorylation. In: Biochemical and Biophysical Research Communications 516 (3), P. 880-887. DOI: 10.1016/j.bbrc.2019.06.120.

Zhong, L.; Tang, L.; He, X. (2022): Angiopoietin-like 3 (ANGPTL3) drives Cell Proliferation, Migration and Angiogenesis in Cervical Cancer via Binding to Integrin Alpha v Beta 3. In: Bioengineered 13 (2), P. 2971-2980. DOI: 10.1080/21655979.2021.2024951.

Zhou, J.; Ahmad, F.; Parikh, S.; Hoffman, N. E.; Rajan, S.; Verma, V. K.; Song, J.; Yuan, A.; Shanmughapriya, S.; Guo, Y.; Gao, E.; Koch, W.; Woodgett, J. R.; Madesh, M.; Kishore, R.; Lal, H.; Force, T. (2016): Loss of Adult Cardiac Myocyte GSK-3 Leads to Mitotic Catastrophe Resulting in Fatal Dilated Cardiomyopathy. In: Circulation Research 118 (8), P. 1208-1222. DOI: 10.1161/CIRCRESAHA.116.308544.

Zhu, W.; Zhang, E.; Zhao, M.; Chong, Z.; Fan, C.; Tang, Y.; Hunter, J. D.; Borovjagin, A. V.; Walcott, G. P.; Chen, J. Y.; Qin, G.; Zhang, J. (2018): Regenerative Potential of Neonatal Porcine Hearts. In: Circulation 138 (24), P. 2809-2816. DOI: 10.1161/CIRCULATIONAHA.118.034886.

Zhu *, W.; Zhao, M.; Mattapally, S.; Chen, S.; Zhang, J. (2018): CCND2 Overexpression Enhances the Regenerative Potency of Human Induced Pluripotent Stem Cell-Derived Cardiomyocytes: Remuscularization of Injured Ventricle. In: Circulation Research 122 (1), P. 88-96. DOI: 10.1161/CIRCRESAHA.117.311504.

Printed literatures:

Gilbert, S. F. (2006): Developmental Biology. Sunderland: Sinauer, 8th Edition. Print.

Maton, A.; Lahart, D.; Hopkins, J.; Warner, M. Q.; Johnson, S.; Wright, J. D. (1997). Cells: Building Blocks of Life. New Jersey: Prentice Hall. P. 70-74.

11. Supplementary Data

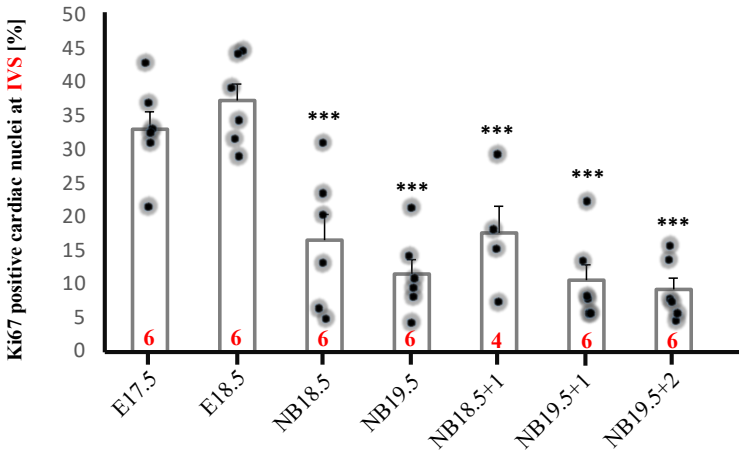

Supplementary Figure 1. Reduced cell cycle activity immediately after birth in the IVS of male mice. Studying the perinatal cell cycle activity in murine ventricular myocardium via immunofluorescence antibody staining against Ki67. The graph represents the percentage of cardiac nuclei demonstrating cell cycle activity (i.e., positive for Ki67) in the interventricular septum (IVS) region at seven represented consecutive stages around birth. The counts of nuclei active in cell cycle shows a steady state between E17.5 and E18.5. At IVS, cell cycle activity drops directly after birth (at NB18.5 and NB19.5). However, cell cycle activity remained unmodified at one and two days after birth (compared to birth). The numbers shown in red represent the sample size n. IVS: Interventricular septum, E: Embryonic stage, NB: Newborn, NB18.5+1 and NB19.5+1: Samples were collected at 24 h after birth, NB19.5+2: Animals were born at day 19.5 and kept for 48 h with mother and then the samples were collected. The results are illustrated as mean values ± SEM, each data point represents one mouse heart. Statistical significance among groups was assessed by one-way ANOVA. ***: $P<0.001$.

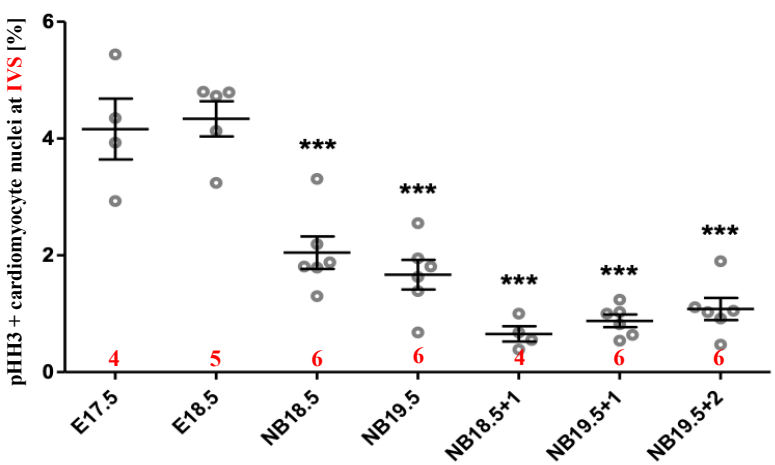

Supplementary Figure 2. Decreased pHH3 rates immediately after birth in CMs located in IVS of male mice. Investigation of the perinatal mitosis rates in CMs at IVS via immunofluorescence antibody staining against pHH3 and Caveolin 3. The graph represents the percentage of CM nuclei showing a mitotic activity (i.e., positive for pHH3) in the interventricular septum (IVS) region at seven demonstrated consecutive stages around birth. Comparing E17.5 and E18.5, the number of mitotically active CM nuclei remained unchanged. At IVS, mitosis incidence reduces directly after birth (at NB18.5 and NB19.5). However, the mitosis rate in CMs reduced further at one day after birth at NB18.5+1 and NB19.5+1, as well as two days after birth compared to birth. The numbers shown in red represent the sample size n. IVS: Interventricular septum, E: Embryonic stage, NB: Newborn, NB18.5+1 and NB19.5+1: Samples were collected at 24 h after birth, NB19.5+2: Animals were born at day 19.5 and kept for 48 h with mother and then the samples were collected. The results are illustrated as mean values ± SEM, each data point represents one mouse heart. Statistical significance among groups was assessed by one-way ANOVA. ***: $P<0.001$.

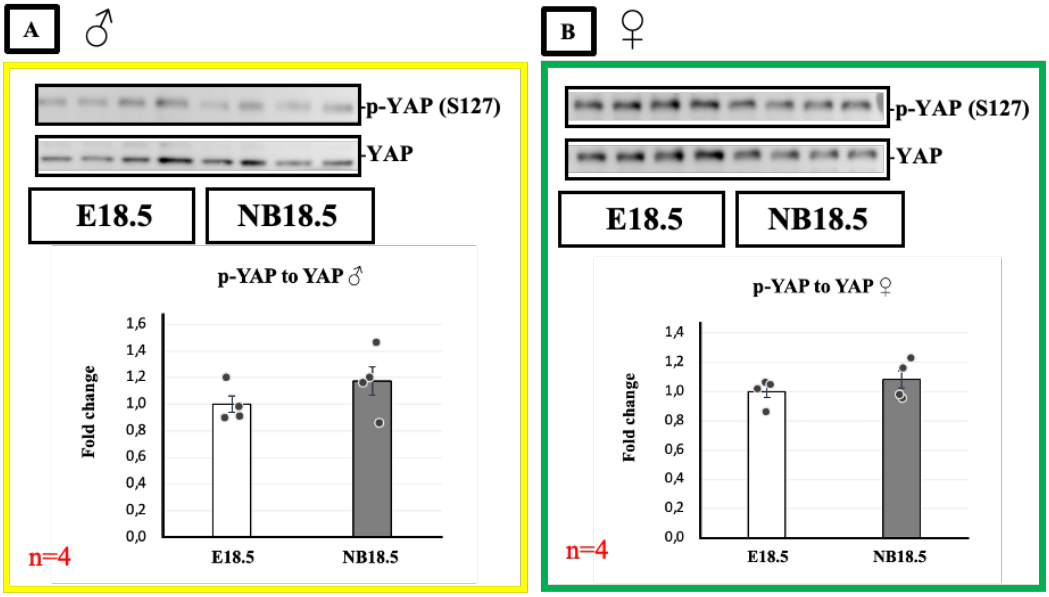

Supplementary Figure 3. Unchanged phosphorylation of YAP in ventricular myocardium of male and female mice directly after birth. The activity of Hippo was monitored by measuring the phosphorylation of YAP using WB experiments. **A)** and **B)** Top, WB using whole heart protein extracts from E18.5 and NB18.5 male (A) and female (B) mice. The phosphorylated form of YAP (at serine 127), and its total protein levels, together with YAP total, were illustrated in yellow (male) and green (female) boxes. **B) (**male**)** and **D) (**female**)** WB quantifications were carried out by normalizing the phosphorylated to the total protein band intensity. The results were normalized to the E18.5 data and were represented as fold change. Data exhibited no modifications in YAP phosphorylation shortly after delivery in male and female mouse hearts. The red numbers reveal the sample size. The results were illustrated as the mean values ± SEM. Statistical significance among groups was assessed by unpaired 2-tailed student *t*-test using SPSS.

Supplementary Table 1. List of cytokines and growth factors showing a significant modification in their availability in male mouse hearts at NB18.5 compared to E18.5 using the cytokine-array kit.

Gene	Protein	Fold change at NB18.5	*P*-Value
Angptl3	Angiopoietin-like 3	0.36	0.003
Cd93	C1q R1/CD93	0.76	0.016
Ccl11	CCL11/Eotaxin	0.73	0.033
RARRES2	Chemerin	0.71	0.01
Chi3l1	Chitinase 3-like 1	0.70	0.047
F9	Coagulation Factor III/Tissue Factor	0.73	0.026
Cxcl16	CXCL16	0.69	0.017
Igfbp3	IGFBP3	0.73	0.029
Igfbp6	IGFBP6	0.68	0.004
Il10	IL-10	0.84	0.032
Il12B	IL-12 p40	0.80	0.021
Il27	IL-27 p28	0.55	0.014
Il33	IL-33	0.87	0.027
Pcsk9	Proprotein Convertase 9/PCSK9	0.39	0.006
Serpinf1	Serpin F1/PEDF	0.58	0.003

Acrp30	Adiponectin/Acrp30	1.53	0.002
Crp	C-Reactive Protein/CRP	1.36	0.003
Col18a1	Endostatin	1.16	0.00026
Igfbp1	IGFBP1	3.74	0.000388
Il6r	IL-6	1.47	0.043
Mmp9	MMP-9	1.36	0.025
Spp1	Osteopontin (OPN)	2.09	0.004
Ptx2	Pentraxin 2/SAP	1.20	0.043
Postn	Periostin/OSF-2	1.42	0.014
Retn	Resistin	1.50	0.000189

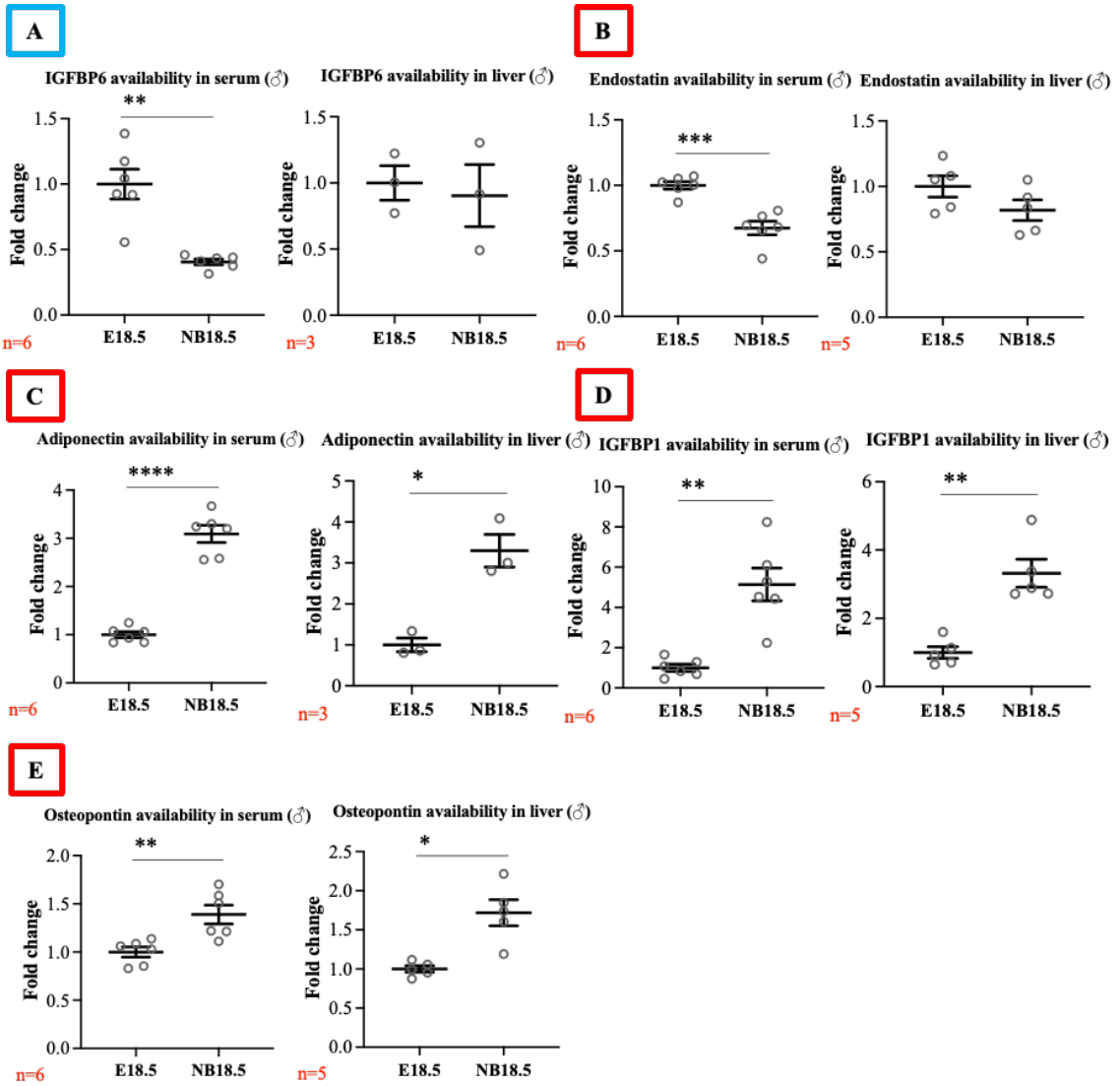

Supplementary Figure 4. Immediate changes in protein levels of IGFBP6, Endostatin, Adiponectin, IGFBP1, and Osteopontin shortly after birth in male mouse serum samples. ELISA experiments were performed using whole liver lysates, as well as serum samples obtained from male mice at E18.5 and NB18.5. **A)** Shortly after delivery (i.e., at NB18.5) the availability of IGFBP6 exhibited significant reduction in serum samples of male mice compared to the fetal stage E18.5, whereas IGFBP6 level in liver remained unchanged. **B)** At NB18.5, the level of Endostatin in serum lysates of male mice was decreased in comparison with shortly before delivery, while this remained unchanged in liver samples at NB18.5 vs. E18.5. **C)** to **E)** ELISA analyses conveyed that Adiponectin, GFBP1, and Osteopontin protein levels exhibited significant reductions in both liver and serum samples obtained from male mice at NB18.5 compared to the fetal stage E18.5. The numbers shown in red represent the sample size. The results are represented as the mean values ± SEM. To perform statistical analyses SPSS software was utilized and the statistical significance among groups was measured by unpaired 2-tailed student *t*-test. *: $P<0.05$, **: $P<0.01$, ***: $P<0.001$, ****: $P<0.0001$.

12. Ehrenwörtliche Erklärung

Hiermit erkläre ich, dass ich die vorliegende Arbeit selbständig und ohne unzulässige Hilfe oder Benutzung anderer als der angegebenen Hilfsmittel angefertigt habe. Alle Textstellen, die wörtlich oder sinngemäß aus veröffentlichten oder nichtveröffentlichten Schriften entnommen sind, und alle Angaben, die auf mündlichen Auskünften beruhen, sind als solche kenntlich gemacht. Bei den von mir durchgeführten und in der Dissertation erwähnten Untersuchungen habe ich die Grundsätze guter wissenschaftlicher Praxis, wie sie in der „Satzung der Justus-Liebig-Universität Gießen zur Sicherung guter wissenschaftlicher Praxis“ niedergelegt sind, eingehalten sowie ethische, datenschutzrechtliche und tierschutzrechtliche Grundsätze befolgt. Ich versichere, dass Dritte von mir weder unmittelbar noch mittelbar geldwerte Leistungen für Arbeiten erhalten haben, die im Zusammenhang mit dem Inhalt der vorgelegten Dissertation stehen, und dass die vorgelegte Arbeit weder im Inland noch im Ausland in gleicher oder ähnlicher Form einer anderen Prüfungsbehörde zum Zweck einer Promotion oder eines anderen Prüfungsverfahrens vorgelegt wurde. Alles aus anderen Quellen und von anderen Personen übernommene Material, das in der Arbeit verwendet wurde oder auf das direkt Bezug genommen wird, wurde als solches kenntlich gemacht. Insbesondere wurden alle Personen genannt, die direkt und indirekt an der Entstehung der vorliegenden Arbeit beteiligt waren. Mit der Überprüfung meiner Arbeit durch eine Plagiatserkennungssoftware bzw. ein internetbasiertes Softwareprogramm erkläre ich mich einverstanden.

_____ _____

Ort, Datum Unterschrift

13. Acknowledgement

First of all, I would like to express my special appreciation to Prof. Dr. med. Christian Jux for the great opportunity to work in his outstanding group, as well as the excellent feedbacks, guidance, and all the essential talks and crucial decisions during the entire period of my project.

Special thanks go to Prof. Dr. Dr. habil. Thomas Braun for his excellent comments, feedbacks, and valuable time concerning my project.

I ow my deepest gratitude to PD Dr. med. Jörg-Detlef Drenckhahn for his outstanding and incredible supervision, support, and feedbacks, as well as his fantastic guidance and being always there for me, during the entire period of my doctoral thesis.

Also, special thanks go to Kirstin Salser for her fantastic supports performing the western blot analyses (*in vitro*) and essential optimization steps (immunofluorescence staining (IF)), as well as teaching me every method in details, being always there for me.

I would also thank to Janina Sommer for her outstanding support concerning the large scale IF experiment for pHH3 analyses on female mouse hearts.

My sincere appreciations go to Michaela Tirre for her excellent help in the precisely performed Cyclin D3/MEF2 – IF experiments, as well as the WB approaches for Glycolysis-involved enzymes.

Moreover, my special thanks go to Simon Pyschny for his great support for kindly conducting the RT-qPCR experiments for Glycolysis-associated enzymes.

Hereby, I would like to express my special appreciations to Jamie-Lee Sauer for her outstanding supports performing the large scale IF staining and Imaging of the pHH3/Caveolin 3 and BrdU-incorporation measurements using image analysis software (*in vitro*), as well as her great personality and presence.

Furthermore, my sincere appreciations go to my parents for being always there for me and supporting me during my entire educational journey in lovely Germany.

Hereby I would like to thank Benedikt Dörflinger for reading giving feedbacks on the abstract part of my thesis. Additionally, I am way thankful for his positive energy and enthusiasm which motivates everyone in the lab.

Last but not least, I owe my deepest gratitude to the entire members of the Institute of Pediatric Cardiology at the Justus Liebig University Giessen for their unconditional support, and for making my doctoral stay such an unforgettable time.

14. Table of Publications

Adibi, P.; Jux, Ch.; Drenckhahn, J. D. (2021): Investigation of the Dynamics of Perinatal Cell Cycle Regulation in the Mouse Ventricular Myocardium. Presentation in: DGPK Jahrestagung: Herzmedizin, 27.02.2021, Wiesbaden, Germany.

Adibi, P.; Jux, Ch.; Drenckhahn, J. D. (2021): Identification of Growth Factors and Regulatory Cytokines during Postnatal Cell Cycle Exit in Cardiomyocytes. Presentation in: Science Day at Medical Faculty of Justus Liebig University, 12.11.2021, Giessen, Germany.